Electron Beam Lithography for Vapor-Phase Deposition of Organosilanes

by

Christopher Ryan Fetterly

A thesis submitted in partial fulfillment of the requirements for the degree of

Doctor of Philosophy

Department of Chemistry

University of Alberta

© Christopher Ryan Fetterly, 2018

Abstract

Self-assembly of functional groups on metal and metal oxide surfaces has been a foundation technology in micro- and nanofabrication. Confinement of reactive groups to a single molecular layer on a surface has been a rich field of scientific advancement, particularly with alkanethiolates on gold and silanes on silicon oxide. The ability to design interfaces that self-organize in the nanoscale regime for interesting macroscale applications has lead to advancements in fields such as genetics, energy storage, and textiles. Precise positioning of self-assembled monolayers in discrete regions on a surface allows for addressibility of a surface when the locations of reactivity are known. As feature sizes shrink towards the sub-10 nm regime, the density of functional elements increases on a surface, resulting in increased information density and higher throughput devices.

Electron beam lithography (EBL) has been a longstanding tool used in the semiconductor industry to define nanoscale features on a surface. Unlike photolithography, EBL is not limited by the diffraction limit of light; EBL permits the design of arbitrary pattern geometries and at high resolution. Surfaces designed with EBL can be used to guide self-assembly, or to tailor pre-assembled surface chemistries. The result is a functional nanoscale pattern, with diverse application potential.

This thesis is based on vapor-phase deposition of organosilanes. Using EBL to pattern a polymeric resist as a template, the system can be used to guide the deposition of

organosilanes to discrete locations on a silicon oxide surface, confining reactive functional groups to defined nanoscale dimensions.

Three different aspects of the method were investigated, which guided the arrangement of the thesis. The first was the use of the method to precisely position gold nanoparticles on a silicon surface, which was achieved by guiding the deposition of positively charged amine groups, which could bind negatively charged citrate-capped gold nanoparticles. The second aspect was the first report of EBL-defined condensation features with 3D morphology when depositing 3-aminopropyltrimethoxysilane. These structures were explored, with special attention to using these features as a spacer deposition process analogous to approaches used in semiconductor manufacturing. And finally, two lithographic approaches were compared for the construction of a fluorescent nanoarray.

The thesis concludes with directions for optimization of each of these three aspects of EBL-guided vapor-phase deposition of organosilanes, and describes preliminary work to guide future efforts. The nanoparticle work may couple to existing research group directions in plasmonics. The 3D reactive amine features could be applied to established work in density doubling techniques, or directed self-assembly approaches. Lastly, the fluorescent nanoarray could be optimized to improve its application in super-resolution microscopy techniques.

Preface

Chapter 1 provides the background for self-assembled monolayers and introduces the concept of patterned self-assembled monolayers. Methods of patterning organosilanes were reviewed, concluding with discussion of electron beam lithography for patterning self assembled monolayers via vapor-phase deposition.

Chapter 2 stresses the importance of choosing an appropriate electron beam lithography resist for patterning aminosilanes from the vapor phase. Patterned aminosilanes were used to form high fidelity patterns of gold nanoparticles, and the interactions between the resist and aminosilane vapor were examined. The chapter has been published in *Langmuir* as of April 3, 2018, and is titled "Vapor-Phase Nanopatterning of Aminosilanes with Electron Beam Lithography: Understanding and Minimizing Background Functionalization". I performed the experiments and wrote the initial draft with Erik Luber. The final manuscript was reviewed and revised by Jillian Buriak, Brian Olsen, Erik Luber, and me.

Chapter 3 describes the formation of three dimensional condensation structures that form as a result of confining vapor-phase deposition of aminosilanes into nanoscale geometric templates created with electron beam lithography. The work is framed in the context of spacer formation for the semiconductor industry. To the best of our knowledge, the chapter is the first report on intentional creation of these high-aspect ratio structures using electron beam lithography.

Chapter 4 describes fabrication of a nanoscale fluorescent array, the initial goal for the thesis project. Two general patterning approaches were used, and the merits of each were examined. The results of this work spurred investigation into the structures described in chapter 3, and the particle patterning methodology in chapter 2.

Chapter 5 highlights initial work done to optimize the work in each of the previous chapters and outlines potential routes for extending the work in the thesis.

Acknowledgment

I would like to thank my supervisor, Dr. Jillian Buriak for her encouragement, patience, and mentorship. I am grateful for the incredible freedom you provided me during my studies and the guidance you provided for both my work and development as a junior scientist. My deep thanks to the impeccable group members in the Buriak Group, with whom conversations alleviated stress and illuminated new pathways in both life and science. A very special thanks to my mentor and friend Dr. Erik Luber; I am a better scientist and person for having met you. Thanks to Brian Olsen for your diverse technical and conversational skills. Tate Hauger, thank you for your eagerness to lend a helping hand or good book. Kelli Luber thank you for the warmth you bring to everyone you interact with. A very big thank you to previous and current group members Dr. Cong Jin, Dr. Bing Cao, Chengcheng Rao, Dr. Fenglin Liu, Jennifer Ozdoba, Hezhen Xie, Hao Wang, Minjia Hu, Dr. Peter Kalisvaart, Dr. Sayed Youssef Sayed, Mahmoud Almadhoun, Dr. Jeremy Bau, Dr. Jeffrey Murphy, Dr. Nathanael Wu, Gayashani Ginige, Jasper Woodard, and Aaron Kirkey. You are all my experimental brothers and sisters in arms; thank you for your support, inspiration, assistance, and encouragement.

My sincere grattitude to my supervisory committee members Dr. Christopher Cairo and Dr. Robert Campbell. Without your support I would not have been able to experience such a rich breadth of scientific experience during my PhD studies. Thank you to my candidacy committee members Dr. Mark McDermott and Dr. Nils Petersen for your thoughtful examination of my work and my knowledge. Thank you to my external defense examiner Dr. Matthew Paige for your thorough examination of my thesis. Thank you Dr. Bob Jordan for chairing my defense examination.

Thank you to all of the staff of NRC-NINT for enjoyable conversations and truly excellent scientific expertise: Paul Conception, Jennifer Ozdoba, Dr. Ken Harris and Mike Xia. My deep thanks to the staff of the nanoFAB, whose professionalism was top-tier in answering my inquiries, and supporting me in my experimental journeys: Dr. Eric Flaim, Dr. Aaron Hryciw, Peng Li, Stephanie Bozic, Glenn Elaschuk, Melissa Hawrelechko, Dr. Anqiang He, Dr. Shihong Xu, Scott Munro, and Les Schowalter.

My thanks to all Department of Chemistry technical, teaching, and support staff, who work tirelessly to ensure myself and other graduate students are able to meet the challenges we face: Anita Weiler, Matthew Kingston, Bernie Hippel, Andrew Yeung, Dr.

Karlene Lynch, Jason Dibbs, Dieter Starke, Paul Crothers, Dr Hayley Wan, and Ryan Lewis. Dr. Anna Jordan thank you for your delightful grammatical insight into my work. Thank you to the wonderful community of chemistry graduate students, particularly in the Chemistry Graduate Students' Society and U of A Nanogroup, who went over and beyond to ensure a valuable experience for all chemistry grads. I would also like to thank my sources of funding, including the National Sciences and Engineering Research Council of Canada, Alberta Innovates, and the University of Alberta.

And of course thank you to my entire family. My love and thanks to my parents Carol and Jim Fetterly, and brother Nicholas who lovingly supported me throughout my entire academic career. A fuzzy thanks to Suki and Odin who greet me warmly every single day. My biggest thanks is reserved for my love and partner in life, Kasia Caputa. I would never have made it this far without you. Thank you to my heart, my little Edith, who raises me up with the slightest smile and brings me the fullness of the human experience.

Table of Contents

Abstract....ii

Preface....iv

Acknowledgment....vi

1 Introduction....1

1.1 Overview of the Thesis....1

1.1.1 Historical Framework of Self-Assembly on Surfaces....2

1.1.2 From Surface Tension to Organosilanes and Alkanethiolates....5

1.1.3 Self-Assembly of Organosilane Monolayers....8

1.1.4 Surface Cleaning and Activation....16

1.1.5 Vapor-Phase Processing with Organosilanes....18

1.2 Lithography with Organosilanes....20

1.2.1 Photolithography of Organosilanes....21

1.2.2 Electron Beam Lithography of Organosilanes....25

1.3 Scope and Thesis Statement....29

1.3.1 Thesis Statement....29

1.3.2 Chapter 1 Scope....29

1.3.3 Chapter 2 Scope....30

1.3.4 Chapter 3 Scope....30

1.3.6 Chapter 4 Scope....30

1.3.7 Chapter 5 Scope....31

2 Electron Beam Lithography Nanopatterning of Aminosilanes from the Vapor Phase: Pattern Selectivity of Colloidal Gold Self Assembly....32

2.1 Introduction....32

2.2 Results and Discussion....35

2.2.1 Vapor-phase Deposition of Aminosilanes on Unpatterned surfaces....35

2.2.2 Morphology of Patterned Aminosilanes....37

2.2.3 Gold Colloid Self-Assembly on Aminosilane Nanopatterns....39

2.2.4 Vapor-phase Permeation of Aminosilanes through EBL Resists....43

2.2.5 PMMA and ZEP520A: Understanding Differences in Background Functionalization with APTMS....49

2.2.6 Patterning of Au Nanoparticles using APDIPES and ZEP520A....55

2.3 Conclusions....57

2.4 Experimental....58

2.4.1 EBL Mask Fabrication....58

2.4.2 Vapor-phase Deposition....59

2.4.3 Gold Nanoparticle Conjugation....60

2.4.4 Characterization....61

2.4.5 Surface and Sample Preparation....63

3 Aminosilane Nanostructures Formed by Vapor-Phase Directed Self Assembly as Trench and Hole Spacers....64

3.1 Introduction....64

3.2 Results and Discussion....67

3.2.1 Mask Characterization..67

3.2.2 Hole Spacer Morphology...68

3.2.3 Trench Spacer Morphology..73

3.2.4 Conformality of Spacers in Alternative Geometries.................................77

3.2.5 Pitch Limitations in Contact Hole Spacers..79

3.2.6 Pitch Limitations in Trench Spacers...82

3.2.7 Potential Frequency Doubling of Wider Linewidths.................................86

3.2.8 Structure Formation Mechanism and Alternative Organosilanes...............90

3.2.9 Aminosilane Nanostructures as Spacers: Relevance to Density
Multiplication Strategies...94

3.3 Conclusion...99

3.4 Experimental...102

3.4.1 surface and Sample Preparation..102

3.4.2 Mask Fabrication...102

3.4.3 Vapor-Phase Deposition...103

3.4.4 Reactive Ion Etching...103

3.4.5 AFM Imaging..104

3.4.6 SEM Imaging...104

3.4.7 Helium Ion Microscope (HiM) Imaging..105

4 Lithographic Approaches for Patterning Organosilanes in Fluorescent Nanoarray
Applications...106

4.1 Introduction...106

4.1.1 Lithography for Fluorescent Nanoarray Fabrication....107
4.1.2 Super-Resolution Fluorescence Microscopy....109
4.2 Results and Discussion....112
4.2.1 Positive Tone Array Fabrication Patterning....113
4.2.2 Negative Tone Array Fabrication....120
4.2.3 Cyanine Labeled Fluorescence Array....126
4.2.5 Evaluation of Surface Passivation....129
4.2.6 Super-Resolution Microscopy Requires Effective Background....131
Fluorescence Reduction....131
4.3 Summary....136
4.4 Experimental....137
4.4.1 Surface and Sample Preparation....137
4.4.2 AFM Imaging....138
4.4.3 Vapor-Phase Deposition Verification....138
4.4.4 Mask Fabrication....139
4.4.5 Vapor-Phase Deposition....141
4.4.6 Fluorescent Imaging and Mounting....141
4.4.7 Image Reconstruction....143
5 Thesis Summary and Outlook....144
5.1 Summary of Chapters....144
5.1.1 Chapter 1....145
5.1.2 Chapter 2....145

5.1.3 Chapter 3..146

5.1.4 Chapter 4..148

5.2 Process Development for Future Research Optimization...............................149

5.2.1 DLVO/XDLVO for Particle Immobilization..149

5.2.2 Hardmasks and Alternative Lithographic Approaches for Patterning Organosilanes..153

5.2.3 Super-Resolution Microscopy..163

References..166

List of Abbreviations

LB	Langmuir-Blodgett
SAM	Self-assembled Monolayer
OTS	n-octadecyltrichlorosilane
APTES	3-aminopropyltriethoxysilane
APTMS	3-aminopropyltrimethoxysilane
TFOCS	tridecafluoro-1,1,2,2-tetrahydrooctyl-1-trichlorosilane
MPTMS	3-mercaptopropyltrimethoxysilane
APDIPES	3-aminopropyldiisopropylethoxysilane
MPTES	3-mercpaptopropyltriethoxysilane
HMDS	hexamethyldisalazane
CVD	chemical vapor deposition
HSQ	hydrogen silsesquioxane
EBL	electron beam lithography
PMMA	poly(methyl methacrylate)
AFM	atomic force microscopy
PEG	polyethylene glycol
XPS	x-ray photoelectron spectroscopy
MIBK	methyl isobutyl ketone
IPA	isopropyl alcohol
DMAC	N,N-dimethylacetamide
SEM	scanning electron microscopy
RIE	reactive ion etching
ITRS	International Technology Roadmap for Semiconductors
SADP	self-aligned double patterning
EUV	extreme ultraviolet
IC	integrated circuit
LELE	litho-etch-litho-etch
LFLE	litho-freeze-litho-etch
LLE	litho-litho-etch
DTD	dual-tone development
ALD	atomic layer deposition
CMP	chemical mechanical polishing
SAFIER	Shrink Assisted Film for Enhanced Resolution
RELACS	Resolution Enhancement Lithography Assisted by Chemical Shrink
TEM	transmision electron microscopy
FIB	focused ion beam
STORM	stochastic optical reconstruction microscopy
TIRF	total internal reflectance microscopy
DCE	dichloroethane
FITC	fluoroscein isothiocyanate

SDS	sodium dodecyl sulfate
3D	three dimensional
CY5	cyanine-5
FFT	fast fourier transform
DT20	DDS-Tween20
DDS	dichlorodimethylsilane
NA	numerical aperture
GLOX	glucose oxidase
DIC	differential interference contrast
DLVO	Derjaguin, Landau, Verwey, and Overbeek
MHA	16-mercaptohexadecanoic acid
TMAH	tetramethylammonium hydroxide
ICPRIE	inductively coupled plasma reactive ion etching

List of Figures

Figure 1.1: Paraphrased from Reference 11. Schematic illustration of a Langmuir trough. Liquid is placed in an enameled tray T. Above the tray is a balance with a knife edge K resting on a glass plate G fastened to a support S. One end of the balance beam has a counterweight, while the other has a knife edge K′ from which hangs a pan P. Glass rods R and R′, cemented to the knife edge, pass through two small holes in a strip of paper B, which floats upon the surface of the water in the tray. To prevent the paper from being softened by the water, it is dipped in a solution of paraffin in benzene. The length of the paper strip B is less than the width of the tray so that it can move freely without touching the sides of the tray. The surface of the water between the strips A and B is covered by an oil film. As strip A is moved toward B, the oil film is pushed ahead of it until it begins to exert a force on the paper strip B. Reprinted with permission from reference 9. Copyright 1917 American Chemical Society....4

Figure 1.2: Schematic illustration of the transfer of a monolayer film from a water surface to a solid surface. Films are prepared as described in Figure 1.1 with the exception of the addition of lever L, hand winch W, and pinch clamps J attached to rod H. By winding the winch W, the rod can be raised, lifting glass slide G, or lowered. Continuous pressure must be applied on the film to maintain monomolecular structure. Reprinted with permission from reference 13. Copyright 1935 American Chemical Society....5

Figure 1.3: Chemisorption of n-octadecyltrichlorosilane (OTS) on glass. Reprinted with permission from reference 18. Copyright 1980 American Chemical Society....7

Figure 1.4: Schematic diagram of an ideal, single-crystalline SAM of alkanethiolates supported on a gold surface with a (111) texture. The anatomy and characteristics of the SAM are highlighted. Reprinted with permission from reference 22. Copyright 2005 American Chemical Society....8

Figure 1.5. Five of the most common organosilanes used for formation of self-assembled monolayers on metal oxide surfaces. a) n-octadecyltrichlorosilane (OTS), b) tridecafluoro-1,1,2,2-tetrahydrooctyl-1-trichlorosilane (TFOCS), c) 3-aminopropyltriethoxysilane (APTES), d) 3-aminopropyltrimethoxysilane (APTMS), and e) 3-mercaptopropyltrimethoxysilane (MPTMS)....10

Figure 1.6. Three-step mechanism for monolayer formation by silanes on OH-terminated surfaces. Note in Step 3, condensation ideally proceeds to form a covalently bound monolayer that is also laterally cross-linked (bottom right), but insufficient control over the water content and other reaction conditions may yield disordered inhomogeneous multilayers (bottom left). Reprinted with permission from reference 17. Copyright 2014 John Wiley and Sons....11

Figure 1.7: AFM images showing the initial deposition of small islands, followed by secondary nucleation, filling in of the empty space, and finally complete formation with outlines of the initial islands. Deposition times are a) 15 s immersion, b) 1 min immersion, c) 5 min of immersion, and d) 35 min of immersion. Reprinted with permission from reference 58. Copyright 1995 American Chemical Society....................14

Figure 1.8: Schematic representation of dynamic equilibration of siloxane linkages on a native oxide-capped silicon surface. Lateral rearrangement of Si-O bonds is assumed to take place continuously within a two-dimensional hexagonal lattice defined by the packing of hydrocarbon tails. Reprinted with permission from reference 70. Copyright © 1995 Published by Elsevier Ltd..15

Figure 1.9: (a) Cartoon representation of the OTS SAM on silica based on results from multiple transmission-reflection (MTR) IR results. (b) Cartoon representation of possible “lipid-like” arrangement of alkyl chains with C1–C2 gauche defects to account for the problem of volume constraints of the alkyl chains. Reprinted with permission from reference 73. Copyright 2013 American Chemical Society...16

Figure 1.10: (a) Schematic of an idealized vapor deposition process. (b) Realistic vapor deposition in which agglomeration occurs before binding to the surface. (c) Realistic vapor deposition with an oil barrier layer showing agglomerates diffusing slowly through the barrier layer relative to individual SCA molecules. An example of a trifunctional silane coupling molecule is depicted, with the binding groups highlighted in blue and the R group shown as a linear alkane chain. Reprinted with permission from reference 101. Copyright 2012 American Chemical Society...20

Figure 1.11: Overview of photolithography scheme with positive and negative tone photoresists. Following development, resists often are used for pattern transfer into the surface via an etching step..22

Figure 1.12: Schematic of the process for patterned, selective copper CVD on aminosilanes patterned via photolithography. Reprinted with permission from reference 121. Copyright 1995 American Chemical Society..23

Figure 1.13: a) Overview of light-directed spatially addressable parallel chemical synthesis by photodeprotection utilizing aminosilane linkages. b) Spatially localized photodeprotection and fluorescent labeling. Reprinted with permission from reference 134, adapted. Copyright 1991 The American Association for the Advancement of Science...24

Figure 1.14:.Schematic representation of the basic steps of electron beam lithography process. Reprinted with permission from reference 146, adapted. Copyright 2009 IOP Publishing Ltd..26

Figure 1.15: Lateral force AFM images of binary patterning of chloro- and alkoxysilanes through a PMMA mask. Schematic representation on the right. Reprinted with permission from reference 153(adapted). Copyright 2004 American Chemical Society....................27

Figure 1.16: Schematic representation of positive tone molecular liftoff technique for depositing aminosilanes through EBL patterned PMMA masks. Then, PMMA is removed and DNA origami structures can be assembled on a patterned organosilane film. Reprinted with permission from reference 156. Copyright 2014 American Chemical Society....................28

Figure 1.17: Schematic representation of negative tone patterning technique using EBL patterned HSQ. Aminosilane is functionalized on patterned SiO_x features, which are utilized for DNA origami assembly. Reprinted with permission from reference 158. Copyright 2012 American Chemical Society....................29

Figure 2.1. AFM images of APTMS (a) and APDIPES (b) as deposited on (100) silicon with native oxide. Reprinted with permission from reference 159 Copyright 2018 American Chemical Society....................35

Figure 2.2 Chemical structures of aminosilanes and resists used in this work: (3-aminopropyl)trimethoxysilane (APTMS), 3-aminopropyldiisopropylethoxysilane (APDIPES), poly(methylmethacrylate) (PMMA), MW = 950,000 and ZEP520A, MW = 57,000. Reprinted with permission from reference 159. Copyright 2018 American Chemical Society....................36

Figure 2.3 SEM micrograph of patterned ZEP520A(57k) after EBL exposure and development, with 30 nm diameter holes with a 500 nm square pitch. Scale bar is 1 µm. Reprinted with permission from reference 159. Copyright 2018 American Chemical Society....................37

Figure 2.4 Patterned APTMS and APDIPES after resist removal. a) SEM image of APTMS features post-liftoff of resist. b) AFM height map of APTMS dot array showing tall tubular morphology. c) SEM image of APDIPES features post-liftoff of resist. d) AFM height map of APDIPES dot array showing a low profile morphology. Corresponding AFM height profiles shown below, taken along the horizontal direction going through the center of the dots. The thick line (black) is the median of all the individual height profiles (12 per image). All scale bars are 1 µm. Reprinted with permission from reference 159. Copyright 2018 American Chemical Society....................38

Figure 2.5 SEM micrographs of homogeneous layers of APTMS and APDIPES deposited on silicon conjugated to gold nanoparticles without patterning a) APTMS on silicon with gold nanoparticles and b) APDIPES on silicon with gold nanoparticles. Reprinted with permission from reference 159. Copyright 2018 American Chemical Society....................40

Figure 2.6 Au nanoparticle conjugation of aminosilane features patterned using PMMA(950k) and ZEP520A(57k) resist masks. a) APTMS patterned through PMMA(950k), b) APTMS patterned through ZEP520A(57k), c) APDIPES patterned through PMMA(950k), and d) APDIPES patterned through ZEP520A(57k). All scale bars are 1 μm. Reprinted with permission from reference 159. Copyright 2018 American Chemical Society..........41

Figure 2.7 SEM micrographs of unpatterned resists undergoing particle conjugation after resist removal. a) PMMA (950k) after APTMS deposition b) ZEP520A (57k) after APTMS deposition. All scale bars are 1 μm. Reprinted with permission from reference 159. Copyright 2018 American Chemical Society..........44

Figure 2.8. SEM micrographs of unpatterned resists undergoing particle conjugation after resist removal. a) PMMA (950k) after APDIPES deposition b) ZEP520A (57k) after APDIPES deposition. Reprinted with permission from reference 159. Copyright 2018 American Chemical Society..........45

Figure 2.9 High resolution XPS scans of the N(1s) region after APTMS deposition (a) on bare, clean silicon with native oxide, (b) unpatterned film of PMMA(950k) which was then removed, and (c) on an unpatterned film of ZEP520A(57k) which was then removed. Reprinted with permission from reference 159. Copyright 2018 American Chemical Society..........47

Figure 2.10 High resolution XPS scans of the N(1s) region after APDIPES deposition (a) on bare, clean silicon with native oxide, (b) unpatterned film of PMMA(950k) which was then removed, and (c) on an unpatterned film of ZEP520A(57k) which was then removed. Reprinted with permission from reference 159. Copyright 2018 American Chemical Society..........48

Figure 2.11 SEM micrographs of unpatterned resists undergoing particle conjugation after resist removal. a) ZEP520A (57k) after removal and nanoparticle solution immersion for 48 h and b) PMMA (950k) after resist removal and nanoparticle solution immersion for 48 h. Scale bars are 1 μm. Reprinted with permission from reference 159. Copyright 2018 American Chemical Society..........50

Figure 2.12 SEM micrographs of unpattered APTMS (a) and patterned APTMS (b) through PMMA(495k) resist conjugated with gold nanoparticles. Scale bars are 2 μm. Reprinted with permission from reference 159. Copyright 2018 American Chemical Society..........51

Figure 2.13 SEM micrographs of patterned APDIPES utilizing ZEP520A (57k) following 48 h gold nanoparticle conjugation and rinsing. a) 50 nm, 200 nm pitch line grating. b) 500 nm pitch square dot array. c) 30 nm minimum separation distance between Fresnel

pattern lines. d) 650 nm base width triangle. Reprinted with permission from reference 159. Copyright 2018 American Chemical Society..56

Figure 2.14. Schematic of typical procedure for organosilanes deposition used in this study. Reprinted with permission from reference 159. Copyright 2018 American Chemical Society..62

Figure 3.1. Formation of APTMS nanostructures by electron beam lithography and vapor-phase deposition..66

Figure 3.2: Helium ion images of clusters of APTMS hole spacer structures 105 nm diameter at 250-nm pitch on glass coverslips. a) Clusters show clear penetration to the surface, residual resist is seen on this surface as the resist was stripped via organic solvent instead of plasma, and b) Closeup of ring structures showing uniform sidewall thicknesses and complete pore depth to the surface...67

Figure 3.3: Example of masks utilized in this study patterned through ZEP520(57k) mask. a) Dot shot features for contact hole spacers, b) line structures for trench spacer formation, and c, d) alternate geometries for conformality testing and size effects..........68

Figure 3.4: AFM image of SiOx hole spacers. a) Clusters of three hole spacers at 250 nm pitch, separated by 500 nm from the neighbouring cluster, b) Height profile of line selection shown in a, and, c) 3D render of SiOx hole spacers indicating full depth pore profiles...69

Figure 3.5: Contact hole spacer structures as seen in SEM. a) top down of 81 nm diameter hole spacers b) tilt image of hole spacer array c) higher density hole spacers, 104 nm diameter and d) higher magnification tilt image suggesting tube morphology of spacers. 70

Figure 3.6: Height of SiO_x hole spacers as a function initial template height before removal. Above 200 nm thick resists, hole spacers were prone to breakage, thus 200 nm resists were settled on as a default resist thickness...71

Figure 3.7: Swelling ratio of hole spacers at a deposition temperature of 80 °C versus exposure dose. Spacer diameter is stable for effective clearance dose regime, matching initial template dimensions...72

Figure 3.8: SEM images of trench spacers of SiO_x formed from line grating masks patterned in ZEP520A. a) Top-down view of 150 nm pitch line structures, b) Tilt image of line structures, 500 nm pitch, c) Higher magnification of 150 nm pitch structures showing edge effects, and d) Single line structure showing appearance of closed cap morphology...73

Figure 3.9: AFM image of SiO_x line structures with 100 nm wide nominal resist width. a) 100 nm wide structures with 500 nm pitch, b) Height profile of line selection shown in a, and c) 3D rendering of SiO_x line indicating height dip at ridge and overall height...........75

Figure 3.10: AFM image of SiO_x line structures, 500 nm pitch, at varied deposition times. a) 18 h deposition time, b) 2 h deposition, c) 30 min deposition, and d) 15 min deposition. 76

Figure 3.11: Plot of SiO_x line structures heights versus varied deposition time. 15 min deposition time did not reach full temperature...76

Figure 3.12: SEM images of SiO_x spacer structures created with varied geometries. a) Squares ranging from 100 nm to 1 µm in diameter, b) Large diameter holes, 100 nm to 1 µm with edge structures, c) Triangular structures ranging from 100 nm to 1 µm in edge length, and d) Closeup of triangular condensation edge structures..................................78

Figure 3.13: SEM images of SiO_x line structures with varying intersection gap widths. a) 500 nm pitch square lattice b, c) Square lattice structure of SiO_x lines where intersection gap is 70 nm d) close-up of closed intersection e, f) Lattice of SiO_x line structures where intersection gap is greater than 112 nm and has lead to open pores at square intersection. g) close-up of an open pore intersection..79

Figure 3.14: SEM images of SiO_x hole spacers at varying pitches, centre-to-centre a, c, e, and g) are 25k magnifications of hole arrays with pitches of 250, 150, 100, and 75 nm, respectively, and b, d, f, and h are images of each respective array showing the effect of high density on morphology..81

Figure 3.15: Helium ion microscope images of SiO_x line grating structures formed via EBL and 2 h vapor deposition of APTMS through ZEP520A mask with plasma removal. Single pixel line grating template at increasing pitches of 500 nm (a), 200 nm (b), 100 m, (c), 90 nm (d), 80 nm (e) and 70 nm (f)..83

Figure 3.16: SEM images of SiO_x line grating structures formed via EBL and 2 h vapor deposition of APTMS through ZEP520A mask with plasma removal. Single pixel line grating template had increasing pitches of a) 500 nm, b) 200 nm, c) 150 nm, d) 100 nm, e) 90 nm, f) 80 nm, g) 70 nm, and h) 40 nm..85

Figure 3.17: SEM images of SiO_x line grating structures formed in with area exposure at varying linewidths. Each image shows 500 nm pitch lines and is followed by it's 1:1 duty cycle image where the gap width between lines was set to equal the linewidth. Dimensions are design linewidths and pitches. a) 100 nm linewidth at 500 nm pitch b) 100 nm linewidth with 100 nm pitch, c) 90 nm linewidth at 500 nm pitch, d) 90 nm linewidth at 90 nm pitch, e) 80 nm linewidth at 500 nm pitch, f) 80 nm linewidth at 80 nm pitch, g) 70 nm linewidth at 500 nm pitch, h) 70 nm linewidth at 70 nm pitch, i) 60

nm linewidth at 500 nm pitch, j) 60 nm linewidth at 60 nm pitch, k) 50 nm linewidth with 500 nm pitch, and l) 50 nm linewidth at 50 nm pitch..87

Figure 3.18: Tilted SEM images of single pixel lines forming SiO_x structures with 5 nm Cr coating. Trenches were milled by Ga column in a Zeiss HiM instrument. a) 500 nm pitch lines showing ridge formation b) Tilt image of shallow and deep Ga-FIB trench, c) Cross section of single line at deep trench and d) Closeup of c.......................................89

Figure 3.19: Tilted SEM images of SiO_x spacer structures (18 h deposition time) after an oxide etch to open central pores and troughs. a) 500 nm pitch contact hole spacers b) Tilt image of a single contact hole spacer c) Top down view of 150 nm pitch lines after oxide etch and d) Closeup of end of lines showing loss of ridge-like cap and opening of central gap matching contrast of surrounding surface...90

Figure 3.20: Line and circular edge structures formed by vapor-phase deposition of aminosilanes. a) Line structures formed in PDMS soft lithography templates reprinted with permission from refs [238] and [239], and b) Ring structures formed by vapor deposition of aminosilanes in particle lithography reprinted with permission from reference 182. Copyright American Chemical Society..92

Figure 3.21. AFM images of MPTMS spacer structures formed through a ZEP mask after solution based removal with sonication. a) Large diameter circle features, b) Line height profile of circular feature shown in a, c) Large square shaped features, and d) Line height profile of square in c..93

Figure 3.22. Example of density doubling multiplication strategies from the International Technology Roadmap for Semiconductors. Reprinted with permission from reference [245] Copyright Semiconductor Industry Association (SIA) 2009..96

Figure 3.23: Overview of chemical shrink process using the RELACS system. a) Process flow of patterning contact holes, coating, baking, and development, and b) Achievable shrinkage metrics for the RELACS approach. Reprinted with permission from reference [269]. Copyright 2015 SPIE..97

Figure 3.24. Potential shrinking scheme for line and hole nanostructures formed by APTMS deposition through EBL defined templates..98

Figure 3.25: Example of a commercial CVD system for application of silanes from the vapor phase by YES Engineering. Reprinted with permission from YES Engineering.. 100

Figure 4.1: Example of a fluorescent nanoarray created with semiconductor processes (photolithography) and vapor deposition of aminosilanes as anchors. a) Four color composite scanned array with 700-nm centre-to-centre positions, and b) Cluster plot of normalized intensities of test array shown with 4.2 pixels per spot. Reprinted with

permission from reference [280]. Copyright © 2010, American Association for the Advancement of Science......108

Figure 4.2: a) Conventional image of closely spaced fluorescent molecules that form the shape of a boxing glove. The resolution of the image is limited by diffraction. b–e) By sequentially switching on and imaging different subsets of molecules (b,c), the location of each molecule corresponding to the centre of the emitted fluorescence point spread function, can be precisely determined (d,e), and f) A super-resolved image is created by plotting the positions of all localized molecules. Reprinted with permission from reference [308] © 2016 Nature Publishing Group, a division of Macmillan Publishers Limited......111

Figure 4.3: Positive tone fabrication scheme for fluorescent nanoarrays. First the surface is coated with the resist of choice. Following exposure and development, the chip with exposed holes is placed into a desiccator with neat organosilane. Following deposition, the chip is removed and the resist is removed in a solvent such as dichloroethane (DCE). Finally, the chip is immersed in the labeling solution containing the reactive fluorophore of interest......113

Figure 4.4: Hole profiling and liftoff to confirm effective clearance dose on glass surfaces for clustered and regular arrays. a) AFM tapping mode height image. 30 kV, 30 µm, 250 nm pitch, 12 fC/dot, 60 s O_2 plasma 500 mTorr descum, b) AFM tapping mode height image. 30 kV, 30 µm, 150 nm pitch, 12 fC/dot, 60 s O_2 plasma 500 mTorr descum, c) AFM tapping mode trench profile of a, and d) AFM tapping mode height image. 15 nm AuPd metal lift-off......115

Figure 4.5: Overall labeling scheme used for labeling surface bound amine functional groups with FITC and Cy5 fluorophores. La belling in this work followed conditions shown here, unless otherwise stated......116

Figure 4.6. Sparse and dense layout distances for fluorescent nanoarrays......116

Figure 4.7: Total internal reflectance fluorescence, 60X magnification images of APTMS arrays labeled with FITC on No. 1.5 glass coverslip. Initial dense array design and effect of moving to a sparse, clustered design. a) Raw TIRF image with 500-nm pitch clusters, 3 features per cluster separated by 250 nm, b) Processed image after background subtraction of a, c) FFT of a dense cluster array, d) Raw TIRF image with 3-µm pitch clusters, 3 features per cluster separated by 500 nm, e) Processed image after background subtraction of d, and f) FFT of a sparse cluster array......118

Figure 4.8: Magnified total internal reflectance fluorescence images captured with 60X TIRF objective of APTMS arrays labeled with FITC on No. 1.5 glass coverslip. a) TIRF image with background removed of 500-nm pitch clusters, 3 features per cluster separated by 250 nm, b) Line profile plot of first 20 µm of array showing mean column

intensity cannot separate cluster features, c) Processed TIRF image of 2-µm pitch clusters, 3 features per cluster separated by 500 nm, and d) Line profile plot of first 20 µm of array showing mean column intensity is able to show separation of features within clusters......120

Figure 4.9: Negative tone fabrication scheme for fluorescent nanoarrays. First, the surface is coated with a negative tone resist HSQ. Following exposure and development, the chip is coated with a layer of sacrificial PMMA. Next, the PMMA layer is etched back in oxygen plasma to expose and activate the tops of SiO_x pillars. The sample with exposed pillars is placed into a desiccator with neat organosilane. Following deposition, the chip is removed and immersed in a labeling solution containing a reactive fluorophore of interest. Finally, the sacrificial resist is removed in a solvent such as dichloroethane (DCE)......121

Figure 4.10: Scanning helium ion imaging of pillar arrays and etch profiling to confirm pillar clearance above the sacrificial PMMA film. a) Helium ion microscope image of 250-nm pitch, 35-nm diameter SiO_x fabricated by EBL on glass coverslip, b) Tilt Helium ion microscope 500-nm pitch, 35-nm diameter SiO_x fabricated by EBL on glass coverslip, c) AFM tapping mode height image. Glass coverslip with 2 feature clusters of 35-nm diameter SiO pillars fabricated on glass coverslip. Height profile below of line selection, and d) AFM tapping mode height image. Glass coverslip with 2-feature clusters of 35-nm diameter SiO_x pillars fabricated on glass coverslip after etching of sacrificial pmma layer with oxygen for 70 s. Height profile below......123

Figure 4.11: Total internal reflectance fluorescence images of APDIPES-SiO_x arrays labeled with FITC on No. 1.5 glass coverslip captured with 60X TIRF objective. a) Raw TIRF image with a 500-nm square array of features, b) Processed image after background subtraction of a, c) FFT of the 500-nm array, d) Raw TIRF image with 250-nm pitch features, e) Processed image after background subtraction of d, and f) FFT of the 250-nm pitch array......124

Figure 4.12: Total internal reflectance fluorescence images of APDIPES-SiO_x arrays labeled with FITC on No. 1.5 glass coverslip captured with 60X TIRF objective. a) Processed TIRF image of a 500-nm square array, b) Line profile plot of first 20-µm of array showing mean column intensity can separate features at 500 nm, c) Processed TIRF image of a 250-nm square array, and d) Line profile plot of the first 20 µm of a 250-nm square array showing intensity peaks cannot be used to separate 250-nm features........125

Figure 4.13: Comparison of signal: background separation and overall signal intensity between positive tone and negative tone fluorescent array methods using FITC. a) Histogram of a FITC 500-nm pitch array over the entire detector range, b) Range of signal including background for a FITC positive tone 500-nm array, c) Histogram of a FITC 500-nm pitch array over the entire detector range, and d) Range of signal and background exist as discrete intensity distributions for a HSQ negative tone array........126

Figure 4.14: Total internal reflectance fluorescence images of APDIPES-SiO_x arrays labeled with Cy5 on a No. 1.5 glass coverslip captured with 60X TIRF objective. a) Raw TIRF image with a 500-nm square array of features, b) Processed image after background subtraction of a, c) FFT of a 500-nm array, d) Raw TIRF image with 250-nm pitch features, e) Processed image after background subtraction of d, and f) FFT of a 250-nm pitch array....128

Figure 4.15: Total internal reflectance fluorescence image of APDIPES-SiO_x arrays labeled with Cy5 on a No. 1.5 glass coverslip captured with 60X TIRF objective. a) Processed TIRF image of a 500-nm square array, and b) Line profile plot of the first 20 µm of the array showing that the mean column intensity can separate features at 500 nm. 128

Figure 4.16: Raw montage of TIRF images captured with 60X TIRF objective. Glass coverslip with variable pitch SiO_x pillar arrays of APDIPES with Cy5. Each column's number heading indicates the separation distance, in nm, of the features inside each cluster. Each column consists of 3 clusters of variable distances, and each cluster is separated from the neighbouring cluster by 2 µm....129

Figure 4.17: Total integrated intensities for spots on each control surface at given Cy5 labeling concentrations. Control surfaces were homogeneous surfaces of NH_2 (APDIPES), mPEG-silane, and bare glass....131

Figure 4.18: Raw and reconstructed images of SiO_x pillar arrays of 350-, 375-, 475-, and 500-nm pitches functionalized using APDIPES with Cy5. Reconstruction used the Localizer stand-alone processing tool, a) Raw fluorescent image of 350- and 375-nm array columns, b) Closeup of section of a 375-nm column, c) Reconstructed image of 350- and 275-nm array columns, d) Closeup of reconstruction of a 375-nm array section, e) Raw fluorescent image of 475- and 500-nm array columns, f) Closeup of section of a 500-nm array column, g) Reconstructed image of 475- and 500-nm array columns, and h) Closeup of a reconstructed 500-nm array column....134

Figure 4.19: Example of current fluorescent nanoarray background prevention strategies. a) High density fluorescent nanoarray utilizing polyethylene glycol (PEG) as a background passivation scheme. Left image is PEG, right image is PEG after coating the native glass with hydrogen silesquioxane (HSQ). Reprinted with permission from Wind *et al*.[157], and b) Alternative passivation scheme as tested on unpatterned glass using dichlorodimethylsilane (DDS) and Tween-20 treatment compared to PEG conjugated directly to a glass surface. Reprinted with permission from Hua *et al.* 2014. [320]....136

Figure 4.20: Vapor deposition confirmation on homogeneous surfaces, glass coverslips. a) AFM tapping mode height image. Glass coverslip No. 1.5 after 15-min piranha, area RMS roughness: 0.3 nm. Inset is snapshot of a water sessile contact angle < 5 °, and b) AFM tapping mode height image. Glass coverslip after 18 h APTMS deposition with area

RMS roughness: 0.3 nm. Inset is snapshot of a water sessile contact angle measured to be 67 °..139

Figure 4.21: Brightfield and fluorescent images of lower left section of pattern locator outline used in the majority of fluorescent patterns made with HSQ. a) Brightfield, 60X magnification image of outline, utilized to locate pattern quickly, and b) Fluorescent image of pattern outline..140

Figure 4.22 General process of mounting fabricated nanoarrays for imaging. a) Clean culture dish, b) Remove lid, flip dish, and drill a ⅜" hole through bottom. Clean excess material and sonicate in water, c) Obtain and orient the chip which was fabricated on a No 1.5 high tolerance glass coverslip, and d) Place the coverslip on the bottom of the dish, seal with aquarium glue or VaLaP type wax sealant. Let dry and flip over for imaging in standard culture dish mounts. Ensure adequate volume of imaging solution (~ 3 mL)..142

Figure 5.1: Energy balance diagrams ΔG vs *l* of erythrocyte suspensions, on a logarithmic scale in mJ/m^2. a) Electrostatic (EL) and Lifshitz–van der Waals (LW) interactions, combined in b) The classical DLVO plot with the primary minimum of attraction (MIN-1), the secondary maximum of repulsion (MAX-1), and the secondary minimum of attraction (MIN-2), c) The AB interaction (repulsion) in addition to the EL repulsion, yielding in d) The combined curve that depicts the total interaction more realistically than the DLVO plot. The most important aspect of the complete curve shown in d is the absence of a primary minimum of attraction (still visible in b), owing to the AB-repulsion, which gives rise to superstability in vivo. Figure and caption reprinted with permission from reference [344]. Copyright © 2006 by Taylor & Francis Group, LLC......150

Figure 5.2: Application of interaction energy calculations for gold nanoparticle assembly on patterned amino silane surfaces. a) Interaction energy between gold nanoparticle and 3-aminopropyltriethoxysilane (APTES) surface, b) Interaction energy between gold nanoparticle and 16-mercaptohexadecanoic acid (MHA) surface, and c) Depiction of large sale assembly and applications of electrostatic funneling for charged line and single nanoparticle placement. Reprinted with permission from reference 199. Copyright 2007 American Chemical Society...153

Figure 5.3: SEM images of wet etched magnesium (40 nm) on silicon after etching for 3 min in IPA:H_2O 10:1, through a PMMA(950k) mask. a) Etched trenches through PMMA lines, b) Large diameter hole etch showing silicon surface post-etch, c) A 250-nm pitch hole array with etch/liftoff residue, and d) closeup of a 250-nm pitch hole array post etch. 155

Figure 5.4. Overall process scheme of a HSQ/PMMA bilayer system for metallic hole array mask production. HSQ is spin coated on top of PMMA. HSQ is exposed and developed in 2.5% TMAH. SiO_x dots are then directionally etched in plasma. Metallic mask material is deposited on top of bilayer posts. After deposition, bilayer posts are removed in a PMMA liftoff solvent. Organosilanes deposited through hole array, silanes are available for functionalization pre- or post- etch..156

Figure 5.5. SEM images after attempting a HSQ/PMMA bilayer liftoff approach using 30 nm of HSQ on 110 nm of PMMA and a 30-nm Mg deposition. a) Top down of 250-nm pitch SiO_x dots after development on top of a PMMA film, b) Tilted SEM of SiO_x dots on top of PMMA after RIE etching with substantial undercut, c) Tilted SEM of SiO_x/PMMA bilayer posts sputter coated with Mg, d) Top down view of Mg/SiO_x/PMMA 250-nm pitch hole array with 0% liftoff yield, e) Successful curved line liftoff with 50-nm minimum width features, and f) Close-up of smallest achievable liftoff (100-nm diameter square) with approach showing that underlying silicon surface appears to be clear of residual...158

Figure 5.6. Overall process scheme of HSQ negative tone liftoff for metal hole array mask production. HSQ is spin coated on top of PMMA. HSQ is exposed and developed. Metallic mask material is deposited on top of SiO_x posts. After deposition, bilayer posts are removed in vapor or aqueous HF. Organosilanes deposited through hole array, silanes are available for functionalization pre- or post- etch of metal mask..............................159

Figure 5.7. SEM images of 240-nm tall posts of a Ma-N2403 resist sputter coated with 40 nm of Mg and removed by acetone sonication. a) Ma-N2403 posts after development, 350-nm pitch. b) Mg coated Ma-N2403 posts, 250-nm pitch. c) Square feature array after removal of Ma-N2403 and d) Closeup of square Ma-N2403 hole after removal showing silicon surface and surrounding liftoff residue...160

Figure 5.8. SEM images of 110-nm SiO_x posts with 20 nm of gold deposited overtop by electron beam evaporation. a) 20 nm of gold with a 1-nm Cr adhesion layer, b) 20 nm gold with no adhesion layer, c) 20 nm gold with molecular adhesion layer (MPTMS), and d) A hole array after HF post removal with 20 nm gold, 1 nm Cr..................................162

Figure 5.9: a) SEM images of silica-clad QDs sitting on Al_2O_3 pads, b) Dark-field microscope images of 160-nm silica-clad QDs on 160-nm pads with a 2-μm pitch composed of Y_2O_3, c) Confocal scan image of a 12 μm × 12 μm array of UCNPs, and d) Example $g^{(2)}(t)$ curves for bright sites in the scan image. Reprinted with permission from reference [358] (adapted). Copyright 2015 American Chemical Society............................164

List of Tables

Table 1.1: Snapshot of methods for patterning self assembled monolayers. List adapted from table in reference [118] with permission. Copyright 2010 American Chemical Society. 21

Table 2.1 Density of Conjugated Au Nanoparticles in the Background (Unfunctionalized) Regions of Patterned surfaces. Background Particle Densities Marked as < 1 Particle/μm^2 did not have a Statistically Significant Number of Particles within the SEM Field of View to be Determined with Greater Precision. Reprinted with permission from reference 159. Copyright 2018 American Chemical Society....42

Table 2.2 Measured Surface Energy Parameters of Different Surfaces Investigated in this Work. Reprinted with permission from reference 159. Copyright 2018 American Chemical Society....54

Table 3.1 Diameter of SiO_x ring spacer structures vs sidewall thickness....72

1

Introduction

1.1 Overview of the Thesis

This thesis examines the combination of two general categories of nanoscale design processes. A top-down design perspective is employed by using nanoscale patterning tools, and a bottom-up perspective is used to guide the arrangement of silicon-containing molecules, known as silanes. Through techniques similar to those used in the semiconductor industry, a versatile methodology is demonstrated with three varied applications: precise positioning of gold nanoparticles on a surface; a proposed approach to surface feature density multiplication; and a nanoscale array for microscopy applications. The work is aimed at enhancing research efforts in these distinct fields, demonstrating the effectiveness of creating lithographically defined patterns of chemical functionality by patterning organosilanes from the vapor phase.

This chapter will provide the necessary background for the thesis, providing a snapshot of the field of self-assembled monolayers and organosilanes. The details of organosilane self-assembly on surfaces and the methodologies of applying silanes to a surface will be introduced. Current methods of patterning organosilanes will be reviewed, with a focus on patterning with photolithography and electron beam lithography which are used in semiconductor manufacturing. The chapter will conclude with a discussion of electron beam lithography and photolithography of organosilanes, ending with attention to vapor-phase deposition of organosilanes through fabricated masks.

1.1.1 Historical Framework of Self-Assembly on Surfaces

Human civilization has been observing nanoscale phenomena without nanoscale insight for thousands of years, interpreting their macroscopic results to various ends. Perhaps one of the earliest records of this is an obscure form of divination from ancient Mesopotamia.[1,2] This curious practice known as "Lecanomancy" is found in Openheim's *'Ancient Mesopotamia: portrait of a dead civilization'* as well as in an early work by Trurnit in 1951.[3,4] Trurnit's description reads:

> "The prescientific utilization of surface phenomena, however, is probably older than written history. The first record seems to be a cuneiform inscription, about 4,000 years old, found in the ruins of ancient Babylon. It describes in detail the use of sesame oil in fortune telling. The priest dropped some oil in a fiat wooden bowl filled with water, looking at the surface against the rising sun, The colors and movements of the oil film and the shape and shifting of these droplets which reached the bottom of the bowl indicated the course of public and private affairs."

This was arguably the first noted record of human observation of *self-assembly* of organic molecules on a surface. The idea that molecules could arrange themselves continued to develop

as curiosity into surface tension grew based on observations of oil-water interactions. The early academic investigations into self-assembly were spurred on by historical anecdotes of oil interactions with water, particularly with early recounts by Benjamin Franklin. Franklin was a prominent figure in these early writings on oil-water surface tension effects. Between 1763 and 1785 he wrote about his experiences witnessing cooking oil being dumped from the side of ships, reducing their wake.[5,6] He repeated an experiment of dropping spoonfuls of oil on ponds opportunistically during windy weather, and was likely the first to describe the films in terms of particles:

> "If there be a mutual repulsion between the particles of oil, and no attraction between oil and water, oil dropt on water will not be held together by adhesion to the spot whereon it falls; …"

Later, Lord Rayleigh in 1890 suggested that these films were indeed monolayers. It wasn't until 1891 that Agnes Pockels reported the first direct measurement of surface tension using her "Pockels" trough employed in her kitchen sink.[7] After numerous attempts to communicate her work to the scientific community, and encouragement from Lord Rayleigh, her findings were published in *Nature*.[8] Later, her trough design would be expanded on extensively by Irving Langmuir,[9] and later with Katherine Blodgett.[10] It was Pockels' work that would lead to Langmuir–Blodgett films,[11,12] which gave the first insight into the nature of self-assembly of molecules. The trough design, as adapted by Langmuir, consisted of a long tray and series of wax-coated paper strips that permitted the measurement of surface tension, as shown in Figure 1.1. The currently termed Langmuir–Blodgett trough is still used today for forming monolayers on liquid surfaces. Inevitably, the trough became adapted to transfer films onto solid surfaces,[13] as shown in Figure 1.2; this tool was a major development in the study of self-assembled

monolayers on solid surfaces. The method also was used to transfer successive films of fatty acids onto glass surfaces.[13]

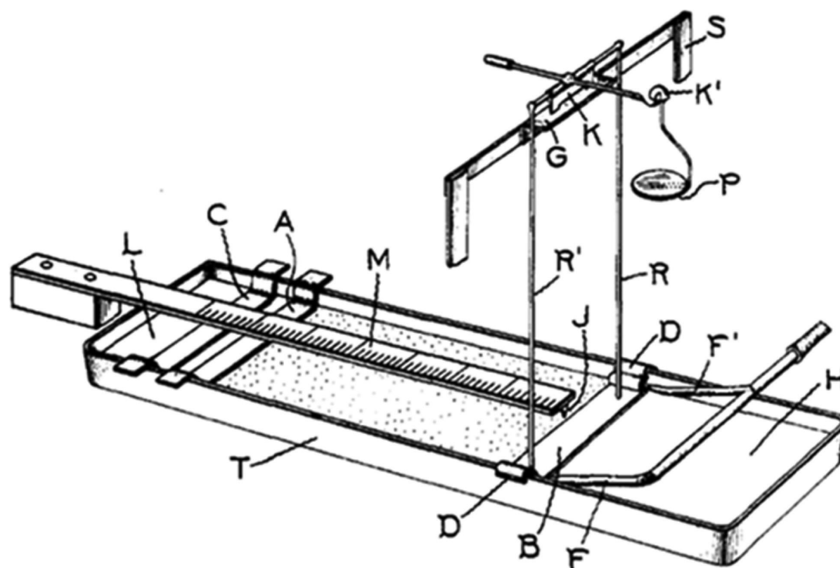

Figure 1.1: Paraphrased from Reference 11. Schematic illustration of a Langmuir trough. Liquid is placed in an enameled tray T. Above the tray is a balance with a knife edge K resting on a glass plate G fastened to a support S. One end of the balance beam has a counterweight, while the other has a knife edge K′ from which hangs a pan P. Glass rods R and R′, cemented to the knife edge, pass through two small holes in a strip of paper B, which floats upon the surface of the water in the tray. To prevent the paper from being softened by the water, it is dipped in a solution of paraffin in benzene. The length of the paper strip B is less than the width of the tray so that it can move freely without touching the sides of the tray. The surface of the water between the strips A and B is covered by an oil film. As strip A is moved toward B, the oil film is pushed ahead of it until it begins to exert a force on the paper strip B. Reprinted with permission from reference 9. Copyright 1917 American Chemical Society.

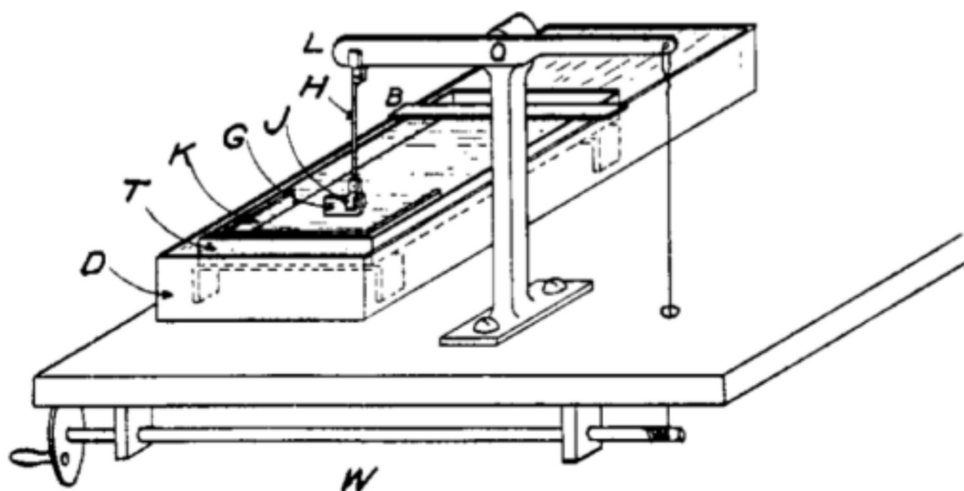

Figure 1.2: Schematic illustration of the transfer of a monolayer film from a water surface to a solid surface. Films are prepared as described in Figure 1.1 with the exception of the addition of lever L, hand winch W, and pinch clamps J attached to rod H. By winding the winch W, the rod can be raised, lifting glass slide G, or lowered. Continuous pressure must be applied on the film to maintain monomolecular structure. Reprinted with permission from reference 13. Copyright 1935 American Chemical Society.

As the Langmuir–Blodgett (LB) method grew in popularity, Zisman and co-workers in 1946 published their work using long chain hydrocarbons on polar surfaces.[14] They showed that oleophobic coatings could be assembled from solution, instead of the air-water interface, and described the packing and orientation of monolayers on surfaces. This result was another leap forward in the burgeoning field of self-assembled monolayers.

1.1.2 From Surface Tension to Organosilanes and Alkanethiolates

It was not until the 1980's that the phrase "self-assembling monolayer" was introduced in a publication of *New Scientist*,[15] which described Netzer and Sagiv's work on controlling the self-assembly process to produce multilayers on surfaces. There are two main models for the broad field of self-assembled monolayers (SAMs): thiols, or organothiolates,[16,17] and silanes, or organosilanes.[18] Several excellent reviews describe the rich history and work to understand and use SAMs.[19–22] This section will highlight the two models, introducing important considerations

for examining SAMs, with attention to organosilanes, which are the focus of the patterning work in this thesis.

Jacob Sagiv, working with mixed monolayers,[23] first described the irreversible attachment of silane monolayers using *n*-octadecyltrichlorosilane (OTS) from solution. Amphiphilic self-assembly had been demonstrated by Zisman,[14] but this work was the first description of covalent attachment from solution. Sagiv outlined the approach in 1980, describing the chemisorption of organosilanes from organic solvents.[18] This work also highlighted the method's benefits to larger scale assembly, as opposed to Langmuir–Blodgett techniques. This pioneering first description of self-assembly of organosilanes is shown in Figure 1.3. This scheme is important as it was the first time that experimental evidence had been put forth for the coupling of OTS to the surface by free hydroxyl groups. Sagiv also commented on the importance of using an anhydrous solvent to favor the in-plane polymerization of the silane monolayer.[18]

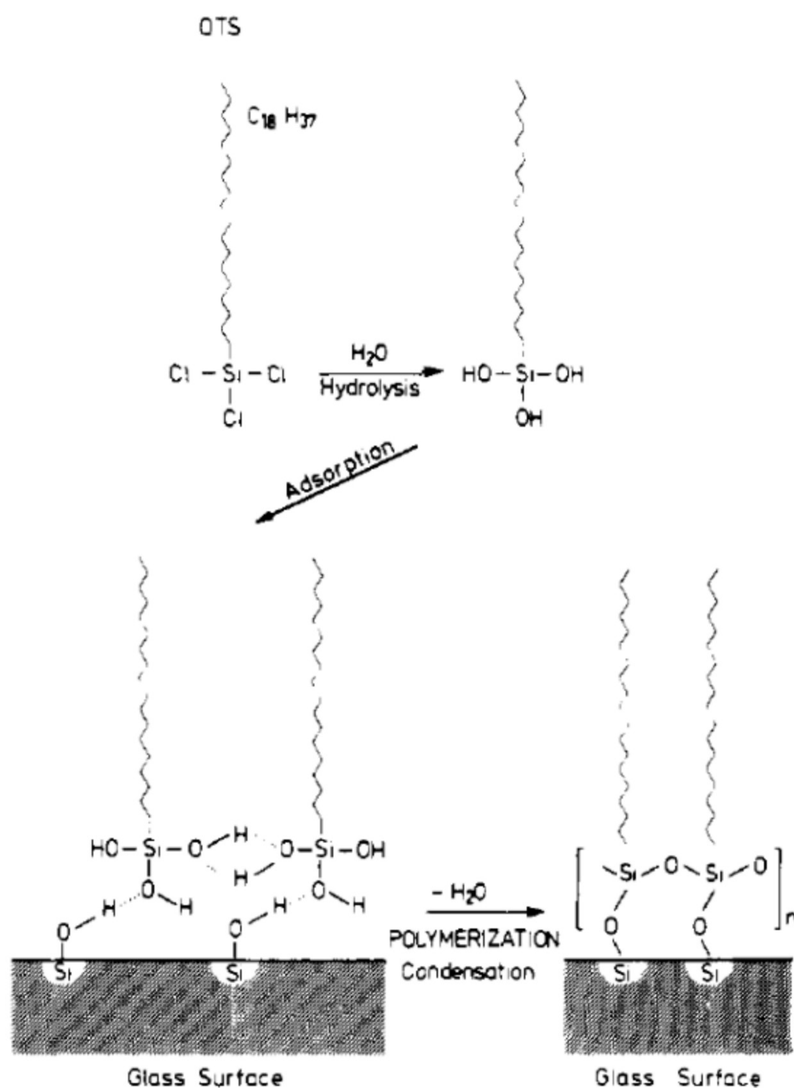

Figure 1.3: Chemisorption of n-octadecyltrichlorosilane (OTS) on glass. Reprinted with permission from reference 18. Copyright 1980 American Chemical Society.

A discussion of the field of self-assembly of organosilanes must acknowledge the immense impact on the field that the investigation of self-assembly of alkanethiolates on gold has had. Ulman's seminal review on SAMs highlights the dominance of thiols on gold over organosilanes as a model system for self-assembly. Solution adsorption preparation of SAMs continued to grow, starting with Nuzzo and Allara's pioneering work on thiol-gold self-assembly in 1983,[16]

which demonstrated the ease and diversity of assembly of disulfides on gold surfaces, in comparison with an LB approach. The immense versatility afforded by thiol SAMs on gold surfaces was the subject of an extensive review by Whitesides and coworkers.[22] Shown in Figure 1.4 is the ideal alkanethiolate SAM on a gold <111> surface (Miller index 111 lattice plane).

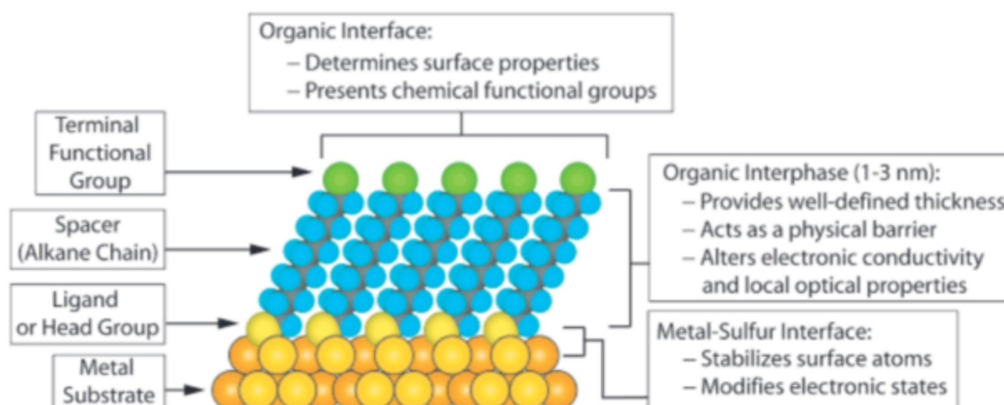

Figure 1.4: Schematic diagram of an ideal, single-crystalline SAM of alkanethiolates supported on a gold surface with a (111) texture. The anatomy and characteristics of the SAM are highlighted. Reprinted with permission from reference 22. Copyright 2005 American Chemical Society.

Here, the headgroup, chain length, chain tilt, and terminal functionality are shown, which are critical characteristics of SAMs of organosilanes. With gold surfaces, Figure 1.4 highlights the substantial chain tilt on gold surfaces that occurs as a result of van der Waals attractions between alkyl chains and the dense packing of the film. Organosilane monolayers, as shown in the next section, have almost no tilt compared to alkanethiolate analogues.[24] Although the thiol–gold system has generated substantial knowledge about SAMs as a nanostructuring element for design, the field of organosilane self-assembly has become a rich field with diverse applications.

1.1.3 Self-Assembly of Organosilane Monolayers

The typical used organosilane for formation of self-assembled monolayers on metal oxide surfaces is $R_1SiX_{(4-n)}$ or $R_3SiX_{(4-n)}$, where n = 1 to 3; R is an alkyl chain group of varying lengths,

a fluorinated alkyl chain, or functional group bearing alkyl chain; and X is a leaving group, (such as a chloro or alkoxy group). The field of organosilane SAMs was established by Sagiv's work with the chlorinated alkylsilane n-octadecyltrichlorosilane. Chlorine groups are excellent leaving groups, but their high reactivity with water can make moisture control a challenge.[19] Less reactive leaving groups such as methoxy and ethoxy are routinely used to form organosilane SAMs on metal oxide surfaces. A wide variety of silanes are commercially available; popular examples of organosilanes for surface modification are alkylchlorosilanes[25,26], aminoalkoxysilanes,[27–30] and fluorinated alkoxy- and chlorosilanes.[24,31–33] A search from Scifinder reveals that the five most common organosilanes used to form self-assembled monolayers on metal oxide surfaces are 3-aminopropyltriethoxysilane (APTES), 3-aminopropyltrimethoxysilane (APTMS), octadecyltrichlorosilane (OTS), tridecafluoro-1,1,2,2-tetrahydrooctyl-1-trichlorosilane (TFOCS), and 3-mercaptopropyltrimethoxysilane (MPTMS); their structures are shown in Figure 1.5.

Figure 1.6 provides an overview of the process of liquid-phase organosilane monolayer formation on metal oxide surfaces. Formation of organosilane monolayers has several steps, of which the order depends on reaction conditions. Organoilanes diffuse to the surface, and depending on the concentration of water in solution, hydrolysis occurs in solution or at the solvent/oxide interface. Hydrolysis of one of the hydrolyzable groups can occur by trace water in solution[19,34] or by water adsorbed directly to the surface, to form silanol groups.[35] If sufficient water is present in solution, the silanols can condense with neighboring organosilanes prior to reaching the surface, forming a pre-made polysiloxane network which then diffuses to the surface.

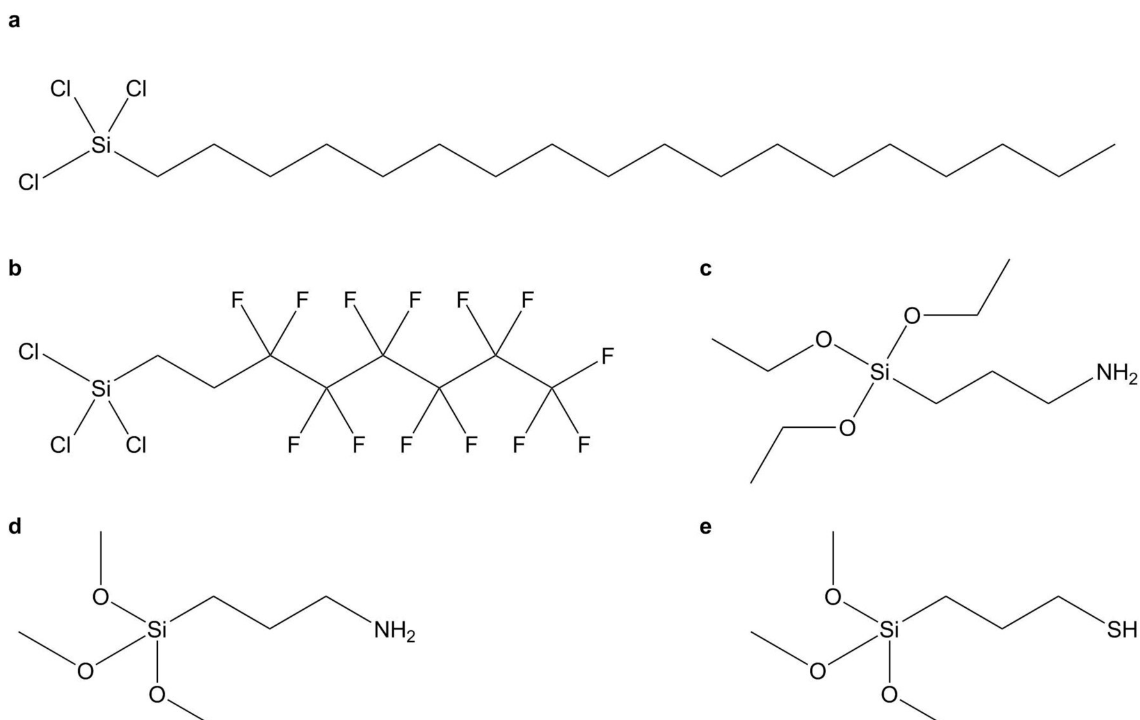

Figure 1.5. Five of the most common organosilanes used for formation of self-assembled monolayers on metal oxide surfaces. a) n-octadecyltrichlorosilane (OTS), b) tridecafluoro-1,1,2,2-tetrahydrooctyl-1-trichlorosilane (TFOCS), c) 3-aminopropyltriethoxysilane (APTES), d) 3-aminopropyltrimethoxysilane (APTMS), and e) 3-mercaptopropyltrimethoxysilane (MPTMS)

Under strict anhydrous conditions, organosilanes are likely to reach the surface intact before reacting with neighboring species, or in the case of using monoreactive organosilanes such as 3-aminoropyldiisopropylethoxysilane (APDIPES). Once physiadsorbed to the metal oxide surface, species at the surface hydrogen bond with the surface hydroxyl groups.[36] At the surface, water condensation reaction can take place between the surface and the preformed polysiloxane networks or individual silanes to form the Si-O-M linkage, where M is the metal oxide surface.[34,37] With alkoxysilanes and anhydrous conditions, an alcohol condensation reaction precedes silanization of the surface.[38]

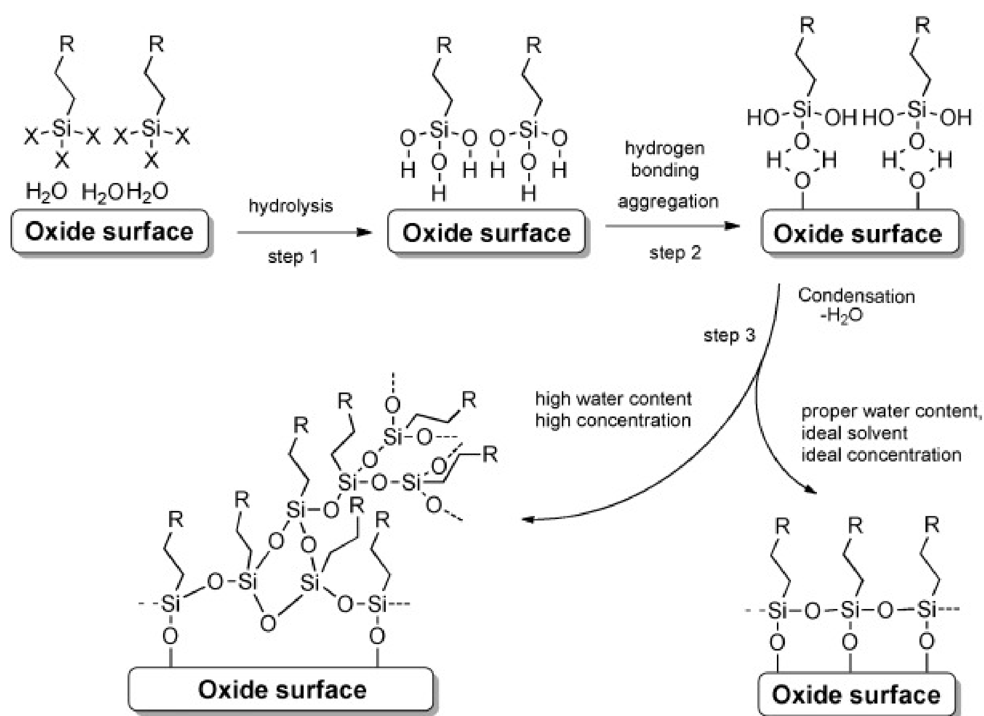

Figure 1.6. Three-step mechanism for monolayer formation by silanes on OH-terminated surfaces. Note in Step 3, condensation ideally proceeds to form a covalently bound monolayer that is also laterally cross-linked (bottom right), but insufficient control over the water content and other reaction conditions may yield disordered inhomogeneous multilayers (bottom left). Reprinted with permission from reference 17. Copyright 2014 John Wiley and Sons.

Organosilanes can be used to modify a variety of surfaces, but the reactivity of the surface towards the organosilane is contingent on the presence of hydroxyl groups (OH); a higher density of -OH groups and high hydrolytic stability will result in surfaces that can be coated with robust monolayers, and therefore, oxide-capped silicon and silica surfaces form the most stable monolayers. Organosilane monolayers can be formed on a variety of metal oxides[17], examples of which include iron,[39,40] aluminum,[41,42] zirconium,[43,44] zinc,[45] germanium,[46] titanium,[43,44,47] hafnium,[44] and tin.[48] Surfaces can be activated by plasma activation or solution oxidation, as described in the surface cleaning and activation section.

The vast majority of work with organosilanes has focused on deposition from solution, typically with organic solvents such as toluene or bicyclohexyl. In several reviews,[19] careful control of the amount of water in the deposition solution is paramount to quality monolayer formation. Uncontrolled amounts of water in solution can lead to excessive aggregation and vertical polymerization, particularly for organosilanes with three hydrolyzable groups. Premature aggregation in solution can lead to particle formation in solution and thus aggregate deposition on the metal oxide surface.[49] Work by Thompson *et al.* detailed that for OTS, in addition to the necessity of using anhydrous solvents, aromatic solvents, such as toluene, can be an excellent choice due to their ability to extract moisture from the surface into the bulk solvent, improving deposition density.[25] The choice of solvent also was reported to be critical as retention of solvent at monolayer defect sites is possible.[41] The presence of surface adsorbed water has been shown to be a critical aspect of monolayer formation in solution. In the case of OTS on silica, surface-bound water was shown to be vital to achieving sufficient density to deposition;[37] this result was confirmed by LeGrange *et al.* who argued that that surface hydration is a primary consideration influencing monolayer coverage and that dehydrated surfaces can be rehydrated by immersion in aqueous solution prior to deposition.[50] Allara and coworkers also indicated that surface hydration has a strong effect on the structure of the monolayer formed, showing that monolayers of OTS can be formed on gold surfaces that are hydrated.[51] Wunder and Wang compared various hydration states on the surface of silica by monitoring changes in silanol coverage by Fourier-transform infrared spectroscopy (FTIR), and confirmed that for improved density of deposition, control of surface water is critical for reactions of OTS with the silica surface.[52] Careful control of water content has been the dominant focus in optimizing deposition from solution, although

some work has indicated that agglomerates of TFOCS deposited on the silicon oxide surface can be planarized by a post-deposition curing step.[53] The counter argument was later made that surface water is not necessary for monolayer formation if sufficient deposition time is used (> 18 h).[54] In addition to forming surface bonds, water has been shown as necessary for alkoxysilanes in order to hydrolyze unreacted side groups of the surface bound layer, improving lateral polymerization.[55]

In addition to extensive work on the role of water in solution and at the surface,[56,57] the impact of several additional parameters on the ultimate surface structure of the organosilane monolayer should be considered. Chain length,[58,59] solvent choice,[35] chemical structure,[60] organosilane concentration,[61] deposition time,[62] and temperature[61,63–66,67]are all important factors that can be adjusted in the pursuit of optimal monolayer deposition of organosilanes.

The growth regime mechanism for thiols on gold was proposed early as rapid adsorption and subsequent organization; however, with there were initially mixed views on growth regimes and chain packing of organosilanes on oxide capped silicon.[68] These views were influenced largely by steric limitations with silane-surface bonding in comparison with alkanethiolates on gold. It was shown by AFM that growth of silane monolayers takes place by island growth (see Figure 1.7) for OTS, but not for smaller chains.[58] Later, island growth was confirmed with both time-resolved XPS and AFM analysis.[69]

Sagiv and coworkers proposed a dynamic structural model for OTS monolayer assembly to reconcile steric limitations imposed by the van der Waals radii (2.59 Å).[70] The model was substantiated with X-ray, FTIR, and Raman characterization.[71] Figure 1.8 shows a schematic of the first experimental evidence indicating that the structure of the silane monolayer surface is

generally one with chains oriented perpendicular to the surface, in contrast to the tilt normally seen with long-chain alkanethiolates. In this work, Sagiv indicated that the nearest neighbor distance between hydrocarbon chain axes occupies a hexagonal lattice with a spacing of 4.91–4.94 Å. This spacing results in a fundamental mismatch as the largest possible distance between adjacent Si atoms linked through Si-O-Si bonds is on the order of 3.3–3.3 Å.[70]

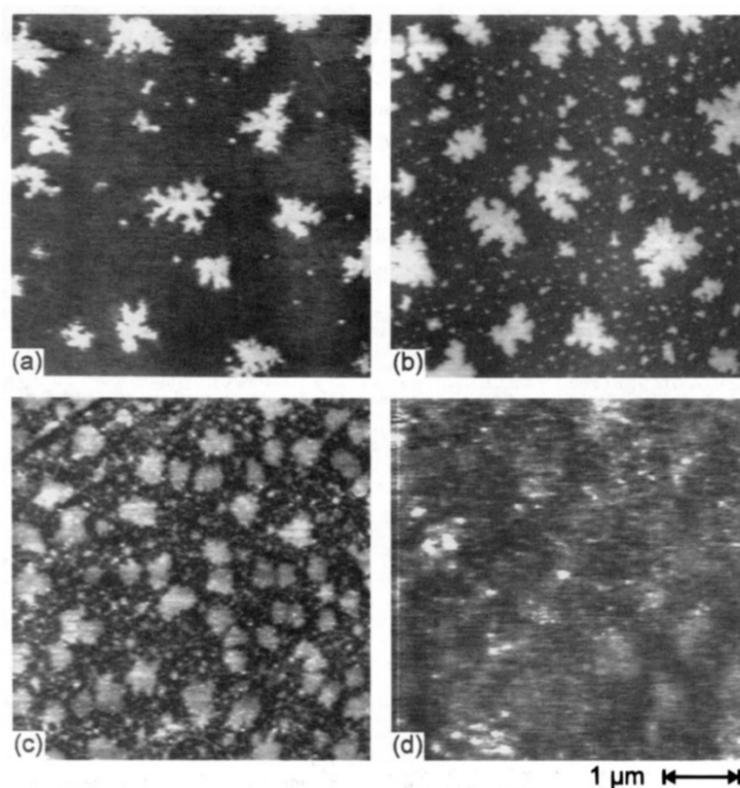

Figure 1.7: AFM images showing the initial deposition of small islands, followed by secondary nucleation, filling in of the empty space, and finally complete formation with outlines of the initial islands. Deposition times are a) 15 s immersion, b) 1 min immersion, c) 5 min of immersion, and d) 35 min of immersion. Reprinted with permission from reference 58. Copyright 1995 American Chemical Society.

The strain is accommodated by allowing bending of the hydrocarbon chains near the Si atoms, via gauche conformations at the first two to three carbon atoms. In addition, it has been shown for SiO_2 surfaces that these steric limitations result in as little as 10–20% of chains

actually bonding to the surface.[72,73] The study of organosilane monolayers continues to be a subject of intense research, particularly from an atomistic viewpoint. Newer techniques, such as molecular dynamics, show that with higher packing of chains there is bonding to the underlying silica surfaces.[24,38] Recent work with multiple transmission reflection IR (MTR) also has shown that the inherent strain of mismatched silane-hydroxyl bonding and adjacent van der Waals chain packing is the main driver for monolayer structure; this is shown in Figure 1.9.

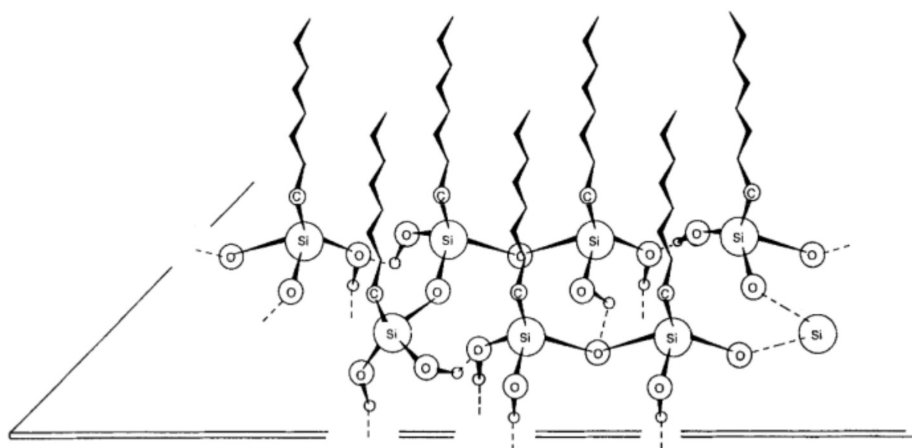

Figure 1.8: Schematic representation of dynamic equilibration of siloxane linkages on a native oxide-capped silicon surface. Lateral rearrangement of Si-O bonds is assumed to take place continuously within a two-dimensional hexagonal lattice defined by the packing of hydrocarbon tails. Reprinted with permission from reference 70. Copyright © 1995 Published by Elsevier Ltd.

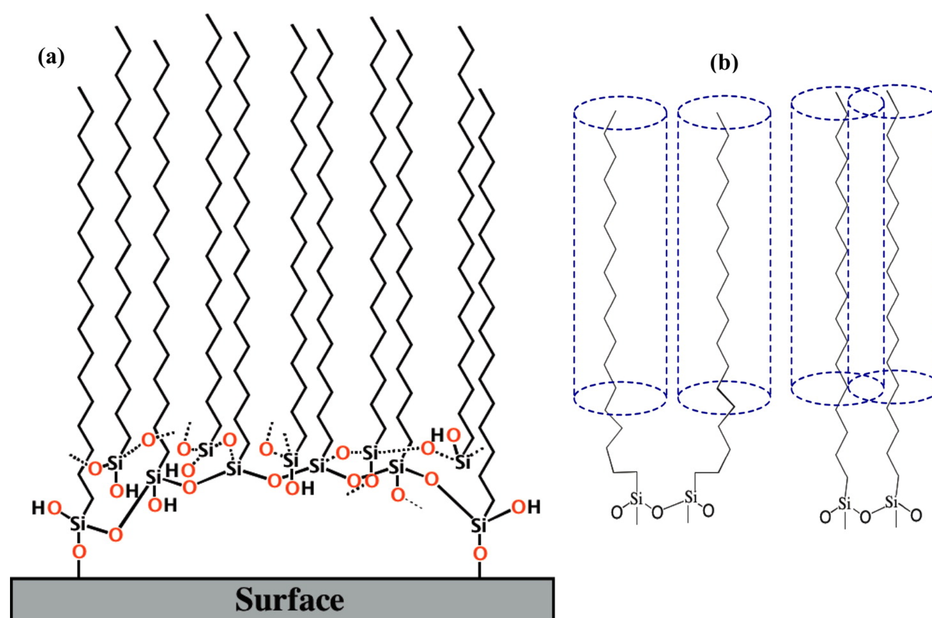

Figure 1.9: (a) Cartoon representation of the OTS SAM on silica based on results from multiple transmission-reflection (MTR) IR results. (b) Cartoon representation of possible "lipid-like" arrangement of alkyl chains with C1–C2 gauche defects to account for the problem of volume constraints of the alkyl chains. Reprinted with permission from reference 73. Copyright 2013 American Chemical Society.

1.1.4 Surface Cleaning and Activation

Successful formation of organosilane monolayers depends on sufficient activation of the underlying surface to produce required silanols on both silicon oxide and silicates.[74,75] Clean surfaces are of primary concern for all nanoscale device manufacture, many of which use wet cleaning methods. Protocols for silicon surface cleaning and activation primarily come from the semiconductor industry, which established protocols such as the RCA clean (from Radio Corporation of America) for silicon wafers (circular pieces of silicon measuring 25 – 300 mm in diameter, 1 mm thick of crystalline silicon) in the 1970s.[76] Preliminary cleaning often uses sonication for removing large particles before using chemically aggressive steps, whose function

is to oxidize and remove organic contaminants.[77–79] Numerous reviews on cleaning methods exist in the literature.[79–82]

There has been some evaluation of cleaning methodologies with regards to subsequent SAM formation. Gold electrode cleaning[83] and gold nanohole recycling[84] are a few examples emphasizing the recyclability and cleaning of gold surfaces for self assembly. There has been some work in the organosilane literature evaluating surface cleaning methods for subsequent silanization, particularly for silica and native oxide-capped silicon. Ligler *et al*. compared eight wet cleaning methods of soda lime glass slides prior to functionalization with a mercaptosilane.[85] They found that a 1:1 solution of methanol:hcl, followed by sulphuric acid, was effective for removal of organic contaminants and producing robust monolayers of (3-mercaptopropyl)triethoxysilane (MPTES) on glass. Other work indicated that a solution of 1:1 MeOH:hcl is effective for subsequent silanization with aminosilanes, particularly with sensitive device layers where leaving thin oxide layers is desirable.[86] Recent literature utilizing organosilanes appears to rely on strong oxidizing cleans such as piranha, to both remove organic surface contaminants and generate surface silanols. "Piranha solution" consists of sulfuric acid and hydrogen peroxide in ratios ranging from 5:1 to 1:1.[27,28,87–89]

Another approach to cleaning surfaces for monolayer deposition of organosilanes is based on plasma techniques.[90,91] These methods rely on oxidation of organic contaminants to produce volatile products that can be pumped out during plasma generation. It has been shown that plasma methods can result in less carbon contamination when compared with liquid peroxide based cleaning methods.[92] Plasma cleaning systems are integrated easily into chemical vapor deposition (CVD) systems for in-situ cleaning prior to deposition.[93] Prior work has suggested

that silicon oxide silanols are present in higher density after plasma and wet cleaning than after plasma or wet cleaning alone.[94] X-ray photoelectron spectroscopy (XPS) and surface analysis showed increased oxygen content on silicon surface after plasma cleaning due to silanol generation.[31] Alternative plasmas also have been used to enhance subsequent silanization, such as hydrogen[95] and air plasma.[96] There is some indication that deposition results can be independent of the activation method used, so the mode of cleaning may be application-dependent.[97]

Following surface cleaning and activation, organosilanes usually are applied from solution and occasionally by using alternative methods, such as spincasting.[98] However, a growing body of literature suggests that vapor-phase deposition of organosilanes has substantial benefits over solution deposition.

1.1.5 Vapor-Phase Processing with Organosilanes

Following the advancements in moving from silane deposition from the solution/air interface to assembly from solution, vapor-phase deposition of organosilanes began to be explored in the 1990's.[99] Just as solution deposition has several advantages over the Langmuir-Blodgett (LB) technique, vapor-phase deposition is advantageous over solution-phase processing. Its advantages include increased reproducibility,[29] improved coverage,[100,101] reduced aggregation,[93,102] moisture control by utilizing vacuum, reduced surface roughness,[103] lower reagent usage by avoiding excessive solvent, and wafer level scalability.[104,105]

Vapor-phase deposition is a long-standing technique for adhesion promotion in resist spin-coating, primarily with hexamethyldisalazane (HMDS).[106] Alkoxysilanes also have been used in chemical vapor deposition (CVD) apparati since 1985.[107] A vapor deposition of a perfluorosilane, such as [tridecafluoro-1,1,2,2-tetrahydrooctyl-1-trichlorosilane (TFOCS)], is

often a preliminary step for PDMS mold release from silicon oxide surfaces.[108] The deposition process is similar once contact with the surface has been made by the gas-phase organosilane. Organosilanes become volatile as their vapor pressure is increased,[109] typically by treatment with heat and vacuum. The reagent then diffuses from the neat solution to the surface, contacts a surface hydration layer, and reacts with the surface. This bulk diffusion regime can result in increased deposition times for vapor-phase deposition,[110] up to 24 h reported for n-octadecyltrichlorosilane (OTS). The compatibility with manufacturing processes and the ease of preparation of biofunctional surface coatings spurs continuous development in vapor-phase deposition applications, such as click chemistry-ready surfaces.[111]

Recent literature has shown that very high thermal stability can be achieved (425 and 500 °C) with chlorosilanes TFOCS and dimethyldichlorosilane (DDMS), respectively. In addition, reduced coating aggregation and surface roughness on a clean silicon surfaces was obtained in these examples.[112] Reduced aggregation is a particularly attractive feature of vapor-phase deposition as stringent anhydrous conditions usually are required in solution-phase depositions. Optimizing vapor-phase deposition is required to reduce the small amount of agglomerates that can occur. Diebold and Clarke have outlined four routes for agglomerate-free vapor-phase deposition:

1. dry environment,
2. short deposition time,
3. lower deposition temperature, and
4. monofunctional silane coupling agents[101]

As with solution-phase deposition, the amount of surface hydration is important as it has been shown that there is an optimum hydration state for fluorosilane deposition from the vapor phase.[113] The surface layer, shown in Figure 1.10, indicates that even in the vapor phase,

aggregation can occur in the atmosphere. This can be mitigated by utilizing a perfectly dry atmosphere, which is impractical, or by the addition of a barrier layer.[101] It has been shown that water is necessary to ensure hydrolysis of side groups in the case of alkoxysilanes, as demonstrated by introducing water vapor into the deposition chamber using known amounts of magnesium heptahydrate.[114]

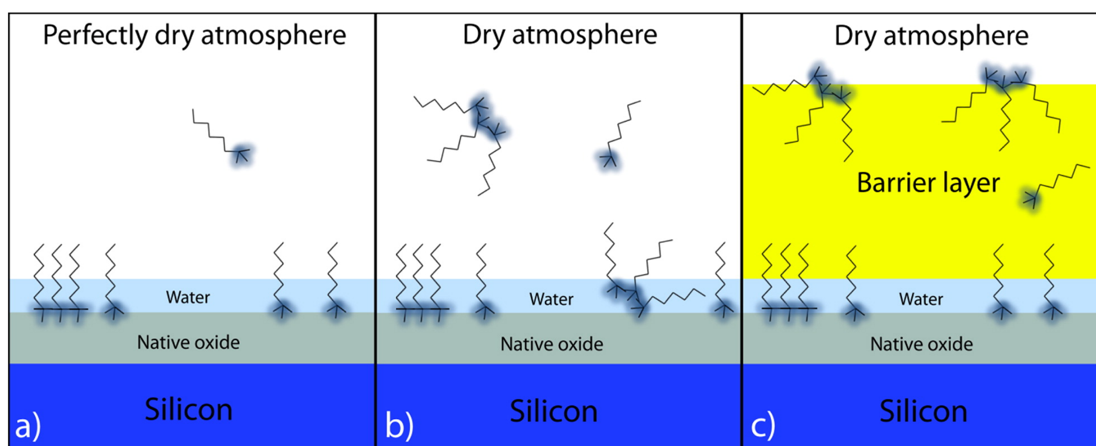

Figure 1.10: (a) Schematic of an idealized vapor deposition process. (b) Realistic vapor deposition in which agglomeration occurs before binding to the surface. (c) Realistic vapor deposition with an oil barrier layer showing agglomerates diffusing slowly through the barrier layer relative to individual SCA molecules. An example of a trifunctional silane coupling molecule is depicted, with the binding groups highlighted in blue and the R group shown as a linear alkane chain. Reprinted with permission from reference 101. Copyright 2012 American Chemical Society.

1.2 Lithography with Organosilanes

Patterning self-assembled monolayers has been a long-standing pursuit of SAM research,[22,115] and the methods are diverse as shown in Table 1.1. Patterned organosilanes are particularly attractive for biological applications such as cellular adhesion promotion,[116,117] which couple the effectiveness of using optically transparent surfaces, and integration with silicon-based semiconductor manufacturing processes. There are many different methodologies for patterning organosilanes; and they are a focus of excellent reviews.[17,118–120]

Each method of patterning has a host of advantages and disadvantages. Here, I will focus on introducing the major lithographic techniques that have special relevance to the semiconductor industry and manufacture of micro- and nano-arrays; these are photolithography and electron beam lithography.

Table 1.1: Snapshot of methods for patterning self assembled monolayers. List adapted from table in reference [118] with permission. Copyright 2010 American Chemical Society.

Microcontact Printing	Ink-Jet Printing	Electron-Beam Lithography
Nanotransfer Printing	Topographically Directed Assembly	Chemically Specific Laser Patterning of SAMs
Microfluidic Patterning	Orthogonal Self Assembly	Directed Self-Assembly
Area Selective Atomic Layer Deposition	Scanning Tunneling Microscope (STM)	Atomic Beam Lithography
Microdisplacement Printing	Nanoimprint Lithography	X-Ray Lithography
Microcontact Insertion Printing	Molecular Ruler Method	Photolithography
Multilayer Transfer Printing	Lithography Assisted Chemical Patterning	Laser Interference Lithography
Dip Pen Nanolithography	Electron Beam Chemical Nanolithography	Tapping Mode AFM Nanolithography
Nanografting Nanoshaving	Direct Laser Patterning (DLP)	

1.2.1 Photolithography of Organosilanes

Early patterning of functional organosilanes took place with masked UV light.[121] Shown in Figure 1.11 is a general scheme for the process of photolithography. An optical mask is placed in front of a UV light source, which selectively allows UV light to irradiate the surface at defined locations. The surface would have been coated in a photosensitive resist, or photoresist, which depending on its tone, will be removed or left behind following post-exposure development. The resist is then used as an etch mask with wet or dry methods.

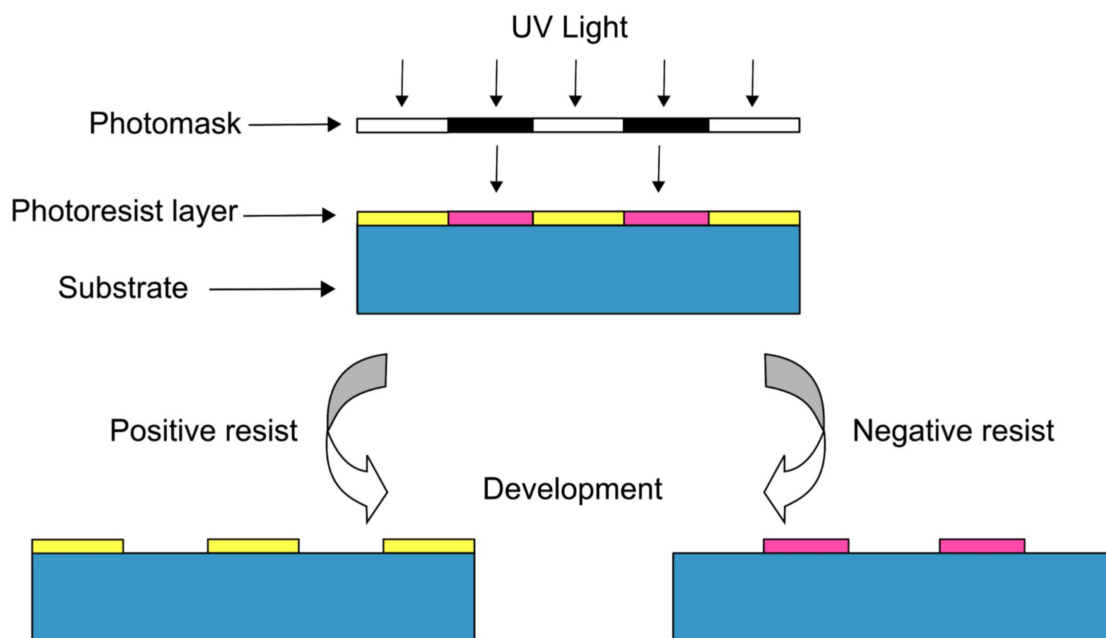

Figure 1.11: Overview of photolithography scheme with positive and negative tone photoresists. Following development, resists often are used for pattern transfer into the surface via an etching step.

Early work utilizing UV to pattern organosilanes relied primarily on photodegradation or photomodification of the SAMs in the exposed regions.[122,123] In these cases, the layer of photoresist was replaced effectively with a homogeneous SAM of an organosilane, rather than guiding the assembly to defined locations. The approach of patterned *removal* by photolithography can be useful, for example in electroless plating (plating without applied external power) applications.[124,125] Biomedical applications also have benefited by this approach, for example, in guiding cellular growth processes.[126,127] It was shown that photodecomposition of inert SAMs can render the SAM reactive to conjugation to functional silanes.[32] Photodegradation continues to be used, for example, by inducing changes in wettability and ordering of alkylsilane surfaces on silicon.[128]

The first example of the use of photolithography to define functional locations rather than degraded positions on inert backgrounds was in 1995,[121] and the general scheme is shown in Figure 1.12. By defining locations for aminosilanes, the authors were able to perform selective copper CVD on diamond surfaces.

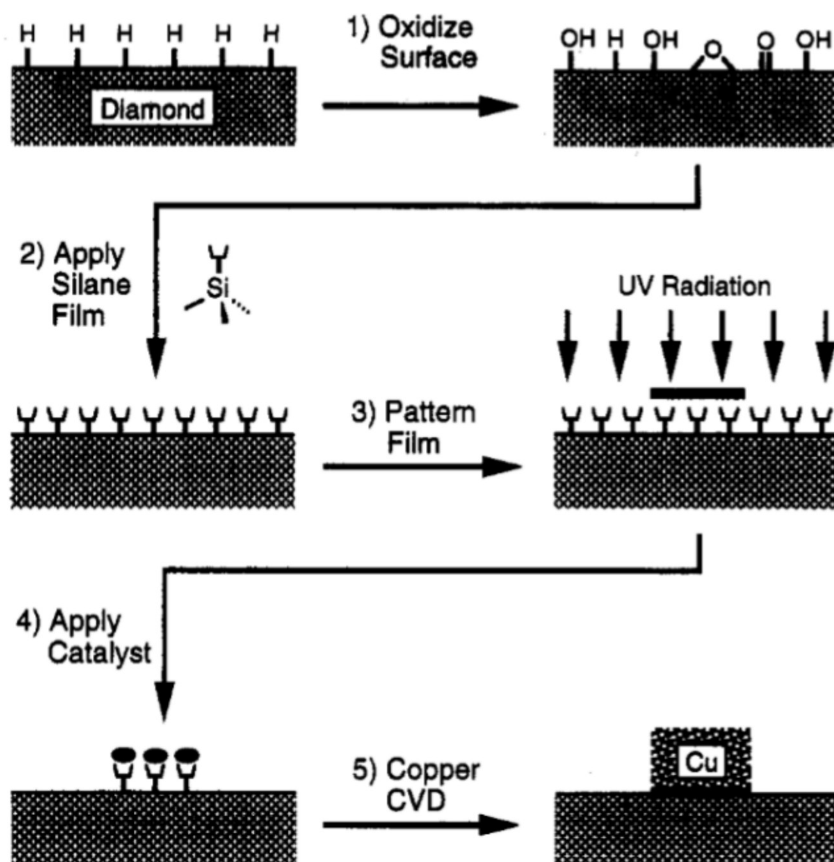

Figure 1.12: Schematic of the process for patterned, selective copper CVD on aminosilanes patterned via photolithography. Reprinted with permission from reference 121. Copyright 1995 American Chemical Society.

Moving towards site-selective chemical functionality was a major shift in photolithographic patterning of organosilanes, particularly with the introduction of patterned deprotection strategies.[129,130] These strategies, together with a growing interest in addressable

fluorescent readouts, enabled photolithography to become the dominant methodology to fabricate biomolecular microarrays, such as DNA chips[131,132] and protein microarrays.[133] Figure 1.13 is an example of a photosynthetic workflow using photolithography and silane linkers in a genetic sequencing application. Here, this seminal work demonstrated the application of photodeprotection of aminosilane functionalized surfaces to on-chip synthesis.[134]

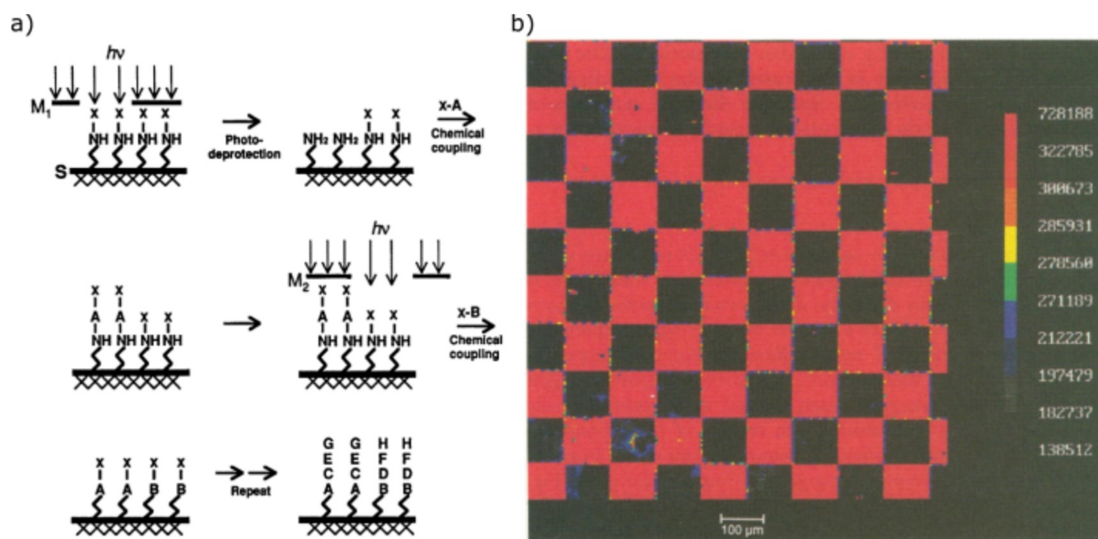

Figure 1.13: a) Overview of light-directed spatially addressable parallel chemical synthesis by photodeprotection utilizing aminosilane linkages. b) Spatially localized photodeprotection and fluorescent labeling. Reprinted with permission from reference 134, adapted. Copyright 1991 The American Association for the Advancement of Science.

Chemical functionality provided by organosilane linkages to the surface via SAMs has been at the foundation of major advances in microarray manufacture,[135,136] a \$4 billion dollar world market as of 2016 estimates.[137] On-chip synthesis enabled by photolithography with organosilanes has helped spur this economic growth in big data genomics.[138,139] It was the method established by one of the largest gene sequencing companies in the world, Affymetrix.[138] By utilizing photolithography, arrays with high information density can be produced, with

addressable locations for fast readouts. However, the drive towards higher information density with patterned organosilane applications faces the limitations of optical lithography. Newer semiconductor manufacturing processes such as extreme ultraviolet (EUV) which uses wavelengths down to 13 nm, enable extremely small scale patterning;[140] however, cost and access are likely barriers to entry for research-level application. Photolithography is an accessible patterning methodology for research groups to examine the potential of array fabrication methods. However, with the growth of user-trained facilities, higher resolution techniques (such as electron beam lithography) are also being explored for their utility in patterning organosilanes.

1.2.2 Electron Beam Lithography of Organosilanes

Electron beam lithography (EBL) is a maskless ,or direct-write, technique to pattern surfaces. Shown in Figure 1.14 is the general route for nanofabrication with EBL. An electron beam lithography systems consists of an electron source, a series of magnetic lenses for focusing and shifting the beam, and a means of beam blanking. The highly collimated beam of electrons is focused onto the surface, at which point the energetic electrons interact with the surface and electron beam resist; the beam is rastered in the desired pattern. Figure 1.14 indicates the two tones of electron beam lithography, positive and negative.

Some of the earliest usage of electron beam lithography with organosilanes relied on ablation or damage of a homogeneous octadecyltrichlorosilane layer,[141] which was demonstrated in the early 90's using monolayers deposited from solution.[142–144] These were the first examples

of using SAMs as candidate materials for 'high resolution resists', with some early successes in pattern transfer via wet etching.[145]

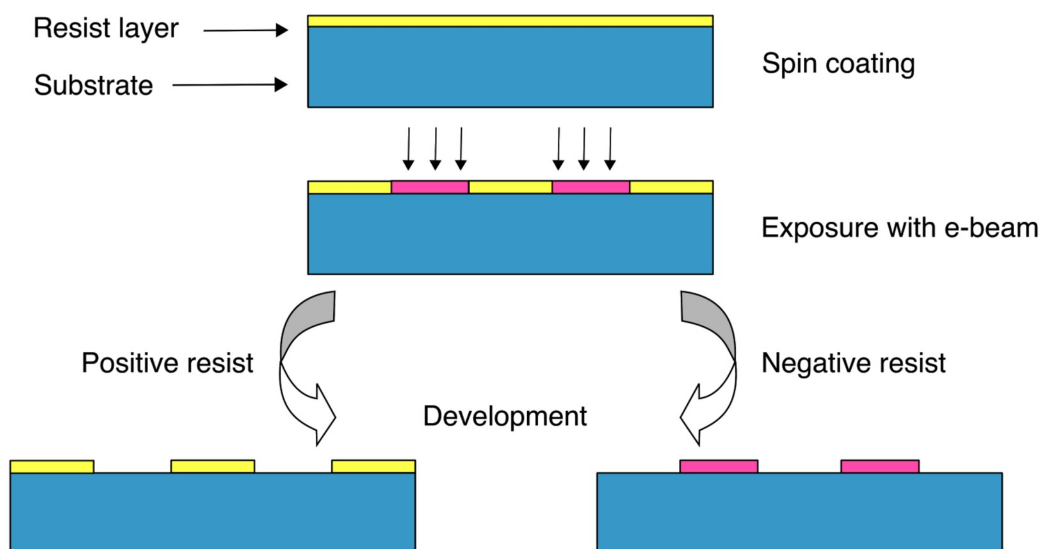

Figure 1.14:.Schematic representation of the basic steps of electron beam lithography process. Reprinted with permission from reference 146, adapted. Copyright 2009 IOP Publishing Ltd.

Plasma etching patterned SAMs is possible as it causes oxygenation of carbonaceous material left over after electron beam irradiation of alkylsilanes, leading to improved resistance to reactive ion etching (RIE).[141] This approach was promising for applications in high density data storage.[147] Organosilane SAMs also have been shown to be "back-fillable" after degradation, as was the case for aminosilane functionalization after irradiation of fluorinated silanes[148] or trimethylsilyl layers.[149] Functional aminosilane films also have been intentionally damaged to enable colloidal assembly on undamaged areas.[150]

Interest continued to grow in coupling the high resolution capabilities of electron beam lithography with the chemical functional group versatility afforded by organosilanes. In the later half of the 90's, the positive tone resist began to be used as a template for deposition of

organosilanes such as aminosilanes.[151] The method was used for electrostatic self-assembly of gold nanoparticles. Carbon nanotubes could also be assembled in this way after depositing aminosilanes through a PMMA based mask.[152] Vapor deposition has a clear advantage when combined with electron beam lithography resists, that is, the avoidance of solvent which would normally dissolve electron beam resists. It was shown by Nysten *et al*. that after exposure to EBL, PMMA masks could used for patterning a variety of organosilanes from the vapor phase; following mask removal, subsequent silanizations could take place to achieve contrasting functionality (See Figure 1.15).[153]

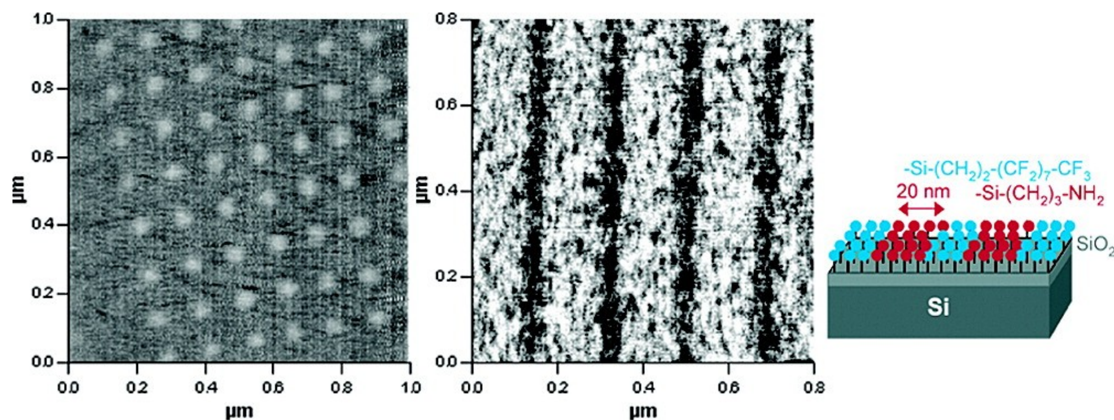

Figure 1.15: Lateral force AFM images of binary patterning of chloro- and alkoxysilanes through a PMMA mask. Schematic representation on the right. Reprinted with permission from reference 153(adapted). Copyright 2004 American Chemical Society.

Many array-based technologies have been explored using positive tone patterning with gold as anchors after physical vapor deposition of gold through PMMA masks.[154,155] By using organosilanes instead of depositing gold, functional groups can be coupled directly to an oxide surface. The extensive variety of organosilane functional groups available makes vapor-phase deposition of organosilanes amenable to applications in gene array technologies where

addressible reactivity is useful. One interesting application is guided assembly of DNA origami nanostructures by exposing PMMA and utilizing an aminosilane, as shown in Figure 1.16. This "molecular liftoff" methodology is becoming used more often; the approach is used for a variety of applications after DNA structure attachment.[156]

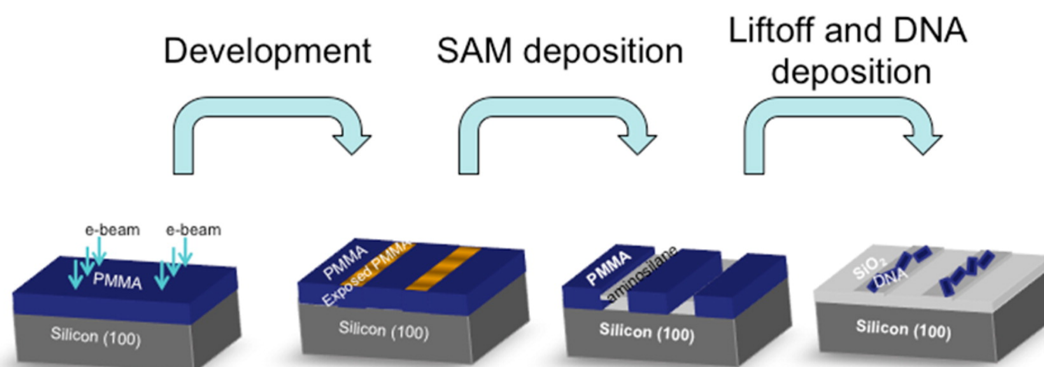

Figure 1.16: Schematic representation of positive tone molecular liftoff technique for depositing aminosilanes through EBL patterned PMMA masks. Then, PMMA is removed and DNA origami structures can be assembled on a patterned organosilane film. Reprinted with permission from reference 156. Copyright 2014 American Chemical Society.

It is possible also to pattern organosilanes using a negative tone patterning scheme with resists, such as hydrogen silsesquioxane (HSQ) following piranha cleaning (5 min) and oxygen plasma exposure (3 min). HSQ has been reported to contain surface silanol groups, which can be used for organosilane coupling;[157] an example is shown in Figure 1.17. Following HSQ exposure and development, patterns of SiO_x presenting reactive -OH groups are functionalized with an aminosilane. This array can go on to be used to anchor biomolecules, in this case DNA origami.[158]

There are a variety of lithographic approaches that can be taken with both photolithography and electron beam lithography by varying resist materials, mask materials, surfaces, and organosilanes.

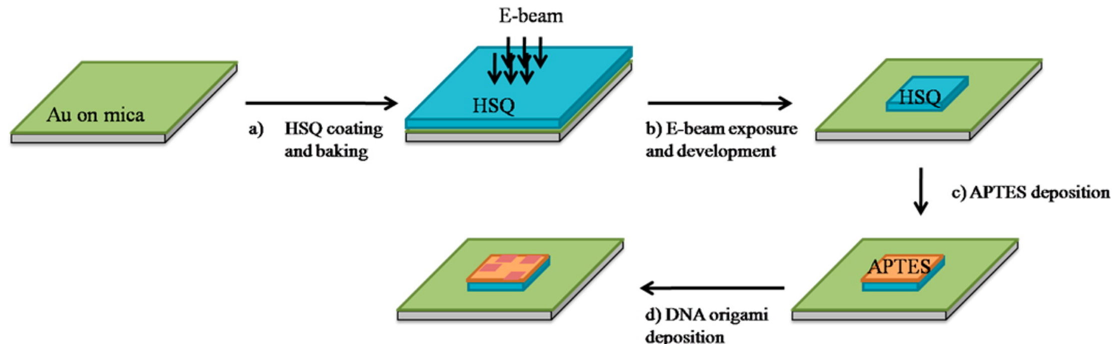

Figure 1.17: Schematic representation of negative tone patterning technique using EBL patterned HSQ. Aminosilane is functionalized on patterned SiO_x features, which are utilized for DNA origami assembly. Reprinted with permission from reference 158. Copyright 2012 American Chemical Society.

1.3 Scope and Thesis Statement

This section outlines the thesis statement of the research conducted. The scope for each chapter is provided.

1.3.1 Thesis Statement

Semiconductor tools and techniques which use electron beam lithography are an effective means to develop methods for patterning organosilanes on silicon and silica surfaces with arbitrary geometries and high resolution.

1.3.2 Chapter 1 Scope

Chapter 1 provides an overview of organosilanes, detailing some of the rich history of organosilane self-assembled monolayer development and exploration. The chapter provides the historical context for organosilane assembly, surface reactions, and introduces the reader to the techniques of self-assembly. It highlights vapor-phase processing and introduces the concepts of lithography and patterning organosilanes to allow nanoscale design of functional surfaces.

1.3.3 Chapter 2 Scope

Chapter 2 discusses the interaction between vapor-phase deposition of aminosilanes and commonly used EBL resists. The combination of the two are optimized to produce nanoscale arrays of aminoalkoxysilanes used for electrostatic self-assembly of gold nanoparticles. The nanoparticles are used also as imaging fiducials to evaluate interactions between organosilanes and resist types. A version of this chapter has been published in *Langmuir*.[159]

1.3.4 Chapter 3 Scope

This chapter details the application of organosilane deposition to intentionally form condensation structures. To my knowledge, this is the first report of these structures created using EBL and attempted control over their deposition characteristics. The work in this chapter revealed that condensation structures of aminoalkoxysilanes can be created with electron-beam lithography guided vapor-phase with controlled dimensions and morphology.

1.3.6 Chapter 4 Scope

Chapter 4 reports on the results of applying both positive tone and negative tone lithography approaches to the production of fluorescence nanoarrays using the vapor deposition of aminosilanes. This chapter compares these two methods with two fluorophores and describes how the array developed could be utilized for super-resolution microscopy application. The work confirmed that *EBL*-guided vapor-phase deposition of aminoalkoxysilanes can be used on electrically insulating and optically transparent surfaces for creation of a fluorescent nanoarray. Changes in lithographic approach (positive- vs negative- tone resists) improved nonspecific background fluorescence.

1.3.7 Chapter 5 Scope

Chapter 5 concludes the thesis and introduces future work and preliminary optimization attempts to improve the vapor deposition of organosilanes using EBL lithography. Alternative methodologies are introduced that may help extend the research discussed in the previous chapters.

2

Electron Beam Lithography Nanopatterning of Aminosilanes from the Vapor Phase: Pattern Selectivity of Colloidal Gold Self Assembly

2.1 Introduction

One of the most heavily used chemical approaches to functionalize metal oxide surfaces relies upon activated organosilanes.[18,19,29] These molecules contain either chloro- or alkoxysilane groups that condense with surface M-OH groups to covalently bind through M-O-Si bonds. If the organosilane contains an ω-termination through which further chemistry can take place, such as an amino or thiol group, these surfaces can then be further functionalized to produce more sophisticated interfaces.[18,19,160–169] Aminoproplyalkoxysilanes, which contain a primary amine, are workhorse silanes due to the propensity of these molecules to self-catalyze the silica

condensation step, and the ease of subsequent coupling of a range of functional groups with the amino group.[29,170,171] Aminoproplyalkoxysilanes have seen extensive use for biomedical applications, such as interfacing of biomolecules,[172] dyes,[173,174] nanoparticles[175], and antifouling agents to metal oxides.[176]

Many applications also require precise nano- or microscale patterning of the organosilanes to the metal oxide surface. With respect to aminopropylalkoxysilanes, recent examples of patterning strategies include microcontact printing, colloid and DNA origami-based lithography, and light-driven deprotection with near-field optical microscopy. Microcontact printing with PDMS stamps using an aminopropylalkoxysilane ink has been shown to produce micron-scale patterns down to a lower limit of ~200 nm.[177,178] Aminopropylalkoxysilanes have also been vapor-deposited within the open channels of an overlayed PDMS stamp.[179,180] Colloid lithography, which uses hexagonal arrays of polystyrene spheres, has been shown to produce ~100 nm diameter nanorings of condensed alkoxysilane features from the vapor phase.[181–185] Colloidal lithography is limited to hexagonal ordering, circular geometries, and the height is defined by the curvature of the latex spheres.[181,182,182,186] DNA origami masks have been used to produce triangular alkoxysilane features (~ 200 nm), but this interesting approach lacks control over long range order or pattern placement.[187] Recently, near-field microscopy has been used for patterned deprotection of (methoxyheptaethylene glycol)nitrophenylethoxycarbonyl-protected aminopropyltriethoxysilane monolayers, producing 150-200 nm amino-terminated features upon illumination using confocal optical techniques.[188,189]

Over a decade ago, very small nanoscale features (~20-25 nm) were shown to be accessible via electron beam lithography (EBL) using a thin sacrificial resist mask of

poly(methyl methacrylate) (PMMA) with a variety of alkoxy- and chlorosilanes, including aminopropyloalkoxysilanes. While promising, background contamination of alkoxysilanes in unpatterned areas following lift-off appeared to be an issue, as suggested by atomic force microscopy (AFM). Thus, the use of sacrificial polymer resists for EBL, followed by alkoxysilane deposition and complete removal of the resist, has seen little attention. EBL is, however, of great interest for the preparation of precise patterns of any desired shape, particularly in biomedical fields. Examples in which the resist itself is biologically active - a carbohydrate, silk, or polyethyleneglycol (PEG) - include patterned antibody-based chips,[190,191] enzyme immobilization,[192] surfaces to enable study of cancer cell adhesion,[193] among others.[153,194,195]

The possibility of a general approach to EBL patterning and functionalization using a commercially available EBL resist to enable area-selective deposition of alkoxysilanes is of interest since the EBL parameters would not need to be optimized for each new resist material. The alkoxysilane, if it has a functionalizable chemical handle such as an amino group, $-NH_2$, could then be used as a linker for the given application. Background contamination is an important consideration for applications such as sensors where nonspecific (background) adsorption of analytes may degrade signal to background ratios. In this work we used electron beam lithography to pattern aminopropyloalkoxysilanes on silicon surfaces, and varied the choice of both resist and aminosilanes to investigate how background functionalization was impacted. The degree of background functionalization was evaluated via electrostatic assembly of citrate-capped Au nanoparticles on these amino-terminated surfaces. We determined that vapor-phase deposition of aminosilanes can permeate through poly(methyl methacrylate) (PMMA) resists, leading to undesirable background conjugation. We found that the resulting

background levels can be reduced by utilizing a more sterically hindered alkoxyaminosilane, and by selecting an alternative commercial resist, ZEP520A.

2.2 Results and Discussion

2.2.1 Vapor-phase Deposition of Aminosilanes on Unpatterned surfaces.

Prior to patterning of the aminopropyloalkoxysilanes through a developed polymer mask, it was necessary to establish a baseline for the deposition of the silanes APTMS and APDIPES (Scheme 2) on unpatterned silicon surfaces (with native oxide). Both molecules were chosen because of their utility for subsequent conjugation via the amino group, and to contrast the reactivity of the trimethoxysilane moiety versus the diisopropylethoxy version. Earlier work had shown that vapor-phase deposition of APTMS would result in thick gels, whereas the monoethoxy version, led to more controlled monolayer formation.[153] Under the conditions studied here, vapor-phase deposition of APTMS and APDIPES resulted in smooth surfaces with sub-nanometer RMS roughness (0.4 nm and 0.1 nm, respectively, Figure 2.1).

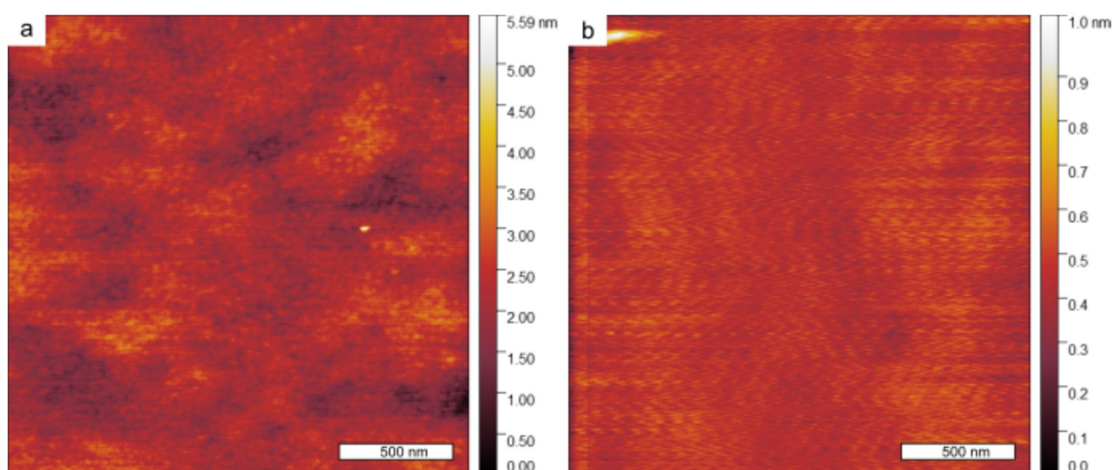

Figure 2.1. AFM images of APTMS (a) and APDIPES (b) as deposited on (100) silicon with native oxide. Reprinted with permission from reference 159 Copyright 2018 American Chemical Society.

These values are consistent with the literature as APTMS is expected to be more prone to multilayer formation than APDIPES.[196] Water contact angles for APTMS and APDIPES surfaces were measured to be 68.3 ± 1.6° and 85.1 ± 3.4°, respectively. A range of values for vapor deposited films of APTMS on silicon has been reported (55°-81°),[30,197] but APTMS is generally lower than that of APDIPES (97°).[96] XPS analysis confirmed the presence of nitrogen 1s peaks for both APTMS and APDIPES **vide infra**.

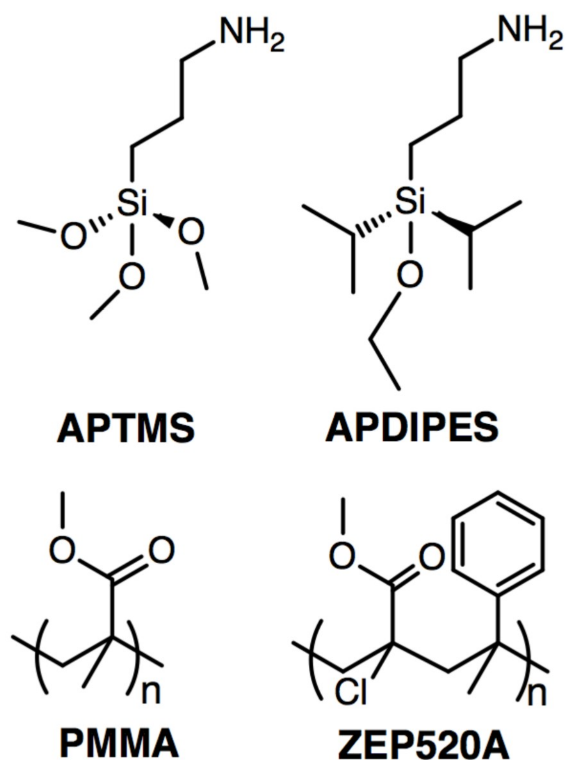

Figure 2.2 Chemical structures of aminosilanes and resists used in this work: (3-aminopropyl)trimethoxysilane (APTMS), 3-aminopropyldiisopropylethoxysilane (APDIPES), poly(methylmethacrylate) (PMMA), MW = 950,000 and ZEP520A, MW = 57,000. Reprinted with permission from reference 159. Copyright 2018 American Chemical Society.

2.2.2 Morphology of Patterned Aminosilanes.

Shown in Figure 2.3 is an example of the prototypical sacrificial mask pattern used in this work.

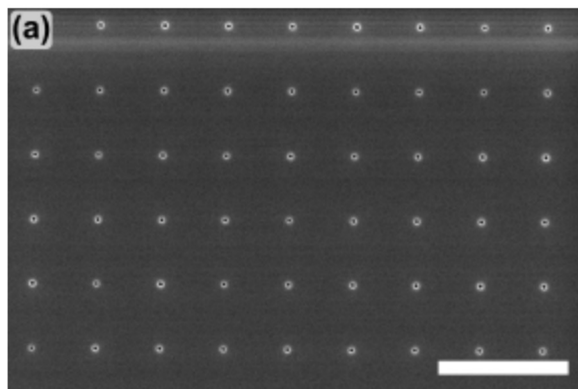

Figure 2.3 SEM micrograph of patterned ZEP520A(57k) after EBL exposure and development, with 30 nm diameter holes with a 500 nm square pitch. Scale bar is 1 µm. Reprinted with permission from reference 159. Copyright 2018 American Chemical Society.

The mask in Figure 2.3 consists of an EBL-patterned resist nanohole array (30 nm diameter) with a pitch of 500 nm. These resist masks were then used for patterning aminopropyloalkoxysilane features, shown in Figure 2.4. As seen in the SEM micrographs, well-defined alkoxyaminosilane structures formed in the exposed locations on the silicon surface, and they have a high degree of contrast from the silicon background, sufficient for imaging by SEM.

APTMS deposition (Figure 2.4 a) was found to form ring-shaped features within the hole array for all resists. The APTMS ring features were found to vary extensively in height across a sample, and from sample to sample, likely due to sonication-induced collapsing or breakage; an AFM micrograph of APTMS rings with a height of ~15-20 nm is shown in Figure 2.4 b. The ring features resulting from APTMS deposition are closely related to the edge features reported previously for alkyltrialkoxysilanes deposited from the vapor phase within the empty volumes underneath a PDMS stamp on silicon surfaces.

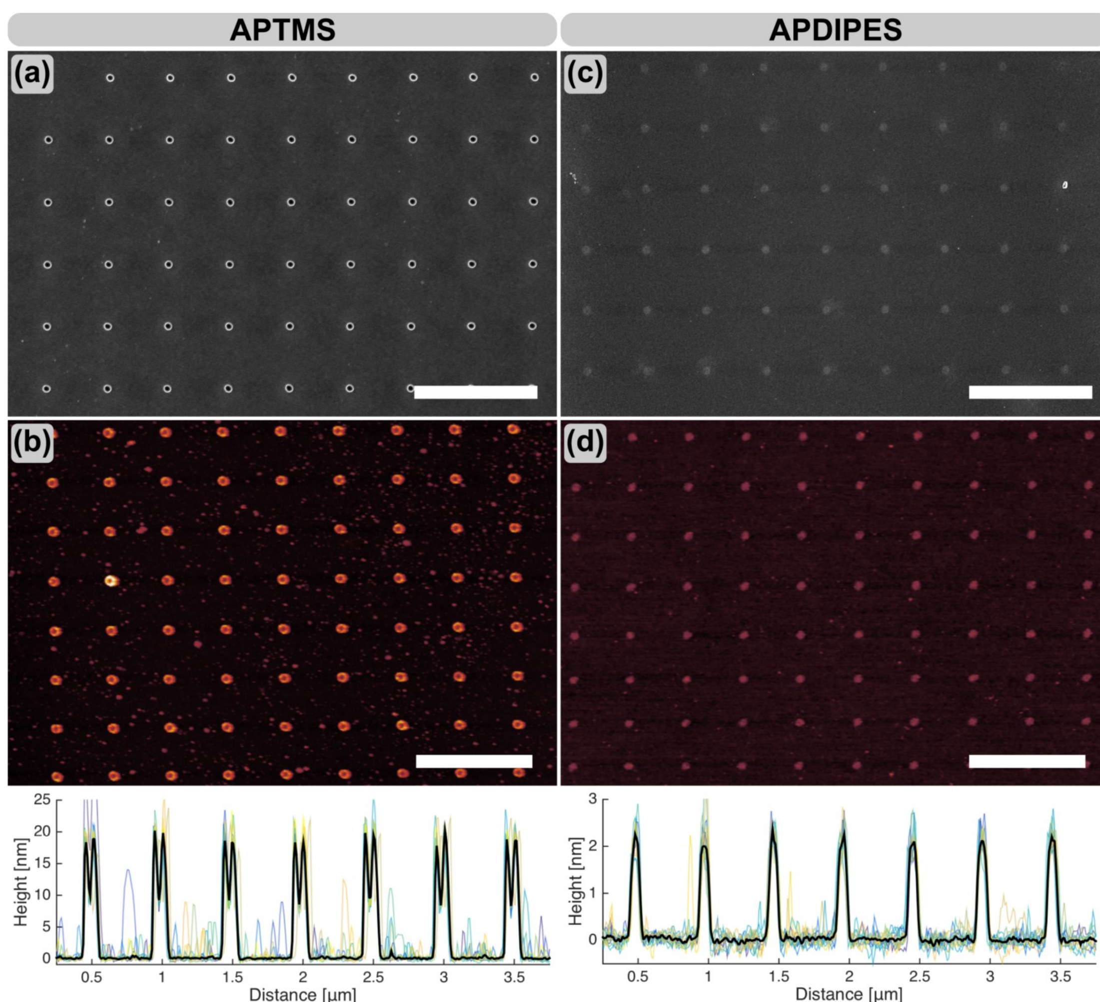

Figure 2.4 Patterned APTMS and APDIPES after resist removal. a) SEM image of APTMS features post-liftoff of resist. b) AFM height map of APTMS dot array showing tall tubular morphology. c) SEM image of APDIPES features post-liftoff of resist. d) AFM height map of APDIPES dot array showing a low profile morphology. Corresponding AFM height profiles shown below, taken along the horizontal direction going through the center of the dots. The thick line (black) is the median of all the individual height profiles (12 per image). All scale bars are 1 µm. Reprinted with permission from reference 159. Copyright 2018 American Chemical Society.

Mutlilayer APTMS deposition took place at the contact point of the PDMS wall and the surface[179,181] A plasma-based resist removal method that does not involve sonication could enable the observation of consistent height profiles of rings prepared using APTMS, but this aggressive resist stripping method would almost certainly eliminate the terminal amino groups entirely.[198] APDIPES deposition was also patterned, and the resulting features were found to be more

uniform in height and area, measuring 2.0 ± 0.6 nm in height (Figure 1d) with no visible pore or ring shape like that seen with APTMS (Figure 1c). The less reactive and sterically hindered monofunctional silane limits polymerization of the siloxane moiety within the confined environment of the resist film.[153,179] APDIPES should be restricted to forming a monolayer on an oxide surface since the molecule has only one reactive ethoxy group, but potential hydrogen bonding to the surface with the amine group in an inverted orientation is a possibility. Aminosilanes have been known to deposit onto silicon surfaces in a variety of orientations,[29] including via hydrogen bonding between the amine hydrogens and surface hydroxyl groups of the native oxide, as well as electrostatic attraction between the surface and/or neighbouring species.

2.2.3 Gold Colloid Self-Assembly on Aminosilane Nanopatterns.

Although the patterns are visible in the SEM micrographs due to sufficient morphological contrast between the patterned alkoxyaminosilane nanostructures and the surface, it is necessary to characterize the *chemical* contrast of these functional nanopatterns. We assume that the patterned regions are capped with amino functionalities, which should be demonstrated. It has been previously shown that negatively charged citrate-capped gold nanoparticles will bind to positively charged amine-terminated surfaces.[177,199] As such, we utilized gold nanoparticles as fiducials for SEM imaging of aminosilane nanopatterns through electrostatic conjugation of the particles to the prepared surfaces. Colloidal self-assembly of gold nanoparticles on surfaces is an active field of research,[200–203] and patterning their assembly is of its own interest for a number of applications.[204–207] In this work, the background unpatterned areas are still capped with a native oxide whose negatively charged Si-O^- groups prevent citrate-capped gold nanoparticles from

binding due to electrostatic repulsion. On the other hand, the positively charged -NH_3^+ functional groups in the patterned domains should enable localized capture of the net negatively charged gold nanoparticles. After immersion of the alkoxyaminosilane-functionalized surfaces in a gold nanoparticle solution, the samples were rinsed to remove nonspecifically bound particles. Prior to gold nanoparticle conjugation of patterned alkoxyaminosilane surfaces, the particle conjugation density of unpatterned APTMS and APDIPES monolayers was measured as a baseline. Homogeneous APTMS and APDIPES surfaces were immersed in a solution of citrate-capped gold nanoparticles via immersion in an aqueous gold nanoparticle solution for 48 h. Upon successive sonication in 10 min H_2O and IPA to remove unbound gold nanoparticles, near-complete coverage and uniform nanoparticle deposition was confirmed for both surfaces by SEM (Figure 2.5).

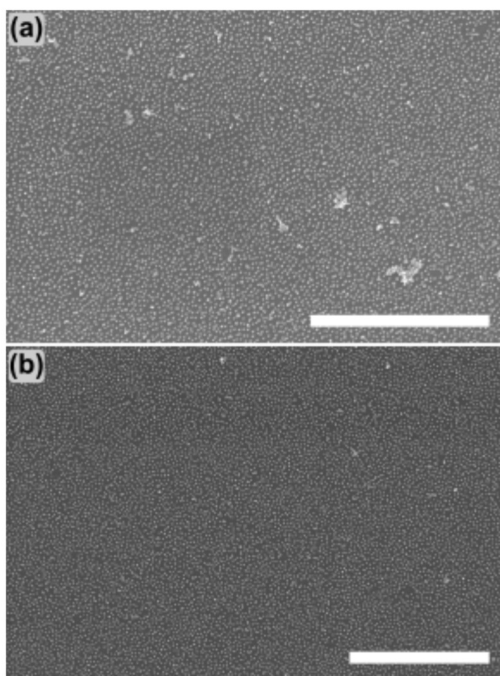

Figure 2.5 SEM micrographs of homogeneous layers of APTMS and APDIPES deposited on silicon conjugated to gold nanoparticles without patterning a) APTMS on silicon with gold nanoparticles and b) APDIPES on silicon with gold nanoparticles. Reprinted with permission from reference 159. Copyright 2018 American Chemical Society.

APTMS surfaces were found to conjugate 1328 particles/μm^2, while APDIPES conjugated 1308 particles/μm^2 (Table 1). Figure 2.6 shows dot arrays with a square pitch of 500 nm patterned using two different resists: PMMA(950k) and ZEP520A(57k).

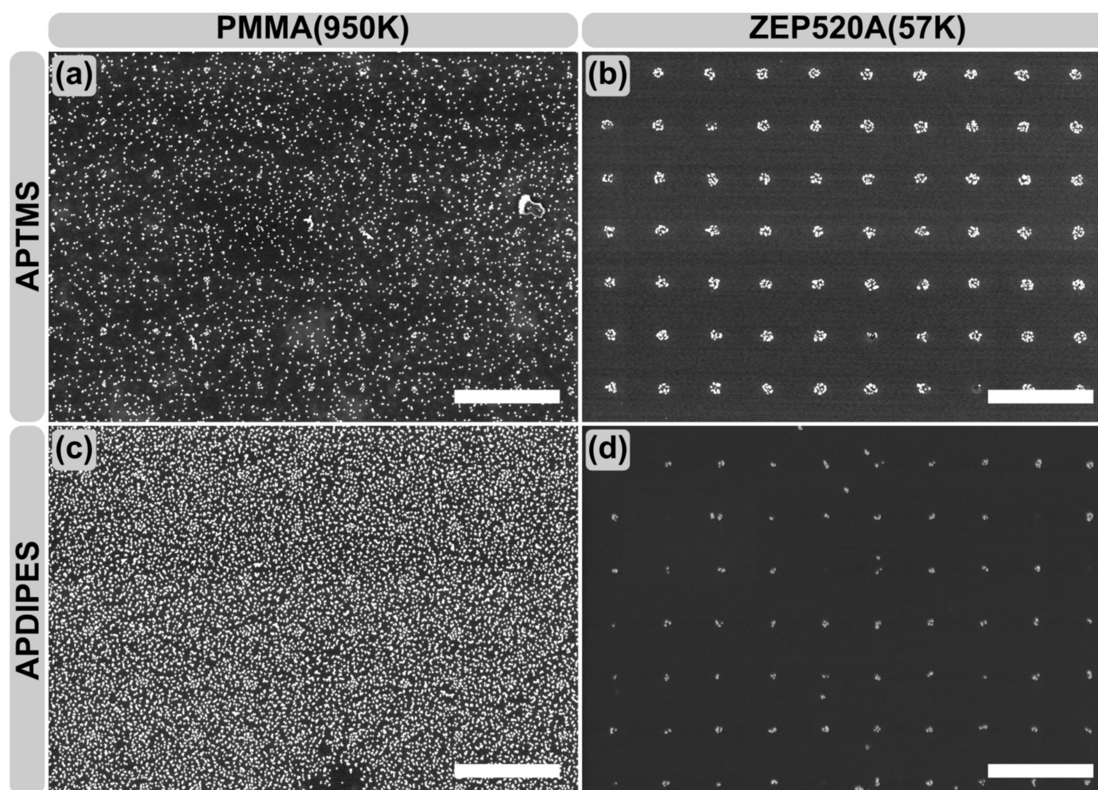

Figure 2.6 Au nanoparticle conjugation of aminosilane features patterned using PMMA(950k) and ZEP520A(57k) resist masks. a) APTMS patterned through PMMA(950k), b) APTMS patterned through ZEP520A(57k), c) APDIPES patterned through PMMA(950k), and d) APDIPES patterned through ZEP520A(57k). All scale bars are 1 μm. Reprinted with permission from reference 159. Copyright 2018 American Chemical Society.

Figure 2.6 indicates that for PMMA(950k) masks (Figure 2.6 a), a substantial number of particles are bound to the unpatterned areas that should be unfunctionalized native oxide (with a net negative charge). For APTMS patterned through PMMA(950k), nonspecific binding, as evidenced by particles located in unpatterned areas (that should be silicon oxide), measured 177 particles/μm^2 for PMMA(950k). Conversely, near-zero background particle density in unpatterned areas was found (~1 particle/μm^2) when using a ZEP520A(57k) resist mask (Figure

2b). As shown in Figure 2.6 c–d, functionalizing patterned surfaces with APDIPES resulted in similar conjugation selectivity to that seen with APTMS. Following immersion of patterned APDIPES surfaces prepared using both PMMA(950k) and ZEP520A(57k) patterned resists in the gold nanoparticle solution, extensive background conjugation was found for PMMA(950k) (Figure 2.6 c), while minimal background conjugation was observed for the ZEP520A(57k) resist (Figure 2.6 d). Again, a large difference in conjugation selectivity is present between resist types (PMMA vs ZEP520A), as measured by the background particle conjugation counts (Table 1).

Table 2.1 Density of Conjugated Au Nanoparticles in the Background (Unfunctionalized) Regions of Patterned surfaces. Background Particle Densities Marked as < 1 Particle/μm^2 did not have a Statistically Significant Number of Particles within the SEM Field of View to be Determined with Greater Precision. Reprinted with permission from reference 159. Copyright 2018 American Chemical Society.

Resist	Silane	Background Particle Density (particles/μm^2)
PMMA(950k) - Patterned	APTMS	177
PMMA(950k) - Unpatterned	APTMS	198
PMMA(495k) - Patterned	APTMS	198
PMMA(495k) - Unpatterned	APTMS	89
ZEP520A(57k) - Patterned	APTMS	< 1
ZEP520A(57k) - Unpatterned	APTMS	< 1
PMMA(950k) - Patterned	APDIPES	419
PMMA(950k) - Unpatterned	APDIPES	19
PMMA(495k) - Patterned	APDIPES	122
PMMA(495k) - Unpatterned	APDIPES	< 1
ZEP520A(57k) - Patterned	APDIPES	< 1
ZEP520A(57k) - Unpatterned	APDIPES	< 1
No Resist	APTMS	1328
No Resist	APDIPES	1308

It is observed that APDIPES samples have on average a lower number of conjugated gold nanoparticles per circular templated feature than APTMS (5 ± 2 compared to 17 ± 4, respectively). This effect may may be due to the presence of fewer amino groups in each circular domain, compared to the taller APTMS ring structures that have higher net surface areas. Several instances of 1—2 nanoparticles per circular area were noted, as well as a few empty domains (zero nanoparticles per templated feature), and thus there may be potential to optimize for a single nanoparticle per feature by varying the sizes of nanoparticles (choosing a larger nanoparticle), or by further reducing the patterned feature size.

2.2.4 Vapor-phase Permeation of Aminosilanes through EBL Resists.

Although both PMMA and ZEP520A form compact films, it is possible that the vapor-phase aminosilane molecules diffuse through these films and reach the silicon/resist interface, which could explain the high background observed in the case of the PMMA resist. If APTMS or APDIPES remain at the silicon surface after resist removal, they will react with unpatterned areas during rinsing, leading to the observed background gold nanoparticle conjugation. Therefore, to test if diffusion of vapor-phase silanes was occurring through the full thickness of the films, we prepared unpatterned (no EBL exposure) films of each resist, and then exposed the films to alkoxysilane vapor as per the normal procedures. After APTMS deposition, resist removal and subsequent gold nanoparticle conjugation, it was found that unpatterned PMMA resists suffered from substantial quantities of conjugated gold nanoparticle binding (198 particle μm^2, Figure 2.7 a) while ZEP520A(57k) films exposed to APTMS showed few conjugated gold nanoparticles (~0.1 particle/μm^2, Figure 2.7 b).

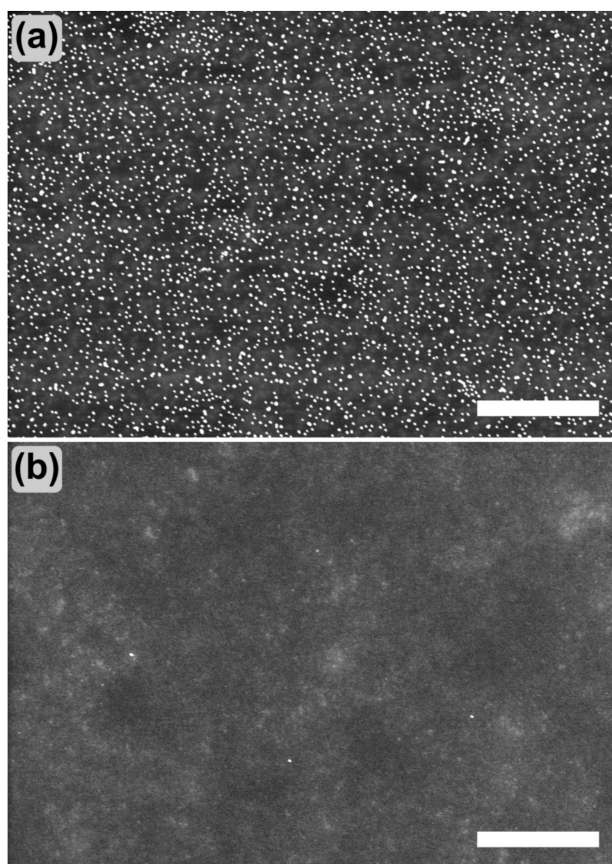

Figure 2.7 SEM micrographs of unpatterned resists undergoing particle conjugation after resist removal. a) PMMA (950k) after APTMS deposition b) ZEP520A (57k) after APTMS deposition. All scale bars are 1 μm. Reprinted with permission from reference 159. Copyright 2018 American Chemical Society.

Interestingly, the PMMA samples subjected to APDIPES deposition behaved somewhat differently. Specifically, unpatterned films exposed to APDIPES deposition had lower densities of conjugated gold nanoparticles (~ 1-20 particle/μm^2) than those exposed to APTMS (~ 90-200 particle/μm^2). These results are in line with the reported diffusion coefficients of molecules absorbed from the vapour phase through PMMA thin films. It was found that a 1 Å increase in the mean molecule diameter resulted in a ~10^3 decrease in the diffusion coefficient.[208] Therefore, the bulkier APDIPES (Scheme 2) would be expected to have a lower diffusion rate through the PMMA. However, it is also noted that patterned PMMA films having undergone APDIPES

deposition had similar background conjugation densities (~100-400 particle/μm^2) compared to APTMS. Furthermore, SEM investigation of the unpatterned films revealed spatially non-uniform patches of regions with and without conjugated nanoparticles (Figure 2.8).

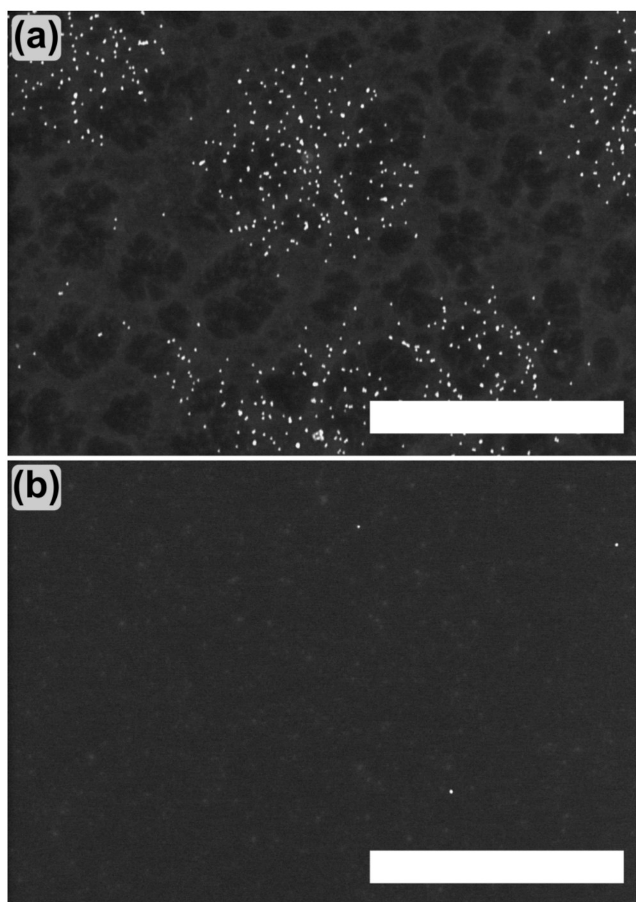

Figure 2.8. SEM micrographs of unpatterned resists undergoing particle conjugation after resist removal. a) PMMA (950k) after APDIPES deposition b) ZEP520A (57k) after APDIPES deposition. Reprinted with permission from reference 159. Copyright 2018 American Chemical Society.

Given these discrepancies, further investigation will be required to better understand the differences between APDIPES and APTMS deposition through PMMA resists. XPS analysis was also performed to better understand the permeation of these alkoxyaminosilanes through the different resists. Samples for XPS analysis were prepared in an identical fashion as those in

Figure 2.7, except the final particle conjugation step was not performed. Detection of aminosilane molecules on the silicon surfaces was carried out by analyzing the N(1s) XPS spectra. Figure 2.9 a shows two peaks (at 400.9 and 402.8 eV) for a sample of silicon that was only treated with with APTMS vapor, and no resist. The peak at 402.8 eV is assigned to protonated APTMS, and the peak at 400.9 eV is assigned to non-protonated APTMS.[209] Similarly, in Figure 2.10 b, the fitted components are shown for the APDIPES on silicon surface (again, no resist), with the higher binding energy peak corresponding to the presence of protonated amine. Comparison of the N(1s) spectra of APTMS and APDIPES samples reveals that there is roughly twice as much total signal from the APTMS layer, which is expected due to the higher propensity of APTMS to polymerize.

From the XPS signal in Figure 2.9 b we can conclude that nitrogen is present on the silicon surface after vapor deposition of APTMS through unpatterned PMMA(950k). These data suggest that for the PMMA(950k) resist, APTMS can diffuse through the thickness of the film and reach the silicon/resist interface. Conversely, there is no detectable nitrogen remaining on the surface of the silicon after APTMS vapor deposition through ZEP520A(57k) (Figure 2.9 c). Analogous results were found for vapor deposition of APDIPES through PMMA(950k) and ZEP520A(57k) (Figure 2.10).

While little work has been done examining organosilane/resist interactions, there has been some previous experimental work about water adsorption by polymer thin films. PMMA films have been known to absorb water, and they have been used as the basis for capacitance type humidity sensors.[210] PMMA films have been shown to hydrogen bond with water in molecular dynamics studies,[211] and it has been suggested that hydrogen bonding is a major factor

in the water sorption behavior of other resists.[212] It has also been suggested that higher temperature lithography process steps enhance diffusion,[212] which would increase water sorption and quickly lead to non-zero equilibrium water content in the resist.

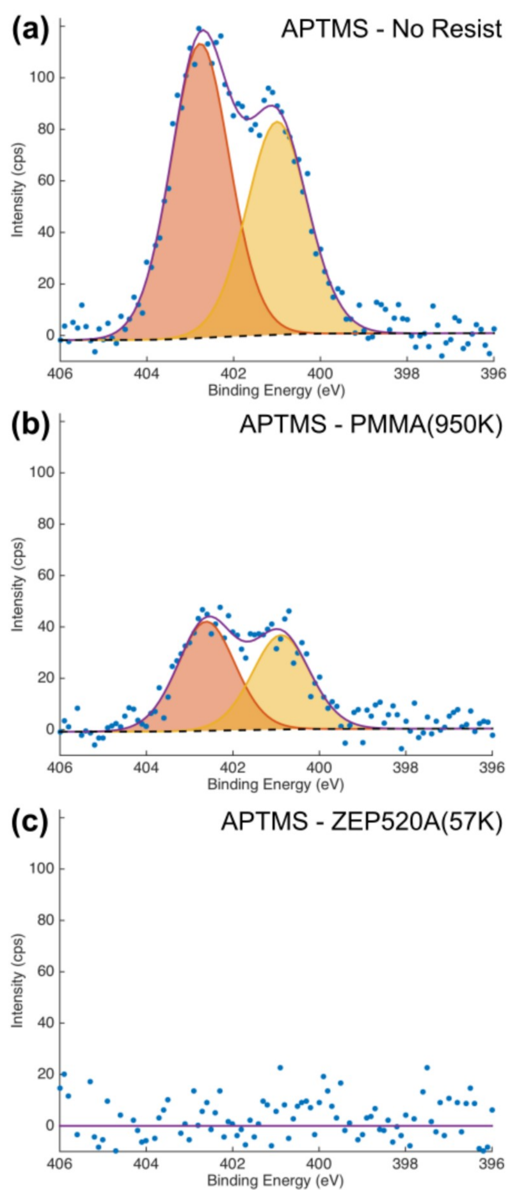

Figure 2.9 High resolution XPS scans of the N(1s) region after APTMS deposition (a) on bare, clean silicon with native oxide, (b) unpatterned film of PMMA(950k) which was then removed, and (c) on an unpatterned film of ZEP520A(57k) which was then removed. Reprinted with permission from reference 159. Copyright 2018 American Chemical Society.

As our deposition occurs at 80 °C for 18 h, it is likely that any residual water in the deposition chamber would be absorbed by the films during silane deposition. As the elevated temperature also enhances diffusion through the film, it is likely that the organosilane film penetration is also enhanced. The ZEP520A resist has not, unfortunately, been studied with respect to water absorption.

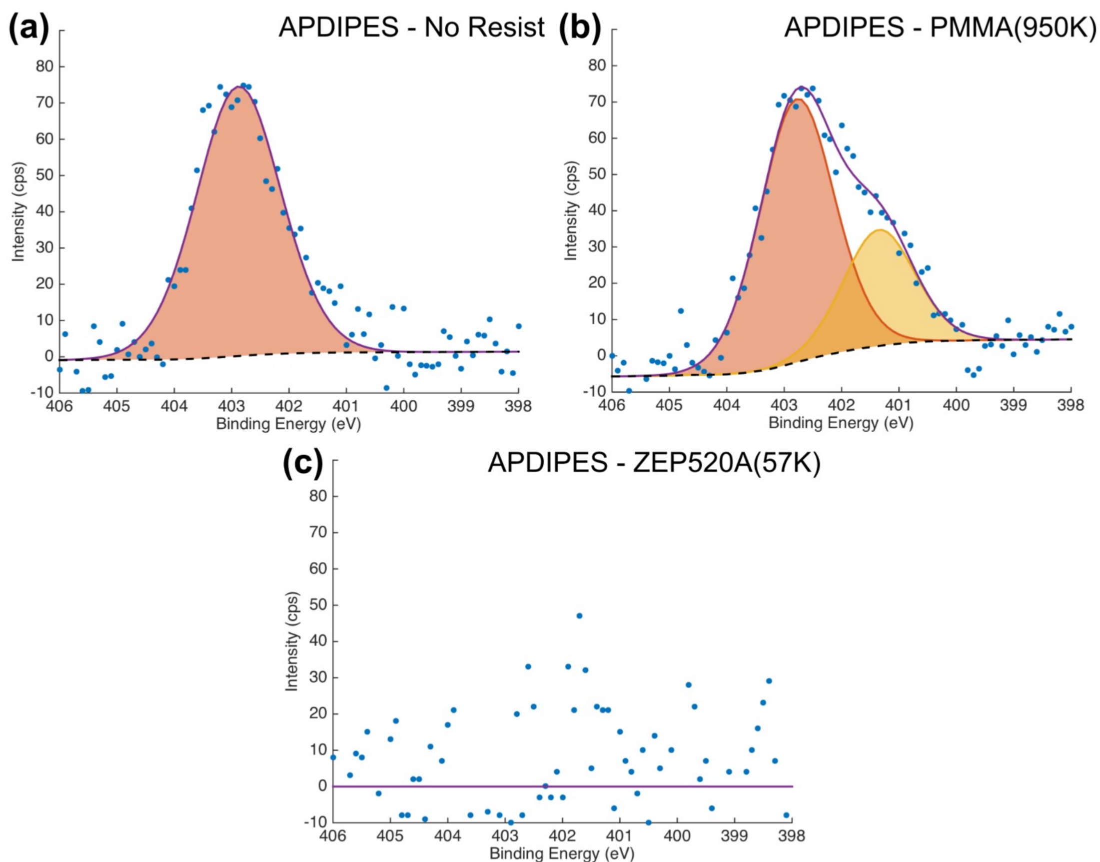

Figure 2.10 High resolution XPS scans of the N(1s) region after APDIPES deposition (a) on bare, clean silicon with native oxide, (b) unpatterned film of PMMA(950k) which was then removed, and (c) on an unpatterned film of ZEP520A(57k) which was then removed. Reprinted with permission from reference 159. Copyright 2018 American Chemical Society.

2.2.5 PMMA and ZEP520A: Understanding Differences in Background Functionalization with APTMS.

Given the stark contrast in background conjugation of Au nanoparticles after vapor-phase deposition of aminosilanes through a PMMA or ZEP520A resist, we sought to understand the origin of these differences. Although there is a strong correlation between background conjugation of gold nanoparticles and alkoxyaminosilane surface concentrations at the silicon surface after vapor deposition through unpatterned resists,(as measured by XPS), other possible mechanisms by which the Au nanoparticles would bind to the background regions should be considered. When using solvent-based methods for resist removal, there will typically be a very thin layer of residual resist left on the surface, often referred to as scum.[213] It is possible that this residual resist, the scum, is playing a role. To test this possibility, additional nanoparticle conjugation controls were prepared for resist-only samples. Unpatterned surfaces of PMMA(950k) and ZEP520A(57k) were subjected to all deposition conditions, with the exception of exposure to the alkoxyaminosilane. The resists were removed and the surfaces were immersed in a gold nanoparticle solution. Figure 2.11 indicates these samples did not result in measurable nanoparticle conjugation after the resists were been removed (~ 1 particle/μm^2). These results clearly indicate that the residual resist does not contribute binding of gold nanoparticles to the surface. Therefore, the alkoxyaminosilanes are responsible for the observed gold nanoparticle conjugation.

Another important factor differentiating PMMA(950k) and ZEP520A(57k) is their significant difference in molecular weights. As previously shown by Turner,[214] low molecular weight PMMA was found to have a smaller water diffusion coefficient than high molecular

weight PMMA. However, this effect of molecular weight on diffusion coefficient was very weak, and was even more muted when the PMMA samples were prepared in the glassy state, which is likely the case for the thin films utilized in this work. As such, we attempted to test the effect of molecular weight by utilizing PMMA with a different molecular weight, 495k. This resist, while only close to half the molecular weight of PMMA(950k), is also a commonly utilized lithography resist.

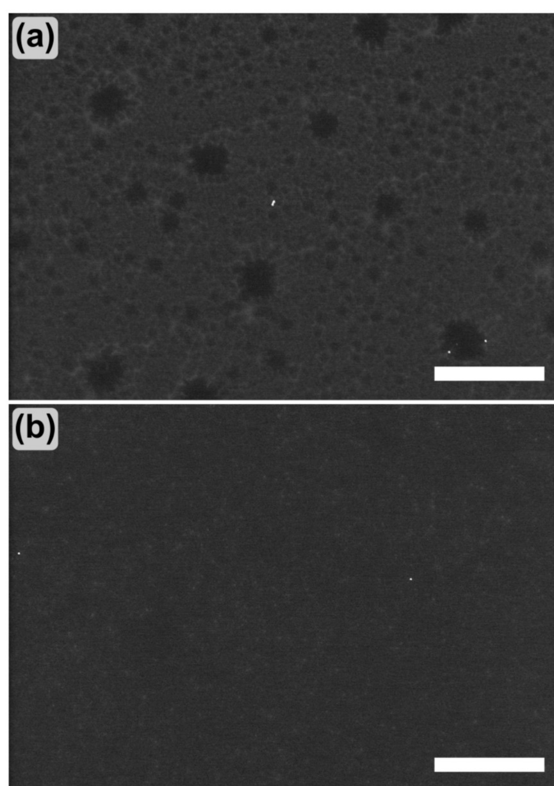

Figure 2.11 SEM micrographs of unpatterned resists undergoing particle conjugation after resist removal. a) ZEP520A (57k) after removal and nanoparticle solution immersion for 48 h and b) PMMA (950k) after resist removal and nanoparticle solution immersion for 48 h. Scale bars are 1 μm. Reprinted with permission from reference 159. Copyright 2018 American Chemical Society.

We observed similar behavior for the PMMA(495k) - large amounts of gold nanoparticles were found to bind to unpatterned areas of silicon (Figure 2.12, Table 1) and resist residue control experiments inspected in SEM also confirmed the likelihood of alkoxyaminosilane film

penetration for APTMS. Although these results are not conclusive regarding the role of molecular weight given that halving the molecular weight of the PMMA did not have any appreciable effect on gold particle conjugation density, it is unlikely that differences in molecular weight are significant.

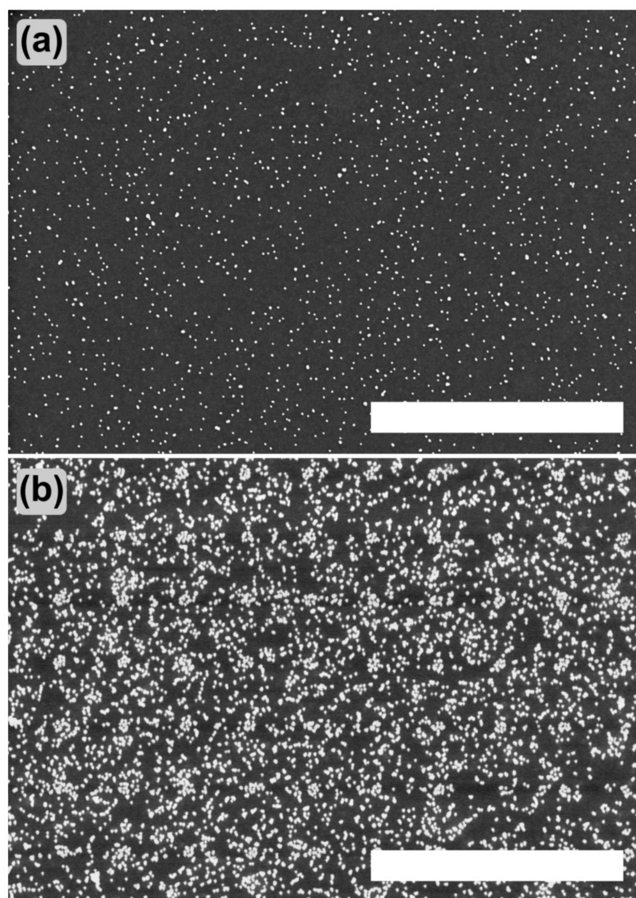

Figure 2.12 SEM micrographs of unpattered APTMS (a) and patterned APTMS (b) through PMMA(495k) resist conjugated with gold nanoparticles. Scale bars are 2 μm. Reprinted with permission from reference 159. Copyright 2018 American Chemical Society.

From the XPS data we can conclude that vapor-phase APTMS and APDIPES can diffuse through compact films of PMMA(950k) and react with the silicon surface, which remain after solvent removal of the PMMA resist. Conversely, there are no aminosilanes observed on the

silicon surface after removal of the ZEP resist. These observed differences must be related to the chemical composition of each resist. While PMMA contains repeat units of methylmethacrylate groups, ZEP520A is a copolymer of methyl styrene and chloromethyl acrylate (Scheme 2). The increased hydrophobicity of ZEP520A may reduce the diffusion of these very polar alkoxyaminosilane molecules in ZEP520A. However, there is only a small difference in the measured water contact angle of PMMA(950k) (70 ± 2°) and ZEP520A(57k) (76 ± 0.8°) films, making it unlikely that any differences in hydrophobicity would be sufficient to account for the observed differences in background reactivity. Moreover, if differences in diffusion coefficients were primarily responsible for the differences in background conjugation densities, this would require the diffusion coefficient of APTMS in PMMA(950k) to be ~10^8 greater than ZEP520A(57k) (assuming that the diffusion distance is given by $\sqrt{D}$), given that the background conjugation density of PMMA(950k) is ~10^4 times greater than ZEP520A(57k).

SEM inspection of the silicon surfaces after resist removal shows distinct morphological differences between PMMA(950k) and ZEP520A(57k) (Figure 2.11). Specifically, for PMMA(950k) there is a patchy morphology of what appears to be residual film (bright regions) with a high density of holes (dark regions). Conversely, for ZEP520A(57k) there is very little contrast variation across the image. This suggests that there is significantly more residual resist remaining from the the PMMA(950k) film than ZEP520A(57k) (Figure 2.11). If the standard solvent removal of PMMA is less efficacious than for ZEP520A, alkoxyaminosilane absorbed within the PMMA could then react with the silicon, accounting for the observed differences in background gold nanoparticle conjugation. Indeed, ZEP520A has been reported to adhere only weakly to clean native oxide-capped silicon surfaces.[215] Assuming that APTMS or APDIPES

present following solvent removal would be partially embedded in the resist, improved resist removal could also improve removal of these groups near the silicon/resist interface. Although the SEM images suggest a greater degree of residual resist from the PMMA films, quantitatively assessing these differences via SEM imaging of potentially nanometer-thick layers is challenging. To this end, we employed contact angle measurements to determine differences in surface energy parameters of bare silicon (with native oxide), silicon after PMMA(950k) film removal and silicon after ZEP520A(57k) film removal. Surfaces of residual resist were prepared consisting of silicon <100> on which resists had been prepared, and then removed following a faux deposition with no alkoxyaminosilane present.

To determine surface energy components, the Young–Dupré equation for polar systems is:

(2.1) $$(1 + \cos\theta)\gamma_L^{tot} = 2\left(\sqrt{\gamma_S^{LW}\gamma_L^{LW}} + \sqrt{\gamma_S^{+}\gamma_L^{-}} + \sqrt{\gamma_S^{-}\gamma_L^{+}}\right)$$

where γ_L^{Tot} is the total interfacial energy, θ is the contact angle of the probe liquid against solid surface *S*, γ^{LW} is the Lifshitz–Van der Waal component, γ^+ and γ^- are the Lewis acid and base components of the surface (*S*) and probe liquid (*L*), respectively. Therefore, by measuring the contact angle of a surface with a minimum of three well characterized probe liquids, one can determine the individual surface energy components for an unknown surface. The probe liquids used here were water, diiodomethane, formamide, and ethylene glycol, as described in the experimental section.

Table 2.2 summarizes the surface energy components quantified for each surface. Having determined the surface energy components of native oxide-capped silicon, PMMA(950k), and ZEP520A(57k), we can use these values as comparative baselines for the silicon surfaces that have had the resist removed. Native oxide-capped silicon is found to have the highest total surface energy of 51 mJ/m^2, and donicity (Lewis base component) of 57 mJ/m^2. PMMA(950k) and ZEP520A(57k) films have slightly lower total surface energies (39 and 45 mJ/m^2, respectively) but significantly lower donicities (14 and 7 mJ/m^2, respectively). With these distinctions in mind, we can see that the silicon surface after ZEP520A(57k) removal is very similar to the native silicon oxide, as it has both similar surface energy, 50 mJ/m^2, and donicity of 50 mJ/m^2. The results suggest that there is very little residual resist left on the surface, or we would have expected to see a much lower donicity, similar to that of pure ZEP520A(57k). Conversely, for the silicon surface after PMMA(950k) removal, we see a slight decrease in total surface energy 45 mJ/m^2 and significant drop in donicity to 23 mJ/m^2. In agreement with SEM observations, these results also suggest that there is significant residual resist left on the silicon surface after PMMA(950k) removal.

Lastly, it is noted that our choice of dichloroethane as a solvent to remove PMMA was motivated by work done Bernstein and co-workers,[216] who found that this was the best solvent for PMMA, when compared to dichloromethane and acetone. However, from our analysis there may be more effective solvents available for PMMA removal. For ZEP520A(57k), removal in N,N-dimethylacetamide appears to minimize background residue remaining after soaking and sonication, as inspected by SEM and per contact angle determination.

Table 2.2 Measured Surface Energy Parameters of Different Surfaces Investigated in this Work. Reprinted with permission from reference 159. Copyright 2018 American Chemical Society.

Surface	γ_L^{Tot} (mJ/m²)	γ_S^{LW} (mJ/m²)	γ_S^{+} (mJ/m²)	γ_S^{-} (mJ/m²)
Blank Si	50.8 ± 0.1	40.0 ± 0.3	0.5 ± 0.0	57.4 ± 0.5
^{a}Si/PMMA(950K)	44.7 ± 2.0	43.4 ± 0.8	0.1 ± 0.1	23.2± 5.0
^{a}Si/ZEP520A(57K)	50.3 ± 1.0	42.9 ± 2.0	0.3 ± 0.2	50.3± 4.0
PMMA(950K)	38.9 ± 0.8	38.9 ± 0.8	0.0 ± 0.0	13.7± 1.0
ZEP520A(57K)	44.6± 1.0	44.6 ± 1.0	0.0 ± 0.0	7.1 ± 0.6

^{a}Silicon surface after removal of the corresponding resist.

In summary, several reasons for nonspecific conjugation were investigated, and it was found that halving the molecular weight of the PMMA resist did not reduce the observed nonspecific conjugation of gold nanoparticles. Differences in APTMS diffusion coefficients in PMMA(950k) and ZEP520A(57) were also unlikely to be the culprit, as a ratio of ~10^8 would be required. However, through SEM investigation and contact angle measurements, it was shown that solvent removal of the PMMA resulted in a large amount of resist scum, which would leave embedded aminosilanes on the surface. Conversely, solvent removal of the ZEP520A left the surface in a pristine state, similar to that of native silicon dioxide.

2.2.6 Patterning of Au Nanoparticles using APDIPES and ZEP520A.

We were able to pattern sub-100 nm lines, arrays of small particle clusters, and geometric shapes by patterning APDIPES through ZEP520A(57k) masks. Patterns with extremely low nonspecific binding were produced, simply using the native oxide for charge repulsion in lieu of a second passivation step (Figure 6). Figure 6a indicates lines consisting of ~2 gold nanoparticles-wide. The small clusters obtained in the square dot array arrangement are attractive as gold nanodots

are regularly used in the literature as to anchor reactive ligands to the surface in a range of applications.[155] Figure 6c points to low nonspecific deposition, as shown by the fine 30 nm empty negative space between larger patterned lines (> 250 nm) from a Fresnel lens pattern. Additionally, geometric shapes with sharper corners such as triangles (Figure 6d) may have applications for studying plasmonic coupling and edge enhancement.[217] Previous literature has shown successful patterning of gold nanoparticles on alkoxyaminosilane-functionalized surfaces, but the results shown here suggest that a second functionalization step to prevent non-specific interactions may be unnecessary, even for small sub-30 nm features or domains.[177,180,199] Through optimal selection of mask material and silane coupling agent, one can produce small nanoscale patterns of arbitrary geometries with high fidelity.

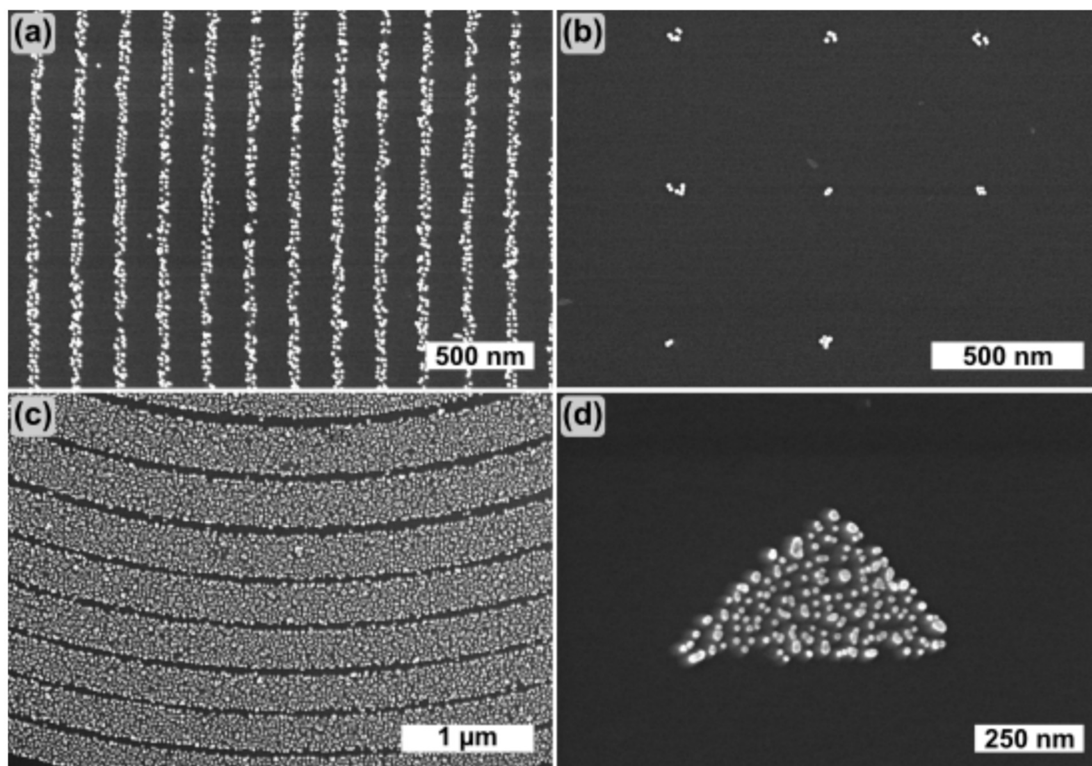

Figure 2.13 SEM micrographs of patterned APDIPES utilizing ZEP520A (57k) following 48 h gold nanoparticle conjugation and rinsing. a) 50 nm, 200 nm pitch line grating. b) 500 nm pitch square dot array. c) 30 nm minimum

separation distance between Fresnel pattern lines. d) 650 nm base width triangle. Reprinted with permission from reference 159. Copyright 2018 American Chemical Society.

2.3 Conclusions

The results in this chapter demonstrate that standard positive-tone electron beam lithography resists can be used as masks to guide vapor-phase deposition of aminoalkoxysilanes, however this is not broadly applicable. ZEP520A is growing in use however PMMA is still the dominant EBL resist of choice. This chapter has shown that resist selection did improve non-specific deposition. PMMA is a well characterized resist, and many recipes exist for working with PMMA.[218] We have, however, highlighted the potential impact of more subtle issues associated with working with PMMA that do not appear to be in play with ZEP520A. Specifically, if the EBL resist is to be used as a mask for vapour phase patterning of any functional molecule, it is not only the patterned locations that need to be considered, but unpatterned background areas as well. Ideally, the unexposed (unpatterned) portions of the resist mask should be completely removable, for potential backfill with another coupling or passivation agent, or for use as the native surface. The ideal scenario would be to preserve both chemical reactivity of the organosilane in question, and remove all residual resist in unpatterned areas, leaving a background of near pristine surface.

This work has highlighted the impact of resist choice when patterning alkoxyaminosilanes from the vapor-phase for further functionalization. Our data suggest that APTMS vapor is able to diffuse through EBL resist films of PMMA, and that this contamination can have dramatic effects on background functionalization. With potential sensor or imaging applications, this effect would lead to a large increase in background noise. By utilizing

ZEP520A(57k) as the resist, however, one can greatly reduce background functionalization, opening up avenues for more advanced and sensitive design. Low background levels of silane deposition, as quantified through determination of the density of conjugated gold nanoparticles, were consistently observed with the ZEP520A resist. With PMMA, however, only the combination of the APDIPES silane and a lower molecular weight PMMA resist was successful.

In the context of self-assembly of domains of colloidal gold, the self-assembly of clusters of gold nanoparticles with virtually zero nonspecific conjugation by using a ZEP520A(57k) resist and a simple immersion deposition protocol. The combination of APDIPES and ZEP520A(57k) shows great potential in patterned colloidal self-assembly of negatively charged nanoparticles on silicon surfaces, moving towards single nanoparticle localization at wafer scale.

2.4 Experimental

2.4.1 EBL Mask Fabrication

Three commercial positive tone EBL resists were compared for this study: PMMA (950k and 495 k molecular weight, MicroChem Corp) and 57k molecular weight ZEP520A (Zenon Chemicals). PMMA(950k), PMMA(495k), and ZEP520A(57k) resists were spin-coated (Brewer Cee Spinner) to thicknesses of 148 nm, 141 nm, and 147 nm, respectively, as measured by white light interferometry (Filmetrics F20). Resist films were inspected in an inverted brightfield microscope (Leitz Ergolux). All resists were subjected to a pre-exposure bake of 30 s at 180 °C. Electron beam exposure was performed on a Raith 150-Two EBL system. Single pixel dot-shot features were created at a 30 keV accelerating voltage and a 22 pA beam current. Alignment mark features were created at 30 keV with a 1396 pA beam current. This high dose regime

created negative tone behavior for the alignment features in the resists,[219] which aids in later characterization steps. Mask characterization was carried out to confirm effective clearance doses as well as initial mask dimensions. Single pixel dot features were varied in dose systematically to determine effective clearance doses ranging from 0.1 to 12 fC/dot. Concurrently, this also varies the size of the features, where the smallest dot mask features utilized measured 30 nm in diameter. Post-exposure development of PMMA was performed with with methyl isobutyl ketone (MIBk) and isopropyl alcohol (IPA) in a 1:3 ratio for 90 s with gentle agitation, followed by rinsing for 20 s in IPA. ZEP520A(57k) was developed in ZEDN50 (Zenon) developer for 3 min, followed by a 30 s rinse in MIBk. Samples were blow dried with a stream of N_2. Patterned surfaces were stored in a class 10 cleanroom (~40% relative humidity) until use. Residual resist removal (descuming) was performed in an RIE oxygen plasma (Trion) immediately before use at 200 mTorr and 40 W for 30 s. Oxygen descumming is a commonly used nanofabrication technique to remove residual resist at the bottom of features.[213,220,221] This step reduced the thickness of the PMMA film to 84 nm and the ZEP film thickness to 110 nm. ZEP resists were etched less in the descum step as this resist is more dry-etch resistant than PMMA.[222] After descum, features with adequate film clearance were created in the dose range of 0.5 fC/dot to 12 fC/dot for ZEP520A(57k), and from 4 fC/dot to 12 fC/dot for both PMMA resists.

2.4.2 Vapor-phase Deposition

The vapor-phase deposition protocol was inspired by work completed by Elshof *et al.* (Figure 2.14).[179] To ensure an atmosphere saturated with the alkoxyaminosilane of interest, 100 µL of

neat alkoxyaminosilane was pipetted into a glass vial and placed in the center of the desiccator. surfaces were placed on a ceramic tray inside the desiccator equidistant from the vial. 3-aminopropyltrimethoxysilane (APTMS, Gelest Inc.) and 3-aminopropyldiisopropylethoxysilane (APDIPES, Gelest Inc.) were used as received. The desiccator was pumped down to 1 Torr and placed in an oven at 80 °C for 18 h overnight. Deposition conditions were held constant for both the APTMS and APDIPES silanes. Deposition times vary widely in literature depending on the apparatus used,[100,114,196,223,224] but in general, deposition and curing at elevated temperatures tend to lead to more robust (stable) monolayers.[225] The glass transition temperature of the resists is a critical consideration, particularly with smaller features, and thus deposition was carried out below the T_g at 80 °C (PMMA and ZEP T_g = 105 °C). The desiccator was then removed from the oven and allowed to cool to room temperature. The PMMA masks were removed by soaking for 30 min in dichloroethane (Sigma),[216] and then sonicated for 10 min. ZEP520A masks were dissolved by soaking in N,N-dimethylacetamide (DMAC, Sigma) for 30 min and then sonicated for 10 min. All samples were removed from solvent and then rinsed with a copious flow of Milli-Q water (18 MΩ·cm) and IPA successively before drying in a nitrogen stream.

2.4.3 Gold Nanoparticle Conjugation

Citrate-capped gold nanoparticles (14 ± 1.8 nm) were synthesized following the Turkevich method.[226,227] Briefly, 2 mL of 0.5 mM $HAuCl_4$ was heated to boiling (100 °C). Upon boiling, 100 µL of preheated citrate solution (1% w/v $Na_3C_6H_5O_7$) was injected. The solution remained under heat for 5 min, then was removed and allowed to cool to room temperature before use. Silicon surfaces were placed in freshly prepared nanoparticle solution (pH 8.3) with gentle agitation for

48 h. Rinsing was performed with Milli-q water. Sonication rinsing was completed with 10 min in IPA followed by 10 min in water and then blow dried in a nitrogen stream. The background particle density counts of patterned chips were obtained by first removing the e-beam patterns through Fourier filtering followed by particle detection using Otsu's Method. Briefly, the well defined periodic features from the square mask arrays were filtered by masking out corresponding lattice spots in the 2D Fourier transform the original SEM image. This masked Fourier transform is then returned to real space via inverse Fourier transformation, giving an image with only background particles. This number of particles in the resulting image were then counted using Otsu's method. Background particle densities are in Table 1.

2.4.4 Characterization

Contact angle measurements were carried out using a First Ten Angstroms FTA200 goniometer. Contact angles were collected using the sessile drop method with water, diiodomethane, formamide, and ethylene glycol as probe liquids. Each drop was allowed to equilibrate until a stable contact angle was reached (~15 s). From these measured contact angles the mean and standard deviation were calculated for each surface. A Monte Carlo method of non-negative least-squares was used to determine the surface energy components from these values.[228] XPS experiments were performed using a Kratos Axis spectrometer with monochromatized Al K_{α} ($h\nu$ = 1486.71 eV).

1. Clean substrate and spin resist

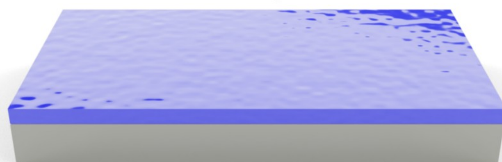

2. EBL exposure and development

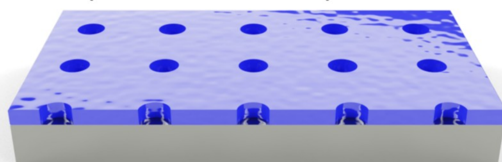

3. Masked vapor deposition of organosilane

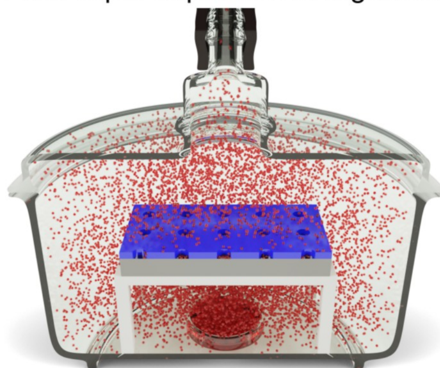

4. Strip resist from substrate

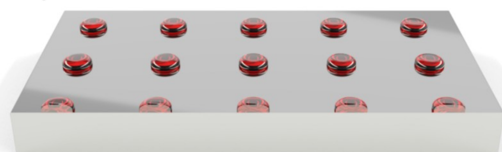

5. Functionalize patterned organosilane

Figure 2.14. Schematic of typical procedure for organosilanes deposition used in this study. Reprinted with permission from reference 159. Copyright 2018 American Chemical Society.

The spectrometer binding-energy scale was calibrated to the Au($4f_{7/2}$) line (84.0 eV), with reference to the Fermi level. The base pressure of the analysis chamber during experiments was better than 5×10^{-10} Torr. A hemispherical electron-energy analyzer working at a pass energy of 20 eV was used to collect core-level spectra while survey spectrum within a range of binding energies from 0 to 1100 eV was collected at an analyzer pass energy of 160 eV. Charging effects were corrected by calibrating to the C(1s) peak at 284.8 eV. All height profiles were acquired using tapping mode atomic force microscopy (AFM) with a Digital Instruments/Veeco multimode atomic force microscope. Collected data were analyzed using the open source software Gwyddion.[229] Scanning electron microscope (SEM) images were taken using a Hitachi S4800 SEM at accelerating voltages of 15-30 keV and a Zeiss Sigma FESEM at 5-30 keV. All SEM micrographs were processed in Gwyddion and Fijji.[230]

2.4.5 Surface and Sample Preparation

Boron doped, p-type Silicon <100> with a resistivity less 0.005 Ω·cm wafers were cut into 1 cm × 1 cm squares with a dicing saw (Disco DAD 321). Diced silicon wafers were cleaned using piranha solution [3:1 v/v sulfuric acid (96%)/hydrogen peroxide (30%)]. [CAUTION PIRANHA REACTS VIOLENTLY WITH ORGANICS AND SHOULD NOT BE DONE WITHOUT PROPER SAFETY PRECAUTIONS]. surfaces and samples were immersed in a piranha solution for 15 min, rinsed with DI water, and dried in a stream of nitrogen.

3

Aminosilane Nanostructures Formed by Vapor-Phase Directed Self Assembly as Trench and Hole Spacers

3.1 Introduction

The nanostructures in this chapter were an unexpected but exciting avenue for my research, and are the focal point of this chapter. As shown in chapter 2, Figure 2.4, we observed that after vapor-deposition of 3-aminopropyltrimethoxysilane (APTMS) through EBL-patterned resists, free-standing condensation structures of APTMS were formed which were conformal to the initial deposition mask.

The deposition process and results described in this chapter are promising in the context for density multiplication in semiconductor manufacturing. To date, there is no reference to the features in this chapter being made intentionally utilizing any standard form of lithography such as photolithography or electron beam lithography. Therefore, we propose these structures are of

interest to the semiconductor industry, particularly for density doubling processes known as self-aligned double patterning, as well as another suite of processes known as contact shrink. These industrial processes rely on deposited sacrificial materials, including SiO_x, in order to shrink pattern dimensions beyond what is achievable with only one patterning step. This chapter describes the work assessing that these condensation features can be made in a controlled fashion. The chapter compares analogous work in the literature, which provides mechanistic insight and concludes with a focused description of its relevance to semiconductor manufacturing processes.

The structures are revealed after removing the resist templates in organic solvent, leaving the features intact on the surface. Similar to the silane deposition processes used in chapter 2 and 4 of this thesis, this work used vapor-phase deposition of APTMS through patterned EBL resists (Figure 3.1). A PMMA(950k) or ZEP520A resist was patterned by EBL producing an array of holes or trenches (lines which expose the surface). This template was exposed to aminosilane vapor as shown in Figure 3.1. This approach was similar to chapter 2 except in this case, gold nanoparticles were not conjugated to the surface. It differs from the protocol in chapter 4 as the patterned features of APTMS are not functionalized for the characterization work. APTMS vapor that diffused through the open holes or lines in the template reached the surface and depending on the template geometry, would result in the formation of high-aspect ratio nanostructures.

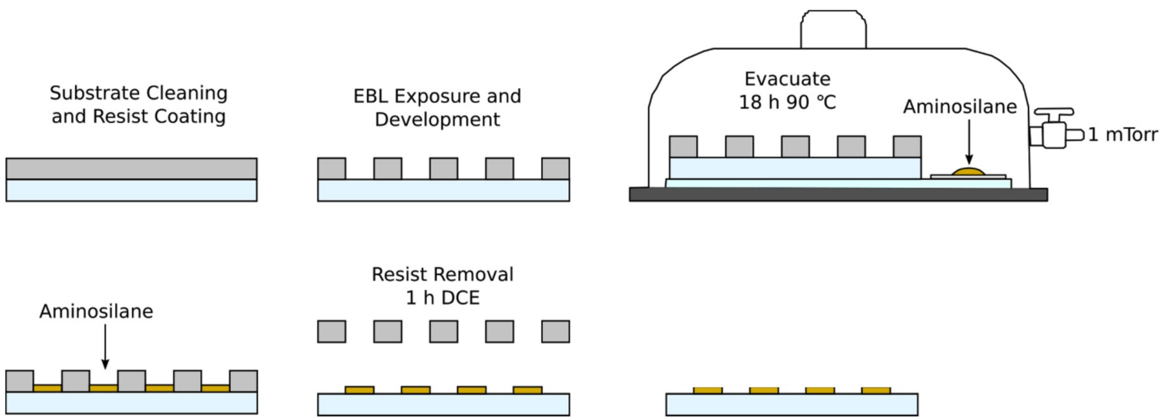

Figure 3.1. Formation of APTMS nanostructures by electron beam lithography and vapor-phase deposition.

This result motivated investigation into previously constructed arrays of APTMS patterned through holes in PMMA on glass coverslips. Shown in Figure 3.2 is an example of the APTMS ring-shaped structures formed, imaged by helium ion microscopy. In this example, the rings had diameters measuring 105 nm (from nominal 100 nm diameter PMMA holes), central open pores with diameters of 75 nm, and sidewalls measuring 13 nm in width. Upon the discovery of this ring morphology taking place after deposition in the circular holes of the EBL resist on glass, the deposition method and lithography were completed primarily on native oxide-capped p-type Si <100> (< 0.005 Ω-cm) surfaces to allow for SEM imaging of the features. Additionally, it was also revealed that by using an oxygen-plasma (RIE) for removal of the patterned resist, complete arrays of intact free-standing structures were observed by SEM while the solvent-based removal in chapter 2 resulted in collapsed structures. Plasma likely removed amine functionality,[198] and thus features which have undergone plasma-based resist removal will be referred to as SiO_x.

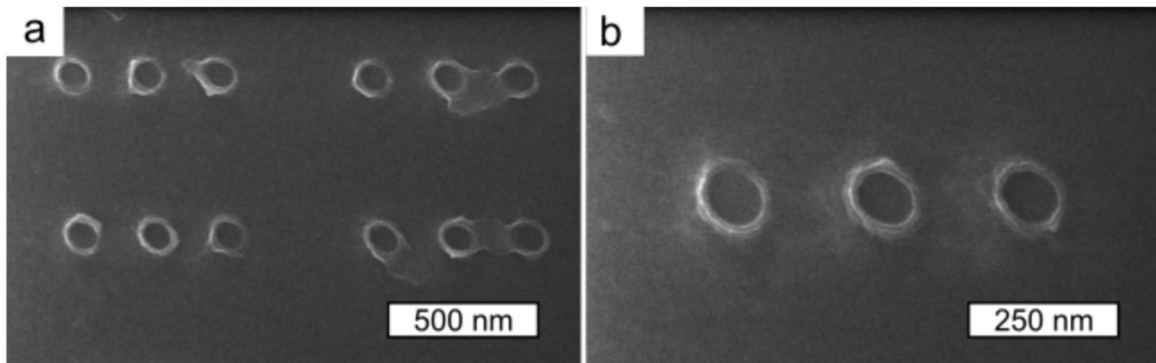

Figure 3.2: Helium ion images of clusters of APTMS hole spacer structures 105 nm diameter at 250-nm pitch on glass coverslips. a) Clusters show clear penetration to the surface, residual resist is seen on this surface as the resist was stripped via organic solvent instead of plasma, and b) Closeup of ring structures showing uniform sidewall thicknesses and complete pore depth to the surface.

Initially 29 nm in height, ring structures of up to 165 nm in height were created using vapor-phase deposition through EBL-defined templates, which were 274 nm thick. Line-shaped structures of SiO_x also were created with a height of 134 nm with aspect ratios of 3:1.

3.2 Results and Discussion

3.2.1 Mask Characterization

EBL-patterned resists functioning as masks were characterized using a combination of SEM and AFM to determine morphology, effective dose ranges for film clearance, and lateral dimensions. Films of the resist ZEP520(57k) of varying thicknesses were produced to vary the heights of the resulting structures. The maximum thickness used was 274 nm (Filmetrics, F20), post-etching. It was found that utilizing thicker resists generally resulted in poor contrast, therefore, most features were created at this thickness or lower. In general, the EBL patterns used were as shown in Figure 3.3, where single pixel dot shot features were utilized for contact holes in combination with lines, area lines, and alternate area exposure geometries, such as squares, triangles, and

circles. For the majority of this work, holes and trenches were the focus, particularly with respect to exploring their potential for line frequency doubling or, in the case of rings, their utilization as a contact hole shrink method.

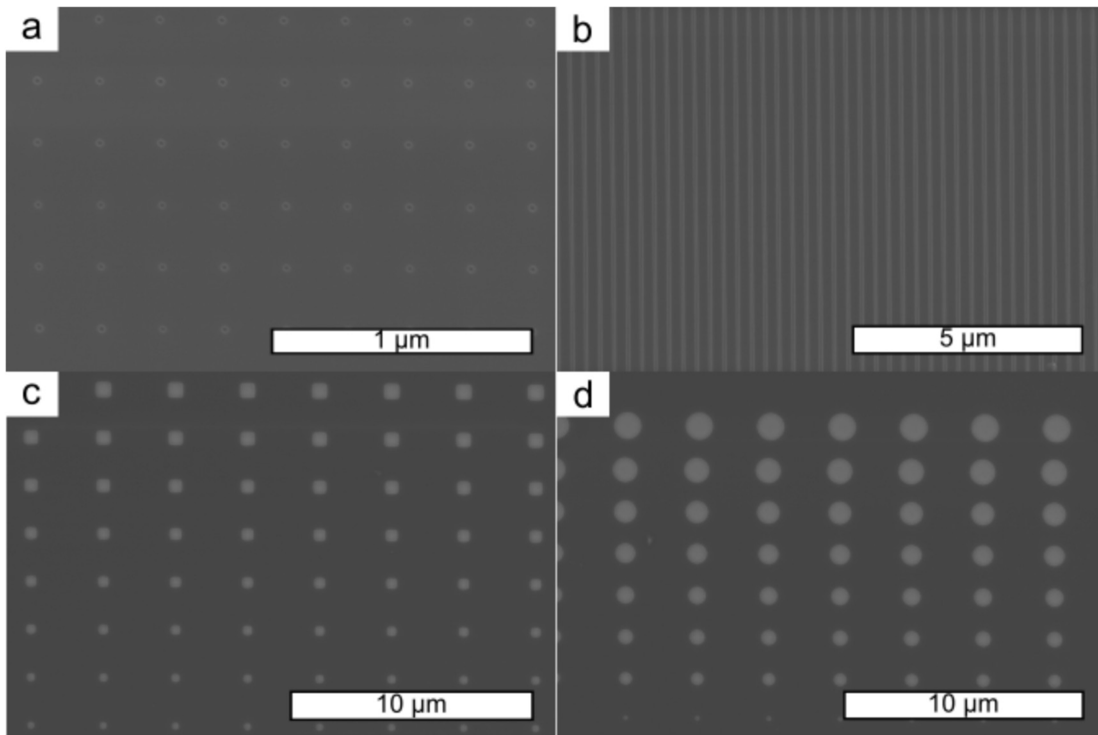

Figure 3.3: Example of masks utilized in this study patterned through ZEP520(57k) mask. a) Dot shot features for contact hole spacers, b) line structures for trench spacer formation, and c, d) alternate geometries for conformality testing and size effects.

3.2.2 Hole Spacer Morphology

Shown in Figure 3.4 are ring shaped nanostructures, hereafter referred to as spacers, which were created in an EBL-patterned PMMA resist (60 nm nominal thickness, see experimental). These were found after removing the PMMA resist in dichloroethane and are shown schematically in Figure 3.24 4b. The feature heights (> 10) measure 29.3 ± 1.9 nm (Figure 3.4 a) and the depth of

the central pores extends to the surface (Figure. 3.4 b). Figure 3.4 c shows a 3D render of the tubes as measured by atomic force microscopy (AFM) for these dimensions.

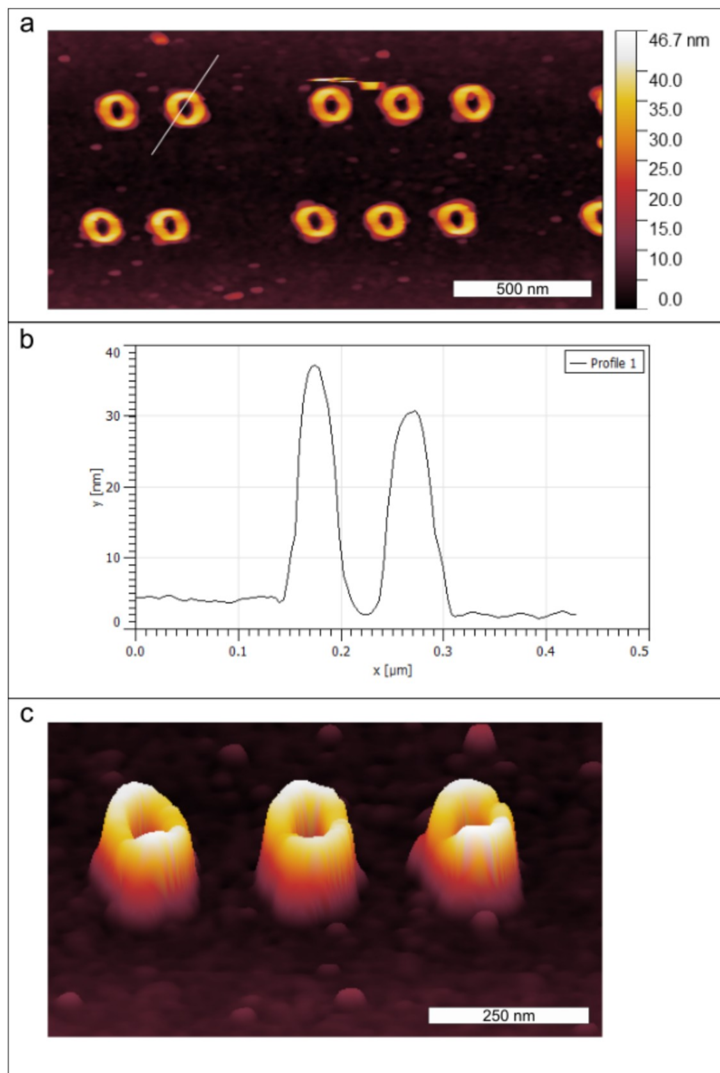

Figure 3.4: AFM image of SiOx hole spacers. a) Clusters of three hole spacers at 250 nm pitch, separated by 500 nm from the neighbouring cluster, b) Height profile of line selection shown in a, and, c) 3D render of SiOx hole spacers indicating full depth pore profiles.

Prior to each method of imaging, the template material was removed for imaging the spacers to get a better understanding of the entire spacer morphology throughout the film. For example, top-down inspection of the hole spacers after removing the template indicated the shape of ring

structures, as shown in Figure 3.5, a and c; the contrast of these images was maximized to reduce apparent sidewall charging as no coating scheme was in use. Tilt imaging, shown in Figure 3.5, b and d, coupled with AFM confirmed that the spacers are likely tube-like, with a central pore.

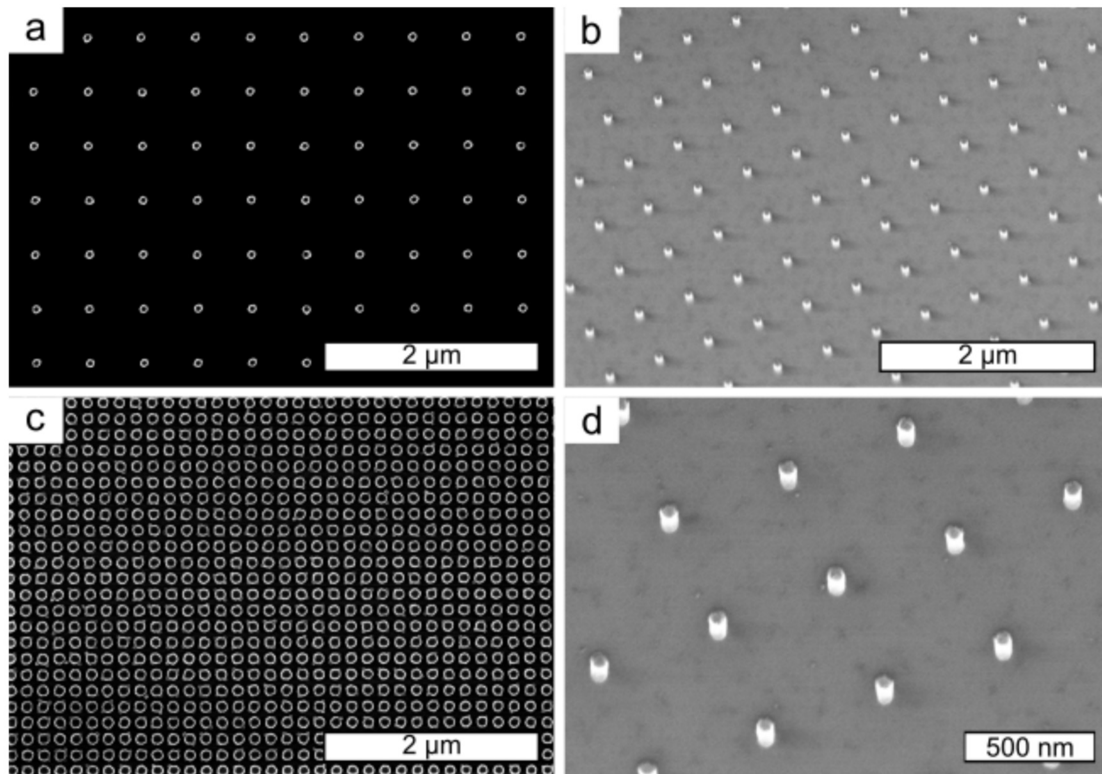

Figure 3.5: Contact hole spacer structures as seen in SEM. a) top down of 81 nm diameter hole spacers b) tilt image of hole spacer array c) higher density hole spacers, 104 nm diameter and d) higher magnification tilt image suggesting tube morphology of spacers.

It was important to analyze the sidewall dimensions (thickness of the outer ring) and pore size (diameter of inner open circle) in order to determine if rings used in a material deposition scenario could shrink contact hole sizes. Minimum sidewall thicknesses measured by SEM were found to be 9 ± 3 nm. Apparent pore size also was increased by changing the outside ring diameter by increasing template dimensions. This change in diameter was analogous to the changes in pore size in particle lithography where sphere diameter alters the pore size of the

resulting spheres. Next, the maximum aspect ratio for these features was investigated. By varying the resist template height, the feature height could reach a maximum of 165 nm for dot features that were templated in a 274-nm thick resist. This feature height was difficult to reproduce, but consistency was obtained by using a nominal resist thickness of 200 nm. This thickness resulted in ring heights of 150 nm, as shown in Figure 3.6.

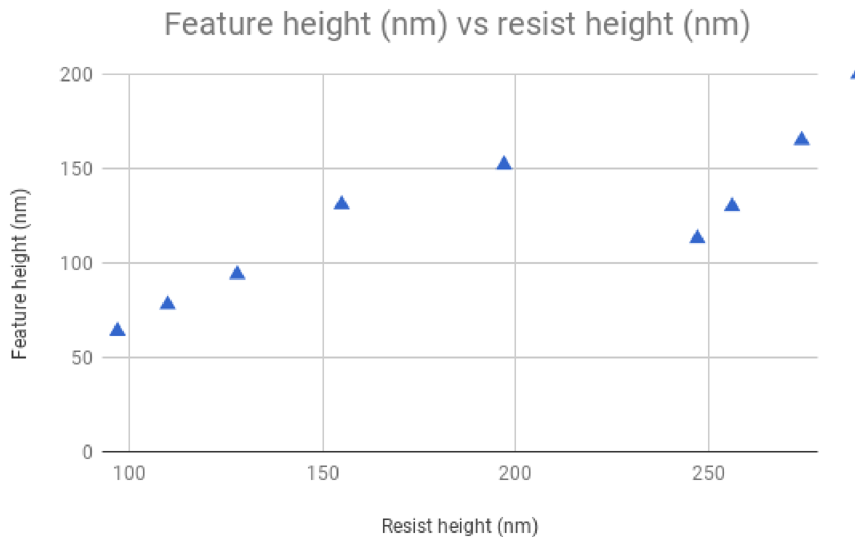

Figure 3.6: Height of SiO_x hole spacers as a function initial template height before removal. Above 200 nm thick resists, hole spacers were prone to breakage, thus 200 nm resists were settled on as a default resist thickness.

If combined with an optimized etching process step, pore dimensions potentially could be transferred into a dielectric device layer, shown schematically in Figure 3.24, step 5a. Interestingly, sidewall thickness appears to be quite consistent between rings, regardless of lateral dimension, as indicated in Table 3.1. Rings with diameters of 81 nm and 104 nm (Figure 3.5 a, and 3.5 c, respectively) both have sidewalls measuring 15 ± 2 nm. Rings measuring 54 nm in diameter have sidewalls that are 13 ± 3 nm thick. These spacer dimensions result in a maximum hole diameter shrinkage of 48% in the case of 54 nm-diameter contact holes and 37%

for 81 nm-diameter holes. Pore depth is difficult to ascertain for these feature heights (150 nm), although it appears from SEM that the spacers have pores with depths that extend the full tube height to the native silicon oxide surface.

Table 3.1 Diameter of SiO_x ring spacer structures vs sidewall thickness.

Ring diameter (nm)	Sidewall thickness (nm)
54	13 ± 3
81	15 ± 2
104	15 ± 2

Lastly, initial deposition temperature of the oven was reduced from 100 °C to 80 °C as it was found that rings could swell beyond the size of the template if the deposition temperature was performed near the glass transition temperature of the template (PMMA, ZEP T_g = 105 °C). High temperature rings would measure 2.5 x the diameter of the initial template dimensions. After reducing the deposition temperature to 80 °C, the swelling ratio was reduced to 1:1, that is, the outside spacer diameter deposited matched that of the initial dimensions of the contact hole mask, regardless of exposure dose (Figure 3.7).

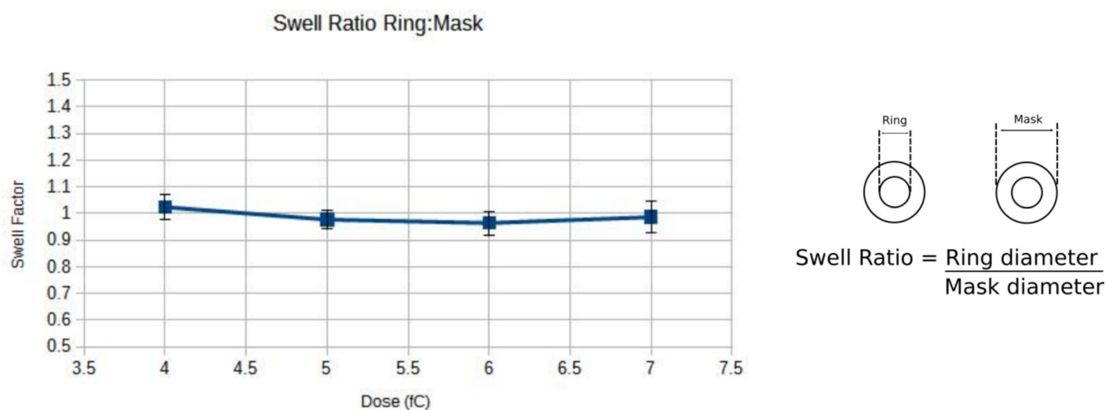

Figure 3.7: Swelling ratio of hole spacers at a deposition temperature of 80 °C versus exposure dose. Spacer diameter is stable for effective clearance dose regime, matching initial template dimensions.

3.2.3 Trench Spacer Morphology

After the high aspect ratio ring/tube morphology was found for contact hole features, the trench mask geometries (line patterns)with varying dimensions were tested. These experiments were done by using the same aminoalkoxysilane (APTMS) and vapor deposition conditions as were used for the ring structures. Top-down views of line structures grown are shown in Figure 3.8, a and c. From the top-down views, it appeared that the line structures consisted of two sidewalls with a central cavity. However, even with an anticharging scheme, SEM imaging of these structures is challenging, and edge effect charging may be an unavoidable consequence of their shape.[231] Tilt imaging (Figure 3.8, b and d), appeared to indicate the presence of a cap, or completely filled morphology.

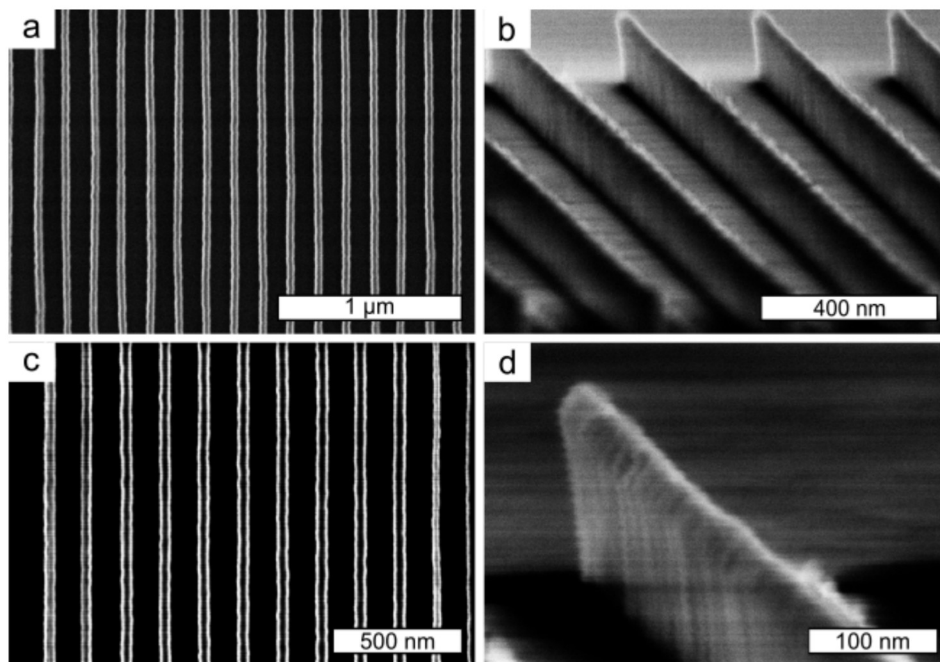

Figure 3.8: SEM images of trench spacers of SiO_x formed from line grating masks patterned in ZEP520A. a) Top-down view of 150 nm pitch line structures, b) Tilt image of line structures, 500 nm pitch, c) Higher magnification of 150 nm pitch structures showing edge effects, and d) Single line structure showing appearance of closed cap morphology.

Linewidths typically measured 47 ± 3 nm, with apparent sidewalls of 12 ± 1 nm and a gap width of 18 ± 2 nm. The smallest linewidths measured this way were 19 ± 2 nm with gap widths of 9 ± 1 nm. These small lines were prone to defects and collapse due to their small size and therefore were not used for further study until growth and control parameters could be established.

Establishing the presence of a central gap was investigated initially by AFM. Samples with varied linewidths for the purpose of central gap inspection were coated with 5 nm of Cr for charge reduction in subsequent SEM imaging. The widest lines measured had a width of 133 nm and a height of 120 nm, shown in Figure 3.9, a and b. The presence of the small reduction in height near the top of each feature (Figure 3.9 b) may indicate the presence of a central gap. In future work, use of a carbon nanotube trench profiling tip would be advantageous as tip convolution for these small features is a strong possibility.[232] A 3D render of the fins created from AFM is shown in Figure 3.9 c. Next, it was important to investigate the growth kinetics of the line structures and whether the formation of a cap or filled morphology had occurred. All initial work on examining line junction behavior, hole behavior, and line spacer formation was completed with a deposition time of 18 h; the vapor deposition used was as described in chapter 2. However, it was thought that deposition times likely could be reduced. Short deposition times are attractive, as any reduction in overall processing time can translate to substantial cost savings with respect to industrial processing. Figure 3.10 shows the change in feature height as a result of reducing the deposition time from 18 h to 15 min. From 18 h to 2 h, only a slight reduction was found in fin height, from 134 nm to 127 nm, as measured by AFM. Reducing this deposition time to 30 min produced 89-nm tall fins while 15 min resulted in 45-nm fins. Deposition times below 15 min could not be tested as it was found that with a deposition of 15 min, the temperature

dropped 20 °C upon initial oven opening and only recovered to a temperature of 72 °C. Unfortunately, AFM profiling of these reduced deposition times did not reveal any morphology changes (Figure 3.11) that could be indicative of an edge-dominated growth (growth up the sidewalls first) rather than a steady filling regime (equal growth in height across feature width).

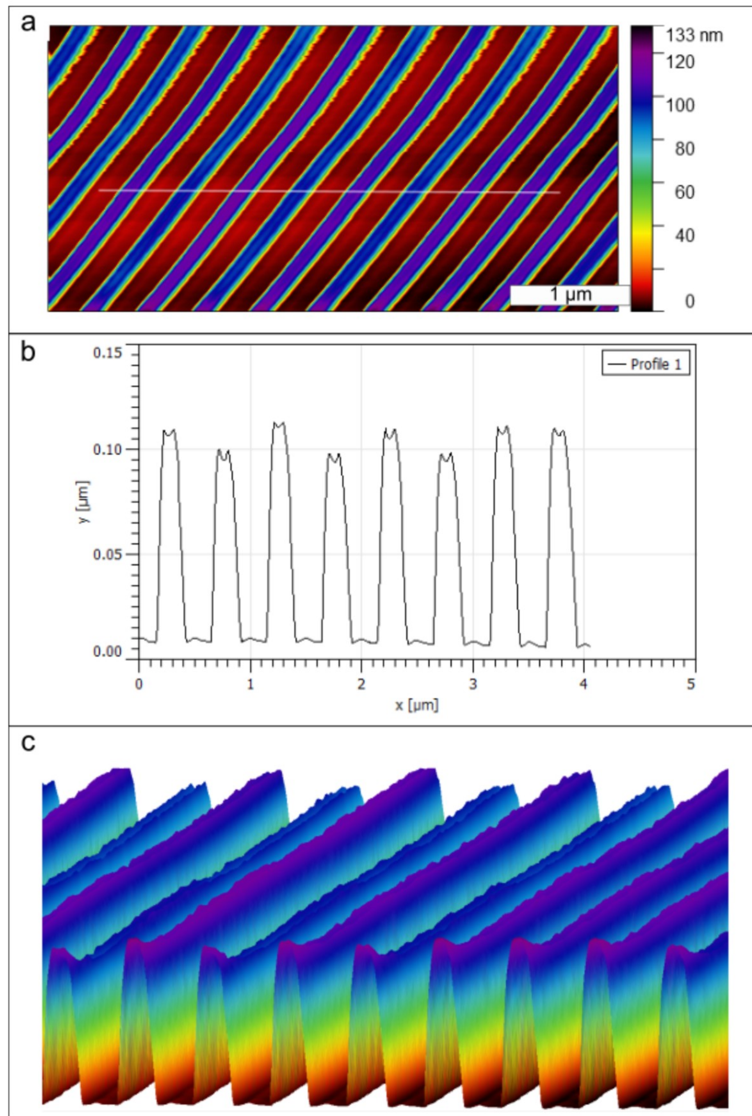

Figure 3.9: AFM image of SiO_x line structures with 100 nm wide nominal resist width. a) 100 nm wide structures with 500 nm pitch, b) Height profile of line selection shown in a, and c) 3D rendering of SiO_x line indicating height dip at ridge and overall height.

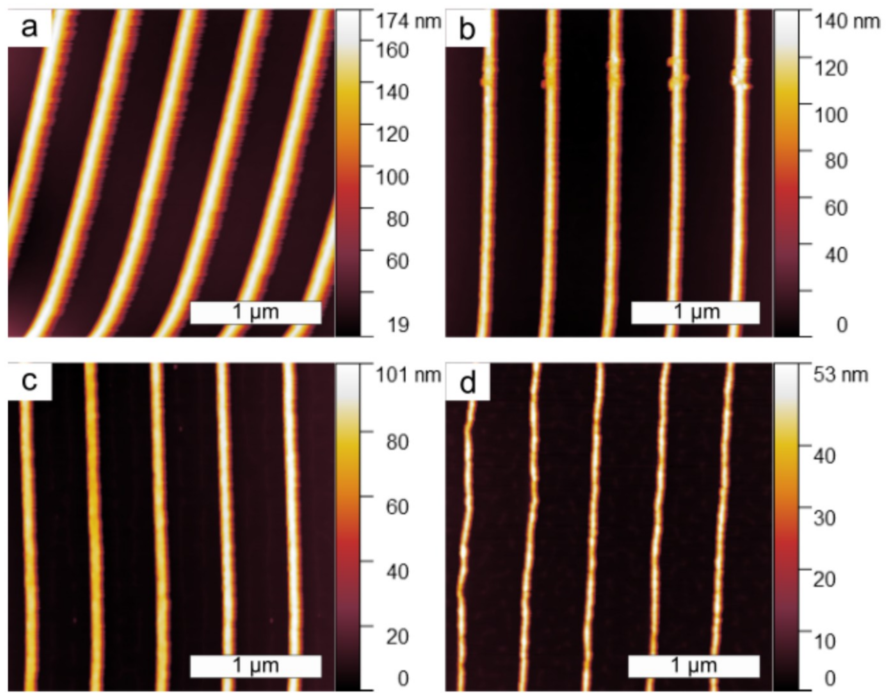

Figure 3.10: AFM image of SiO_x line structures, 500 nm pitch, at varied deposition times. a) 18 h deposition time, b) 2 h deposition, c) 30 min deposition, and d) 15 min deposition.

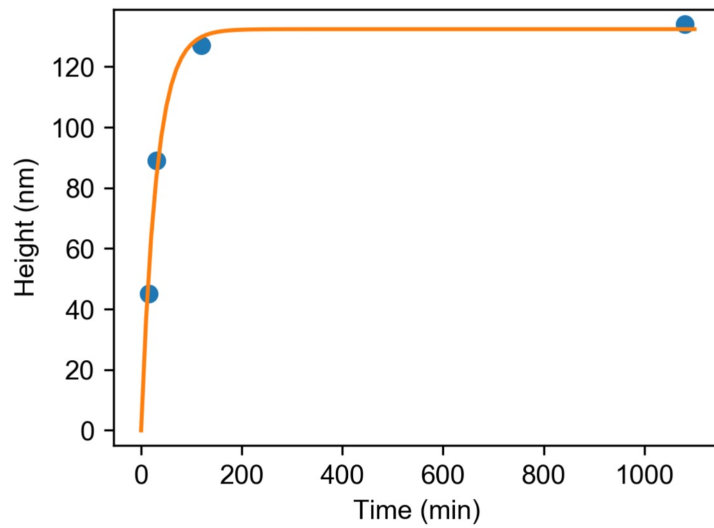

Figure 3.11: Plot of SiO_x line structures heights versus varied deposition time. 15 min deposition time did not reach full temperature.

Figure 3.11 does appear to indicate that the deposition of the line structures follow Langmuir kinetics for surface adsorption[233] given by:

$$h = h_{\infty}\left(1 - e^{-t/\tau}\right) \quad (3.1)$$

where h is the height of the line structures, h_{∞} is the height at infinite time, and τ is the rate constant of the system. This curve was fit using a least squares regression to get best-fit values of (h_{∞}, τ) = (132 nm, 30 min), representing the maximum height and half-life to completion. This fit should be interpreted with caution, however, as there are only four data points being utilized and t = 15 min carries substantial uncertainty due to temperature fluctuation.

3.2.4 Conformality of Spacers in Alternative Geometries

Template conformality was tested by utilizing alternative geometries. Large squares, circles, and triangles, ranging from 100 nm to 1 μm in diameter, were created to examine how SiO_x conformed to these structures. Figure 3.12 shows the results of these tests by top-down SEM inspection. In general, shapes conformed well to initial template shape and dimensions. As features shrink below ~150 nm in diameter, sharpness is more difficult to maintain in the case of triangles and squares (Figure 3.12, a, c, and d), and the corners were seen to adopt a more rounded appearance. The impact of junctions on spacer formation was tested. Figure 3.13 shows a single pixel line grid with scaled EBL dose increases in order to simultaneously investigate linewidth junctions and intersection size effects. The lines formed a square lattice, as shown in Figure 3.13, b and c. Figure 3.13 d appears to indicate that the intersection may be open or hollow as a faint second line can be seen following the edge structure, which may be an internal sidewall.

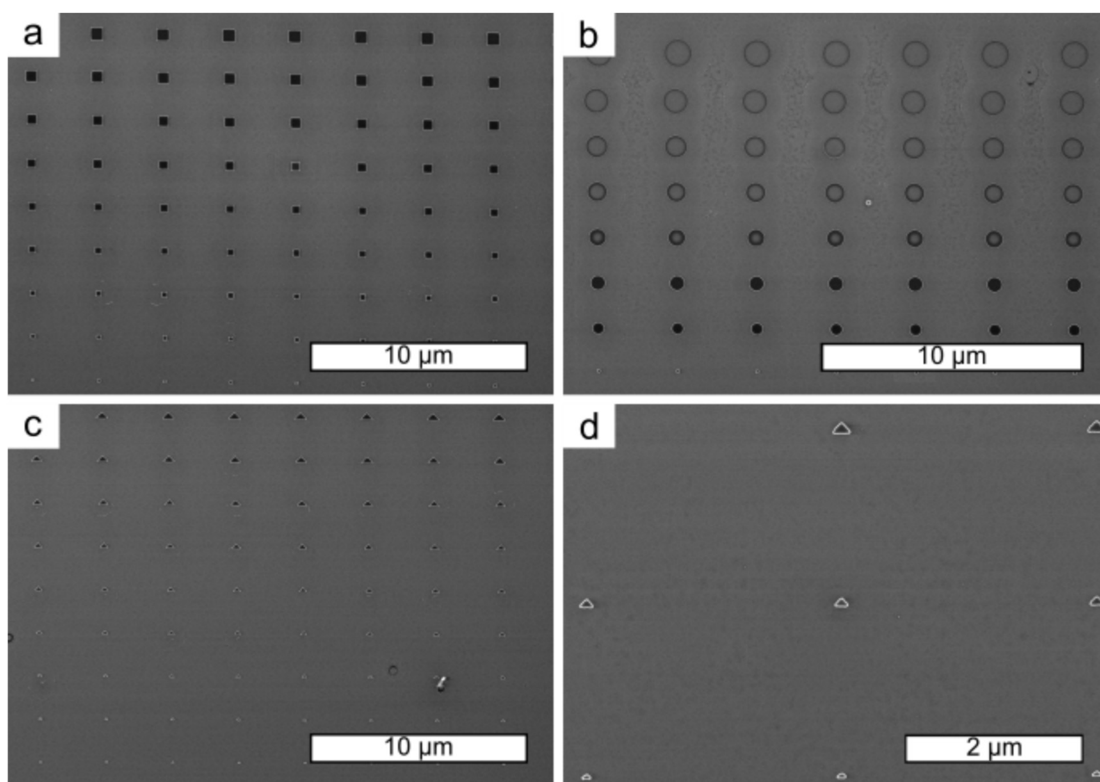

Figure 3.12: SEM images of SiO_x spacer structures created with varied geometries. a) Squares ranging from 100 nm to 1 µm in diameter, b) Large diameter holes, 100 nm to 1 µm with edge structures, c) Triangular structures ranging from 100 nm to 1 µm in edge length, and d) Closeup of triangular condensation edge structures.

The outside edge corner to corner of this intersection gap measured 70 nm, with intersecting line widths at 39 ± 5 nm. The outside walls follow corners conformally against the template sidewalls. An interesting feature was noted when the intersection gap between lines (line width 46 ± 2 nm) was increased to 130 ± 5 nm as shown in Figure 3.13, e, f, and g. At this intersection size, a large open central pore is obvious. Smaller side walls appear to branch out from the centre of the intersecting lines, following the edge where the initial template gap started. This is encouraging for future testing and analysis on sidewall shrinkage as it may indicate that formation of a cap may occur as a result of height, or aspect ratio, which are parameters that could be optimized. These sidewalls measure 17 ± 2 nm, which is consistent with sidewall

thicknesses seen with the contact hole tube dimensions, noting that this sample was coated with 5 nm of Cr. The minimum sized gap, corner to corner, appears to be 112 ± 5 nm, while the maximum measured is 150 ± 5 nm.

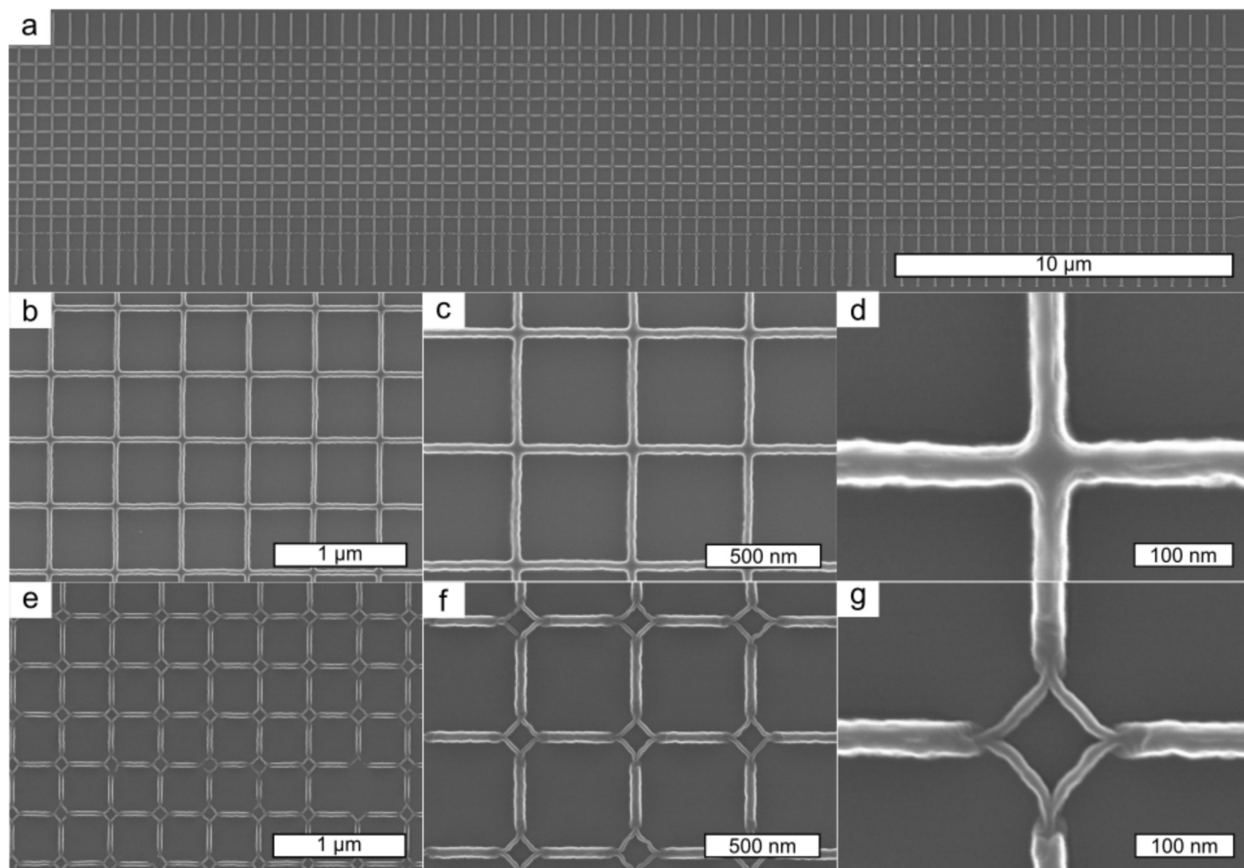

Figure 3.13: SEM images of SiO_x line structures with varying intersection gap widths. a) 500 nm pitch square lattice b, c) Square lattice structure of SiO_x lines where intersection gap is 70 nm d) close-up of closed intersection e, f) Lattice of SiO_x line structures where intersection gap is greater than 112 nm and has lead to open pores at square intersection. g) close-up of an open pore intersection.

3.2.5 Pitch Limitations in Contact Hole Spacers

The contact hole spacers may be useful as a contact shrink method or as a potential plasmonic nanogap approach.[234] A high density of features is desirable, thus, the effects of density on

contact hole spacer formation was tested using the 18 h deposition protocol above. At design pitches of 200 nm, (Figure 3.14, a and b) and 150 nm (Figure 3.14, c and d), hole spacer morphology appears unchanged as the pitch is reduced. At a pitch of 100 nm (Figure 3.14 e and f), issues begin to arise. One can see the formation of thin lines bridging the structures. These features have been seen before in particle lithography and have been termed “water bridges” between features.[185] Additionally, dot placement begins to shift within the lattice, with some features nearly touching one another (Figure 3.14 f, upper right). At this stage, it may be possible to remove these bridge structures during a clean or trim step using SiO_x plasma etch chemistries such as CHF_3/O_2. In the case of photolithography double patterning, initial lithography steps could form isolated hole spacers with ease for subsequent etching. Figure 3.14, g and h, show hole spacers at a design density pitch of 75 nm. In this case, there are obvious defects as the structures are formed very close to one another. Multiple instances of four dots coming together in a “clover leaf” style pattern begin to appear in addition to the continued presence of water bridges. Sections are present where individual spacers are still attached, however, this pitch contains a large number of defects. The clover leaf pattern may be a result of high aspect ratio structures collapsing towards each other due to the surface tension of the developer during drying.[235] The clover shape may also be due to proximity effects of features. In Figure 3.14 g, the effect of overexposure is seen as multiple fields are connected to one another, forming large bridges between dots. Following development, the individual holes in the mask are no longer separated at these overexposed regions, causing APTMS to deposit in these connected regions as well.

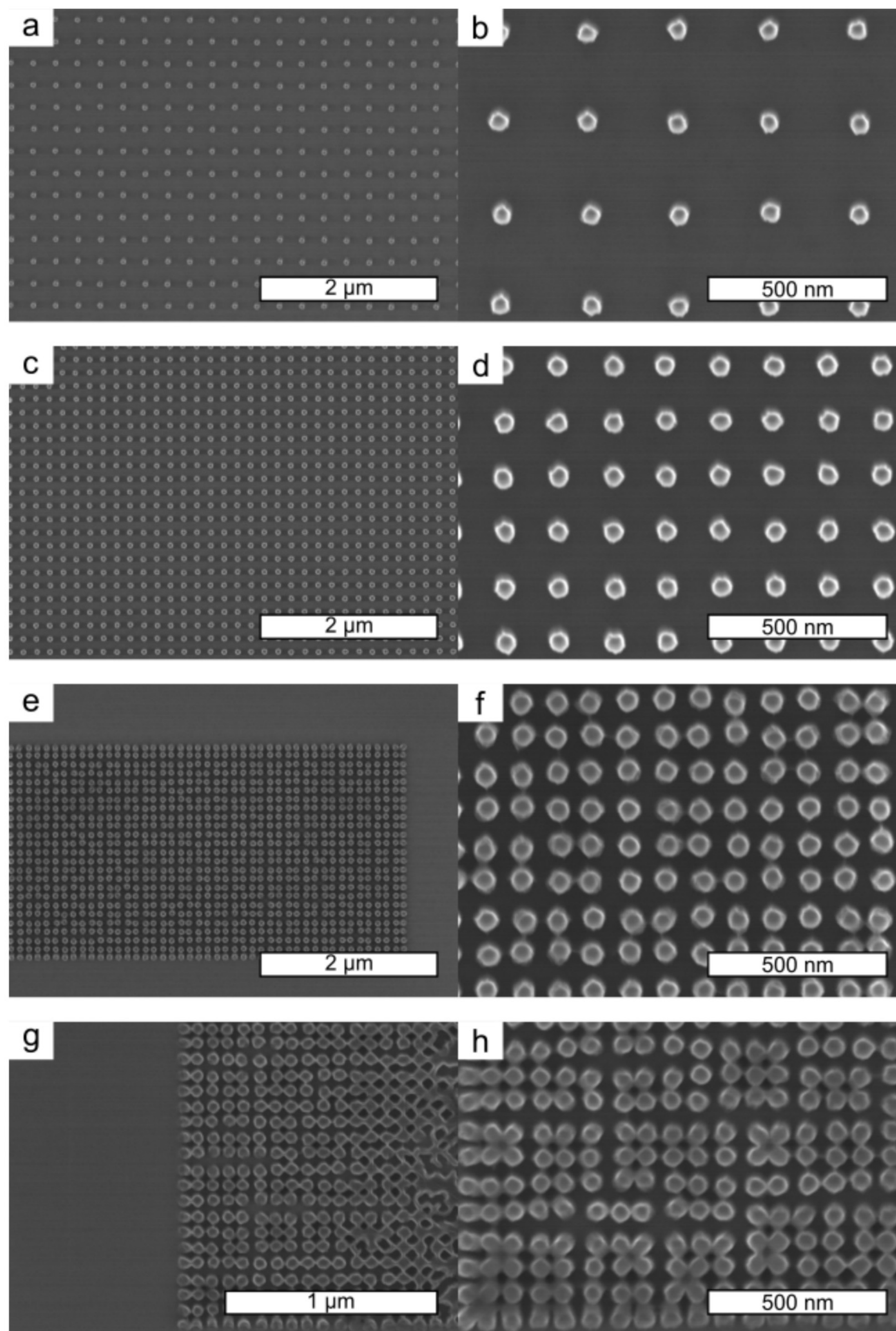

Figure 3.14: SEM images of SiO_x hole spacers at varying pitches, centre-to-centre a, c, e, and g) are 25k magnifications of hole arrays with pitches of 250, 150, 100, and 75 nm, respectively, and b, d, f, and h are images of each respective array showing the effect of high density on morphology.

3.2.6 Pitch Limitations in Trench Spacers

Despite uncertainty regarding multiplication potential of the fin structures, it was still important to test pitch limitations of the line features formed. As negative tone high density features of silica regularly are made with hydrogensilsesquioxane based resists, this method may be a complementary approach to achieve similar features using a positive tone resist. HSQ has been utilized to form mandrels;[236] if the structures are controlled to have a filled morphology, this technique may also be a way to form mandrels rather than spacers. Figure 3.15 shows a set of helium ion images examining different pitches of lines created. Pitches tested were 500 nm, 200 nm, 100 nm, 90 nm, 80 nm, 70 nm, 60 nm, and 50 nm.

The top-down view of line pitches 500 nm (a), 200 nm (b), 100 nm (c), and 90 nm (d) were stable across their dosefield, and features were free of major defects and collapse. Spacer defects begin to appear at an 80-nm pitch (Figure 3.15) with large deviations in apparent width, which are likely to result from the collapse of high aspect ratio structures. At 134 nm in height, these structures have an aspect ratio of 3.1 : 1. Fragility may be an issue at this aspect ratio, especially if the interior of the fins is a hollow trough structure. In that case, with a sidewall thickness of 17 nm, the sidewall aspect ratio more than doubles to 7.9 : 1. The presence of a cap may have a stabilizing effect in preventing feature collapse. Fragility of the structures in solution based removal was noticed routinely; sonication and surface-tension effects during drying were likely to remove the SiO_x line structures from the surface entirely.

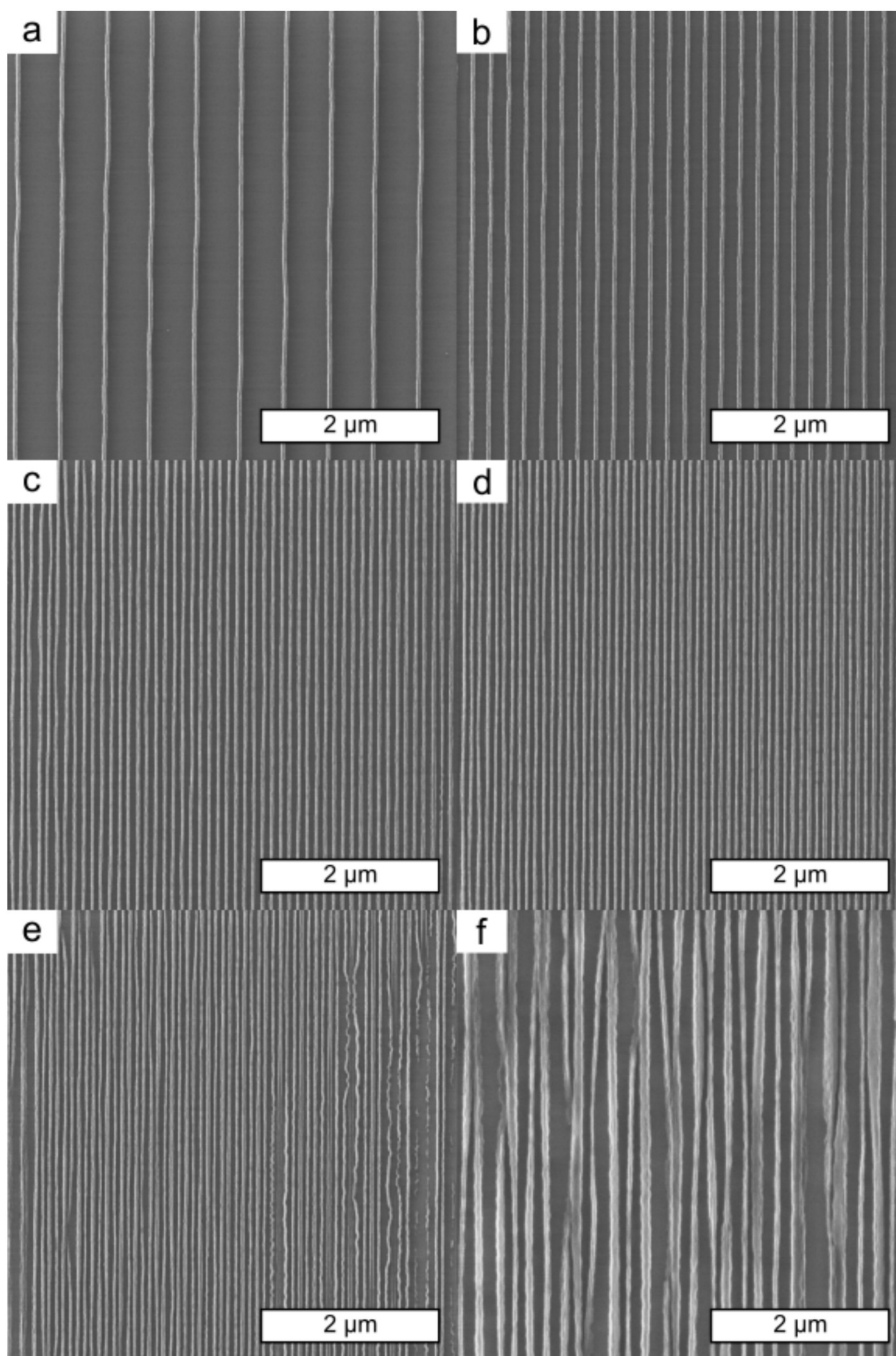

Figure 3.15: Helium ion microscope images of SiO_x line grating structures formed via EBL and 2 h vapor deposition of APTMS through ZEP520A mask with plasma removal. Single pixel line grating template at increasing pitches of 500 nm (a), 200 nm (b), 100 m, (c), 90 nm (d), 80 nm (e) and 70 nm (f).

As noted in Chapter 2, hole spacer structures collapsed due to sonication cleaning. With the line spacer structures, even extended agitation (150 rpm, orbital shaker, 1 h) and subsequent drying broke structures erratically. It is possible, however, that the collapse may be due to surface tension-induced collapse during resist removal and not to mechanical motion during actual resist removal.[235] There may be a potential to avoid feature collapse during template removal by utilizing supercritical CO_2.[237] This method also would have an attractive benefit of preserving reactive functional groups on the surface of the spacers, something that currently does not exist as spacers are typically trimmed in plasma etchback processes. The plasma-based removal used here likely breaks C–C bonds which were linking the amine functional group to the silicon. Collapse appears to be unavoidable at pitches of 70 nm and below, where lines are completely folded over and destroyed (Figure 3.15 f).

With integrated circuit (IC) trace designs, nested line structures in high density are desirable. Lines with modest pitches of 500, 200, 150, 100, 90, 80, 70, and 60 nm were tested and are shown in Figure 3.16. Lines are resolved reasonably at pitches of 500, 200, 150, 100, and 90 nm (Figure 3.16, a-e, respectively). At 80 nm, collapse is evident on straight runs after exiting nested corners (Figure 3.16 f) and complete corner defects occurring at pitches 70 nm and below (Figure 3.16, g and h). This is in similar agreement to straight runs and is encouraging for guided runs of lines where atypical geometries may be utilized for specialized traces.

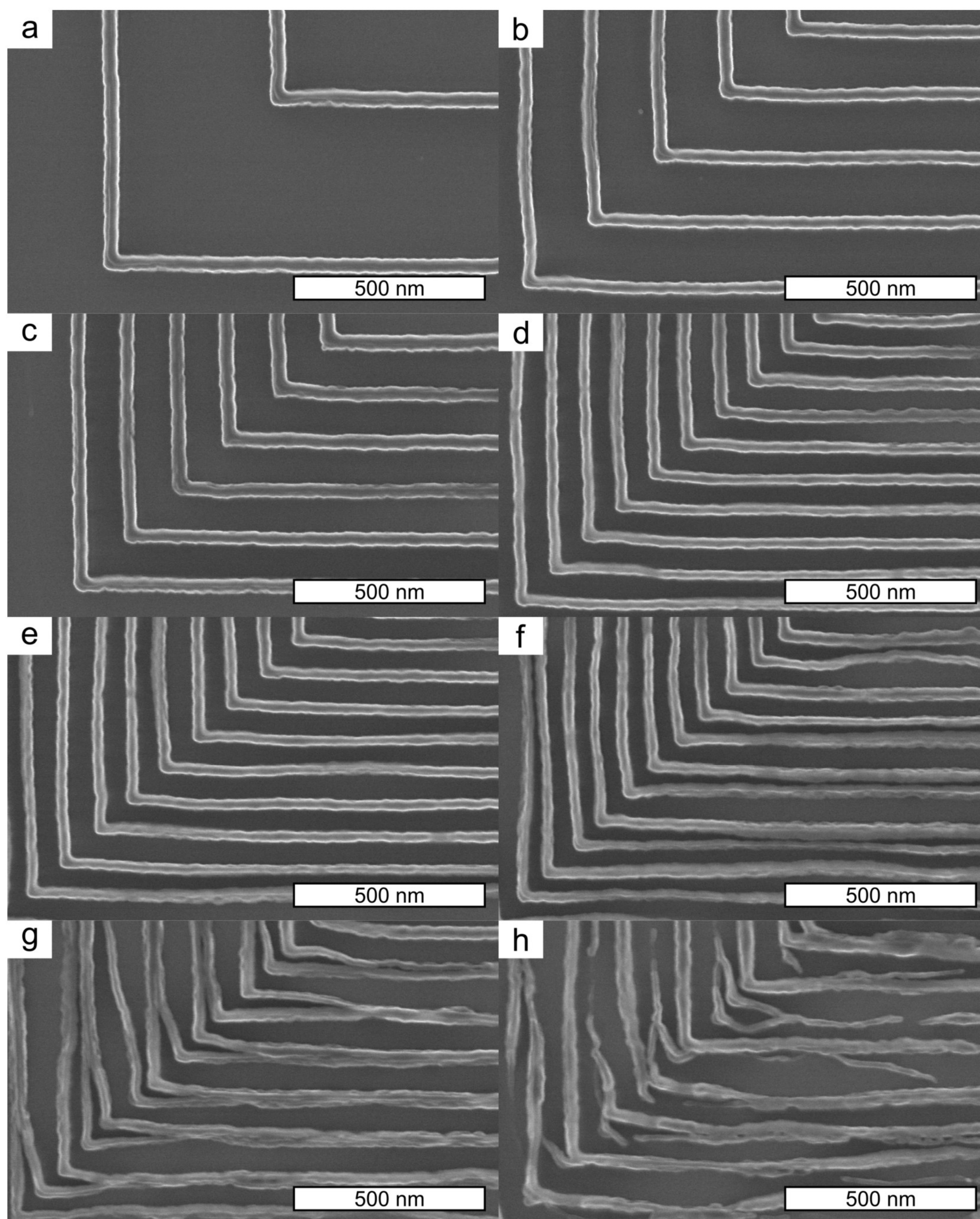

Figure 3.16: SEM images of SiO_x line grating structures formed via EBL and 2 h vapor deposition of APTMS through ZEP520A mask with plasma removal. Single pixel line grating template had increasing pitches of a) 500 nm, b) 200 nm, c) 150 nm, d) 100 nm, e) 90 nm, f) 80 nm, g) 70 nm, and h) 40 nm.

3.2.7 Potential Frequency Doubling of Wider Linewidths

Line frequency doubling and the effect of increasing linewidth with a 1:1 duty cycle (design linewidth = design pitch) were explored simultaneously. Figure 3.17 indicates lines of pitches 100, 90, 80, 70, 60, and 50 nm, with corresponding images of the same linewidths brought to 1:1 pitch = gap width. This design initially was made to determine the growth morphology of increasing linewidths while at the same time investigating what the line frequency doubling could look like at this scale regime. No collapse is seen for all features, regardless of linewidths at large pitches (500 nm, Figure 3.17 a, c, e, g, i, and k).

Feature defects are noticeable at pitches of 60 nm, and 50 nm (Figure 3.17, j and l, respectively). From this work, one can examine what a process flow could produce at these dimensions. The 100-nm design width, as shown in Figure 3.17 b, would result in a 96-nm linewidth, separated from a 76-nm linewidth feature, with a gap distance of 15 nm, in a space of 200 nm. This asymmetry in features is likely a result of proximity widening and could be corrected after further optimization. With the original positive tone process, this approach would result in one 100-nm feature within the 200-nm wide space. The 70-nm process would produce two 55-nm line features, separated by a 15-nm gap space in one field 140 nm wide. It may be possible to improve these dimensions utilizing narrower gaps, however, aspect ratios would need to be lowered substantially to avoid feature collapse that normally is seen with the thinner features. Aiming to utilize line structures as a self aligned doubling process, it was critical to determine if the internal structure is indeed hollow. An attempt was made to use a gallium focused ion beam (Ga-FIB) process to cut and view a side profile of a complete line structure grown at 18 h, the standard deposition time. Unfortunately, imaging at magnifications required to

resolve these structures proved to be challenging in the helium ion microscope (HiM). This difficulty is due to the flood gun's effectiveness, which was severely reduced as these experiments were completed on conductive silicon surfaces to facilitate fabrication in the EBL instrument. The flood gun works by flooding excess electrical charge over the imaging surface to neutralize built up positive charge by the He gun during imaging. However, if the surface itself is conductive, smaller features are unable to be resolved as the charge neutralizing effect is nullified by conducting the flood gun's charge into the surface.

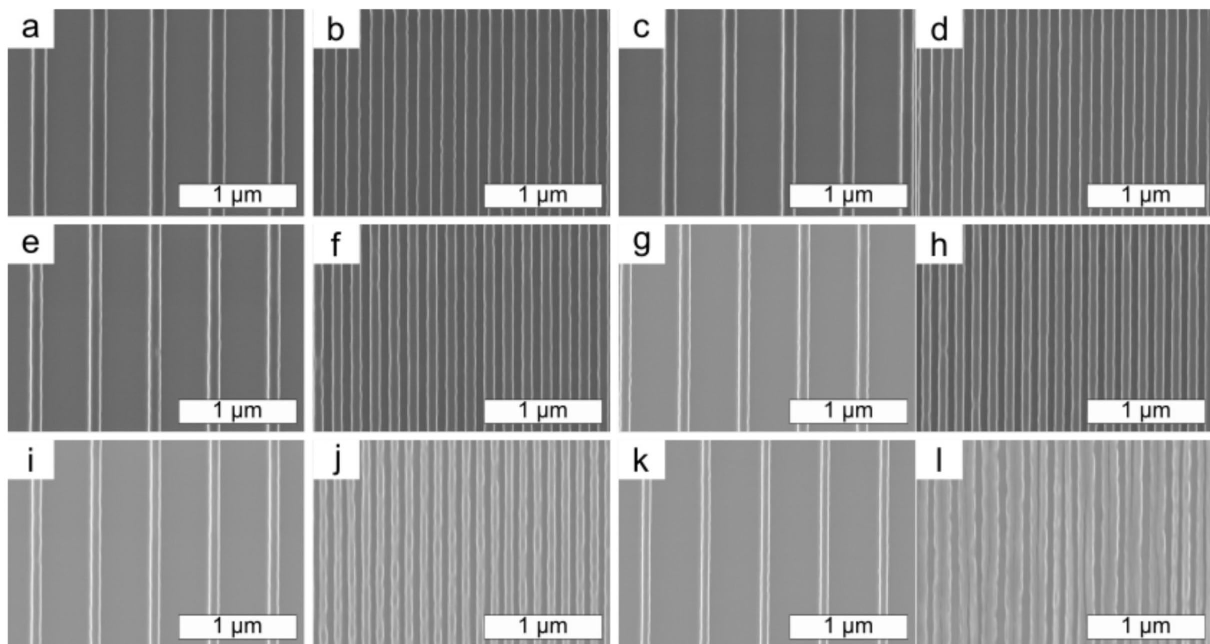

Figure 3.17: SEM images of SiO_x line grating structures formed in with area exposure at varying linewidths. Each image shows 500 nm pitch lines and is followed by it's 1:1 duty cycle image where the gap width between lines was set to equal the linewidth. Dimensions are design linewidths and pitches. a) 100 nm linewidth at 500 nm pitch b) 100 nm linewidth with 100 nm pitch, c) 90 nm linewidth at 500 nm pitch, d) 90 nm linewidth at 90 nm pitch, e) 80 nm linewidth at 500 nm pitch, f) 80 nm linewidth at 80 nm pitch, g) 70 nm linewidth at 500 nm pitch, h) 70 nm linewidth at 70 nm pitch, i) 60 nm linewidth at 500 nm pitch, j) 60 nm linewidth at 60 nm pitch, k) 50 nm linewidth with 500 nm pitch, and l) 50 nm linewidth at 50 nm pitch.

The result is that the structures of interest still retain aspects of edge charging, despite the use of a charge neutralizing imaging modality. This issue places stress on the importance of

surface considerations for later characterization. Future work could make use of a highly insulating surface, such as intrinsic silicon, to make use of the helium ion instrument's charge neutralization capabilities more appropriately.

Figure 3.18 shows the results of Ga-beam milling into SiO_x line structures with pitches of 500-nm. Milling was first completed in the Zeiss HiM instrument, and afterwards the milled surfaces were coated with 5 nm of Cr for SEM imaging. Due to constraints, these features were the only ones available for this analysis, and future analysis would benefit from both wider structures (> 100 nm) and the lack of a conducting surface (glass or instrinsic Si). Figure 3.18, a and b show shallow and deep trenches milled at the end of the line structures with the Ga beam in order to examine a cross-section of the lines using tilted SEM imaging. As shown in Figure 3.18 c, the sidewall of the surface has noticeable texture, which appears to rise towards the bottom of the line feature. However, Figure 3.18 d does not show any discernible contrast difference between the sidewall of the surface, the flat surface of the surface, and the centre of the SiO_x line structure. It appears that there are subtle curved tops to the line features, as seen in Figure 3.18 a, although it is not known if this is a result of the Cr coating a very thin cap or if the structure itself is completely filled.

As an alternative approach, an attempt was made to remove hypothetical caps by utilizing an oxide etch. The effect of a short post-structure formation plasma etching process (See Experimental) to enhance visualization of the actual morphology of the structures was examined. If there was a cap present in the structures, then it may be possible to eliminate this cap by reactive ion etching using oxide etch chemistry like CHF_3/O_2. The etch parameters would

themselves require optimization but could expose the potential hollow centre of the ring and/or line structures.

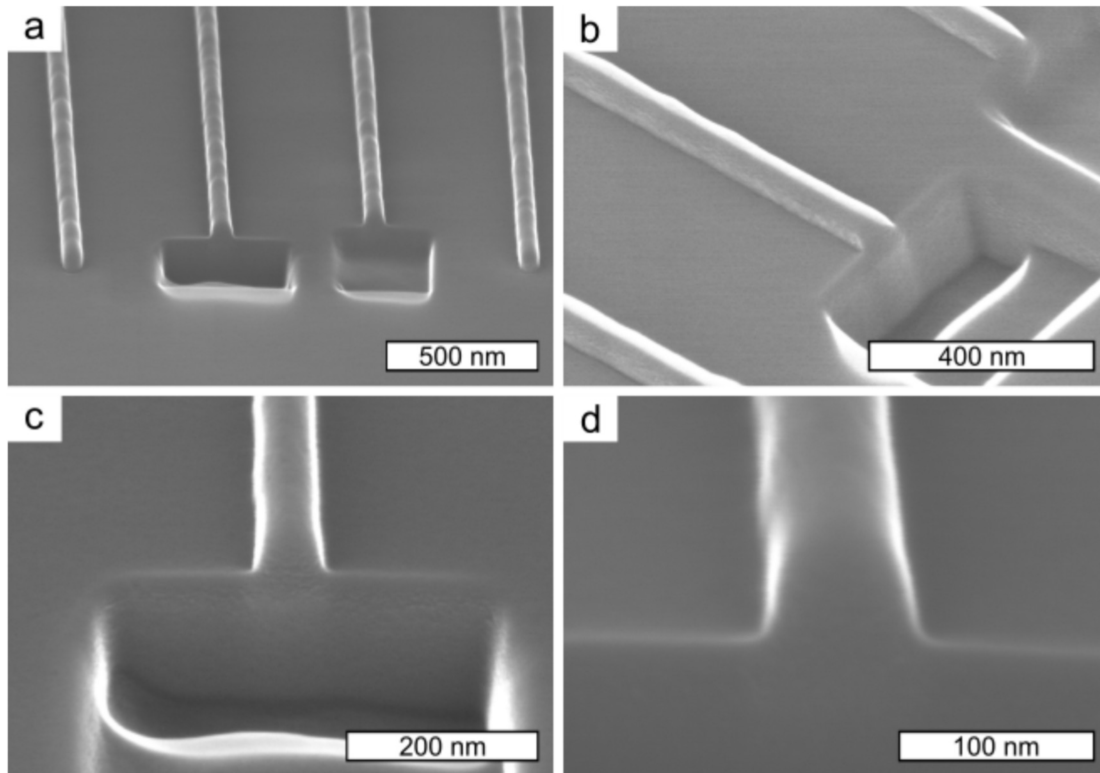

Figure 3.18: Tilted SEM images of single pixel lines forming SiO_x structures with 5 nm Cr coating. Trenches were milled by Ga column in a Zeiss HiM instrument. a) 500 nm pitch lines showing ridge formation b) Tilt image of shallow and deep Ga-FIB trench, c) Cross section of single line at deep trench and d) Closeup of c.

Figure 3.19 shows SEM images of a short etch on line and hole spacer structures. In Figure 3.19 a, the nature of the electron transparency of the features is quite obvious, showing the entire circumference of the base of the features through the walls of the structures. Figure 3.19 b indicates a single hole spacer, with a clear central pore. Figure 3.19, c and d, indicate the effect of this short etch treatment on line structures. In Figure 3.19 d, it would appear that central gaps indeed have opened up, and there is loss of an apparent ridge on the top of the features. The results were incredibly promising for the formation of these structures as spacers.

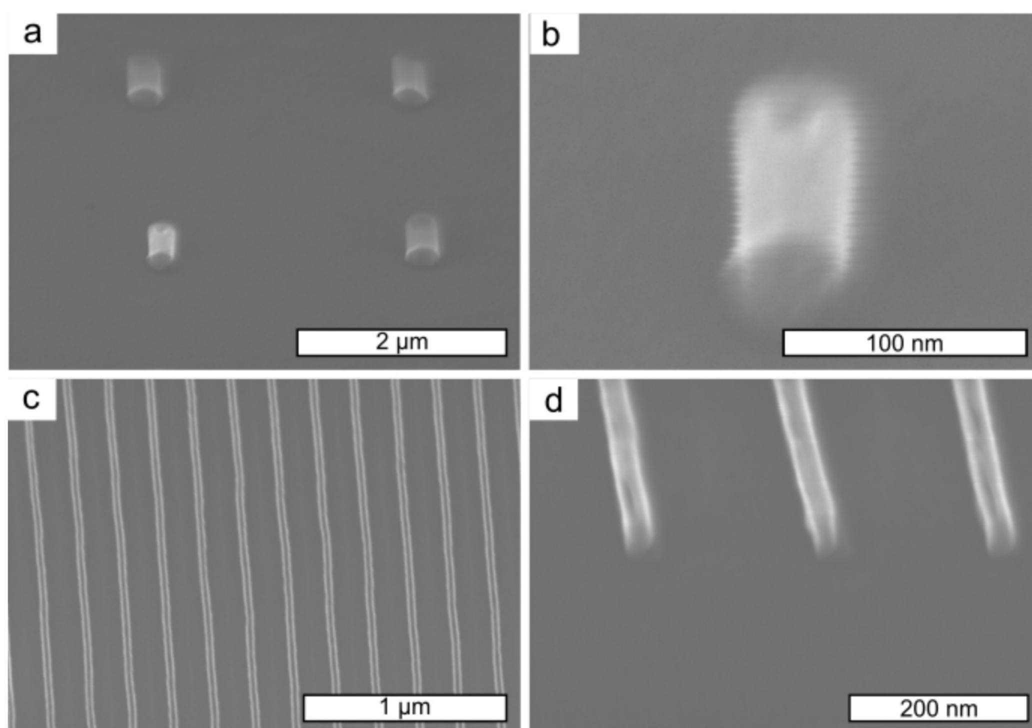

Figure 3.19: Tilted SEM images of SiO_x spacer structures (18 h deposition time) after an oxide etch to open central pores and troughs. a) 500 nm pitch contact hole spacers b) Tilt image of a single contact hole spacer c) Top down view of 150 nm pitch lines after oxide etch and d) Closeup of end of lines showing loss of ridge-like cap and opening of central gap matching contrast of surrounding surface.

3.2.8 Structure Formation Mechanism and Alternative Organosilanes

There are examples in the organosilane deposition literature for formation of organosilane nanostructures at the vapor-surface-template boundary. For line-shaped features, George *et al*. found that upon exposing open channels in PDMS soft lithography templates to APTMS vapor, taller features would form at the edge where micron-scale wide lines in the template met the silicon oxide surface (Figure 3.20 a).[238–240] Following vapor-phase deposition of 3-aminopropyltriethoxysilane (APTES), condensation preferentially occurred at the three phase contact line where the template edges meet the surface, effectively forming high-aspect ratio

structures against the sidewalls of the template (Figure 3.20 a). The structures in Figure 3.20 a are very similar to the line structures described in this chapter.

Similarly, circular aminosilane nanostructures, such as the ones shown in Figure 3.20 b,[182] are observed in the particle lithography literature and form with a variety of organosilanes, in addition to aminoalkoxysilanes. In this case, a single layer of polystyrene or latex particles is prepared on a metal oxide surface, which can serve as a mask by exposing the interstitial sites between the particles. After ambient drying, vapor-phase organosilanes preferentially condense in the residual volume of water surrounding the base of latex particles in a single packed layer which act as the deposition mask.[181] The technique is able to produce large scale homogeneous arrays of organosilane rings with varied functional groups.[181,182,185,241] After removal of the spherical masks, circular organosilane topologies are formed with sizes that vary according to the size of the particles used. This effect is enhanced in aminosilanes, likely due to their self-catalyzing behavior.[170,242] Additionally, tri-alkoxy functional organosilanes are likely to enhance the effect compared to monovalent alkoxysilanes, which are normally employed to avoid such aggregation.[101,196] The ring shaped aminosilane condensation structures in this chapter are similar to those described in Figure 3.20 b, and higher aspect ratios can be formed with the simple electron beam lithography scheme as shown in Figure 3.1. Compared to particle lithography formation of aminosilane nanostructures, EBL enabled higher aspect ratio structures via vertical resist sidewalls and varied shapes on one chip, while particle lithography is limited to particle size to alter condensation dimensions. By creating ZEP-based templates with EBL, multiple parameters of contact hole and trench condensation were tested simultaneously.

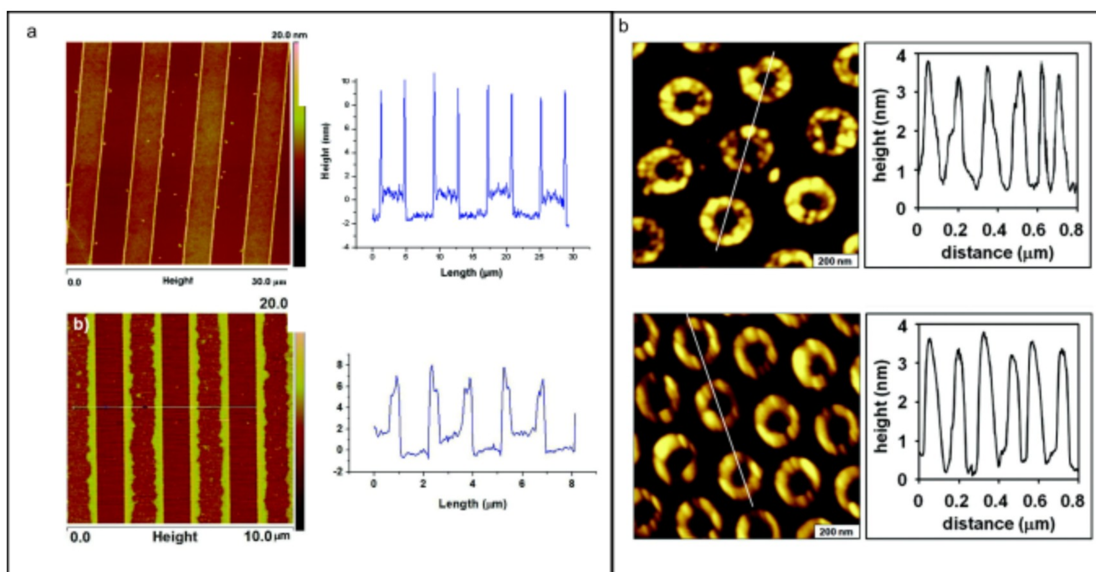

Figure 3.20: Line and circular edge structures formed by vapor-phase deposition of aminosilanes. a) Line structures formed in PDMS soft lithography templates reprinted with permission from refs [238] and [239], and b) Ring structures formed by vapor deposition of aminosilanes in particle lithography reprinted with permission from reference 182. Copyright American Chemical Society.

As shown in Figure 2.4, the use of 3-aminopropyldiisopropyethoxysilane did not result in the formation of high-aspect ratio ring structures, and instead formed features with a flat morphology. For the solution-phase resist template removal described in chapter 2, high-aspect ratio structures of APTMS were regularly prone to collapse. The work in this chapter primarily used plasma-based removal to investigate APTMS structures as this approach avoided the sonication-induced collapse of solution removal. Oxygen plasma removal was not tested with APDIPES.

Earlier work was completed using the organosilane 3-mercaptopropyltrimethoxysilane (MPTMS). With solution removal, the silane produces edge features on both circular and rectangular templates, as in Figure 3.21. MPTMS was not explored further for this work as APTMS deposition resulted in high aspect ratio features while MPTMS-based structures of SiO_x

could not be resolved in SEM after plasma removal. It may be possible that plasma removal is not suitable for all organosilane depositions. MPTMS is therefore promising to explore for future work. As shown in Figure 3.21, b and d, pore depths nearly extend to the surface with both circular and square shaped features. The 3–4 nm high pore floor is likely multilayer MPTMS and perhaps could be removed in a short oxygen etch, leaving the thicker sidewalls intact. Alternate template materials also could be attempted, in tandem with previous lithography schemes presented, to show the effects of the silane deposition on different interfaces.

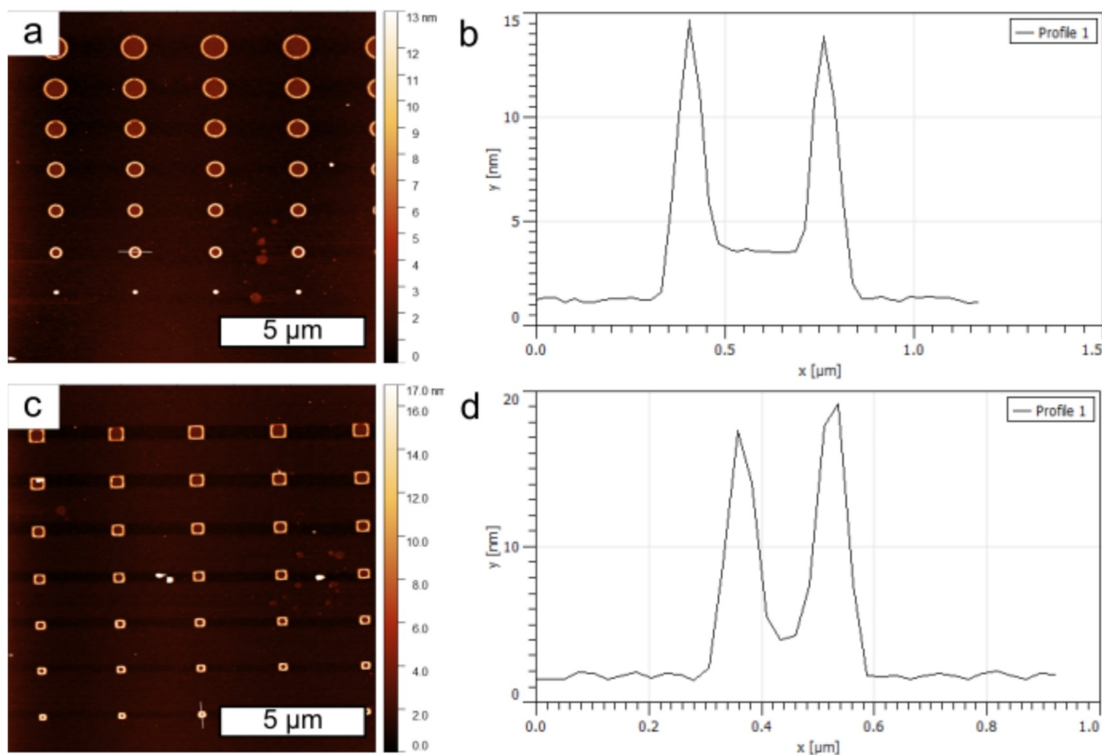

Figure 3.21. AFM images of MPTMS spacer structures formed through a ZEP mask after solution based removal with sonication. a) Large diameter circle features, b) Line height profile of circular feature shown in a, c) Large square shaped features, and d) Line height profile of square in c.

3.2.9 Aminosilane Nanostructures as Spacers: Relevance to Density Multiplication Strategies

The nanostructures in this chapter are similar conceptually to mandrel-type (line shaped) spacers formed (post etchback and trim) as well as chemically shrunk contact holes which are used in semiconductor manufacturing.[243,244] This work may be of value to semiconductor lithography processes which use feature shrink techniques as a means for density multiplication. As photolithography reached its lithographic printing limit using 193-nm wavelength lasers and numerical apertures of 1.35, and features beyond 40–45 nm half-pitch are not achieved without fundamental changes in lithographic approaches.[245] The International Technology Roadmap for Semiconductors (ITRS 2.0) lists multiple patterning as a baseline process, with self-aligned quadruple patterning in current active use.[245] An earlier ITRS report from 2013 indicated that extreme UV (EUV) developments would be needed to keep pace with Moore's scaling. Currently, the newest roadmap reflects that EUV has high production rates, capable of several hundred wafers a day.[245] However, to continue to push deeper into the 11- and 7-nm nodes, EUV will require combination with multiple patterning techniques, such as self aligned double patterning (SADP).[246] Therefore, for advancement of semiconductor scaling, it is important to develop new and cost-effective methods of feature multiplication and shrinkage.

What can be coined collectively as double patterning is a dominant approach for extending the capabilities of optical lithography. Double patterning, performed in succession, results in quadruple patterning, the current mainstay process for achieving small features, and a form of multiple patterning. One broad approach to multiple patterning relies foremost on the lithography tool by way of multiple exposure steps (Figure 3.22, a and b). Double exposure is

expensive,[247] and the multiple lithography steps can be prone to error.[248] Common methods of double exposure include litho-etch-litho-etch (LELE) and litho-freeze-litho-etch (LFLE). Alternative methods, such as litho-litho-etch (LLE)[249] and dual tone development (DTD),[250] are being explored. It is particularly desirable in all of these processes to reduce overall process steps, while maintaining attainable critical dimensions.

The second main approach of double patterning is a process change rather than different uses of the lithography instrument. New techniques increasingly rely on the ability to shrink existing processes after the lithography step. Self-aligned double patterning (SADP), spacer mask patterning, spacer double patterning frequency doubling, or pitch-halving are all terms that have been used interchangeably to describe the approaches of shrinking dimensions after lithography has taken place.[251]

Spacer mask patterning is achieved by forming a spacer of a sacrificial material such as SiO_x and integrating that spacer into later lithography steps, either as a hard mask itself or as a sacrificial material. Spacer materials vary but are predominantly silicon oxide or silicon nitride.[252] Spacer formation often is completed by chemical vapor deposition (CVD)[253] or atomic layer deposition (ALD),[254–256] although alternative methods, such as spin-on sidewalls,[257] continue to see development. Typically, the spacer material is applied over top of a negative feature known as a mandrel. In Figure 3.22 c, the layer marked “Top Hard Mask” forms the mandrels. The spacer is then combined with an etch step and chemical mechanical polishing (CMP).[258] The mandrels are created utilizing optical lithography, although some work has utilized EBL negative tone resists, such as HSQ[236] or other organosilicate materials[259]. There are several applications for lithography utilizing a spacer deposition approach, such as FinFets[252] and NAND flash.[251] The

approach has been used in biosensor fabrication,[260] nanoimprint template fabrication,[261] and in extending capabilities of interference lithography applications.[261]

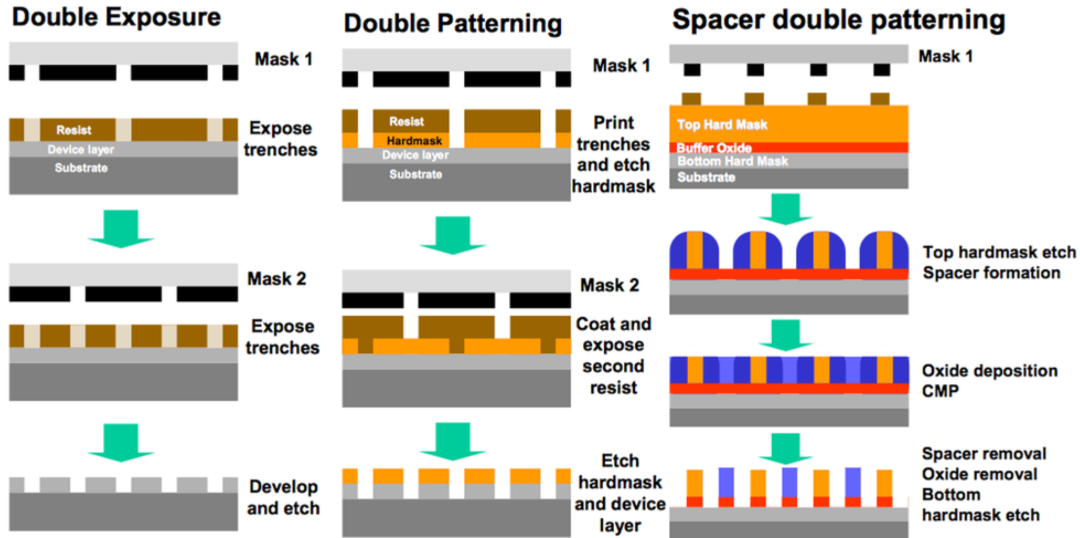

Figure 3.22. Example of density doubling multiplication strategies from the International Technology Roadmap for Semiconductors. Reprinted with permission from reference [245] Copyright Semiconductor Industry Association (SIA) 2009.

As lines continue to narrow by utilizing techniques that deposit sidewall spacers, increasing demand is placed on reducing contact hole sizes.[262,263] Combining contact shrink with the LELE process enables doubling of features not achievable by immersion lithography.[264] One method of shrinking is thermal reflow, which involves careful baking steps to cause the resist to reflow back towards the centre of the developed pattern, reducing its effective dimensions, shrinking contact holes. Typically, thermal reflow is done for photolithography[265,266] but it also has seen application with electron beam lithography resists, such as ZEP.[260]

Another technique for shrinking contact holes can be referred to as the chemical shrink process. There are commercial solutions for this technique, such as Shrink Assisted Film for Enhanced Resolution (SAFIER)[243] used with trenches and Resolution Enhancement Lithography

Assisted by Chemical Shrink (RELACS) for contact holes.[244,267] Contact holes are a feature element that connect wiring layers to transistor elements in deeper layers of the integrated circuit (IC). Contact hole pitches (the distance between hole features) below 50 nm and metal layer half pitches below 30 nm all use multiple patterning to go beyond the resolution limits of optical lithography.[268] Chemical shrink of the RELACS process is shown in Figure 3.23. The resist is patterned, baked, and developed, after which the hole structures have reduced dimensions. Achievable shrinkage is shown in Figure 3.23 b. Both of these techniques deposit materials against the respective sidewalls to reduce dimensions with the intention of density multiplication.

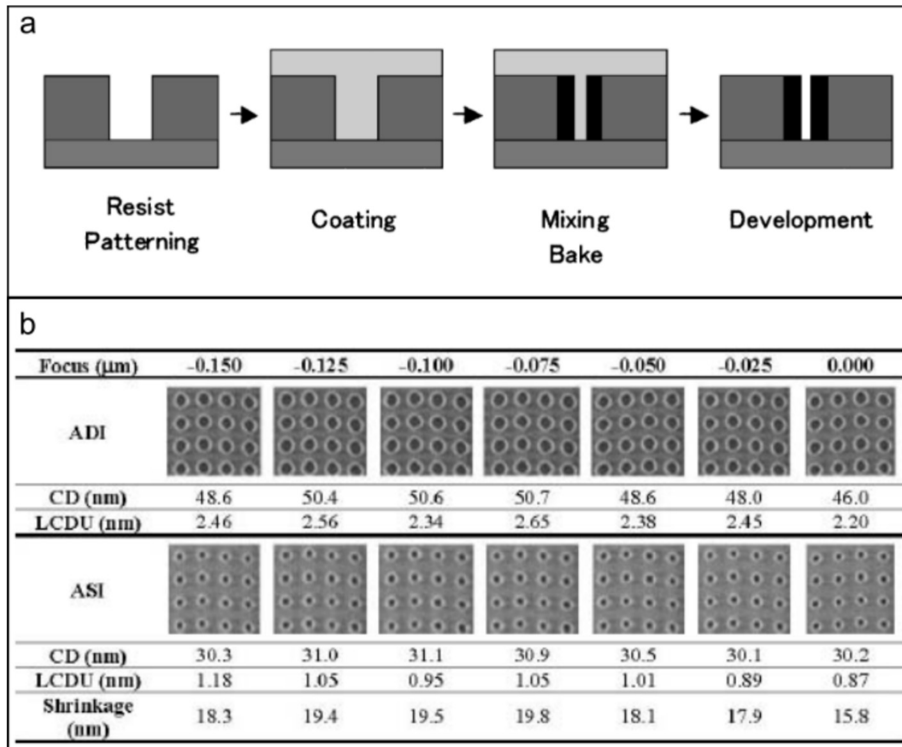

Focus (µm)	-0.150	-0.125	-0.100	-0.075	-0.050	-0.025	0.000
ADI							
CD (nm)	48.6	50.4	50.6	50.7	48.6	48.0	46.0
LCDU (nm)	2.46	2.56	2.34	2.65	2.38	2.45	2.20
ASI							
CD (nm)	30.3	31.0	31.1	30.9	30.5	30.1	30.2
LCDU (nm)	1.18	1.05	0.95	1.05	1.01	0.89	0.87
Shrinkage (nm)	18.3	19.4	19.5	19.8	18.1	17.9	15.8

Figure 3.23: Overview of chemical shrink process using the RELACS system. a) Process flow of patterning contact holes, coating, baking, and development, and b) Achievable shrinkage metrics for the RELACS approach. Reprinted with permission from reference [269]. Copyright 2015 SPIE.

The structures in this chapter are analogous to contact and line shrink spacers formed in self-aligned patterning processes. In the case of patterned holes, we thought the structures may be useful for contact shrinking (Figure 3.24, step 4a to step 6a) and that line structures may be useful for line frequency doubling (Figure 3.24, step 4b to 6b).

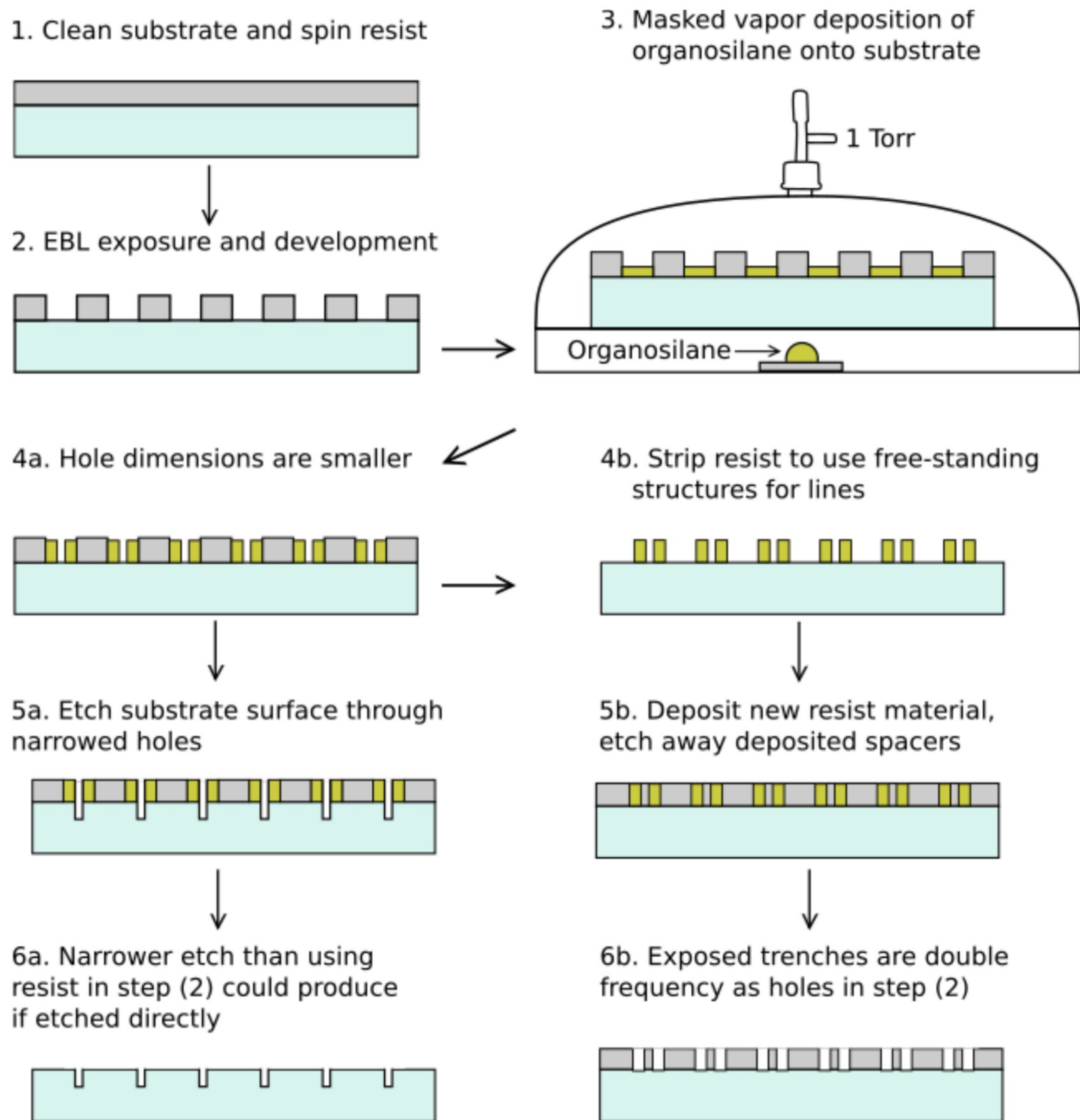

Figure 3.24. Potential shrinking scheme for line and hole nanostructures formed by APTMS deposition through EBL defined templates.

3.3 Conclusion

This chapter examined the notion that condensation structures of aminoalkoxysilanes could be created using EBL resists as masks for vapor-phase deposition, and that morphology of these structures could be controlled. The approach is supported for structure creation but further refinement is needed for tighter control over morphology. It was found that some control over feature height was possible by varying deposition time, however refined control was not possible with this system below times of 15 min. Width of features was controlled with varying pattern widths, as was pitch and pattern geometry. The behavior of organosilane deposition and condensation through ZEP masks was examined, indicating that this process may offer an alternative means for spacer deposition, at lower temperatures compared with ALD or CVD. Using SiO_x nanostructures could remove process steps once formation is optimized.

The next step for this work is to determine the growth and morphology of the line spacer structures in more detail. Very early work showed promise as ring structures were created on glass surfaces and imaged, as shown in Figure 3.2. To maximize use of the flood gun, samples should be prepared on intrinsic silicon, or glass coverslips inside a ZEP resist and then coated in 20 nm of carbon before removing the resist. This will improve cross section analysis with the Ga-FIB beam and maximize the charge reduction capabilities of the flood gun. This will allow for imaging of the wide gap lines and how well they conform to the sidewalls of the resist template. To ultimately determine the structure of the features, TEM analysis should be completed on cross sections of the ring and line features. A properly designed sample can be set up for a specialized dicing/FIB routine where a thin (100 µm) section could be analyzed for cross

section growth in TEM. Doing this analysis with the structures inside the template will allow for accurate determination of the morphology as it conforms to the resist.

After improved characterization of the morphology, tighter control mechanisms can be put in place for this deposition system. The current deposition chamber has very poor control over humidity, pressure, and temperature. While repeatable over longer time frames, I suspect that with small granular changes it will be difficult to interrogate the finer details of this system. There are small, benchtop deposition systems that can be utilized, such as the one shown in Figure 3.25 by YES, which is a benchtop R&D system that can control multiple parameters and utilize various deposition liquids. Aminosilanes have been deposited successfully utilizing systems such as these, which could permit optimization of sidewall growth, application of molecular adhesion layers, and other applications of organosilanes.[196]

Figure 3.25: Example of a commercial CVD system for application of silanes from the vapor phase by YES Engineering. Reprinted with permission from YES Engineering.

Following improved deposition and characterization, the system also can be optimized further by altering the spacer materials being used. An interesting option for template removal could be using supercritical CO_2 as mentioned previously, to preserve reactivity. Following a

successful solution removal, exciting opportunities are available for other leading semiconductor process. For example, using these reactive features as guides with designed surface chemistry for directed self-assembly, influencing how materials such as block-copolymers may interact with the guides themselves.

Lastly, the application of a metal deposition to double line frequency needs to be completed following confirmation of conditions that result in full clearance for the line structures. This could be completed most easily for the contact hole features first, especially the rings >100 nm in diameter. Following spacer deposition, the etch process would take place, ideally exposing the underlying surface while keeping the initial template intact. Then, the template would be removed and, following spacer removal, would produce metal contacts of smaller dimensions. In the case of a metal deposition onto line feature spacers, the template would be removed first, and a metal deposition would follow. Next, the spacers would be etched, leaving metal traces at double the frequency of the original template. Finally, both hole and line doubling should be done using photolithography processing and EUV compatible resists, showing that the spacers can be extended on EUV lines. Afterwards, the potential for SAQP can be explored with double exposure methodologies.

This chapter has shown the effect of depositing APTMS from the vapor phase into EBL guided contact hole and trench templates. The line shaped structures formed in as little as 15 min which may be attractive considering no long pumpdown is required to reach high vacuum conditions needed with other physical deposition processes. Additionally, these structures are all formed below the glass transition temperature of the resists involved; this could avoid resist freezing processes that currently are used. ALD and CVD spacer deposition routinely take place

at a much higher temperature than in the process shown here. These structures also are likely to be complementary to existing thermal reflow and chemical shrink processes, perhaps providing an additional level of shrinkage on current existing spacer formation technologies. The features also appear to be trimmable with further oxide etching to remove any potential cap formation. The semiconductor industry has well established techniques, and spacer formation is a complementary tool that fits into established immersion lithography and newer EUV process flows. This work has shown that the nature of vapor deposition of aminosilanes has potential for density multiplication as a spacer formation technique.

3.4 Experimental

3.4.1 surface and Sample Preparation

Silicon <100> resistivity < 0.005 Ω·cm wafers were cut into 1 cm × 1 cm squares and prepared as in Chapter 2.

3.4.2 Mask Fabrication

Positive tone 57k molecular weight ZEP520 (Zenon Chemicals) was the primary resist utilized for all work in this chapter. Samples were spin-coated (Brewer Cee Spinner) to varied thicknesses with a pre-exposure bake of 30 s at 180 °C. Both 1:2 ZEP520:Anisole and 1:1 ZEP520:Anisole formulations were utilized to achieve thicknesses as needed. Electron beam exposure was performed on a Raith 150-Two EBL system. Single pixel dot-shot features were created at an accelerating voltage of 30 keV and a beam current of 22 pA and were varied in dose systematically. Line features were created with single pixel exposure base doses of 50 pC/cm and

increased by utilizing dose fields of 0.25, 0.5, 1.0, 1.5, 2.0, 3.0, 5.0 and 10.0 multiplied by all base doses in the field. For example, a line feature of dose 50 pC/cm in dose field 2.0 would have an actual exposure dosage of 100 pC/cm. Effective clearance dose varied by film thickness, but for most line features the effective working regime was from 0.5 to 2 pC/cm. Area doses had a base dose of 50 uC/cm^2 and were varied in the same dose fields. Pitches for dots and lines were adjusted as stated above. Following exposure, ZEP520A was developed in ZEDN50 (Zenon) developer for 4 min, followed by rinsing in IPA for 30 s. Samples were blow dried with a stream of N_2. Patterned surfaces were stored in a class 10 cleanroom (40% relative humidity) until use.

3.4.3 Vapor-Phase Deposition

The vapor-phase deposition protocol used was identical to that in Chapter 2, utilizing primarily APTMS. Deposition times were varied up to 18 h, with 18 h being the standard deposition time, unless otherwise stated. Pumpdown time ranged from 5 min to 7 min. Deposition time was determined starting from sealing the desiccator chamber after reaching 1 Torr and immediate loading into the oven (a time lag of ~30 s) to removal and opening of the main desiccator chamber. The temperature of the oven was monitored via a thermometer mounted through a top port in the oven. Desiccators were loaded and unloaded inside a fume hood for all depositions.

3.4.4 Reactive Ion Etching

Following exposure and before immediate use, all samples were descummed in reactive ion etching (RIE, Trion) for 30 s at a power of 40 W, 200 mTorr chamber pressure, and 50 SCCM oxygen flow. This condition removes 37 nm of ZEP520 consistently. Where resists were stripped

completely utilizing a plasma treatment, stripping was completed with RIE oxygen plasma for 240 s, 200 W, 50 mTorr pressure, and 50 SCCM oxygen flow rate. Samples were inspected in a Leica inverted microscope, brightfield, at 10X, 40X, and 100X magnifications for the residual resist post strip step. For samples that were exposed to an oxide etch treatment, conditions were 5 SCCM oxygen flow rate, 40 SCCM CHF_3 flow rate, 125 W, 40 mTorr chamber pressure, for 30 s, unless otherwise stated.

3.4.5 AFM Imaging

All trench and feature height profiles were acquired using tapping mode atomic force microscopy (AFM) with a Digital Instruments/Veeco multimode atomic force microscope. Collected data were analyzed using the open source software Gwyddion.[229]

3.4.6 SEM Imaging

Scanning electron microscope (SEM) images were taken using a Hitachi S4800 SEM at accelerating voltages of 15–30 keV and a Zeiss Sigma FESEM at 5-30 keV. All SEM micrographs were processed in Gwyddion and Fijji.[230] Tilted imaging was completed in the S4800 at an angles ranging from 45–90°. A standard 45 tilt holder was utilized for 45° images and was tilted itself to achieve nearly cross sectional images (~80° tilt). Charge reduction, where used, typically was completed by sputter coating with 5 nm of Cr (Gatan).

3.4.7 Helium Ion Microscope (HiM) Imaging

A Zeiss scanning helium ion beam microscope was utilized for high resolution imaging, charge reduction imaging, and Ga-FIB milling. Imaging was completed at 30.8 keV, 10 μm aperture, 1.59 pA, and a spot size of 4. Milling was completed using the Ga column at a 9 mm working distance in cycles of 5 μs dwell time. Cycles of milling were carried out until visual clearance was noted and and drift compensation was adjusted manually.

4

Lithographic Approaches for Patterning Organosilanes in Fluorescent Nanoarray Applications

4.1 Introduction

The aim of the work in this chapter was to produce a fluorescent nanoarray standard for super-resolution localization fluorescence microscopy applications by using the developed vapor deposition protocol to pattern functional groups, which could be conjugated to fluorophores. This application demonstrated that vapor-phase deposition of organosilanes could be used with electron beam lithography to position flurophores on a transparent and insulating surface. This was also motivated by the fact that no commercially available standard with *multiple regions* of distance calibration on one slide currently exists. The fluorescent array work focuses on the two general fabrication approaches taken to produce the diffraction limited fluorescent arrays. While

super-resolution microscopy imaging below λ/2 was was not achieved, this work laid the groundwork for earlier chapters, as well as establishing an array methodology that can produce competitive centre-to-centre distances to commercial microarrays. The array fabrication and characterization will be described and the potential extension of this work into the sub-diffraction limit regime discussed.

4.1.1 Lithography for Fluorescent Nanoarray Fabrication

Society's obsession with big data continues to push bioanalytics towards increasing throughput. Array-based technologies have been a cornerstone in meeting these demands.[270,271] Creating addressable surfaces for high throughput fluorescence readouts can be achieved in multiple ways. Briefly, some examples include bubblejet printing,[272] photolithography combined with DNA synthesis, [273,274]and mechanical spotting.[275,276] DNA technologies are a large driver in array miniaturization, as well as protein arrays,[277] biosensor development,[278] and enzyme arrays.[279]

Improving the power of microarrays as an analytical tool can be done by maximizing the amount of information per unit area. Increasing the density of information is achieved by shrinking both the probe feature size and their relative pitch to one another.[131] The reduction of feature sizes and pitches has led to the investigation of array technologies with submicron features. Shown in Figure 4.1 is an example of an array technology utilizing nanoscale dimensions for human genome sequencing. By reducing feature dimensions to 700 nm, centre-to-centre, the authors were able to improve the number of DNA spots per image by 3.4 times, compared to 1.29-micron arrays.[280]

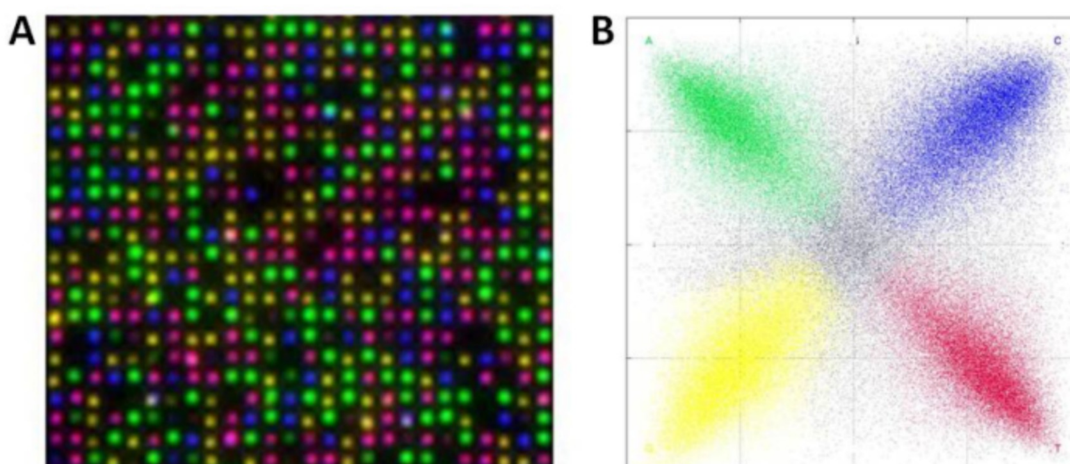

Figure 4.1: Example of a fluorescent nanoarray created with semiconductor processes (photolithography) and vapor deposition of aminosilanes as anchors. a) Four color composite scanned array with 700-nm centre-to-centre positions, and b) Cluster plot of normalized intensities of test array shown with 4.2 pixels per spot. Reprinted with permission from reference [280]. Copyright © 2010, American Association for the Advancement of Science.

Another methodology worth considering is electron beam lithography (EBL), which is becoming a more accessible tool in nanofabrication, particularly with user-based cleanroom facilities. The technique is able to pattern features with sub-10-nm resolution and with arbitrary shapes.[281] While expensive, these specialized tools are becoming more accessible, and their strengths can be exploited in fields outside the semiconductor industry. EBL techniques are now being used to impart chemical and biological functionality to surfaces in designed patterns.

Chemical linkage to the surface is a critical component in array fabrication, providing the reactive groups necessary to anchor molecules of interest to the surface. Self-assembled monolayers, such as silanes, often are relied on to link silanol groups on the glass surface to other small molecules, such as oligonucleotides.[131] As discussed in previous chapters, SAMs can be patterned utilizing EBL and photolithography. Patterns incorporating monolayers of polyethylene glycol (PEG) are particularly advantageous due to its protein resistant

properties.[282,283] In addition to arrays for assay development, the use of micro- and nano-patterned surfaces are becoming valuable tools to investigate and manipulate fundamental cell behavior.[284–293]

Fluorescence microscopy is a foundation measurement tool for acquiring information from the array surface, regardless of its end application. As array dimensions move into the nanoscale regime, developments in fluorescence microscopy techniques are keeping pace with demands for higher resolution. More information can be obtained by circumventing the diffraction limit of light with super-resolution microscopy methods.[294–296] Super-resolution microscopy has proved essential for examining cell behavior below the diffraction limit of traditional fluorescence microscopy.[297,298] To date, few have combined sub-diffraction limit EBL patterned SAMs with super-resolution microscopy to reap their combined benefit.[299,300]

4.1.2 Super-Resolution Fluorescence Microscopy

As discussed in Chapter 1, circumventing the diffraction limit is not only important for diffraction-limited lithography, such as optical photolithography, but also for huge advancements in other visible light technologies like fluorescence microscopy. The 2014 Nobel Prize in chemistry was awarded to Erik Betzig, Stefan Hell, and William Moerner for their development of super-resolution microscopy techniques and circumventing Abbe's law. The Academy has divided super-resolution microscopy methods into two farfield microscopy categories.[296] The first was, "super-resolved single fluorophore microscopy", or localization techniques.[296] The second is point spread function engineering techniques, or "super-resolved ensemble fluorophore

microscopy".[296] Localization microscopy will be introduced here as this technique was a focus for this work's late stage application.

The highest achievable resolution of a far field light microscope is approximately equal to $\lambda/2$, where λ is the wavelength of incident light.[301] With a higher numerical aperture objective and short wavelength of light, resolution is on the order of 200 nm for the far blue. Super-resolved fluorescence microscopy can achieve resolution in the 10's of nanometers, with newer techniques reaching below 10 nm.[302] The super-resolution method discussed here is called Stochastic Optical Reconstruction Microscopy (STORM).[303] STORM techniques are becoming more accessible on existing microscopes, and new commercial STORM systems are becoming available. STORM, like most localization techniques, relies on the repeated localization of fluorescent dyes over time. These dyes are photoswitchable and can be fluorescent proteins,[304] small organic dyes,[305] and, occasionally, quantum dots.[306] Common small organic dyes used include Cy5, Alexa647, Atto488, with new ones constantly being developed.[307] As shown in Figure 4.2, localization microscopies rely on multiple, sparsely located emitters being captured over a large number of imaging frames. A strong laser is utilized initially to cause fluorophores to enter an off state, and then the fluorophores blink as they stochastically return to an on state. Combined with specialized imaging buffers to induce blinking, the on and off states are imaged in each frame, identifying the centre of each fluorophore's point spread function according to a Gaussian distribution of intensity. After many images are collected into a stack, that stack is merged into a single image, which is the reconstructed super-resolution image.

While localization has mathematically unlimited precision, it has several practical limitations. Complicated buffer systems are short lived and often are needed for adequate

imaging. Laser intensities at high power can cause photobleaching and photodamage over the long imaging times required to capture all the frames to produce an image.

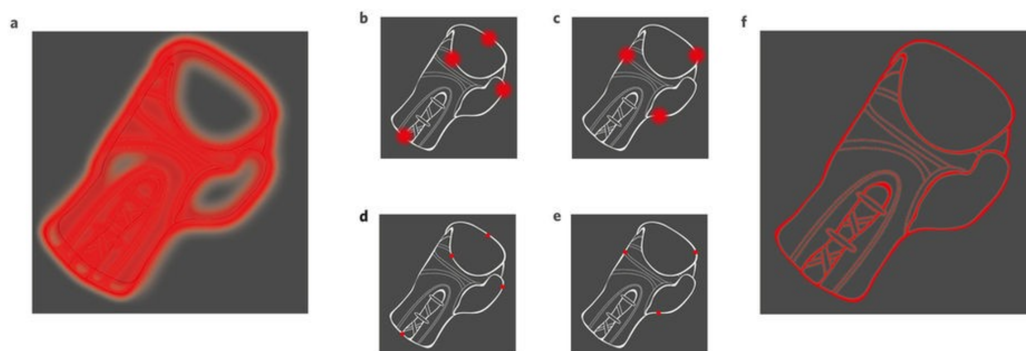

Figure 4.2: a) Conventional image of closely spaced fluorescent molecules that form the shape of a boxing glove. The resolution of the image is limited by diffraction. **b–e**) By sequentially switching on and imaging different subsets of molecules (**b,c**), the location of each molecule corresponding to the centre of the emitted fluorescence point spread function, can be precisely determined (**d,e**), and **f**) A super-resolved image is created by plotting the positions of all localized molecules. Reprinted with permission from reference [308] © 2016 Nature Publishing Group, a division of Macmillan Publishers Limited.

Overlapping fluorophores also reduce localization efficacy; thus, fluorophores should not overlap while in their on state. Overlapping fluorophores were a principal challenge for this work. The fluorophores ideally must blink on and off at regular intervals; thus, random blinking events are harder to utilize, as in the case for quantum dots. Algorithms for reconstruction are often proprietary, and many software packages maintained by individual research groups are for their internal use.[308] Background noise must be kept to an absolute minimum for super-resolution techniques, such as STORM. Often, relative signal to background is very low for the sparse labeling in STORM microscopy and random emitters can cause significant problems for reconstruction algorithms. Lastly, biological structures, such as microtubules, are still the gold standard for verifying localization precision[309] rather than the use of a commercially accepted lateral standard. New, DNA-based standards are seeing use,[310] but a single-slide lateral standard

that rapidly can identify and verify resolution is not presently available. An ideal standard would consist of multiple regions of discrete distances between fluorescent features. After imaging, analysis of this single chip could reveal diffraction limited lateral resolution, as as well as achievable resolution under super-resolution conditions.

This work demonstrated that vapor-phase silane deposition with EBL could be used to position flurophores on an optically transparent surface, in a nanoscale array that could function as a lateral distance standard for STORM. As there are multiple lithographic approaches to achieve this positioning, it was also thought that lithographic approach, positive- or negative-tone would influence the amount of nonspecific background during the labelling steps.

By combining vapor-phase silane deposition with EBL techniques for insulating surfaces, I have developed two general approaches of patterning functional groups for use as chemical linkers. These methods are demonstrated by immobilizing small organic fluorophores in a nanoarray arrangement. These methods offer additional means by which researchers can exploit EBL's resolution to achieve functionalized surfaces with desired molecule placement that is compatible with fluorescent labeling protocols. Here, the capability of the method in standard total internal reflectance fluorescence (TIRF) microscopy was examined, and its potential for use in super-resolution localization microscopy is investigated.

4.2 Results and Discussion

Both positive and negative tone patterning schemes to create the nanoscale fluorescent array were utilized for this work. The methacrylate resist PMMA (950k) initially was selected for the

positive patterning approach as very high resolutions are achievable for single layer liftoff purposes. The vapor deposition scheme for positive tone array fabrication is shown in Figure 4.3.

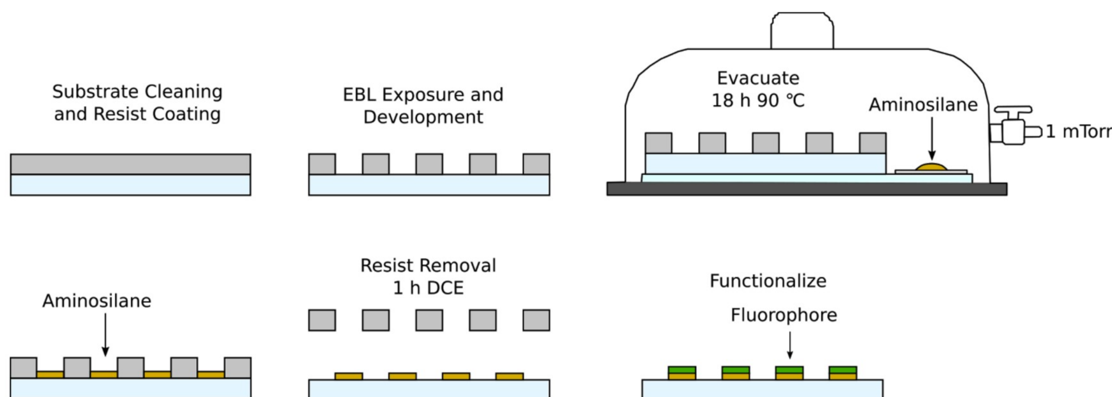

Figure 4.3: Positive tone fabrication scheme for fluorescent nanoarrays. First the surface is coated with the resist of choice. Following exposure and development, the chip with exposed holes is placed into a desiccator with neat organosilane. Following deposition, the chip is removed and the resist is removed in a solvent such as dichloroethane (DCE). Finally, the chip is immersed in the labeling solution containing the reactive fluorophore of interest.

The alkoxysilane 3-aminopropyltrimethoxysilane (APTMS) was used as a fluorophore linker as the amine reactive dyes, such as isothiocyanates and activated NHS esters, are readily available. PMMA(950k) was spin coated to a nominal thickness of 110 nm. Descumming reduced the film height to 50 nm (Filmetrics, AFM). After fabrication, masks were characterized by AFM as all work was completed on insulating surfaces, making imaging by electron microscopy challenging.[311]

4.2.1 Positive Tone Array Fabrication Patterning

It was important to determine that full clearance (complete removal of the patterned area resist) had been made for the resist templates as insufficient development or descumming would result in an inability for APTMS to reach the surface to bind with the exposed native oxide. Hole

profiling and metal liftoff are two methods that can be used to confirm film clearance. Shown in Figure 4.4 a is a clustered design nanoarray with 250-nm pitch holes. After oxygen plasma descumming (Harrick), hole profiling was successful for this template as full film clearance (50 nm) was confirmed by comparing with filmetrics measurements of the film after the descumming step (50 nm, 99.9% goodness of fit). It should be noted that PMMA films etch very fast in oxygen plasmas.[312] A barrel style plasma cleaner, as opposed to reactive ion etching, was used for descumming purposes due to the lower power output. Later negative tone work was able to utilize a more directional RIE etch as thicker sacrificial films could be prepared to achieve reasonable process windows (32 to 50 s). Array template clearances were checked also by metal liftoff deposition. This method is used often to confirm dose clearance and is a principal nanofabrication technique to deposit layers of metals on a surface with known heights. 15 nm of gold–palladium was sputter deposited (Gatan) through a 150-nm pitch square array (Figure 4.4 b). After lift-off in 1,2-dichloroethane, samples were analyzed by AFM to confirm the deposition of metals in their respective dose fields. Successful film clearance was found from 4 fC/dot to 12 fC/dot. After 12 fC/dot, dot features were very large (>100 nm diameter) and at higher doses would cause significant defects, such as hole merger due to proximity effects.[313] After electron beam patterning parameters were determined, fluorescent array layouts were adjusted to determine if patterned APTMS could indeed be resolved in standard, diffraction limited TIRF illumination without the need for super-resolution microscopy first. Fluorescent conjugation with small organic fluorophores is rarely carried out on a patterned surface feature without the use of antibodies or bioconjugates such as biotin-streptavidin.[311]

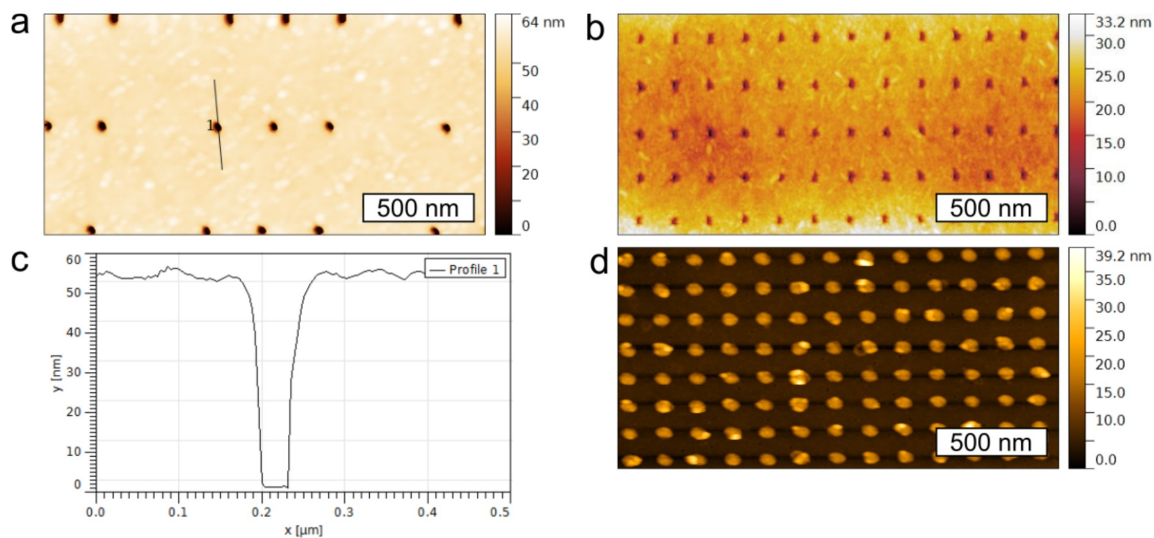

Figure 4.4: Hole profiling and liftoff to confirm effective clearance dose on glass surfaces for clustered and regular arrays. a) AFM tapping mode height image. 30 kV, 30 µm, 250 nm pitch, 12 fC/dot, 60 s O_2 plasma 500 mTorr descum, b) AFM tapping mode height image. 30 kV, 30 µm, 150 nm pitch, 12 fC/dot, 60 s O_2 plasma 500 mTorr descum, c) AFM tapping mode trench profile of a, and d) AFM tapping mode height image. 15 nm AuPd metal lift-off.

Adequate cleaning protocols to remove non-specifically bound fluorophores were examined. Four common surfactants were compared by patterning APTMS, conjugating to fluoroscein isothiocyanate (FITC), and then comparing the resulting array cleanliness by investigating feature intensities with respect to backgrounds after changing the wash surfactants. The general labeling scheme is shown in Figure 4.5 for FITC and Cy5. The use of Cy5 is described in a later section. Different surfactants were used: Tween-20, Triton-X100, urea, and sodium dodecyl sulfate (SDS) at 0.1% vol in H_2O. Tween-20 and urea were the only surfactants found to result in clean arrays, and both SDS and Triton-X100 left large background aggregates over the entire surface. Tween-20 features were more distinguishable by FFT image analysis, thus, for the remaining fluorescent work, Tween-20 was utilized as the primary cleaning agent in the wash steps.

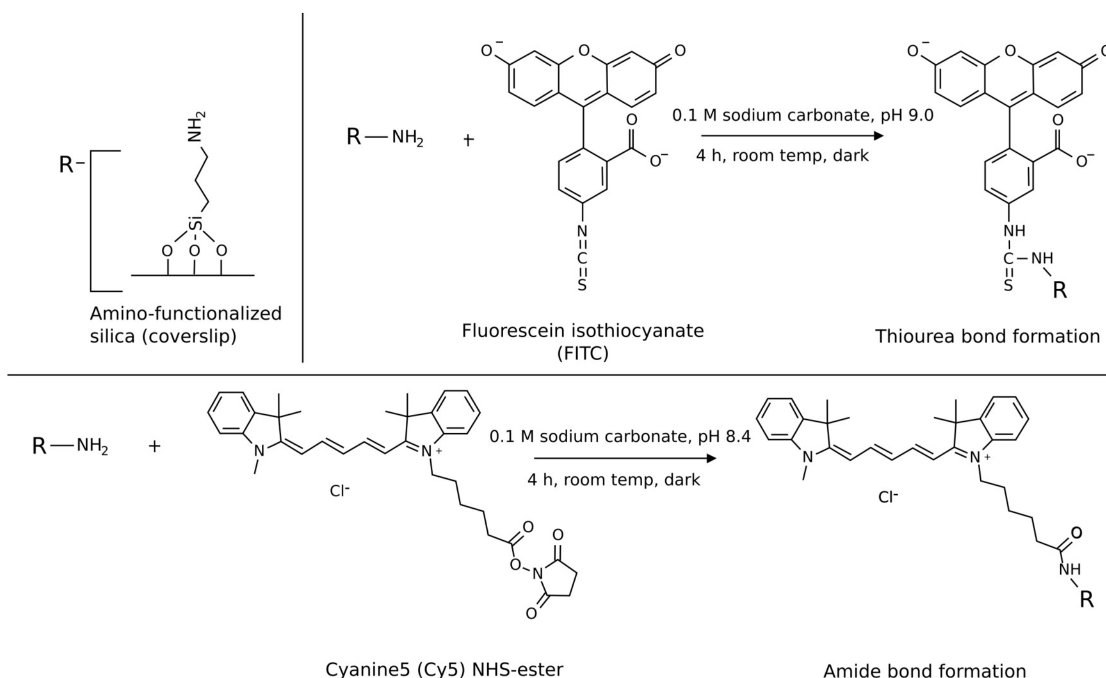

Figure 4.5: Overall labeling scheme used for labeling surface bound amine functional groups with FITC and Cy5 fluorophores. La belling in this work followed conditions shown here, unless otherwise stated.

Figure 4.6 shows the two design spacing schemes used for the fluorescent arrays. The 'sparse' design of 3-feature clusters were separated by 500 nm from each other within each cluster, by 2 µm from each neighbouring cluster of 3 features in the y direction, and 3 µm cluster-to-cluster the x direction. The 'dense' design of 3-feature clusters were separated by 250 nm from each other and by 500 nm to each neighbouring cluster.

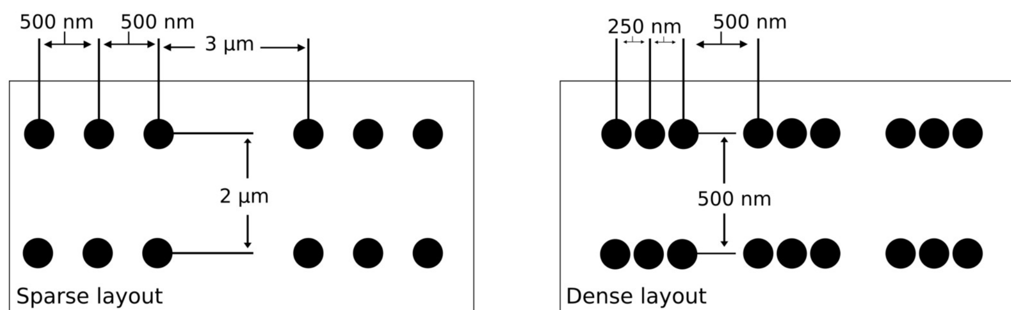

Figure 4.6. Sparse and dense layout distances for fluorescent nanoarrays.

Figure 4.7 shows the results of patterning APTMS for later conjugation to FITC. Initial results confirmed that a fluorescent array had been constructed and that successful conjugation had taken place. Figure 4.7 b shows the FITC-APTMS array with a dense initial design which is a denser layout than examples such as the one shown in Figure 4.1 or the nanoarrays utilized by Wind *et al*. (2016)[155] that measured distances of 1 μm in pitch (Figure 4.18). FFT images were used to confirm the presence of periodic fluorescent features. As the rationale for design was to produce an array that could be utilized for super-resolution applications, this separation of features could be accessed easily following successful application of later STORM localization protocols. It was important to confirm that *individual* features within clustered layouts could be identified laterally before application of more advanced microscopy techniques and switching to a localization appropriate fluorophore. Therefore, the same array was constructed with features separated by 500 nm within each cluster (Figure 4.7, d and e) to confirm that the feature was resolvable and was not connected or aggregated with neighbouring features. FFT again confirmed that periodic arrays were created. A common issue was the presence of interference fringes, as shown in Figure 4.7, a and b. The cause of these interference fringes was not determined, abut is is likely due to uneven illumination or imperfections in the beam path of the instrument, and this may be unique to each sample.[314] Additionally, an obvious issue noticeable in Figure 4.7, a and d, is background haze. This haze was a very significant problem, which will be discussed in a later section.

After confirming that periodic fluorescent arrays had been created, an attempt was made to resolve each individual feature within 250-nm and 500-nm clusters without the use of super-

resolution techniques to confirm individual feature reactivity and whether the limit of resolution for the microscope was being challenged with these arrays. With the current setup, the resolution for FITC features should be equal to 200 nm. The resolution can be expressed as:

(4.1) $$Resolution(r) = 0.61\,\lambda / NA$$

Where λ is the imaging wavelength and NA is the numerical aperture of the microscope, assuming perfect alignment of optical components in the system.

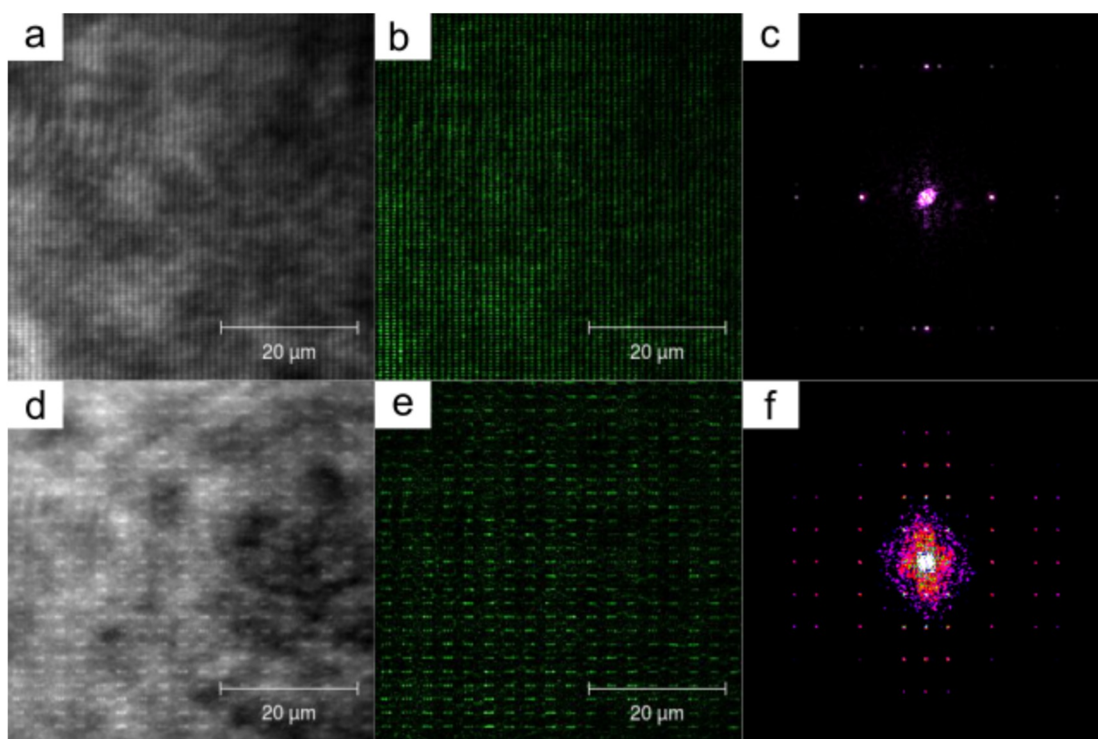

Figure 4.7: Total internal reflectance fluorescence, 60X magnification images of APTMS arrays labeled with FITC on No. 1.5 glass coverslip. Initial dense array design and effect of moving to a sparse, clustered design. a) Raw TIRF image with 500-nm pitch clusters, 3 features per cluster separated by 250 nm, b) Processed image after background subtraction of a, c) FFT of a dense cluster array, d) Raw TIRF image with 3-µm pitch clusters, 3 features per cluster separated by 500 nm, e) Processed image after background subtraction of d, and f) FFT of a sparse cluster array.

As the 250-nm centre-to-centre features were likely to exist as circular doughnuts, edge-to-edge distance is more likely to be closer to 200 nm, assuming a 50-nm diameter feature shape created at this dose (4 fC). The edge-to-edge of the features would be the shortest distance between

fluoropore centroids, assuming equal labeling of the feature. At a 200-nm separation, this would be a minimum of 20% reduction in achievable resolution for a 488-nm sample.

FFT analysis of the sparse and dense cluster designs in Figure 4.7 indicated some discrepancy in distance between fluorescent features and actual designed pitches. These distances were measured in inverse space (inverse pixels) from the centre of the FFT image, and then converted back into real space. For the sparse design, distance measured via FFT analysis in Gwyddion suggests a cluster-to-cluster distance in the X direction of 2.83 µm, rather than 3 µm. Similarly in the Y direction, the sparse design FFT indicated cluster-to-cluster distances measuring 1.88 µm rather than 2 µm. These discrepancies may be due to broadening of fluorescence features due to uneven labelling, or unintended increases in actual feature size. In both cases of the cluster-to-cluster distances, FFT measurements indicate shorter pitches than expected, which may be a result of the edges of larger features shifting the centroids of the feature fluorescent signals closer towards the outside edge of the actual features. The FFTs also confirmed that feature-to-feature distances in the dense layout could not be resolved.

Figure 4.8 shows a comparison between the mean column intensity for each feature, moving horizontally across the arrays. This method has been utilized before to confirm locations of fluorescent nanoarray features.[157] As shown in Figure 4.8, a and b, the 250-nm clusters were able to be separated by line intensity profiles, but each feature within the cluster could not be resolved. Each cluster had the appearance of a horizontal fluorescent spot after background subtraction. After adjusting the cluster pitch to 2 µm, it was confirmed that with the 500-nm pitch features, the system could resolve each individual cluster of features at a 500-nm centre-to-centre distance. Considering the feature edge-to-edge distance in the 500-nm array, the resolved

distance (Figure 4.7) is closer to 450 nm. It is clear from the profile that there is room to move features closer together to determine this limit, and this approach was taken in later design arrays.

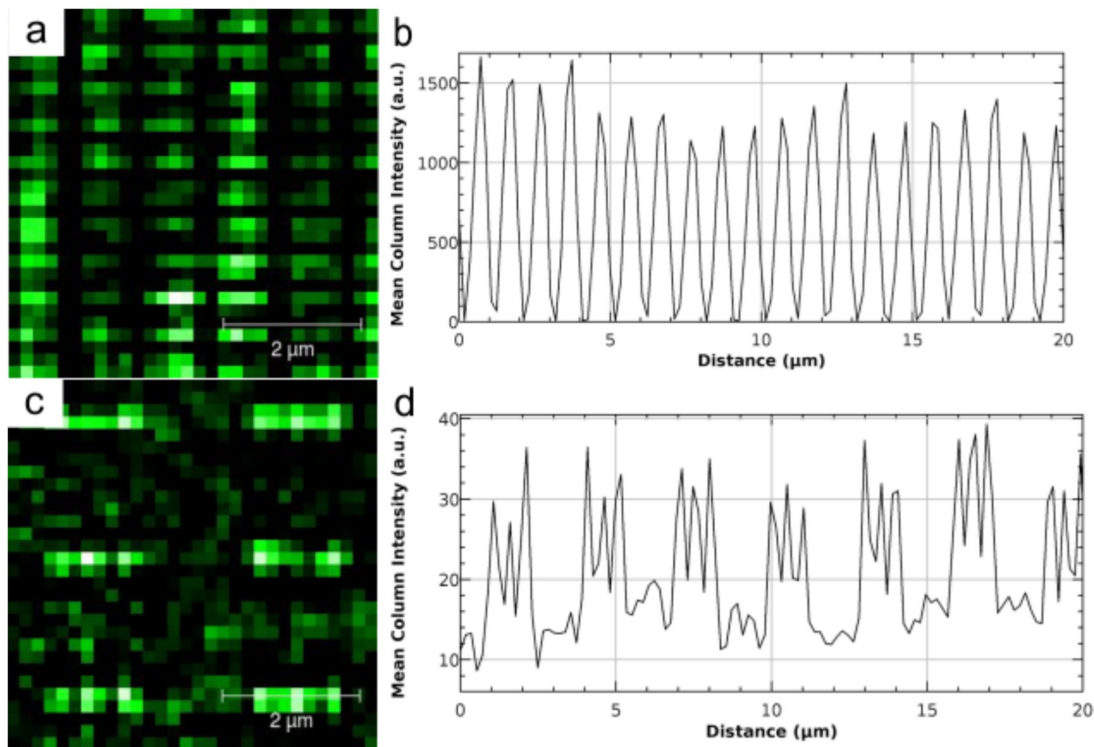

Figure 4.8: Magnified total internal reflectance fluorescence images captured with 60X TIRF objective of APTMS arrays labeled with FITC on No. 1.5 glass coverslip. a) TIRF image with background removed of 500-nm pitch clusters, 3 features per cluster separated by 250 nm, b) Line profile plot of first 20 μm of array showing mean column intensity cannot separate cluster features, c) Processed TIRF image of 2-μm pitch clusters, 3 features per cluster separated by 500 nm, and d) Line profile plot of first 20 μm of array showing mean column intensity is able to show separation of features within clusters.

4.2.2 Negative Tone Array Fabrication

Figure 4.9 shows the second methodology tested for producing fluorescent nanoarrays. This negative-tone approach was an attempt to circumvent the potential for nonspecific background binding of fluorophores in order to reduce the overall background signal floor. After exposure

and development of feature pillars from HSQ, a sacrificial layer of PMMA(950k) was used to vertically confine silanes (and thus fluorophores) on the SiO_x posts. This approach possibly could improve feature localization by allowing for non-specifically bound fluorophores to be washed away with the sacrificial layer, preventing their adsorption to the surface. Additionally, this design could be attractive for 3 dimensional (3D) imaging applications.[315]

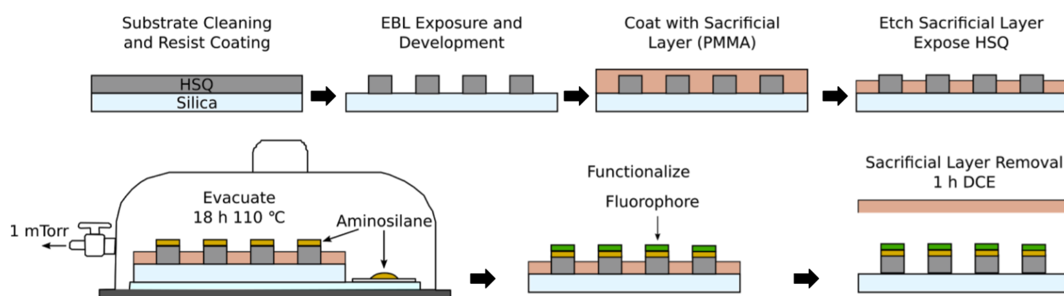

Figure 4.9: Negative tone fabrication scheme for fluorescent nanoarrays. First, the surface is coated with a negative tone resist HSQ. Following exposure and development, the chip is coated with a layer of sacrificial PMMA. Next, the PMMA layer is etched back in oxygen plasma to expose and activate the tops of SiO_x pillars. The sample with exposed pillars is placed into a desiccator with neat organosilane. Following deposition, the chip is removed and immersed in a labeling solution containing a reactive fluorophore of interest. Finally, the sacrificial resist is removed in a solvent such as dichloroethane (DCE).

Negative tone pattern fabrication and processing also was confirmed prior to fluorescent labeling. This approach to axial confinement of surface area for vapor deposition of organosilanes is entirely novel, to the best of our knowledge. Figure 4.10 shows the pillar arrays before coating with sacrificial PMMA.

Ideally, the array format would consist of discrete regions of different feature separation distances; this format was attempted with later work. Figure 4.10 b shows some features that have fallen over, likely due to handling and cleaning of these samples before imaging. Figure 4.10 c is an AFM example of features before coating with the sacrificial layer. Heights of SiO_x

features were nominally 100 nm. Figure 4.10 d shows feature clusters after oxygen plasma etchback, exposing 10 nm of the underlying SiO_x pillars. Films initially were coated at thicknesses that would allow more granular tuning of the PMMA etch rate. Coating the 100-nm pillars to a full film thickness of 200 nm, and then etching for 50 s in oxygen plasma at 40 W exposed 10 nm of the SiO_x pillars.

There are multiple parameters to adjust to optimize this approach. The choice of resist, which is discussed in Chapter 2, has enormous implications for the later removal of resist films that have been exposed to aminosilane vapor. Before detailed examination on silicon surfaces, it was found that using the more sterically hindered APDIPES for pillar labeling improved film removal by brightfield optical inspection (Leica, 4X magnification). Use of the negative tone method introduced the complexity of cleaning the surfaces with fragile features in comparison to the positive tone scheme. As sonication in the case of the SiO_x pillars would damage and destroy features, the most effective solution based removal combination to achieve labeling of the features and permit resist removal was APDIPES in combination with PMMA and DCE. Large resist pieces visible to the naked eye were found routinely on the surface after soaking in DCE when using APTMS. As was found later, APTMS film permeation into PMMA films is a large contributor and, in addition to hampering resist removal attempts, likely was causing significant background labeling. Permeated silanes would be present in the positive tone scheme as the patterned surface was being labeled. These would be labeled themselves and could be the reason for the significant background haze seen in the positive tone patterning route.

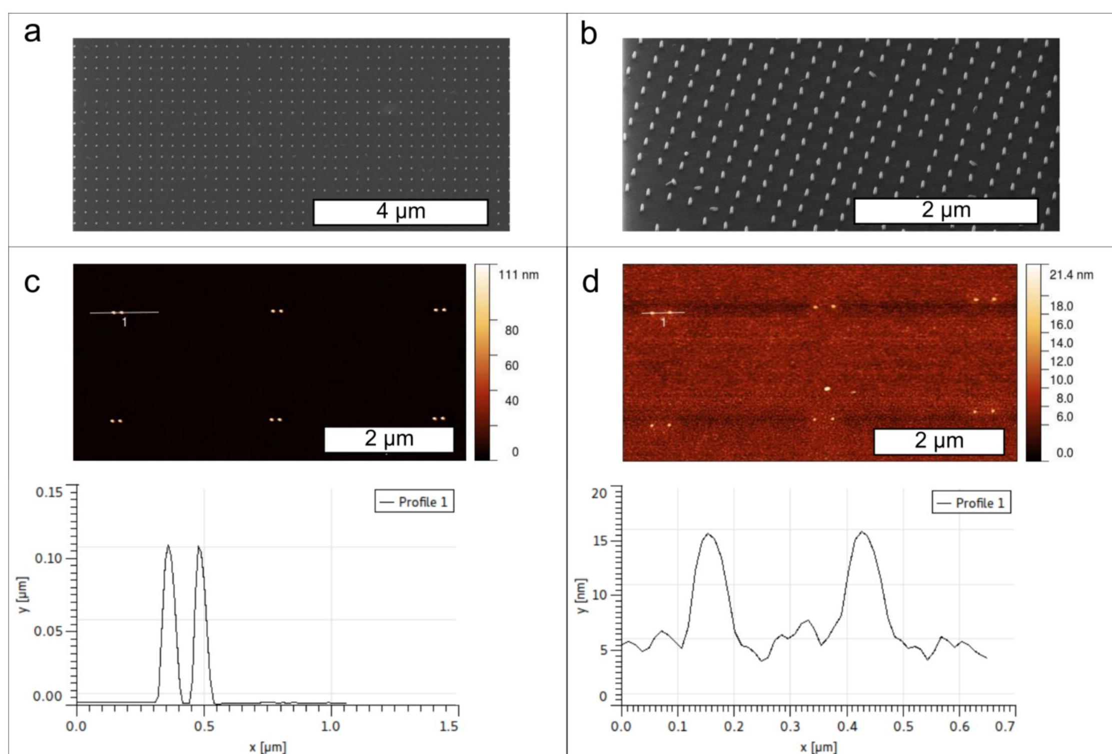

Figure 4.10: Scanning helium ion imaging of pillar arrays and etch profiling to confirm pillar clearance above the sacrificial PMMA film. a) Helium ion microscope image of 250-nm pitch, 35-nm diameter SiO_x fabricated by EBL on glass coverslip, b) Tilt Helium ion microscope 500-nm pitch, 35-nm diameter SiO_x fabricated by EBL on glass coverslip, c) AFM tapping mode height image. Glass coverslip with 2 feature clusters of 35-nm diameter SiO pillars fabricated on glass coverslip. Height profile below of line selection, and d) AFM tapping mode height image. Glass coverslip with 2-feature clusters of 35-nm diameter SiO_x pillars fabricated on glass coverslip after etching of sacrificial pmma layer with oxygen for 70 s. Height profile below.

Labelling for the HSQ based arrays was conducted in the same way as the positive tone scheme, with the exception that the sacrificial layer was present during labeling of the features. A clustered design was eschewed for a design utilizing regions of square feature placement rather than clustered features. Array performance again was checked first by utilizing FITC (Figure 4.5) and was labeled as described in the experimental methods. Figure 4.11 shows the results of the initial arrays produced by the negative tone patterning method. Figure 4.11, a and b, show the 500-nm pitch features. FFT was utilized to confirm that a periodic arrangement of fluorescent features was identifiable.

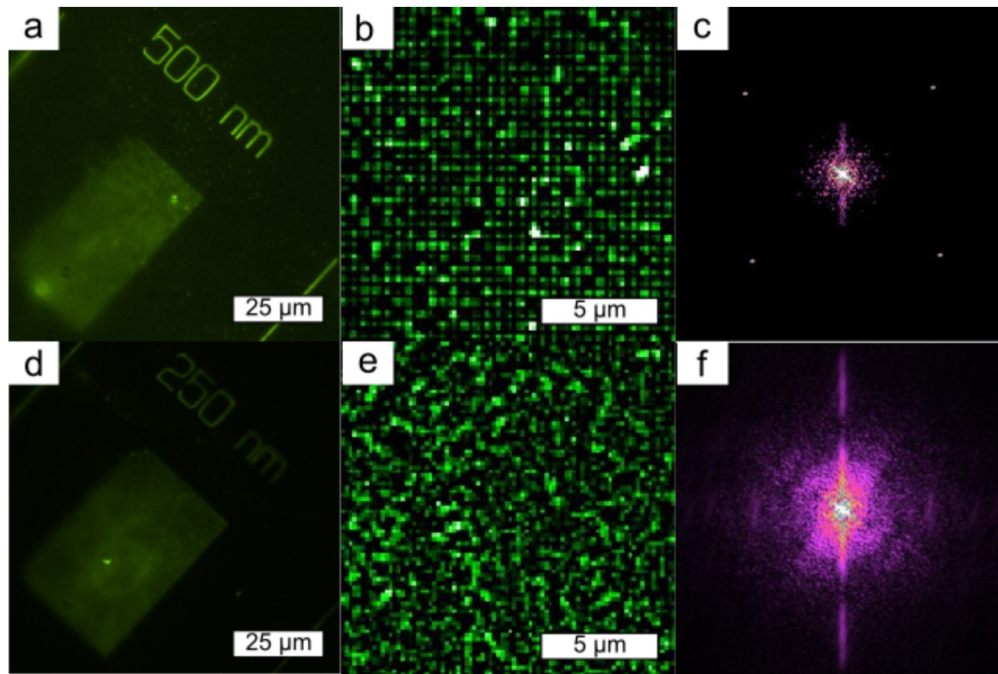

Figure 4.11: Total internal reflectance fluorescence images of APDIPES-SiO_x arrays labeled with FITC on No. 1.5 glass coverslip captured with 60X TIRF objective. a) Raw TIRF image with a 500-nm square array of features, b) Processed image after background subtraction of a, c) FFT of the 500-nm array, d) Raw TIRF image with 250-nm pitch features, e) Processed image after background subtraction of d, and f) FFT of the 250-nm pitch array.

Figure 4.11, b and e, indicate similar results to the positive tone work at 250 nm, the evidence that periodic structures exist is lost as there are no larger distance clusters to identify with FFT.

The next concern was whether features identified by fluorescence matched expected distances created by design for the negative tone scheme. Figure 4.12 shows the comparison of mean column intensities used to compare resolvable features between 500- and 250-nm features. With a 500-nm separation distance, features are located correctly by intensity and correlate with initial design dimensions after background subtraction. At a pitch of 250 nm, however, the visualization of the array and line profiling is not able to resolve features separated by this distance. Comparing the two fabrication processes, an important improvement is noted by utilizing the negative tone process in comparison with the positive tone process.

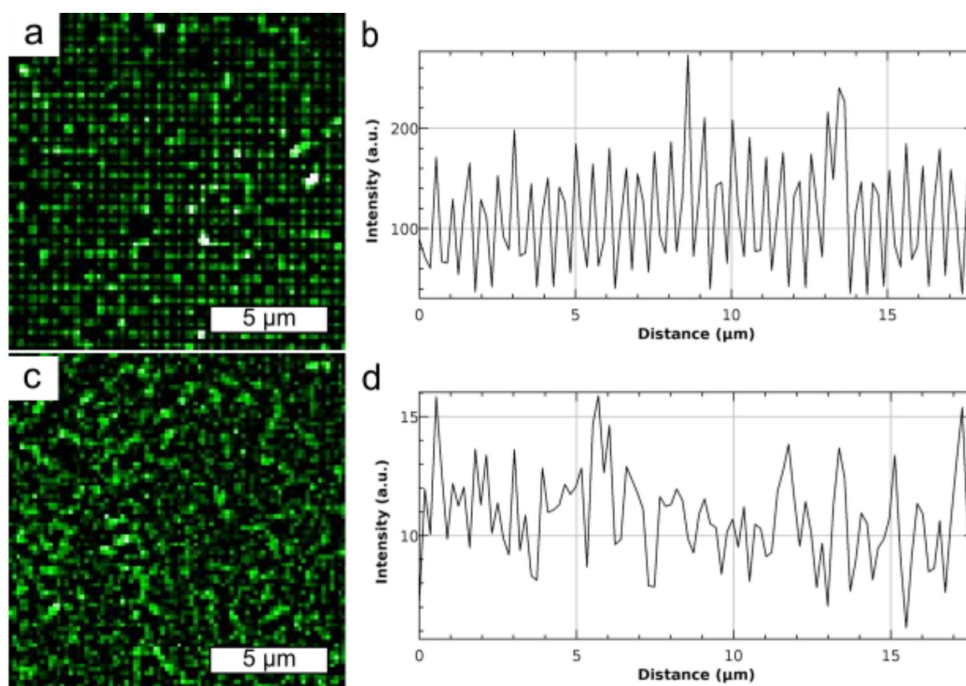

Figure 4.12: Total internal reflectance fluorescence images of APDIPES-SiO_x arrays labeled with FITC on No. 1.5 glass coverslip captured with 60X TIRF objective. a) Processed TIRF image of a 500-nm square array, b) Line profile plot of first 20-µm of array showing mean column intensity can separate features at 500 nm, c) Processed TIRF image of a 250-nm square array, and d) Line profile plot of the first 20 µm of a 250-nm square array showing intensity peaks cannot be used to separate 250-nm features.

Figure 4.13 reveals that for the positive tone arrays, the available signal relative to the detector range for the array is quite low and, from the histogram, it is not easily separated from the intensity due to background fluoresence. This issue has implications for later filtering steps, particularly in adjusting brightness and contrast and allowing the separation of features of interest using intensity based segmentation, or thresholding. Thresholding algorithms are a critical component of rapid identification of microarray features, thus, easily separated intensity populations reflect directly on the array's performance. Figure 4.13, c and d, of the SiO_x pillar array method, show a bimodal distribution of intensities. This separation of intensity populations makes automated segmentation an easier task and is promising for the methodology overall.

After verifying that the SiO_x pillar negative tone method was the best in terms of signal fidelity, I elected to test a different fluorophore that could be applied to localization-based microscopies.

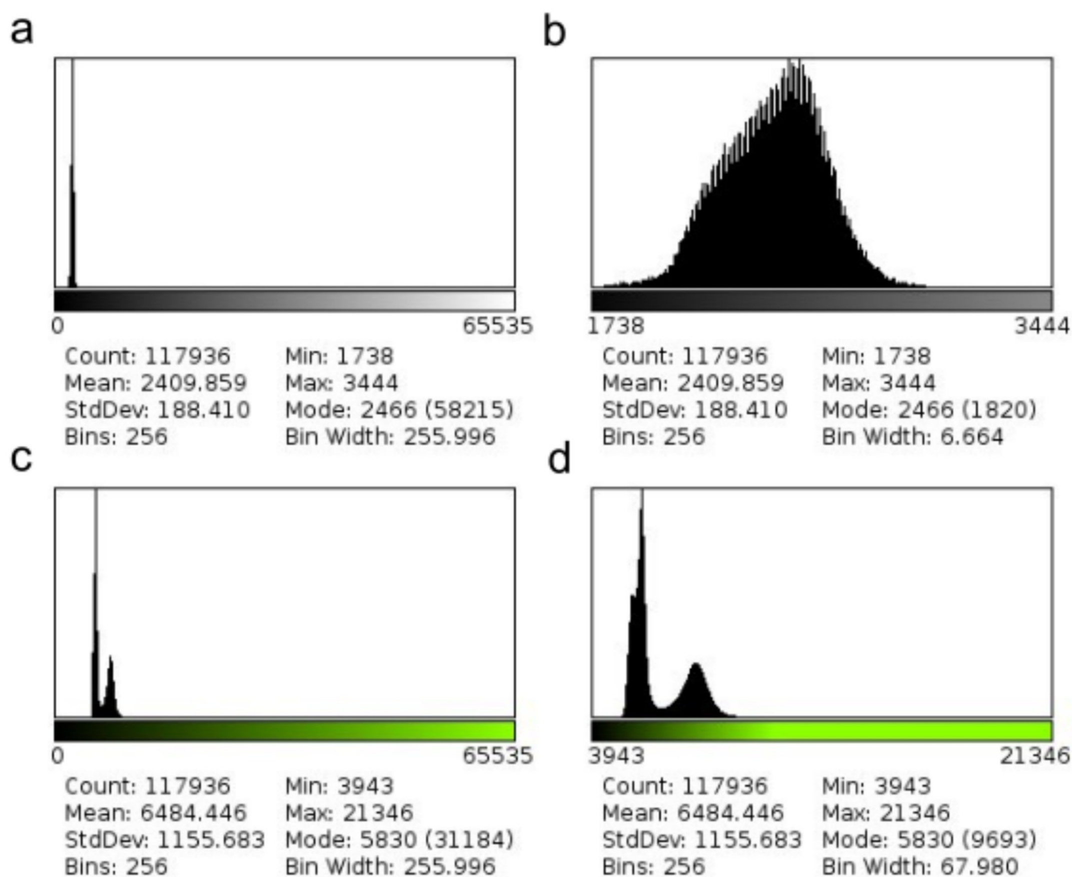

Figure 4.13: Comparison of signal: background separation and overall signal intensity between positive tone and negative tone fluorescent array methods using FITC. a) Histogram of a FITC 500-nm pitch array over the entire detector range, b) Range of signal including background for a FITC positive tone 500-nm array, c) Histogram of a FITC 500-nm pitch array over the entire detector range, and d) Range of signal and background exist as discrete intensity distributions for a HSQ negative tone array.

4.2.3 Cyanine Labeled Fluorescence Array

Localization microscopies can take advantage of a number of available fluorophores. One commonly used fluorophore is the cyanine-based dye, Cy5.[316] Cyanine dyes and their derivatives are of particular interest due to their cost effective application in super-resolution localization

microscopy.[317] These methods rely on the controlled blinking behavior of the dyes under certain buffer and excitation conditions. Cyanine dyes are available as a variety of small molecule conjugates, such as activated esters, maleimides, etc. A Cy5-NHS ester conjugate was utilized for labeling to primary amines on the array surface (Figure 4.5). The performance of Cy5 in TIRF was first evaluated. Figure 4.14 shows the initial results. Figure 4.14, a and b, indicate that the 500-nm square array was clearly defined, with FFT distinguishing the periodic nature of the array. Again, as with FITC, the 250-nm pitch is unable to be resolved.

As the 250-nm arrays are clearly non-distinguishable, line profiling was completed only for the 500-nm pitch array with Cy5 (Figure 4.15). Mean column intensities of the first 20 μm show that peak intensities correlate with expected feature distances for Cy5, with peaks every 500 nm. This correlation was seen method validation in a diffraction limited system and that it could be applied in an arrangement suitable for testing under super-resolution microscopy protocols. As the negative tone patterning scheme was shown to work with APDIPES, HSQ, and Cy5, an array was constructed that simultaneously could aid in identifying lateral resolution limitations in a diffraction limited system and an achievable feature resolution under STORM imaging conditions. The entire array is shown as a montage of individual sections in Figure 4.16. Each column heading consisted of a 500-nm wide linewidth text to delineate the distances between features. Under the column headings, three columns consisting of two features per column were utilized. The distance, centre-to-centre, between each cluster of two features is indicated by the column heading. For example, under the 200-nm heading, the first, leftmost column has clusters of two features which measure 200 nm apart, as does the second and third column.

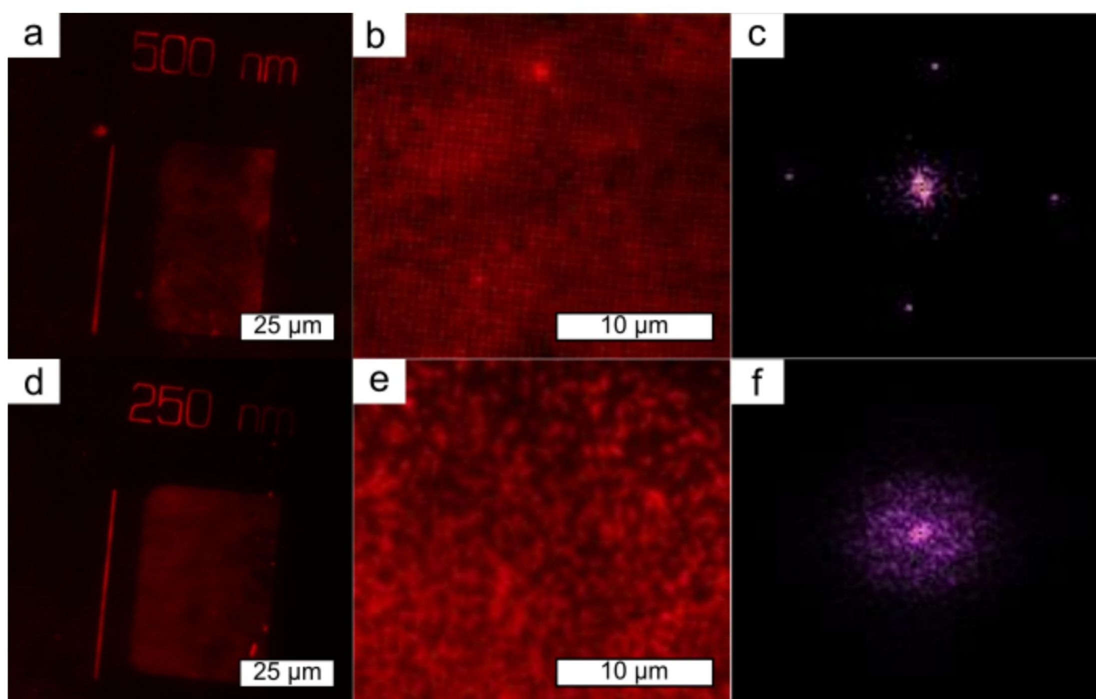

Figure 4.14: Total internal reflectance fluorescence images of APDIPES-SiO_x arrays labeled with Cy5 on a No. 1.5 glass coverslip captured with 60X TIRF objective. a) Raw TIRF image with a 500-nm square array of features, b) Processed image after background subtraction of a, c) FFT of a 500-nm array, d) Raw TIRF image with 250-nm pitch features, e) Processed image after background subtraction of d, and f) FFT of a 250-nm pitch array.

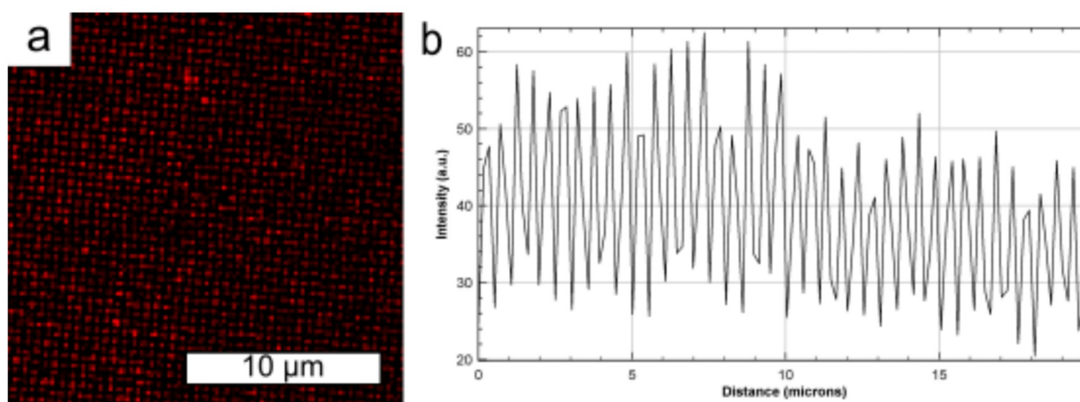

Figure 4.15: Total internal reflectance fluorescence image of APDIPES-SiO_x arrays labeled with Cy5 on a No. 1.5 glass coverslip captured with 60X TIRF objective. a) Processed TIRF image of a 500-nm square array, and b) Line profile plot of the first 20 μm of the array showing that the mean column intensity can separate features at 500 nm.

Unfortunately, evidence of fluorophore aggregation and surface fouling is noticeable on the overall array, with particularly large spots seen between the 100- and 125-nm section. After realizing background contamination was still a substantial issue, even with switching to a negative tone scheme, a surface passivation strategy for the background areas was investigated try to prevent nonspecific surface binding.

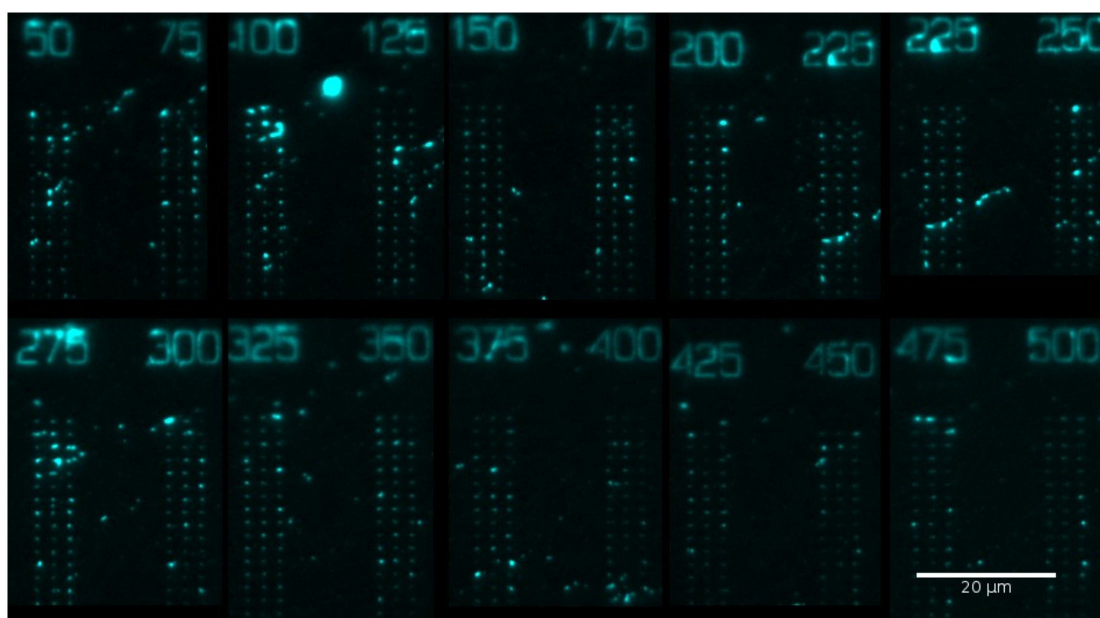

Figure 4.16: Raw montage of TIRF images captured with 60X TIRF objective. Glass coverslip with variable pitch SiO_x pillar arrays of APDIPES with Cy5. Each column's number heading indicates the separation distance, in nm, of the features inside each cluster. Each column consists of 3 clusters of variable distances, and each cluster is separated from the neighbouring cluster by 2 µm.

4.2.5 Evaluation of Surface Passivation

Quantifying the effectiveness of surface passivation strategies is challenging and has been done by simple counting of fluorescent spots per imaging area after surface treatment.[318–321] The well known passivation strategy of applying a monolayer of polyethylene glycol on the background surface areas was examined before attempting the use of two-sequence passivation strategies,

such as the previously mentioned DT20 surface.[320] Control surfaces of -NH_2-only (APDIPES), PEG-only, and bare glass were prepared. As background passivation would occur after features had been defined, a solution deposition protocol for mPEG-silane (5000 MW, Gelest) was used.[223] An overnight deposition of 0.1% volume in dry toluene on piranha cleaned, high tolerance coverslips produced uniform covered surfaces with water contact angles (sessile drop) of 34 ± 4° and RMS roughnesses measuring 0.5 nm over a 4-µm squared area. PEG surfaces were found to be conformal to the glass surface. Surfaces were passivated after EBL exposure and development of the HSQ arrays, immediately following activation by piranha cleaning and before coating with sacrificial PMMA.

After each unpatterned control surface was prepared, it was labeled using the scheme shown in Figure 4.5. Cy5 was aliquoted and diluted to concentrations ranging from 1 nM to 1 mM in 10-fold increments. A minimum of 10 random areas were selected for each area, and spots were segmented and quantified using the spot detector plugin in the standalone imaging software, Icy.[322] Integrated intensities were calculated for all spots and totaled for each surface. As shown in Figure 4.15, it was found that for concentrations of 1 mM and 100 µM of Cy5, PEG-only surfaces produced the fewest amount of random spots compared to bare glass and amine presenting surfaces (Figure 4.15). After 10 µM and further dilution, no improvement was seen for PEG surfaces over any of the remaining surfaces for the amine surface. No difference in total integrated spot intensity was seen for all concentrations on bare surfaces, as well as on PEG surfaces. This indicates that PEG was effective at higher labeling concentrations, but at lower concentrations background passivation appeared to have little impact on nonspecifically bound

fluorophores. A potential route to improve passivation capabilities at lower concentrations is suggested in the following section.

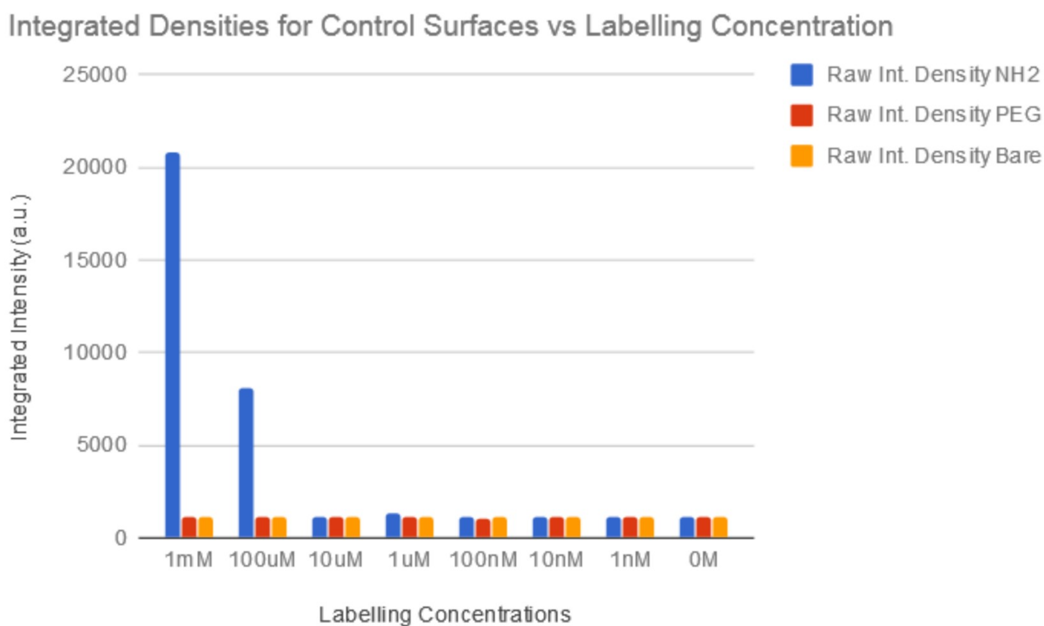

Figure 4.17: Total integrated intensities for spots on each control surface at given Cy5 labeling concentrations. Control surfaces were homogeneous surfaces of NH_2 (APDIPES), mPEG-silane, and bare glass.

4.2.6 Super-Resolution Microscopy Requires Effective Background Fluorescence Reduction

STORM imaging was attempted on the negative tone array. Figure 4.16, a and b, show the raw TIRF images of the respective section before adding STORM imaging buffer to the surface. Figure 4.16, c and d, are the corresponding reconstructed areas of the raw images. With 350- and 375-nm centre-to-centre pitches, sets of two individual fluorescent spots are rarely seen after reconstruction. Figure 4.16 c shows possible reconstructed 2-feature spots, with 6 out of 15 clusters shown. In addition, background spots are obvious in Figure 4.16 c, despite the

application of PEG background passivation strategies. Resolution tests below 350 nm all localized as one discrete feature, with a 0% yield of successfully separated features. Tests at 475 and 500 nm in Figure 4.16, g and h, show 15 of 18 feature clusters with discretely localized features; however, spots are uneven in intensities.

Unevenness in labeling may be one reason for the poor yield in reconstructed spots. For surface arrays of these dimensions, higher concentrations of label generally are required,[157,323] which places more stress on an effective background passivation. The uneven labeling density also has the possibility of overlapping emitters. With super-resolution localization, effectiveness of the reconstruction relies on non-overlapping emitters; if they do overlap, they must both be in an off state, or one can be in an on state. If both emitters are in an on state within a frame capture for reconstruction, the software will interpret this emitter as a single spot, and the PSF will be localized to the centre. Some software, such as Bayesian blinking analysis (3B) is able to deal with overlapping emitters.[324] However, applying this analysis over large areas is computationally expensive and may require access to supercomputing clusters for practical application.[325]

Overlapping emitters is an issue for this work; there are likely several vertically stacked emitters up the sides of the SiO_x pillars, as well as within the area on top of the post. The most substantial problem for the fabrication of these arrays is nonspecific background. Preventing nonspecific adsorption of fluorescent probe molecules is becoming increasingly important, particularly in the context of single molecule studies.[157,320,326]

Nonspecifically bound flurophores can cause the appearance of artifacts during analysis. As fluorescent assay development marches inexorably towards single-molecule imaging,[157,327–331]

it becomes critical to consider the interactions between the dye-conjugate and the underlying surface.[332]

There is a large parameter space for determining why nonspecific binding was such an issue for these array fabrication schemes. It has been shown that the characteristics of the fluorochrome can impact the cell labeling behavior of a dye-conjugate.[333–335] Clarke *et al*. reported that the non-specific binding of fluorescent probes to a glass surface depends primarily on the dye and less on the protein to which it is bound.[318] Dye chemistry has a strong influence on dye-protein conjugates interacting with surfaces nonspecifically.[318,336] Work has been done emphasizing the choice of probe–surface interactions over spectral characteristics.[337] Daniels made the case for using anionic fluorescent probes when examining dye–glass surface interactions due to electrostatic interactions.[337]

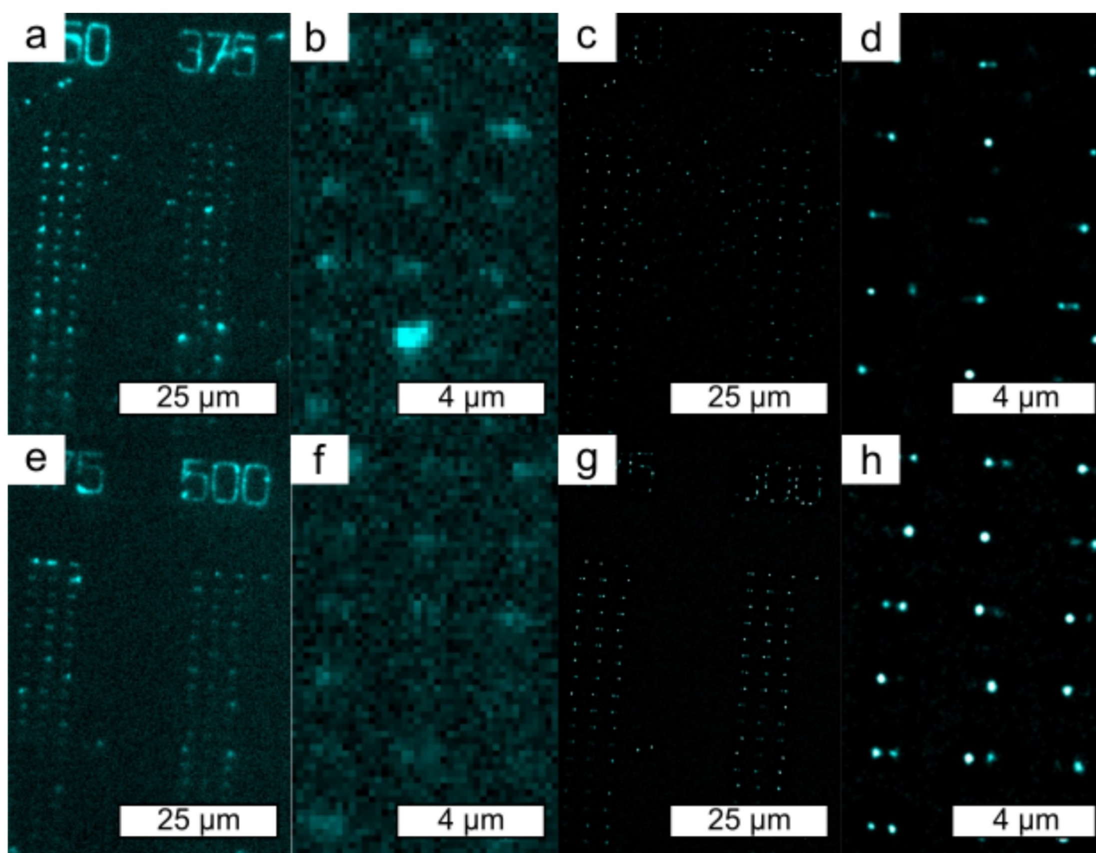

Figure 4.18: Raw and reconstructed images of SiO_x pillar arrays of 350-, 375-, 475-, and 500-nm pitches functionalized using APDIPES with Cy5. Reconstruction used the Localizer stand-alone processing tool, a) Raw fluorescent image of 350- and 375-nm array columns, b) Closeup of section of a 375-nm column, c) Reconstructed image of 350- and 275-nm array columns, d) Closeup of reconstruction of a 375-nm array section, e) Raw fluorescent image of 475- and 500-nm array columns, f) Closeup of section of a 500-nm array column, g) Reconstructed image of 475- and 500-nm array columns, and h) Closeup of a reconstructed 500-nm array column.

A PEG passivation strategy for STORM imaging was attempted. This approach, however, proved to be unsuccessful as reconstruction attempts and even raw imaging revealed the presence of non-specifically bound fluorophores. By and large, the most prominent method of surface passivation is PEG, or polyethylene glycol coating. Other methods rely on self-assembled coating of common surfactants. Recent work has indicated that Tween-20 is effective at preventing nonspecific adsorption,[320] shown below in Figure 4.17 b. The surfactant is self-assembled on a hydrophobic silane monolayer, such as dichlorodimethylsilane (DDS), which

produces a methyl-terminated surface. Alternative surfactants, such as F-127, also have been utilized this way.[338] There also has been analysis of the effectiveness of PEG monolayers on glass surfaces in the context of nanoarrays (Figure 4.17 a). The authors found that glass surfaces, due to impurities during glass formation, are likely to result in formation of patches of PEG. They found that planarization of the surface by spin-coating with HSQ, followed by thermal curing of the HSQ, can help to improve uniformity of surface-presenting silanols, and thus increase passivation effectiveness.

It is important to note that while the super-resolution results for this work were partly successful, the diffraction limited system results were successful. Without the application of super-resolution techniques, 500-nm centre-to-centre distances are distinguished easily with accessible, open access techniques. Sparse arrays with feature pitches of 1 µm have enabled high throughput analysis with much less stringent fluorescent imaging requirements.[323]

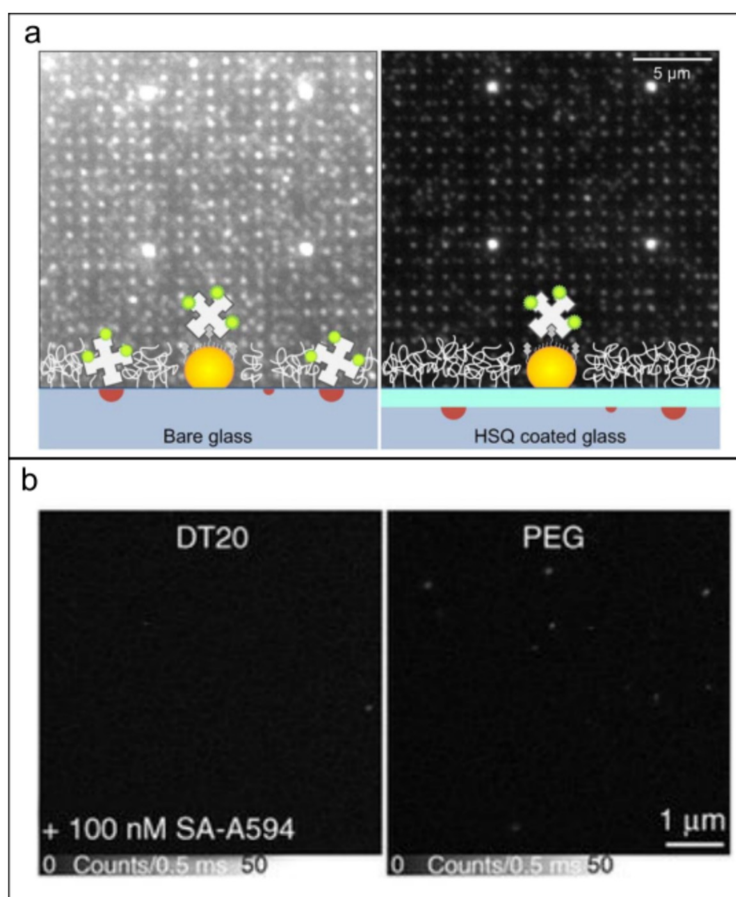

Figure 4.19: Example of current fluorescent nanoarray background prevention strategies. a) High density fluorescent nanoarray utilizing polyethylene glycol (PEG) as a background passivation scheme. Left image is PEG, right image is PEG after coating the native glass with hydrogen silesquioxane (HSQ). Reprinted with permission from Wind *et al.*[157], and b) Alternative passivation scheme as tested on unpatterned glass using dichlorodimethylsilane (DDS) and Tween-20 treatment compared to PEG conjugated directly to a glass surface. Reprinted with permission from Hua *et al.* 2014. [320]

4.3 Summary

In this chapter the fabrication of fluorescent nanoarrays utilizing both positive and negative tone patterning schemes has been shown. It was found that producing negative tone patterns with a sacrificial layer can aid in improving signal:background levels, while enabling axial confinement of vapor deposited aminosilanes. Line profiles and FFT analysis confirms that 500-nm centre-to-

centre dimensions are readily achievable with this technique, and that, after resolving nonspecific background labeling, this technique likely could be pushed further towards rapidly identifying the limits of a fluorescence microscope. It is likely that the majority of the background produced in these experiments was caused by aminosilanes which permeated the protective resist layer during the labeling stage as is described in chapter 2. In addition, substantial residual resist is left by PMMA with solution removal, especially without the application of sonication. It is possible that noncovalent interactions took place between residual resist and the dyes in question. With proper application of background passivation and prevention of silane permeation, this technique may expand into super-resolution work, as will be discussed in the outlook section of chapter 5.

4.4 Experimental

4.4.1 Surface and Sample Preparation

High tolerance glass coverslips No 1.5 were used as patterning and imaging surfaces for all fluorescent experiments. Chips were bulk cleaned by successive sonication for 5 min in methylene chloride, milliQ water, and isopropyl alcohol and blow dried with a gentle nitrogen stream.[339] Next, samples were piranha cleaned in a class 10 cleanroom for 15 min and blow dried with N_2. Samples were piranha cleaned immediately prior to coating for lithography steps and were dried individually, edge-on, to avoid breakage.

4.4.2 AFM Imaging

All trench and feature height profiles were acquired using tapping mode atomic force microscopy (AFM) with a Digital Instruments/Veeco multimode atomic force microscope. Collected data were analyzed using the open source software Gwyddion.[229]

4.4.3 Vapor-Phase Deposition Verification

The vapor-phase deposition protocol utilized was identical to that in Chapter 2 with deposition times of 18 h. As glass surfaces were utilized for this work, high tolerance coverslips were cleaned with piranha and checked in AFM and by water contact angle. Contact angle measurements (FTA-200) were completed for homogeneous monolayers using a sessile drop method with milli-Q water to confirm deposition. Roughness measurements were calculated over 2 μm x 2 μm areas via afm measurements in Gwyddion. For axial confined monolayers on SiO_x pillars, pillar surfaces were fabricated on Si and exposed to mercaptosilane vapor to produce free thiols on top of pillars. This allowed for immersion in colloidal gold solution and then SEM to visualize bound particles confined to the surface.

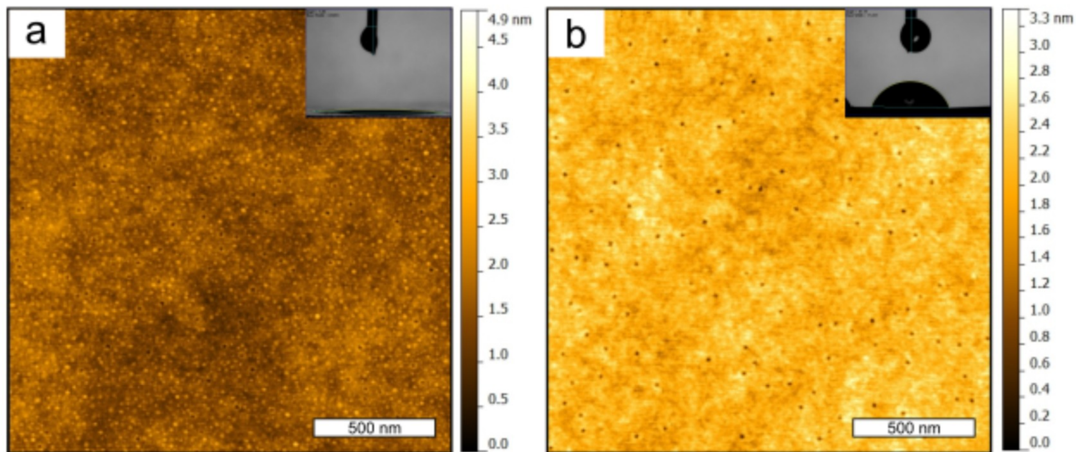

Figure 4.20: Vapor deposition confirmation on homogeneous surfaces, glass coverslips. a) AFM tapping mode height image. Glass coverslip No. 1.5 after 15-min piranha, area RMS roughness: 0.3 nm. Inset is snapshot of a water sessile contact angle < 5 °, and b) AFM tapping mode height image. Glass coverslip after 18 h APTMS deposition with area RMS roughness: 0.3 nm. Inset is snapshot of a water sessile contact angle measured to be 67 °.

4.4.4 Mask Fabrication

All mask preparation and cleaning was completed in a class 10 cleanroom in the user cleanroom facility in the nanoFab at the University of Alberta. For negative tone patterning, HSQ (Dow Corning) 6% in 4-methyl-2-pentanone (MIBK) was spin coated at 4000 rpm for 40 s (Brewer Cee Spinner) to a thickness of 100 nm. Next, samples were baked at 90 °C on a carrier wafer for 4 min in atmosphere. With glass surfaces, an anti-charging scheme was employed by spin coating 70 nm of AquaSave as an anti-charge layer.[340] AquaSave coated samples were baked for 2 min at 90 °C. All electron beam lithography was completed on a Raith 150-Two 30 keV system. Circular surfaces were aligned to the leftmost edge of the full diameter of the chip (15 mm). For optical pattern location, visual alignment marks surrounding the dot or pillar pattern, a minimum of 2 µm wide, were created at an accelerating voltage of 30 keV with a 60-µm aperture, with an area exposure dose of 2000 uc/cm^2 (Figure 4.19).

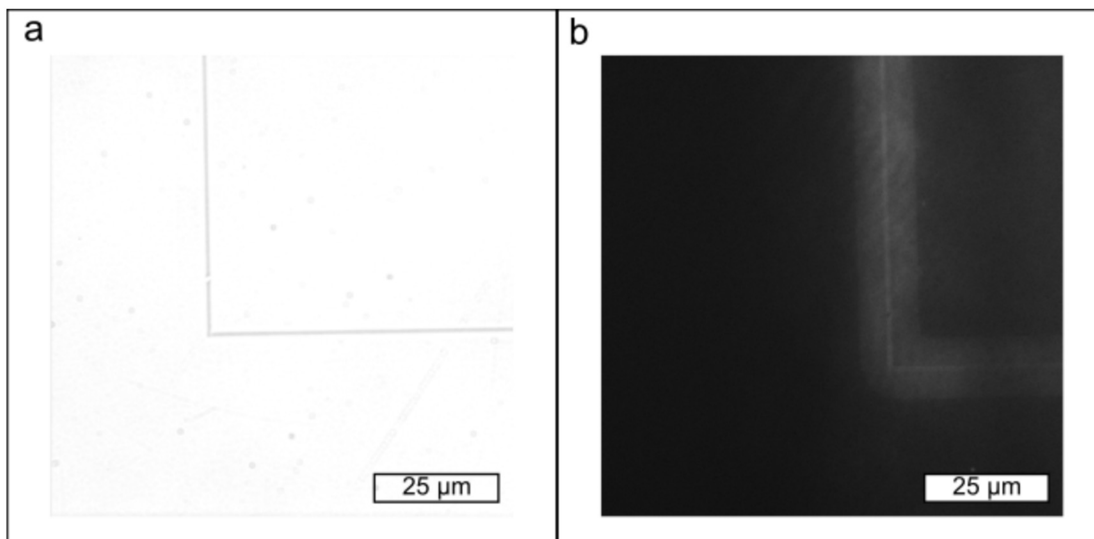

Figure 4.21: Brightfield and fluorescent images of lower left section of pattern locator outline used in the majority of fluorescent patterns made with HSQ. a) Brightfield, 60X magnification image of outline, utilized to locate pattern quickly, and b) Fluorescent image of pattern outline.

Array pillar features were fabricated using single pixel dot-shot features created with an accelerating voltage of 30 keV and a 10-µm aperture at 40–80 fC/dot. AquaSave was removed by dipping in H_2O for 3 s prior to immediately immersing it in the developer. HSQ development was done with a salty developer (1 wt% NaOH, 4 wt% NaCl, in H_2O) for 50 s and rinsed under flowing H_2O. surfaces were blow dried in a nitrogen stream.

Pillars were prepared for silane labeling by first spin-coating the SiO_x pillar surface with a sacrificial layer of PMMA (950k) in anisole at a speed of 4000 rpm for 45 s. After baking at 180 °C for 10 s, the sacrificial layer was etched as needed by RIE Oxygen Plasma (Trion) at 40 W and 50 sccm of oxygen, which also served to hydroxylate the SiO_x pillars. AFM was used to confirm the exposure of SiO_x pillars above the sacrificial layer for all samples prior to vapor deposition.

Positive tone patterning was completed as in prior chapters, utilizing PMMA (950k) as the primary resist for all work in this chapter. Single pixel dot shot features were used for defining deposition features. Pitches for dots were varied according to the array distances being tested. Patterned surfaces were stored in a class 10 cleanroom (40% relative humidity).

Following exposure, ZEP520A was developed in ZEDN50 (Zenon) developer for 4 min, followed by rinsing in IPA for 30 s. Samples were blow dried with a stream of N_2. Patterned surfaces were stored in a class 10 cleanroom (40% relative humidity).

4.4.5 Vapor-Phase Deposition

The vapor-phase deposition protocol utilized was identical to that in Chapter 2, using both APTMS and APDIPES. Deposition times were 18 h, unless otherwise stated. Both positive tone and negative tone arrays utilized the same deposition protocol. Negative tone patterns were functionalized after etchback and AFM confirmation, while positive tone patterns were functionalized after descum etching (RIE, Trion) for 30 s at a power of 40 W, 200 mTorr chamber pressure, and 50 SCCM oxygen flow.

4.4.6 Fluorescent Imaging and Mounting

Fluorescence labelling with FITC (Sigma) was completed by preparing a 1 mg/mL stock solution in 200-µL aliquots. Stock aliquots were frozen at -20 °C until use. The stock was diluted to 2.57 µM in pH 9.0 carbonate buffer before labelling. Labelling was completed by immersing the patterned surface in a vial with the labelling solution in the dark at room temperature for 4 h.

After labelling, surfaces were washed twice in 1% Tween-20 for 10 min, H_2O, and subsequently dried in a nitrogen stream before mounting as shown in Figure 4.21.

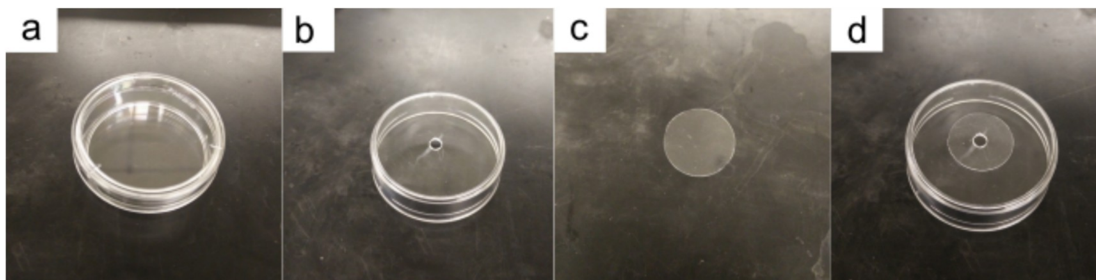

Figure 4.22 General process of mounting fabricated nanoarrays for imaging. a) Clean culture dish, b) Remove lid, flip dish, and drill a ⅜” hole through bottom. Clean excess material and sonicate in water, c) Obtain and orient the chip which was fabricated on a No 1.5 high tolerance glass coverslip, and d) Place the coverslip on the bottom of the dish, seal with aquarium glue or VaLaP type wax sealant. Let dry and flip over for imaging in standard culture dish mounts. Ensure adequate volume of imaging solution (~ 3 mL)

Cy5 labelling was completed by first aliquoting Cy5-NHS ester (Lumiprobe) in dry DMSO to a concentration of 1 mg / mL. Aliquots were frozen at -20 °C until use. The stock solution was diluted as required for labelling. Cy5 labelling was completed at 1.62 µM. An inverted Nikon Eclipse Ti microscope was utilized for all imaging, unless otherwise noted. Filter sets used for imaging were 483–493 nm (excitation), 500–550 nm (emission), and 488 nm (dichroic) for the green channel; 538–548 nm (excitation), 563–637 nm (emission), and 543 nm (dichroic) for the red channel. TIRF imaging was completed using an oil-immersion Apo TIRF 60X objective (NA 1.49) (Nikon) and 1.5x tube lenses multiplier. STORM imaging was attempted utilizing a GLOX based imaging buffer. GLOX buffer consisted of 0.5 mg/mL glucose oxidase, 40 µg/mL catalase, and 10% wt/vol glucose. Imaging buffer consisted of 50 mM TRIS, 10 mM NaCl, 10% wt/vol glucose. The final STORM buffer contained 30 µL GLOX and 200 mM of 2-mercaptoethanol (41.94 µL), made up to 3 mL with imaging buffer. STORM buffer was added to

confocal dishes in volumes of 3 mL and were made immediately before use. Samples were located dry (no buffer) in DIC before adding imaging buffer.

4.4.7 Image Reconstruction

Image reconstruction was attempted utilizing the localizer tool in Igor (32 bit) pro.[341] Images were analyzed as multi-file .TIFF series, using a 3x3 media pre-processing filter, GLRT segmentation, and MLEwG localization algorithm. A minimum of 2000 images was utilized for STORM imaging attempts.[342]

5

Thesis Summary and Outlook

5.1 Summary of Chapters

The overall thesis statement was supported by the work described in experimental chapters 2-4. Electron beam lithography is an effective means to develop methods for patterning organosilanes on silicon and silica surfaces with arbitrary geometries and high resolution. Electron-beam lithography can be used in conjunction with vapor-phase deposition of organosilanes to create high-fidelity nano-patterned surfaces of self-assembled monolayers organosilanes on oxide-capped silicon and silica surfaces for diverse application. This section summarizes the chapters and how each chapter's results supports the use of EBL to pattern SAMs by using vapor-phase deposition.

5.1.1 Chapter 1

In Chapter 1, the concept of lithography and top-down versus bottom-up fabrication schemes was introduced. With this came the introduction of self-assembled monolayers and the pioneering work with silanes and organosilanes. The reactions and conditions which govern the coupling of silanes to various surfaces was reviewed. The methods of deposition of organosilanes was discussed, comparing solution deposition to vapor deposition. Current methods of patterning organosilanes were reviewed over a wide range of techniques. Lastly, electron beam lithography and its working principles were examined. The chapter concluded with a discussion of electron beam lithography for patterning self assembled monolayers, with attention to vapor-phase deposition through fabricated templates.

5.1.2 Chapter 2

Chapter 2 supported the thesis statement by demonstrating that EBL-guided vapor-phase could be used to pattern self-assembled monolayers of aminoalkoxysilanes. In addition chapter 2 tested whether resist choice would impact nonspecific deposition of aminoalkoxysilanes. The importance of resist and organosilane choice was stressed by reporting on the patterning of aminosilanes through EBL resists. Three electron beam lithography resists were used, PMMA(950k), PMMA(495k), and ZEP520(57k). After patterning these resists in EBL, a vapor deposition protocol was introduced, allowing deposition of 3-aminopropyltrimethoxysilane (APTMS) and 3-aminopropyldiisopropylethoxysilane (APDIPES) through the patterned masks onto the exposed silicon native oxide surface. After deposition and template removal, the surfaces were immersed in a gold nanoparticle solution for electrostatic self-assembly. It was

found that substantial non-specific binding occurred for both PMMA resists, while ZEP520 resulted in nearly 0% nonspecifically bound particles. Various control surfaces were prepared for each aminosilane and resist combination and subjected to nanoparticle deposition and surface energy analysis. It was found that each resist leaves a residual on the silicon surface, and that the residual alone is not sufficient for nanoparticle deposition. However, unpatterned PMMA surfaces exposed to vapor deposition were able to bind particles in high quantities, especially for APTMS. This indicated that silanes likely had penetrated the film during deposition, leading to unwanted background deposition. Surface energy analysis was completed to determine the interfacial energy components of the various surfaces at work. It showed that ZEP520 residual on silicon is a highly electron donating surface in comparison to PMMA, possibly indicating more efficient removal. Coupled with analysis by XPS, this also indicated that while nonspecific aminosilane deposition certainly takes place, the aminosilane penetrants may not exists on the surface as a covalently bound contaminant. Ultimately, a ZEP520(57k) and APDIPES deposition produced excellent pattern selectivity for electrostatic self-assembly of gold nanoparticles and, in some cases, resulted in the patterning of single nanoparticles.

5.1.3 Chapter 3

Chapter 3 supported the thesis statement by sowing that EBL-guided vapor-deposition could be used to pattern aminoalkoxysilanes and that by varying deposition conditions, condensation structures of APTMS could be formed with limited morphological control. Condensation structures were created with the deposition protocol, and it was revealed that tighter control and further characterization is required to fully integrate these structures into existing methods of

semiconductor feature multiplication strategies. Chapter 3 explored the promising condensation structures produced by vapor deposition of APTMS through ZEP masks with a perspective for use as spacers in density doubling applications for the semiconductor industry. With the standard deposition method described in Chapter 2, it was found that when APTMS is deposited through ZEP masks, it left both ring-shaped and line-shaped condensation structures, which conformally coat the inside of the template mask. Extensive SEM imaging was completed for these structures as well as AFM to determine that their peak heights are on the order of 150 nm, with line widths of 50 nm and hole spacers with diameters of 81 nm. The hole structures, functioning as spacers, were shown to have complete clearance to the surface; this indicates a high probability of success for a chemical shrink-type process. A potential hole shrinkage of 37 to 48% was found for APTMS in ZEP. The line structures proved difficult to characterize, however a deposition curve was determined. It was found that deposition of these structures occurs in less than 2 h for maximal height features at 80 °C. However, AFM only revealed small trenches in the line shaped structures. It may be that current conditions are causing complete line fill-up with APTMS structures or that characterization methods were insufficient to determine the actual cross-sectional morphology of these structures. Current investigations into the line structures are ongoing as promising oxide etching appears to show the development of a trench-like profile in SEM tilt imaging. HiM imaging and Ga-FIB, as discussed in this chapter helped to determine the likely morphology of the line structures; however, TEM analysis would be the ideal choice for future characterization.

5.1.4 Chapter 4

Chapter 4 supported the thesis statement and demonstrated that the vapor-deposition of aminosilanes through EBL-patterned masks could be used to create a fluorescent nanoarray. Additionally it was shown that positive- and negative-tone strategies influence the labeling performance and nonspecific background of the arrays. In Chapter 4, I discussed the fabrication of a nanoscale fluorescent array, which was the initial device goal for the thesis. As described, two fabrication processes were used, based on positive tone and negative tone strategies. Positive tone work was completed with 500-nm centre-to-centre spacing, patterning APTMS and APDIPES for conjugation with the fluorophore FITC through PMMA(950k). It was shown that single features could be resolved at this resolution, while 250-nm features could not. A novel method was developed utilizing a negative tone resist, HSQ. Pillars of SiO_x 110 nm tall and 35 nm in diameter were coated with a sacrificial PMMA layer to etch back and expose the tops of the pillars for vapor phase functionalization. Potentially, the strategy is very useful for axial confinement of self-assembled monolayers. However, as was shown in Chapter 2, PMMA is subject to silane permeation, and the strategy would benefit from alternative sacrificial layers being examined. Nevertheless, it was shown that Cy5 could be patterned effectively with a 500-nm pitch using the negative tone scheme and that a bimodal distribution of intensities existed when utilizing this route, making the scheme promising for automatic thresholding in an array analysis context. Super-resolution imaging was attempted, but substantial non-specifically bound fluorophores hampered image reconstruction. Ultimately, this search into the cause of background functionalization lead to the discovery of effective colloid patterning in Chapter 2, as well as the discovery of the silane spacer structures in Chapter 3. The array methodology is

exciting for epifluorescence/TIRF approaches. Improvements to remove background and increase labelling efficiency were discussed in this Chapter.

5.2 Process Development for Future Research Optimization

5.2.1 DLVO/XDLVO for Particle Immobilization

The patterning of gold nanoparticles demonstrated in Chapter 2 is attractive in methodology, and the role of resists/organosilanes interactions is clear. However, this type of work would benefit substantially from in depth analysis, particularly making use of Derjaguin, Landau, Verwey, and Overbeek (DLVO), and extended DLVO.[343–345] Shown in Figure 5.1 is an example of an extended DLVO plot, or energy balance diagram, as depicted in Carel van Oss's *Interfacial Forces in Aqueous Media*.[344] Such a diagram is an excellent way to depict the summation of electrostatic, Lifshitz–van der Waals, and acid-base components, demonstrating the effect that each of these components has on the system. Typically, these plots are useful to describe colloidal stability, however, it is possible to utilize DLVO with a sphere and flat plate model.[346] With the surface energy work in Chapter 2, the effect of the apolar AB component also could be demonstrated, similarly to the way the addition of an acid-base component to the system can move a colloid interaction from an unstable (Figure 5.1 b) to a stable system (Figure 5.1 d) by overpowering the electrostatic interaction at close distances to remove the primary minimum for interaction.

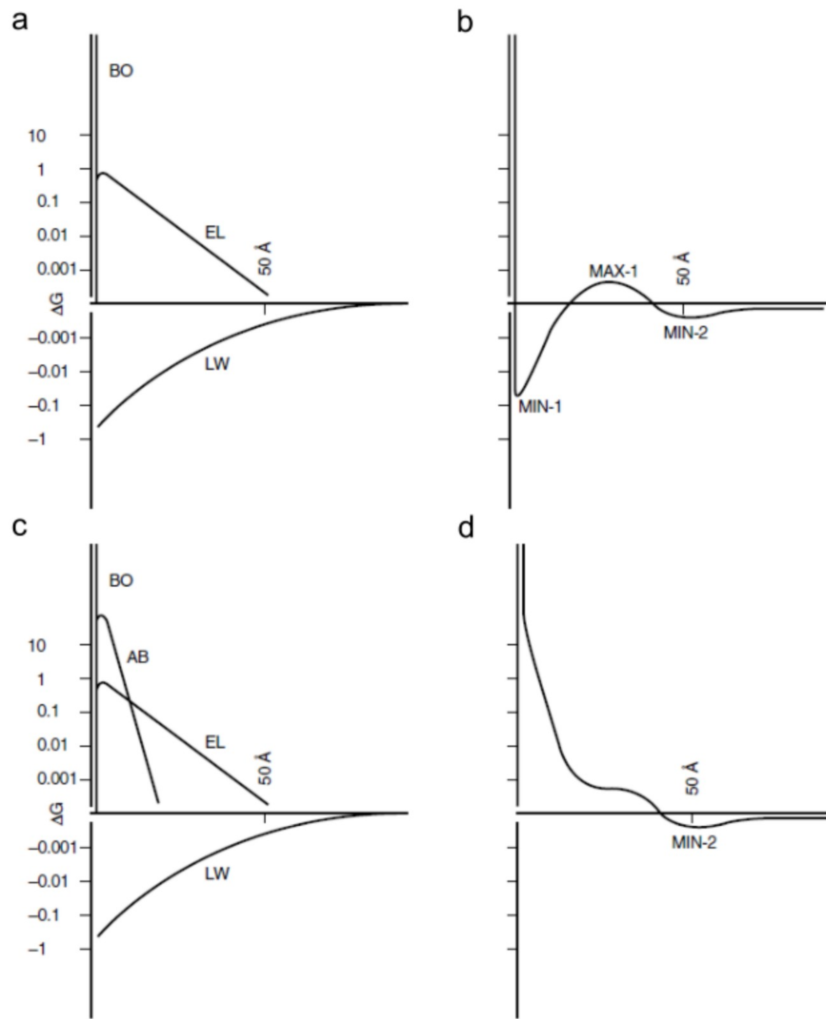

Figure 5.1: Energy balance diagrams ΔG vs *l* of erythrocyte suspensions, on a logarithmic scale in mJ/m^2. a) Electrostatic (EL) and Lifshitz–van der Waals (LW) interactions, combined in b) The classical DLVO plot with the primary minimum of attraction (MIN-1), the secondary maximum of repulsion (MAX-1), and the secondary minimum of attraction (MIN-2), c) The AB interaction (repulsion) in addition to the EL repulsion, yielding in d) The combined curve that depicts the total interaction more realistically than the DLVO plot. The most important aspect of the complete curve shown in d is the absence of a primary minimum of attraction (still visible in b), owing to the AB-repulsion, which gives rise to superstability in vivo. Figure and caption reprinted with permission from reference [344]. Copyright © 2006 by Taylor & Francis Group, LLC.

In Chapter 2, the surface measurements taken utilizing various liquids yielded the individual acid-base and LW components in mJ/m^2 for the surfaces in question according to the Young-Dupre equation:

(2.1) $$(1+\cos\theta)\gamma_L^{tot} = 2\left(\sqrt{\gamma_S^{LW}\gamma_L^{LW}} + \sqrt{\gamma_S^{+}\gamma_L^{-}} + \sqrt{\gamma_S^{-}\gamma_L^{+}}\right)$$

and the free energy balance for the surface can be summarized as:

(5.1) $$\Delta G = \Delta G^{LW} + \Delta G^{AB} + \Delta G^{EDL}$$

From equation 5.1, both ΔG^{LW} and ΔG^{AB} can be plotted as a function of surface/particle distance. ΔG^{LW} can be determined by computing the Hamaker Constant, *A,* utilizing the data from surface energy analysis, as described in Chapter 2. The unretarded Lifshitz–van der Waals energy of interaction for a sphere of radius *R* and a semi-infinite flat plate at distance *l* is:

(5.2) $$\Delta G^{LW} = \frac{-AR}{6l}$$

The Hamaker Constant, *A*, can be determined from the surface energy measurements of the apolar interfacial tensions components by:

(5.3) $A = 24\pi l_o^2 \gamma^{LW}$; where $l_o = 1.57 \pm 0.09$ Å.

Then, the interfacial contribution from the polar surface tensions components can be computed as:

(5.4) $$\Delta G_{SL}^{AB} = -2\sqrt{\gamma_S^{+}\gamma_L^{-}} - 2\sqrt{\gamma_S^{-}\gamma_L^{+}}$$

leaving only the electrostatic double layer component, ΔG^{EDL} remaining. ΔG^{EDL} for a sphere of radius *R* and a flat plate is expressed as:

(5.5) $$\Delta G^{EDL} = R\sqrt{\psi_p\psi_s}\,\varepsilon ln(1+e^{(-\kappa l)})$$

where ψ_p and ψ_s are the surface potentials for both the plate and sphere, respectively. Future work requires more experimental determinations, which are achievable. The gold nanoparticle is readily analyzed by dynamic light scattering instruments, and the surface potential of the plate, or zeta potential of the sphere, can be determined a number of ways, such as the streaming potential measurement in an electrokinetic analyzer. This instrument requires a 4.0-cm minimum span to fit the probe mounting plates, therefore, the processes utilizing this tool would have to use larger surfaces, ideally 7.0 cm long by 3.0 cm wide.

There are relatively few examples where DLVO theory has been utilized to describe gold nanoparticle interactions with *patterned* aminosilanes on a surface and their assembly. A particularly nice example is given in the work by Ma *et al.*,[199] who utilized DLVO to help characterize their electrostatic funneling system, which was used to place single nanoparticles at wafer scale (Figure 5.2). This work was important in demonstrating that larger scale (~100 nm) guiding templates can be used to funnel smaller molecules by engineering the electrostatic gradient the particles experience in solution as they approach the surface. The patterning in Chapter 2 could be extended to a larger scale by using DLVO to help predict assembly and guide the design of future processes.

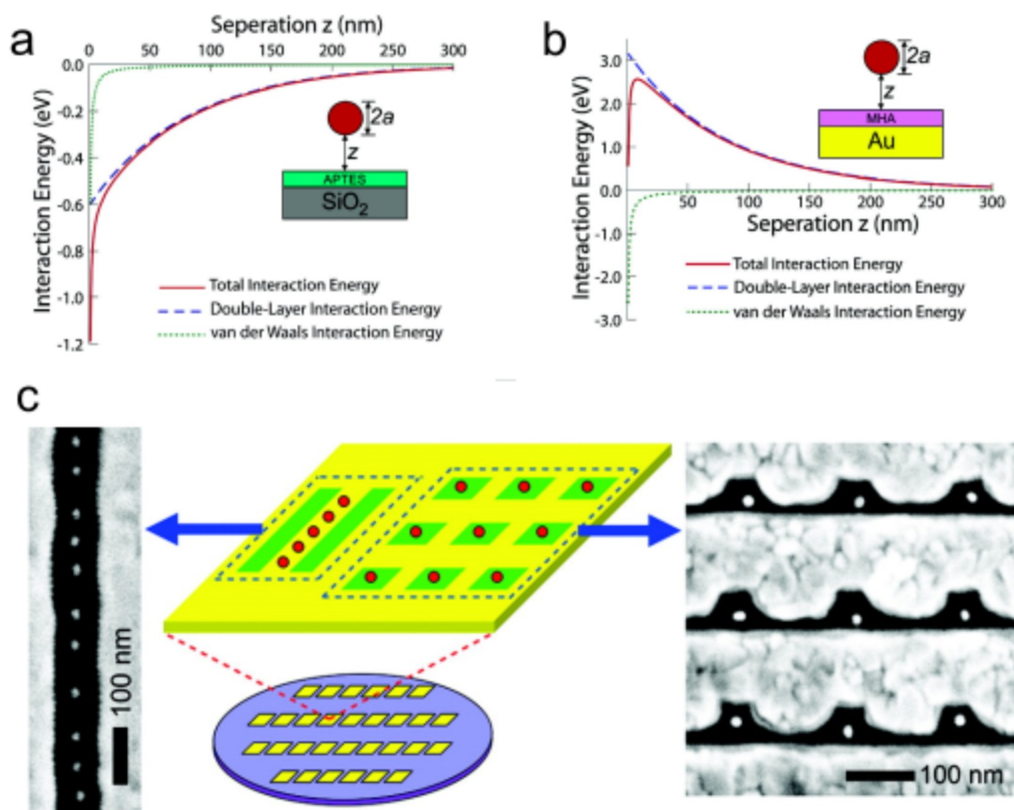

Figure 5.2: Application of interaction energy calculations for gold nanoparticle assembly on patterned amino silane surfaces. a) Interaction energy between gold nanoparticle and 3-aminopropyltriethoxysilane (APTES) surface, b) Interaction energy between gold nanoparticle and 16-mercaptohexadecanoic acid (MHA) surface, and c) Depiction of large sale assembly and applications of electrostatic funneling for charged line and single nanoparticle placement. Reprinted with permission from reference 199. Copyright 2007 American Chemical Society.

5.2.2 Hardmasks and Alternative Lithographic Approaches for Patterning Organosilanes

The work in Chapter 2 and Chapter 3 emphasized the need for an organosilane patterning template that could be removed cleanly and would not allow any vapor permeation. This lead to the exploration of candidate materials that could function as a hard mask for holes and trenches. Ideally, the material would be impermeable to penetration and could be etched in gentle etchants so as not to hydrolyze or react with existing functional groups post-deposition. Magnesium is an excellent candidate material for sacrificial masks. It can be deposited with common deposition

methods, such as sputtering,[347,348] and can be etched in a variety of gentle etchants.[349,350] Figure 5.3 shows the results from etching a 40-nm magnesium layer deposited on a silicon surface by etching through a patterned resist mask. First, the magnesium layer was sputter deposited (1 Å/s, ATC Orion 8, AJA International Inc), and a PMMA(950k) film was spin coated over top of the hardmask layer at a thickness of 110 nm. Following electron beam lithography, development was done in MIBK:IPA 1:3 for 1 min, followed by rinsing in IPA for 20 s. The use of an organic developer was critical as an aqueous developer would dissolve the underlying mask material. After development, the chip was immersed in varying concentrations of IPA in water to achieve a desirable etch rate and minimize anisotropy. Figure 5.3 shows the most promising results for wet etching, utilizing a 1% H_2O in IPA as an etchant for 3 min. The chip was immersed in the etching solution and stirred at 1200 rpm. The sample was positioned to ensure directional flow of etchant into the mask holes before immediate removal and rinsing in acetone. The acetone functions to quench etching as well as to simultaneously remove the PMMA(950k) resist. The masks were examined before any vapor deposition took place. It was found that although larger features appeared to etch completely, small features that were of interest for the work, routinely contained surface contamination. This could potentially be a form of Mg(OH), which has very low solubility.[351] Additionally, repeatable control of a somewhat anisotropic etch was difficult, probably due to fluid access through the PMMA etch mask therefore this idea would require further optimization to improve anisotropy and maintain small feature sizes.

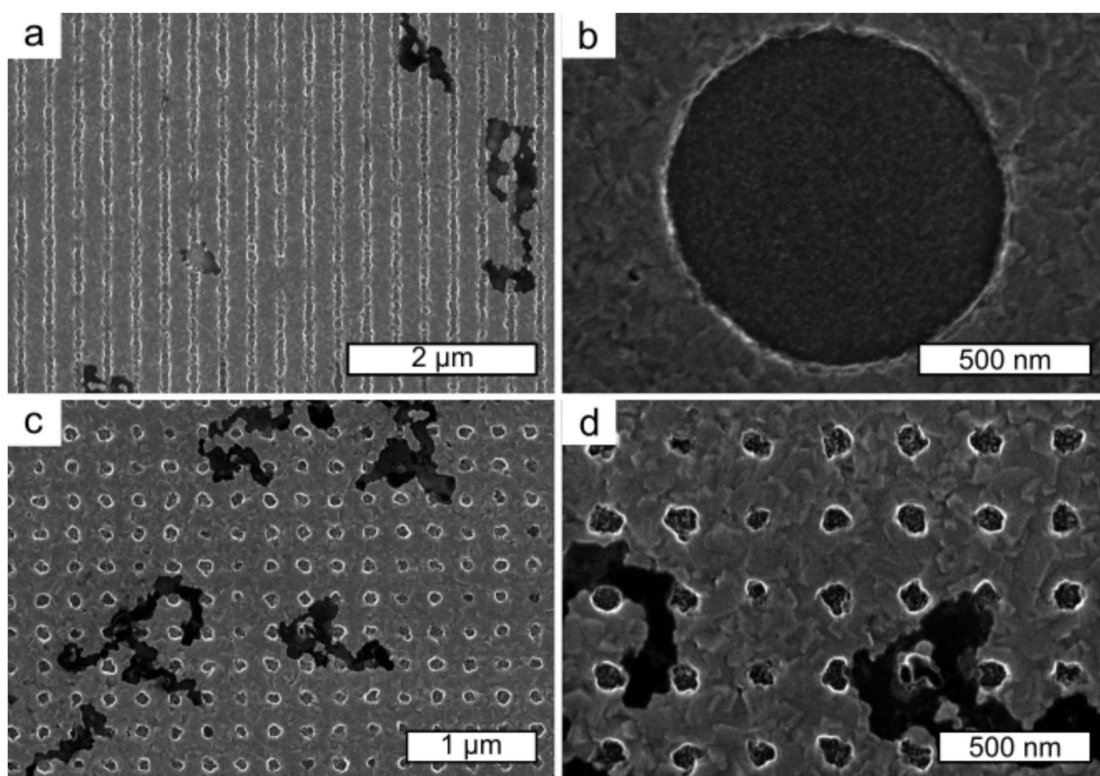

Figure 5.3: SEM images of wet etched magnesium (40 nm) on silicon after etching for 3 min in IPA:H_2O 10:1, through a PMMA(950k) mask. a) Etched trenches through PMMA lines, b) Large diameter hole etch showing silicon surface post-etch, c) A 250-nm pitch hole array with etch/liftoff residue, and d) closeup of a 250-nm pitch hole array post etch.

Figure 5.4 represents the next attempt to improve anisotropy with a magnesium hardmask. One method to achieve this was inspired by work by Currivan *et al.*,[352] who utilized an innovative bilayer stack of negative and positive tone resists, HSQ and PMMA. The overall scheme is presented in Figure 5.4 and is attractive as it avoids etching metal materials and allows for high resolution mask creation. With this approach, it is particularly important to ensure compatibility between the developers of the HSQ etch mask layer and the underlying polymer material.[353] For example, initially it was attempted to develop the HSQ by using a salty NaOH developer as previously described. However, it was found to have negative results, often swelling and removing the underlying PMMA film entirely. Using a lower concentration HSQ developer

(2.5% TMAH), followed by rinsing in water for 30 s, allowed for successful exposure of the upper etch mask layer while keeping the underlying PMMA layer intact.

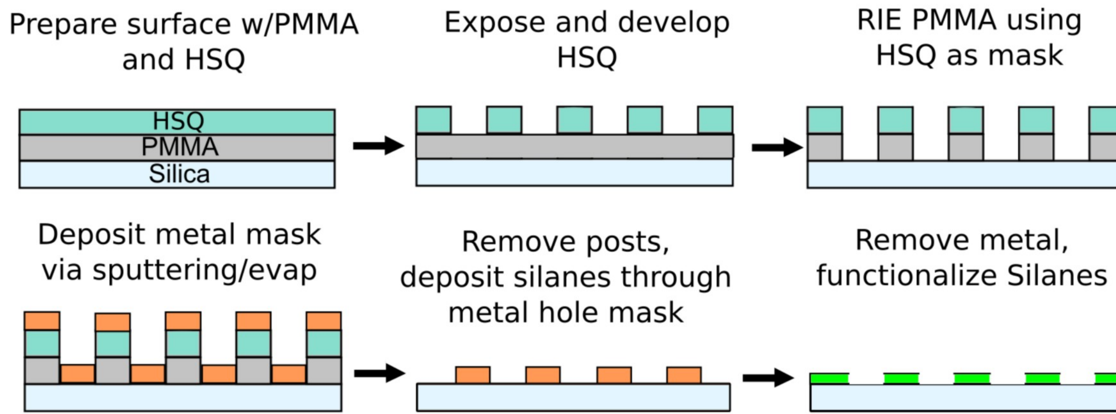

Figure 5.4. Overall process scheme of a HSQ/PMMA bilayer system for metallic hole array mask production. HSQ is spin coated on top of PMMA. HSQ is exposed and developed in 2.5% TMAH. SiO_x dots are then directionally etched in plasma. Metallic mask material is deposited on top of bilayer posts. After deposition, bilayer posts are removed in a PMMA liftoff solvent. Organosilanes deposited through hole array, silanes are available for functionalization pre- or post- etch.

Unfortunately, with this method, the subsequent etch step was difficult to control and would require extensive optimization to achieve maximum directionality at the lateral scales being utilized. Figure 5.5 shows the results of the HSQ/PMMA bilayer process attempted with magnesium. As shown in Figure 5.5 b, reactive ion etching produced substantial undercut in the smaller features. For liftoff, a controlled undercut profile is desirable; however, after sputter coating and attempted removal of the bilayer posts by sonication in acetone, the smaller features of interest (~30 nm diameter) would rarely expose the underlying holes for further descum etching and thus vapor deposition. The system did work well for long line features, such as shown in Figure 5.5 e, and has potential in larger scale features like the square shown in Fig 5.5 f. The underlying surface, by SEM, appears to be clean. This method could be attractive at this scale as literature examples of magnesium in micro- and nanofabrication are scarce,[354] however,

the RIE control requires optimization. This could be done by reducing the overall height of the bilayer post stack so that the exposed PMMA profile underlying the etch mask is less susceptible to sidewall etching. Additionally, other etch parameters, such as alternative etch gases and increased surface, could be explored. ICPRIE (Inductively Coupled Plasma Reactive Ion Etching) capabilities exist at the UAlberta nanoFab and are highly anisotropic. Lastly, as described later, the method of metal deposition likely will play a large role with this negative tone liftout process, and reducing step-edge coverage of the pillars onto the mask background likely would improve yield dramatically.

In an effort to simplify this negative tone liftoff methodology, it was thought that a pure post material would be less complicated as it would entirely remove the RIE etching step. This initially was designed, as shown in Figure 5.6, with the idea of utilizing an HF-based removal to remove the SiO_x posts. This method was inspired by work utilizing HSQ liftoff after germanium and platinum depositions.[355] Before attempting HSQ, however, an attractive option to replace HSQ as a negative resist that utilized organic solvents was found, Ma-N. Ma-N is a negative tone deep UV resist which can be sensitive to electron beam exposure.[356]

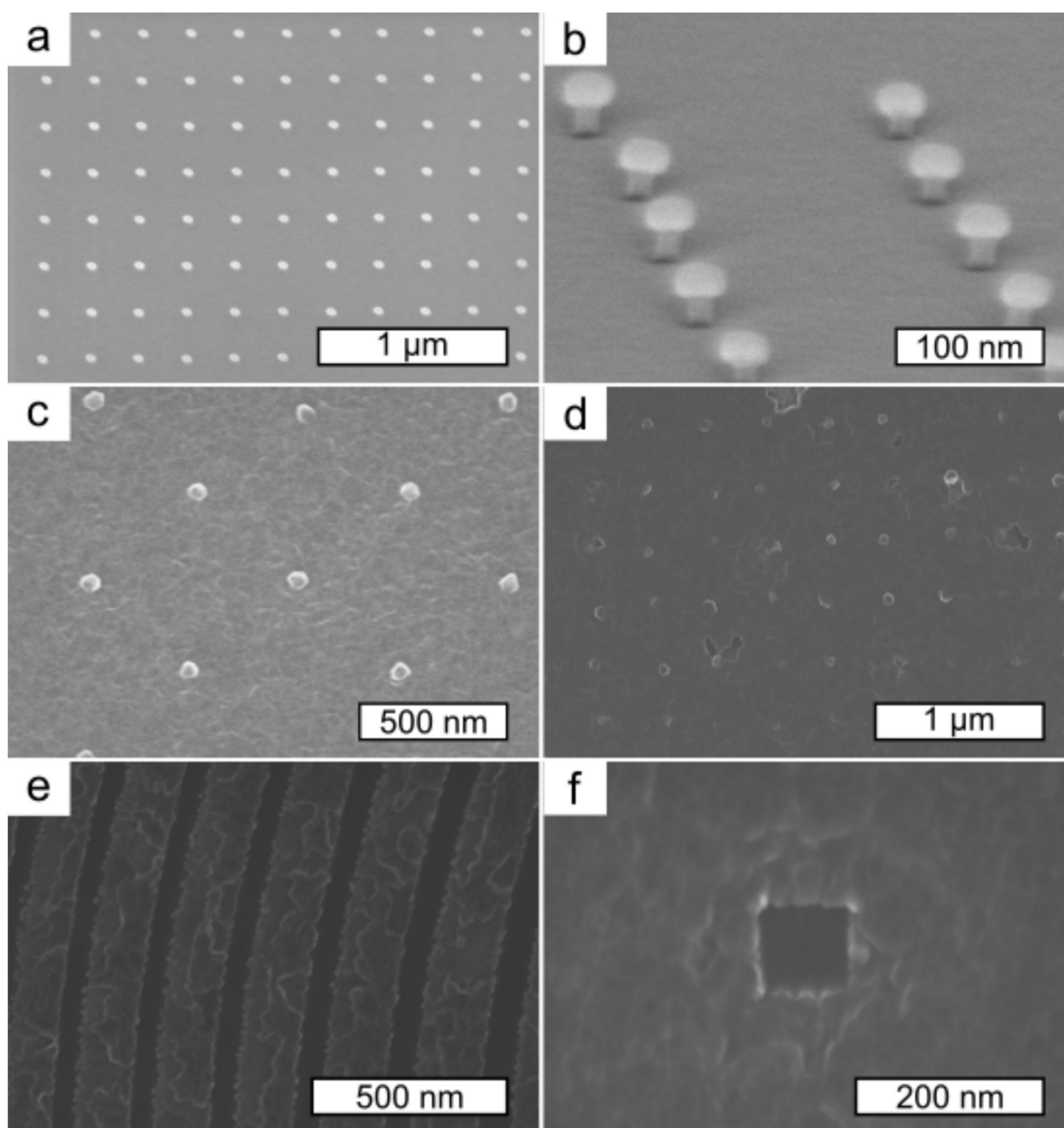

Figure 5.5. SEM images after attempting a HSQ/PMMA bilayer liftoff approach using 30 nm of HSQ on 110 nm of PMMA and a 30-nm Mg deposition. a) Top down of 250-nm pitch SiO_x dots after development on top of a PMMA film, b) Tilted SEM of SiO_x dots on top of PMMA after RIE etching with substantial undercut, c) Tilted SEM of SiO_x/PMMA bilayer posts sputter coated with Mg, d) Top down view of Mg/SiO_x/PMMA 250-nm pitch hole array with 0% liftoff yield, e) Successful curved line liftoff with 50-nm minimum width features, and f) Close-up of smallest achievable liftoff (100-nm diameter square) with approach showing that underlying silicon surface appears to be clear of residual.

Ma-N is a negative tone resist, and like HSQ, any exposed patterns will be left behind after development. An attempt to use Ma-N2403 in place of HSQ, seen in Figure 5.6, was made. Figure 5.7 shows the initial results of utilizing this resist. Large posts were created at 240 nm in height and then were sputter coated with 40 nm of magnesium. The samples were sonicated in acetone to remove the posts and then exposed to a short oxygen plasma descum to remove residual post material, ideally resulting in a clean hole array. Again, the methodology was attractive for larger features, showing very clean removal at the bottom of the features (Figure 5.7, c and d). However, with the smaller features, the conformal nature of sputter coating resulted in firmly anchored features to the metal mask. I believe that this method, combined with metal evaporation and Ma-N2401, is a very strong candidate for high aspect ratio negative tone liftoff under gentle conditions.

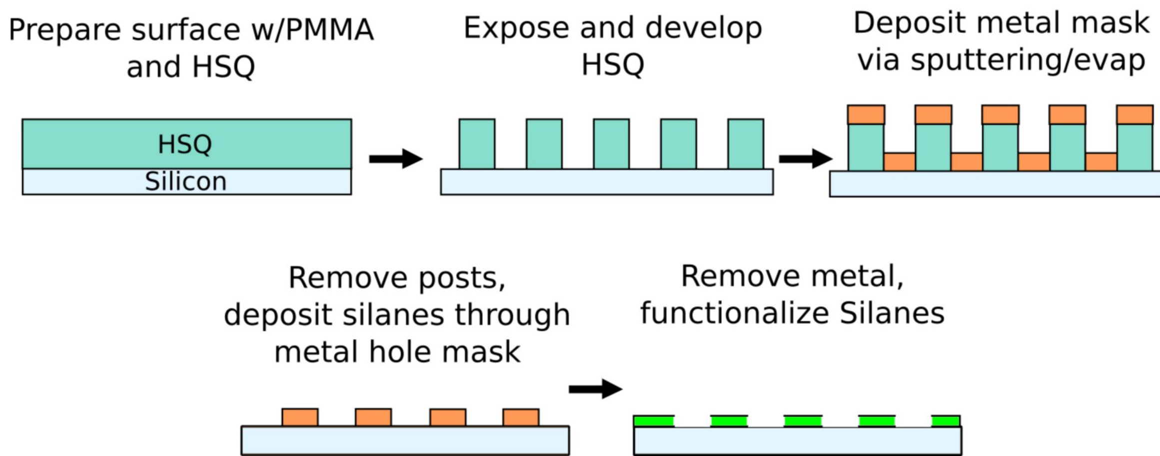

Figure 5.6. Overall process scheme of HSQ negative tone liftoff for metal hole array mask production. HSQ is spin coated on top of PMMA. HSQ is exposed and developed. Metallic mask material is deposited on top of SiO_x posts. After deposition, bilayer posts are removed in vapor or aqueous HF. Organosilanes deposited through hole array, silanes are available for functionalization pre- or post- etch of metal mask.

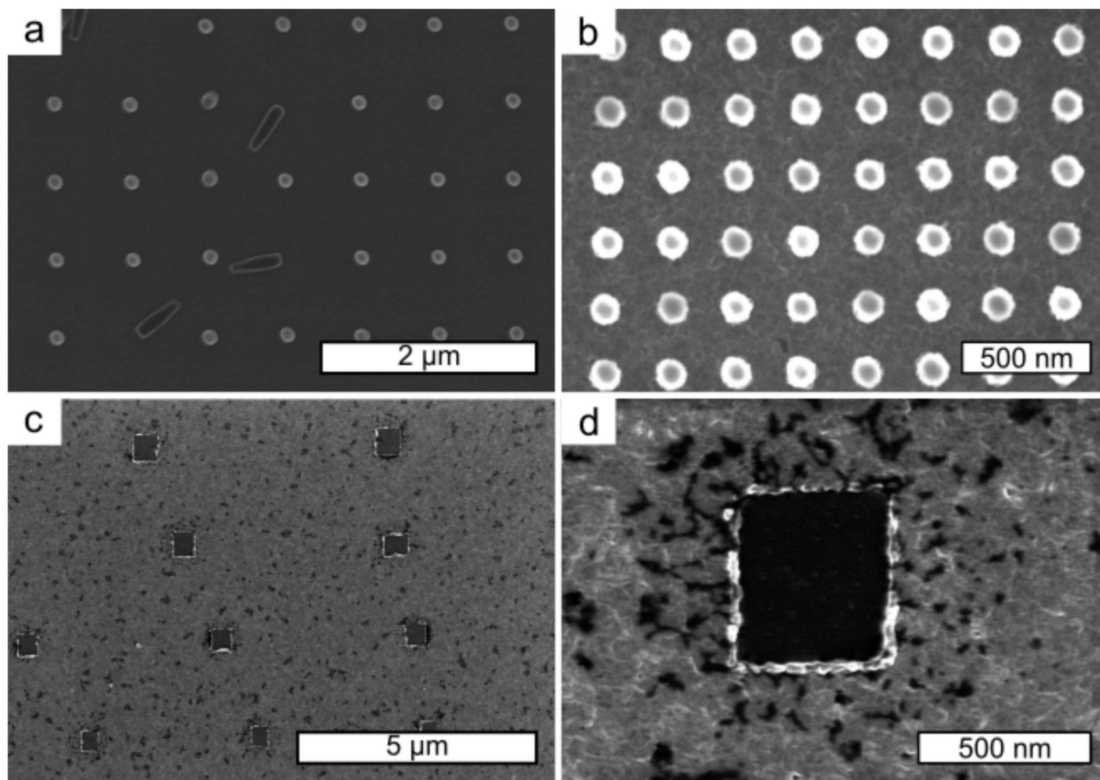

Figure 5.7. SEM images of 240-nm tall posts of a Ma-N2403 resist sputter coated with 40 nm of Mg and removed by acetone sonication. a) Ma-N2403 posts after development, 350-nm pitch. b) Mg coated Ma-N2403 posts, 250-nm pitch. c) Square feature array after removal of Ma-N2403 and d) Closeup of square Ma-N2403 hole after removal showing silicon surface and surrounding liftoff residue.

The last approach, utilizing the negative tone liftoff, yielded promising results that could be explored further. Figure 5.8 shows the result of the overall process described in Figure 5.6, where gold was used instead of magnesium. This was because an electron beam evaporation system was used instead of sputtering and did not have a Mg target. The electron beam evaporation system reduced step coverage substantially. As can be seen in Figure 5.8 a, b, and c, there is a clear separation between the coated posts and the surrounding mask material. With gold deposition on oxide surfaces, it is common to utilize an adhesion layer, such as Cr, and that was done for the initial deposition attempt to check conformality (Figure 5.8 a). Compared with Cr,

the lack of an adhesion layer resulted in a cracked mask film (Figure 5.8 b), making an adhesion layer necessary for preventing permeation to unwanted areas. To avoid a second metal in the hard mask, 3-mercaptopropyltrimethoxysilane (MPTMS) was used as an adhesion layer. Organosilanes are being utilized more often as molecular adhesion layers for both hard[168] and soft lithography surfaces.[357] After HSQ exposure and development, MPTMS was deposited using the vapor deposition protocol on the surface and posts. The surface had 20 nm of gold evaporated on it and was found to have excellent continuity. As in Figure 5.8, the film appears dramatically smoother than its Cr adhesion layer counterpart. Next, an aqueous HF (1%) dip with gentle agitation for 10 s was used. A high yield of liftout in small features of interest is seen in Figure 5.8 d. This procedure is incredibly promising for future work, particularly when combined with Ma-N2401. After removal of the film (Fig 5.8 d), there was an anisotropic undercut present by the HF removal. In the case of vapor deposition, this effectively could increase the feature diameter. However, by utilizing Ma-N2401 with this more directional evaporation deposition, the features likely could be sonicated in acetone and descummed aggressively in oxygen plasma to produce a clean, activated silicon surface in the hole array with vertical sidewalls and no undercut. Then, the mask could be etched in a KI/I_2 solution, although the interactions between gold etchants and the organosilane of choice would have to be considered. This again opens up the possibility of utilizing magnesium; however, a target for Mg will needed for the evaporation system.

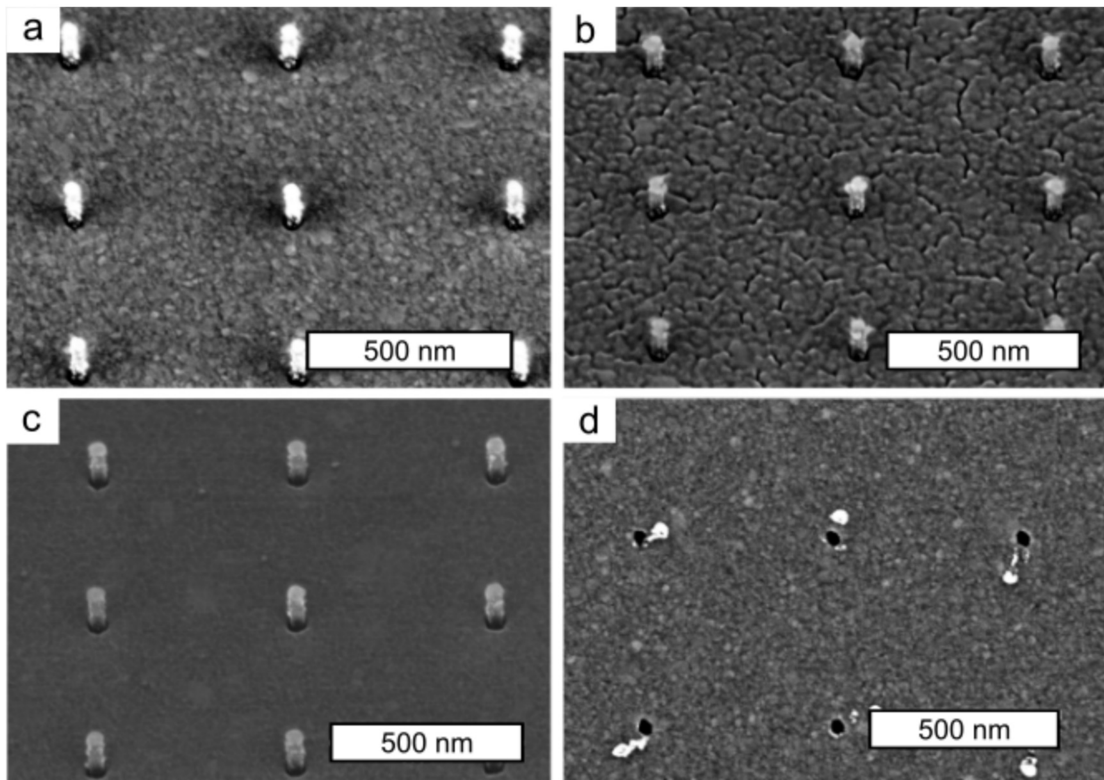

Figure 5.8. SEM images of 110-nm SiO_x posts with 20 nm of gold deposited overtop by electron beam evaporation. a) 20 nm of gold with a 1-nm Cr adhesion layer, b) 20 nm gold with no adhesion layer, c) 20 nm gold with molecular adhesion layer (MPTMS), and d) A hole array after HF post removal with 20 nm gold, 1 nm Cr.

It may be possible to accomplish this work with a pure dry etching scheme not requiring any wet development. Utilizing a ZEP resist on top of an easily etched material, such as aluminum or magnesium, may allow for direct dry etching through the ZEP mask and through the underlying metal mask to the silicon surface. This was attempted initially for aluminum, however, the process would require further optimization to reduce over-etch and maximize metal mask etchant/organosilane compatibility.

5.2.3 Super-Resolution Microscopy

In Chapter 5, the limitations of the lithography approaches used with respect to unwanted background have been addressed. However, there are other improvements that may be done in the construction of a standard for super-resolution microscopies. The first is the use of an inorganic quantum dot pattern rather than that of small organic molecules. Patterning of quantum dots via electrostatic self-assembly has been demonstrated in the elegant work by Jiang *et al*.[358] Their work, shown in Figure 5.9, demonstrated that electrostatic assembly of sparse quantum dot arrays is achievable. Coupled with an accurate picture of zeta potential and patterned surface potentials via XDLVO plots, it may be possible to extend this patterning methodology to patterned organosilanes rather than metal patches of aluminum oxide shown here. With quantum dots, such as QD705, super-resolution is possible by application of Bayesian blinking analysis software like 3B. This, coupled with analysis on a cluster, could produce a very robust pattern of high brightness and photostability normally shown for quantum dots. Additionally, the quantum dots may be able to survive plasma etching if background functionalization is desirable. As patterned streptavidin-biotin has been shown as effective in nanoscale assemblies of a variety of molecules, another potential route to standard fabrication could be by potential collaboration with nanoscale origami research.[310,359]

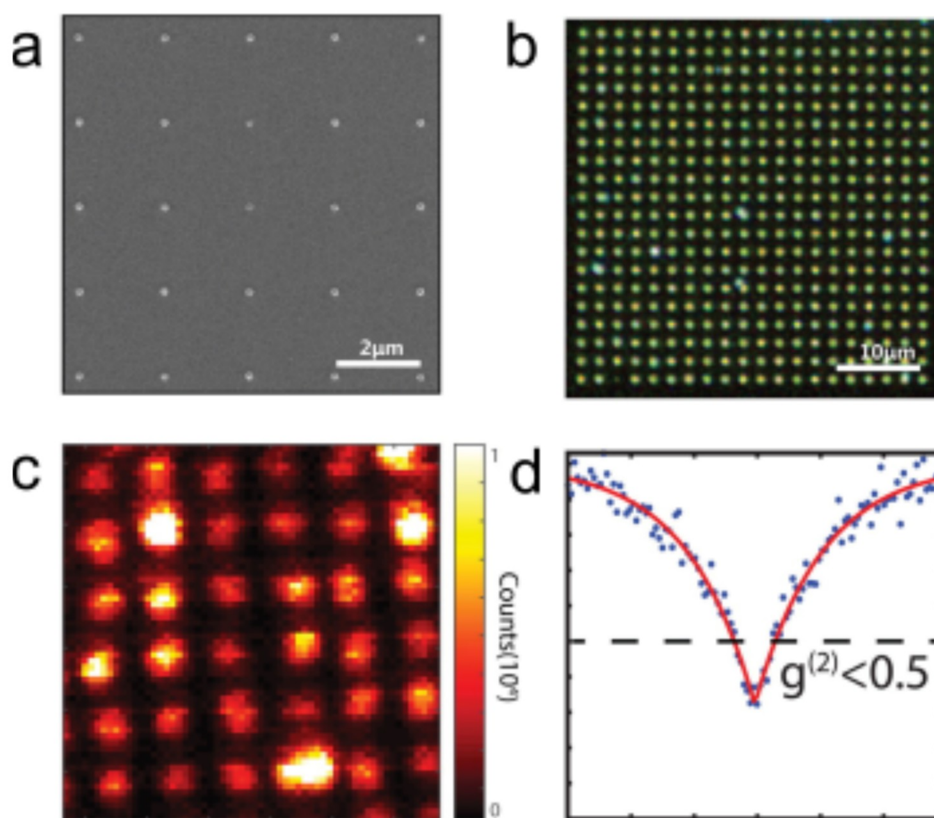

Figure 5.9: a) SEM images of silica-clad QDs sitting on Al_2O_3 pads, b) Dark-field microscope images of 160-nm silica-clad QDs on 160-nm pads with a 2-µm pitch composed of Y_2O_3, c) Confocal scan image of a 12 µm × 12 µm array of UCNPs, and d) Example $g^{(2)}(t)$ curves for bright sites in the scan image. Reprinted with permission from reference [358] (adapted). Copyright 2015 American Chemical Society.

Shown in Figure 5.10 is the application of a DNA nanopillar. These DNA origami structures are very attractive for use in super-resolution calibration experiments as they are able to guarantee single fluorophores at very precise distances. The nanopillars have fluorophores of varying distances of 184 nm and can function as brightness standards in addition to lateral resolution. By using a patterned organosilane to link to biotin/streptavidin and then to one end of a nanopillar, it may be feasible to construct an array of fluorescent standards with 3D topology that could be used to verify 3D calibration as well as fluorophore co-localization.

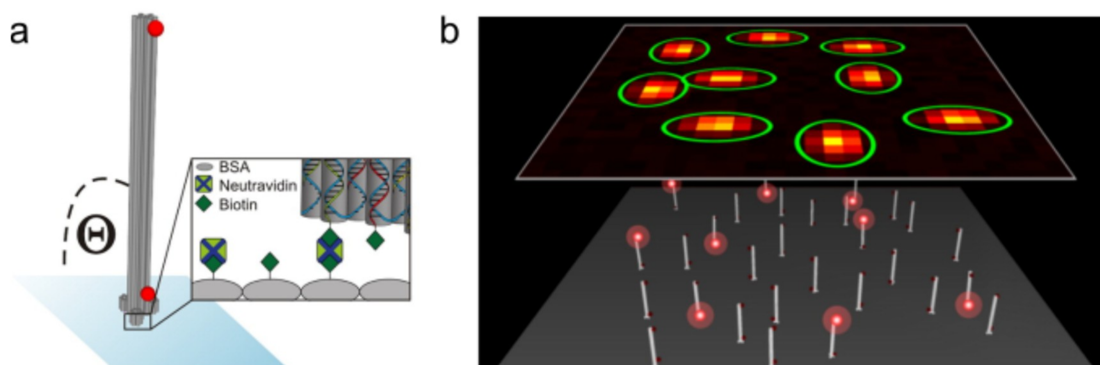

Figure 5.10: Example of DNA origami nanopillar super-resolution standards. a) Single nanopillar with two Alexa647 fluorophores positioned 184 nm apart, and b) Depiction of a vertical array with image localization frame. Reprinted with permission from reference [310] (adapted). Copyright 2014 American Chemical Society.

Lastly, a particularly interesting development in algorithm reconstruction is underway, which may be applied for super-resolution microscopy work. The application of deep learning, or machine learning, is taking a foothold in multiple disciplines in academia and industry. In material sciences I expect the application of machine learning to optimize processes in microscopy where large data sets are available.[360] In the case of super-resolution algorithms, it may be possible to develop a deep learning based reconstruction algorithm that could result in less computational cost or experimental stringency in sample preparation. Software is eating the world. I suspect that the advent of deep-learning enabled super-resolution microscopy will usher dramatic changes, extending the capabilities of existing microscopy setups and enhancing new developments. The co-development of a three dimensional super-resolution microscopy standard for checking machine learning algorithms could be an incredibly useful tool as these techniques continue into the deep nanoscale regime.

~Fin~

References

(1) Tabor, D. Babylonian Lecanomancy: An Ancient Text on the Spreading of Oil on Water. *Journal of Colloid and Interface Science* **1980**, *75* (1), 240–245.

(2) Oppenheim, A. L. *Ancient Mesopotamia : Portrait of a Dead Civilization.*; University of Chicago Press: Chicago, 1964.

(3) Trurnit, H. J. Studies of Enzyme Systems at a Solid-Liquid Interface. I. The System Chymotrypsin-Serum Albumin. *Archives of Biochemistry and Biophysics* **1953**, *47* (2), 251–271.

(4) Trurnit, H. J. Philadelphia, Pa, 1951.

(5) Wang, D.-N.; Stieglitz, H.; Marden, J.; Tamm, L. K. Benjamin Franklin, Philadelphia's Favorite Son, Was a Membrane Biophysicist. *Biophys J* **2013**, *104* (2), 287–291.

(6) Franklin, B.; Brownrigg, W.; Farish. XLIV. Of the Stilling of Waves by Means of Oil. Extracted from Sundry Letters between Benjamin Franklin, LL. D. F. R. S. William Brownrigg, M. D. F. R. S. and the Reverend Mr. Farish. *Phil. Trans.* **1774**, *64*, 445–460.

(7) Pockels, A. Letter to Lord Rayleigh from Agnes Pockels http://cwp.library.ucla.edu/articles/pockels/pockels.html (accessed Mar 17, 2018).

(8) RAYLEIGH. Surface Tension. *Nature* **1891**, *43* (1115), 437.

(9) Langmuir, I. THE CONSTITUTION AND FUNDAMENTAL PROPERTIES OF SOLIDS AND LIQUIDS. PART I. SOLIDS. *J. Am. Chem. Soc.* **1916**, *38* (11), 2221–2295.

(10) Blodgett, K. B. MONOMOLECULAR FILMS OF FATTY ACIDS ON GLASS. *J. Am. Chem. Soc.* **1934**, *56* (2), 495–495.

(11) Greene, J. E. Tracing the 5000-Year Recorded History of Inorganic Thin Films from ∼3000 BC to the Early 1900s AD. *Applied Physics Reviews* **2014**, *1* (4), 041302.

(12) Sella, A. Pockels' trough https://www.chemistryworld.com/opinion/pockels-trough/8574.article (accessed Jan 12, 2018).

(13) Blodgett, K. B. Films Built by Depositing Successive Monomolecular Layers on a Solid Surface. *J. Am. Chem. Soc.* **1935**, *57* (6), 1007–1022.

(14) Bigelow, W. C.; Pickett, D. L.; Zisman, W. A. Oleophobic Monolayers: I. Films Adsorbed from Solution in Non-Polar Liquids. *Journal of Colloid Science* **1946**, *1* (6), 513–538.

(15) Monolayer Films That Assemble Themselves. *New Scientist*. April 7, 1983, p 20.

(16) Nuzzo, R. G.; Allara, D. L. Adsorption of Bifunctional Organic Disulfides on Gold Surfaces. *J. Am. Chem. Soc.* **1983**, *105* (13), 4481–4483.

(17) Onclin, S.; Ravoo, B. J.; Reinhoudt, D. N. Engineering Silicon Oxide Surfaces Using Self-Assembled Monolayers. *Angewandte Chemie International Edition* **2005**, *44* (39), 6282–6304.

(18) Sagiv, J. Organized Monolayers by Adsorption. 1. Formation and Structure of Oleophobic Mixed Monolayers on Solid Surfaces. *J. Am. Chem. Soc.* **1980**, *102* (1), 92–98.

(19) Ulman, A. Formation and Structure of Self-Assembled Monolayers. *Chem. Rev.* **1996**, *96* (4), 1533–1554.
(20) Ulman, A. *An Introduction to Ultrathin Organic Films : From Langmuir-Blodgett to Self-Assembly /*; Academic Press,: Boston :, c1991.
(21) Schwartz, D. K. MECHANISMS AND KINETICS OF SELF-ASSEMBLED MONOLAYER FORMATION | Annual Review of Physical Chemistry. *107-137* **2001**, *52*.
(22) Love, J. C.; Estroff, L. A.; Kriebel, J. K.; Nuzzo, R. G.; Whitesides, G. M. Self-Assembled Monolayers of Thiolates on Metals as a Form of Nanotechnology. *Chem. Rev.* **2005**, *105* (4), 1103–1170.
(23) E.E Polymeropoulos; Sagiv, J. Electrical Conduction through Adsorbed Monolayers: : Vol 69, No 5. *The Journal of Chemical Physics* **1978**, *69* (1836).
(24) Roscioni, O. M.; Muccioli, L.; Mityashin, A.; Cornil, J.; Zannoni, C. Structural Characterization of Alkylsilane and Fluoroalkylsilane Self-Assembled Monolayers on SiO2 by Molecular Dynamics Simulations. *J. Phys. Chem. C* **2016**, *120* (27), 14652–14662.
(25) McGovern, M. E.; Kallury, K. M. R.; Thompson, M. Role of Solvent on the Silanization of Glass with Octadecyltrichlorosilane. *Langmuir* **1994**, *10* (10), 3607–3614.
(26) Britt, D. W.; Hlady, V. An AFM Study of the Effects of Silanization Temperature, Hydration, and Annealing on the Nucleation and Aggregation of Condensed OTS Domains on Mica. *Journal of Colloid and Interface Science* **1996**, *178* (2), 775–784.
(27) Graf, N.; Yeğen, E.; Lippitz, A.; Treu, D.; Wirth, T.; Unger, W. E. S. Optimization of Cleaning and Amino- Silanization Protocols for Si Wafers to Be Used as Platforms for Biochip Microarrays by Surface Analysis (XPS, ToF-SIMS and NEXAFS Spectroscopy). *Surf. Interface Anal.* **2008**, *40* (3–4), 180–183.
(28) Giraud, L.; Nadarajah, R.; Matar, Y.; Bazin, G.; Sun, J.; Zhu, X. X.; Giasson, S. Amino-Functionalized Monolayers Covalently Grafted to Silica-Based Substrates as a Robust Primer Anchorage in Aqueous Media. *Applied Surface Science* **2016**, *370*, 476–485.
(29) Zhu, M.; Lerum, M. Z.; Chen, W. How To Prepare Reproducible, Homogeneous, and Hydrolytically Stable Aminosilane-Derived Layers on Silica. *Langmuir* **2011**, *28* (1), 416–423.
(30) Song, X.; Zhai, J.; Wang, Y.; Jiang, L. Self-Assembly of Amino-Functionalized Monolayers on Silicon Surfaces and Preparation of Superhydrophobic Surfaces Based on Alkanoic Acid Dual Layers and Surface Roughening. *Journal of Colloid and Interface Science* **2006**, *298* (1), 267–273.
(31) Wu, L.; Cai, L.; Liu, A.; Wang, W.; Yuan, Y.; Li, Z. Self-Assembled Monolayers of Perfluoroalkylsilane on Plasma-Hydroxylated Silicon Substrates. *Applied Surface Science* **2015**, *349*, 683–694.
(32) Sugimura, H.; Ushiyama, K.; Hozumi, A.; Takai, O. Micropatterning of Alkyl- and Fluoroalkylsilane Self-Assembled Monolayers Using Vacuum Ultraviolet Light. *Langmuir* **2000**, *16* (3), 885–888.
(33) Bhushan, B.; Kasai, T.; Kulik, G.; Barbieri, L.; Hoffmann, P. AFM Study of Perfluoroalkylsilane and Alkylsilane Self-Assembled Monolayers for Anti-Stiction in MEMS/NEMS. *Ultramicroscopy* **2005**, *105* (1), 176–188.

(34) Tripp, C. P.; Hair, M. L. Reaction of Methylsilanols with Hydrated Silica Surfaces: The Hydrolysis of Trichloro-, Dichloro-, and Monochloromethylsilanes and the Effects of Curing. *Langmuir* **1995**, *11* (1), 149–155.

(35) Rozlosnik, N.; Gerstenberg, M. C.; Larsen, N. B. Effect of Solvents and Concentration on the Formation of a Self-Assembled Monolayer of Octadecylsiloxane on Silicon (001). *Langmuir* **2003**, *19* (4), 1182–1188.

(36) White, L. D.; Tripp, C. P. A Low-Frequency Infrared Study of the Reaction of Methoxymethylsilanes with Silica. *Journal of Colloid and Interface Science* **2000**, *224* (2), 417–424.

(37) Tripp, C. P.; Hair, M. L. An Infrared Study of the Reaction of Octadecyltrichlorosilane with Silica. *Langmuir* **1992**, *8* (4), 1120–1126.

(38) Deetz, J. D.; Ngo, Q.; Faller, R. Reactive Molecular Dynamics Simulations of the Silanization of Silica Substrates by Methoxysilanes and Hydroxysilanes. *Langmuir* **2016**, *32* (28), 7045–7055.

(39) Liu, Y.; Li, Y.; Li, X.-M.; He, T. Kinetics of (3-Aminopropyl)Triethoxylsilane (APTES) Silanization of Superparamagnetic Iron Oxide Nanoparticles. *Langmuir* **2013**, *29* (49), 15275–15282.

(40) Ahangaran, F.; Hassanzadeh, A.; Nouri, S. Surface Modification of Fe<Subscript>3</Subscript>O<Subscript>4</Subscript>@SiO<Subscript>2</Subscript> Microsphere by Silane Coupling Agent. *Int Nano Lett* **2013**, *3* (1), 23.

(41) Gun, J.; Sagiv, J. On the Formation and Structure of Self-Assembling Monolayers: III. Time of Formation, Solvent Retention, and Release. *Journal of Colloid and Interface Science* **1986**, *112* (2), 457–472.

(42) Tillman, N.; Ulman, A.; Schildkraut, J. S.; Penner, T. L. Incorporation of Phenoxy Groups in Self-Assembled Monolayers of Trichlorosilane Derivatives. Effects on Film Thickness, Wettability, and Molecular Orientation. *J. Am. Chem. Soc.* **1988**, *110* (18), 6136–6144.

(43) Marcinko, S.; Fadeev, A. Y. Hydrolytic Stability of Organic Monolayers Supported on TiO2 and ZrO2. *Langmuir* **2004**, *20* (6), 2270–2273.

(44) Fadeev, A. Y.; Helmy, R.; Marcinko, S. Self-Assembled Monolayers of Organosilicon Hydrides Supported on Titanium, Zirconium, and Hafnium Dioxides. *Langmuir* **2002**, *18* (20), 7521–7529.

(45) Watts, B.; Thomsen, L.; Fabien, J. R.; Dastoor, P. C. Understanding the Conformational Dynamics of Organosilanes: γ-APS on Zinc Oxide Surfaces. *Langmuir* **2002**, *18* (1), 148–154.

(46) Garton Andrew. The Crosslinking of Epoxy Resins at Interfaces. I. Germanium, Germanium Dioxide, and Silane‐treated Germanium. *Journal of Polymer Science: Polymer Chemistry Edition* **2003**, *22* (6), 1495–1506.

(47) Helmy, R.; Fadeev, A. Y. Self-Assembled Monolayers Supported on TiO2: Comparison of C18H37SiX3 (X = H, Cl, OCH3), C18H37Si(CH3)2Cl, and C18H37PO(OH)2. *Langmuir* **2002**, *18* (23), 8924–8928.

(48) Allen, C. G.; Baker, D. J.; Albin, J. M.; Oertli, H. E.; Gillaspie, D. T.; Olson, D. C.; Furtak, T. E.; Collins, R. T. Surface Modification of ZnO Using Triethoxysilane-Based Molecules. *Langmuir* **2008**, *24* (23), 13393–13398.

(49) Fadeev, A. Y.; McCarthy, T. J. Self-Assembly Is Not the Only Reaction Possible between Alkyltrichlorosilanes and Surfaces: Monomolecular and Oligomeric Covalently Attached Layers of Dichloro- and Trichloroalkylsilanes on Silicon. *Langmuir* **2000**, *16* (18), 7268–7274.

(50) Le Grange, J.; Markham, J.; Kurkjian, C. Effects of Surface Hydration on the Deposition of Silane Monolayers on Silica. *Langmuir* **1993**, *9* (7), 1749–1753.

(51) Allara, D. L.; Parikh, A. N.; Rondelez, F. Evidence for a Unique Chain Organization in Long Chain Silane Monolayers Deposited on Two Widely Different Solid Substrates. *Langmuir* **1995**, *11* (7), 2357–2360.

(52) Wang, R.; Wunder, S. L. Effects of Silanol Density, Distribution, and Hydration State of Fumed Silica on the Formation of Self-Assembled Monolayers of n-Octadecyltrichlorosilane. *Langmuir* **2000**, *16* (11), 5008–5016.

(53) Bunker, B. C.; Carpick, R. W.; Assink, R. A.; Thomas, M. L.; Hankins, M. G.; Voigt, J. A.; Sipola, D.; de Boer, M. P.; Gulley, G. L. The Impact of Solution Agglomeration on the Deposition of Self-Assembled Monolayers. *Langmuir* **2000**, *16* (20), 7742–7751.

(54) Wang, X.; Hu, W.; Ramasubramaniam, R.; Bernstein, G. H.; Snider, G.; Lieberman, M. Formation, Characterization, and Sub-50-Nm Patterning of Organosilane Monolayers with Embedded Disulfide Bonds: An Engineered Self-Assembled Monolayer Resist for Electron-Beam Lithography. *Langmuir* **2003**, *19* (23), 9748–9758.

(55) Krasnoslobodtsev, A. V.; Smirnov, S. N. Effect of Water on Silanization of Silica by Trimethoxysilanes. *Langmuir* **2002**, *18* (8), 3181–3184.

(56) Liu, Y.; Wolf, L. K.; Messmer, M. C. A Study of Alkyl Chain Conformational Changes in Self-Assembled n-Octadecyltrichlorosilane Monolayers on Fused Silica Surfaces. *Langmuir* **2001**, *17* (14), 4329–4335.

(57) Leitner, T.; Friedbacher, G.; Vallant, T.; Brunner, H.; Mayer, U.; Hoffmann, H. Investigations of the Growth of Self-Assembled Octadecylsiloxane Monolayers with Atomic Force Microscopy. *Mikrochim Acta* **2000**, *133* (1–4), 331–336.

(58) Bierbaum, K.; Grunze, M.; Baski, A. A.; Chi, L. F.; Schrepp, W.; Fuchs, H. Growth of Self-Assembled n-Alkyltrichlorosilane Films on Si(100) Investigated by Atomic Force Microscopy. *Langmuir* **1995**, *11* (6), 2143–2150.

(59) Jin, Z. H.; Vezenov, D. V.; Lee, Y. W.; Zull, J. E.; Sukenik, C. N.; Savinell, R. F. Alternating Current Impedance Characterization of the Structure of Alkylsiloxane Self-Assembled Monolayers on Silicon. *Langmuir* **1994**, *10* (8), 2662–2671.

(60) Plueddemann, E. P. Chemistry of Silane Coupling Agents. In *Silane Coupling Agents*; Springer, Boston, MA, 1991; pp 31–54.

(61) Silberzan, P.; Leger, L.; Ausserre, D.; Benattar, J. J. Silanation of Silica Surfaces. A New Method of Constructing Pure or Mixed Monolayers. *Langmuir* **1991**, *7* (8), 1647–1651.

(62) Leitner, T.; Friedbacher, G.; Vallant, T.; Brunner, H.; Mayer, U.; Hoffmann, H. Investigations of the Growth of Self-Assembled Octadecylsiloxane Monolayers with Atomic Force Microscopy. *Mikrochim Acta* **2000**, *133* (1–4), 331–336.

(63) Davidovits, J. V.; Pho, V.; Silberzan, P.; Goldmann, M. Temperature Influence on the Formation of Silanized Monolayers on Silica: An Atomic Force Microscopy Study. *Surface Science* **1996**, *352–354*, 369–373.

(64) Glaser, A.; Foisner, J.; Friedbacher, G.; Hoffmann, H. Low-Temperature Investigation of the Growth Mechanism of Alkylsiloxane Self-Assembled Monolayers. *Anal Bioanal Chem* **2004**, *379* (4), 653–657.

(65) Reiniger, M.; Basnar, B.; Friedbacher, G.; Schleberger, M. Atomic Force Microscopy of Thin Organic Films on Silicon in Ultrahigh Vacuum and under Ambient Conditions. *Surf. Interface Anal.* **2002**, *33* (2), 85–88.

(66) Brzoska, J. B.; Azouz, I. B.; Rondelez, F. Silanization of Solid Substrates: A Step Toward Reproducibility. *Langmuir* **1994**, *10* (11), 4367–4373.

(67) Parikh, A. N.; Allara, D. L.; Azouz, I. B.; Rondelez, F. An Intrinsic Relationship between Molecular Structure in Self-Assembled n-Alkylsiloxane Monolayers and Deposition Temperature. *J. Phys. Chem.* **1994**, *98* (31), 7577–7590.

(68) Stevens, M. J. Thoughts on the Structure of Alkylsilane Monolayers. *Langmuir* **1999**, *15* (8), 2773–2778.

(69) Wang, Y.; Lieberman, M. Growth of Ultrasmooth Octadecyltrichlorosilane Self-Assembled Monolayers on SiO2. *Langmuir* **2003**, *19* (4), 1159–1167.

(70) Maoz, R.; Sagiv, J.; Degenhardt, D.; Möhwald, H.; Quint, P. Hydrogen-Bonded Multilayers of Self-Assembling Silanes: Structure Elucidation by Combined Fourier Transform Infra-Red Spectroscopy and X-Ray Scattering Techniques. *Supramolecular Science* **1995**, *2* (1), 9–24.

(71) Baptiste, A.; Gibaud, A.; Bardeau, J. F.; Wen, K.; Maoz, R.; Sagiv, J.; Ocko, B. M. X-Ray, Micro-Raman, and Infrared Spectroscopy Structural Characterization of Self-Assembled Multilayer Silane Films with Variable Numbers of Stacked Layers. *Langmuir* **2002**, *18* (10), 3916–3922.

(72) Gooding, J. J.; Ciampi, S. The Molecular Level Modification of Surfaces: From Self-Assembled Monolayers to Complex Molecular Assemblies. *Chem. Soc. Rev.* **2011**, *40* (5), 2704–2718.

(73) Naik, V. V.; Crobu, M.; Venkataraman, N. V.; Spencer, N. D. Multiple Transmission-Reflection IR Spectroscopy Shows That Surface Hydroxyls Play Only a Minor Role in Alkylsilane Monolayer Formation on Silica. *J. Phys. Chem. Lett.* **2013**, *4* (16), 2745–2751.

(74) Zhuravlev, L. T. Concentration of Hydroxyl Groups on the Surface of Amorphous Silicas. *Langmuir* **1987**, *3* (3), 316–318.

(75) Zhuravlev, L. T. The Surface Chemistry of Amorphous Silica. Zhuravlev Model. *Colloids and Surfaces A: Physicochemical and Engineering Aspects* **2000**, *173* (1), 1–38.

(76) Kern, W. Cleaning Solution-Based on Hydrogen Peroxide for Use in Silicon Semiconductor Technology. *RCA Rev.* **1970**, *31* (2), 187–206.

(77) Putner, T. Methods of Cleaning Glass by Vapour Degreasing and Ultrasonically Agitated Solvents. *Br. J. Appl. Phys.* **1959**, *10* (7), 332.

(78) Gale, G. W.; Busnaina, A. A. Removal of Particulate Contaminants Using Ultrasonics and Megasonics: A Review. *Particulate Science and Technology* **1995**, *13* (3–4), 197–211.

(79) Kern, W. The Evolution of Silicon Wafer Cleaning Technology. *J. Electrochem. Soc.* **1990**, *137* (6), 1887–1892.

(80) Cass, A. E. G.; Cass, T.; Ligler, F. S. *Immobilized Biomolecules in Analysis: A Practical Approach*; Oxford University Press, 1998.
(81) Reinhardt, K.; Kern, W. *Handbook of Silicon Wafer Cleaning Technology, 2nd Edition*; William Andrew, 2008.
(82) Mittal, K. L. Surface Contamination: An Overview. In *Surface Contamination*; Springer, Boston, MA, 1979; pp 3–45.
(83) Bhalla, V.; Carrara, S.; Stagni, C.; Samorì, B. Chip Cleaning and Regeneration for Electrochemical Sensor Arrays. *Thin Solid Films* **2010**, *518* (12), 3360–3366.
(84) Hohertz, D.; Romanuik, S. F.; Gray, B. L.; Kavanagh, K. L. Recycling Gold Nanohole Arrays. *Journal of Vacuum Science & Technology A: Vacuum, Surfaces, and Films* **2014**, *32* (3), 031403.
(85) Cras, J. J.; Rowe-Taitt, C. A.; Nivens, D. A.; Ligler, F. S. Comparison of Chemical Cleaning Methods of Glass in Preparation for Silanization. *Biosensors and Bioelectronics* **1999**, *14* (8), 683–688.
(86) Han, Y.; Mayer, D.; Offenhäusser, A.; Ingebrandt, S. Surface Activation of Thin Silicon Oxides by Wet Cleaning and Silanization. *Thin Solid Films* **2006**, *510* (1), 175–180.
(87) Khadka, K.; Strandwitz, N. C.; Ferguson, G. S. Byproduct-Free Route to Aminosiloxane Monolayers on Silicon/Silicon Dioxide. *Langmuir* **2017**, *33* (7), 1639–1645.
(88) Ye, L.; González-Campo, A.; Kudernac, T.; Núñez, R.; de Jong, M.; van der Wiel, W. G.; Huskens, J. Monolayer Contact Doping from a Silicon Oxide Source Substrate. *Langmuir* **2017**, *33* (15), 3635–3638.
(89) Escorihuela, J.; Zuilhof, H. Rapid Surface Functionalization of Hydrogen-Terminated Silicon by Alkyl Silanols. *J. Am. Chem. Soc.* **2017**, *139* (16), 5870–5876.
(90) Vossen, J. L. The Preparation of Substrates for Film Deposition Using Glow Discharge Techniques. *J. Phys. E: Sci. Instrum.* **1979**, *12* (3), 159.
(91) Holland, L. The Cleaning of Glass in a Glow Discharge. *Br. J. Appl. Phys.* **1958**, *9* (10), 410.
(92) Yang, M. G.; Koliwad, K. M.; McGuire, G. E. Auger Electron Spectroscopy of Cleanup-Related Contamination on Silicon Surfaces. *J. Electrochem. Soc.* **1975**, *122* (5), 675–678.
(93) Fiorilli, S.; Rivolo, P.; Descrovi, E.; Ricciardi, C.; Pasquardini, L.; Lunelli, L.; Vanzetti, L.; Pederzolli, C.; Onida, B.; Garrone, E. Vapor-Phase Self-Assembled Monolayers of Aminosilane on Plasma-Activated Silicon Substrates. *Journal of Colloid and Interface Science* **2008**, *321* (1), 235–241.
(94) Williams, T. S.; Hicks, R. F. Aging Mechanism of the Native Oxide on Silicon (100) Following Atmospheric Oxygen Plasma Cleaning. *Journal of Vacuum Science & Technology A: Vacuum, Surfaces, and Films* **2011**, *29* (4), 041403.
(95) Gupta, V.; Madaan, N.; Jensen, D. S.; Kunzler, S. C.; Linford, M. R. Hydrogen Plasma Treatment of Silicon Dioxide for Improved Silane Deposition. *Langmuir* **2013**, *29* (11), 3604–3609.
(96) Fischer, T.; Dietrich, P. M.; Streeck, C.; Ray, S.; Nutsch, A.; Shard, A.; Beckhoff, B.; Unger, W. E. S.; Rurack, K. Quantification of Variable Functional-Group Densities of Mixed-Silane Monolayers on Surfaces via a Dual-Mode Fluorescence and XPS Label. *Anal. Chem.* **2015**, *87* (5), 2685–2692.

(97) Seitz, O.; G. Fernandes, P.; Tian, R.; Karnik, N.; Wen, H.-C.; Stiegler, H.; A. Chapman, R.; M. Vogel, E.; J. Chabal, Y. Control and Stability of Self-Assembled Monolayers under Biosensing Conditions. *Journal of Materials Chemistry* **2011**, *21* (12), 4384–4392.
(98) Ito, Y.; Virkar, A. A.; Mannsfeld, S.; Oh, J. H.; Toney, M.; Locklin, J.; Bao, Z. Crystalline Ultrasmooth Self-Assembled Monolayers of Alkylsilanes for Organic Field-Effect Transistors. *J. Am. Chem. Soc.* **2009**, *131* (26), 9396–9404.
(99) Kurth, D. G.; Bein, T. Quantification of the Reactivity of 3-Aminopropyl-Triethoxysilane Monolayers with the Quartz-Crystal Microbalance. *Angew. Chem. Int. Ed. Engl.* **1992**, *31* (3), 336–338.
(100) Dorvel, B.; Reddy, B.; Block, I.; Mathias, P.; Clare, S. E.; Cunningham, B.; Bergstrom, D. E.; Bashir, R. Vapor-Phase Deposition of Monofunctional Alkoxysilanes for Sub-Nanometer-Level Biointerfacing on Silicon Oxide Surfaces. *Adv. Funct. Mater.* **2010**, *20* (1), 87–95.
(101) Diebold, R. M.; Clarke, D. R. Smooth, Aggregate-Free Self-Assembled Monolayer Deposition of Silane Coupling Agents on Silicon Dioxide. *Langmuir* **2012**, *28* (44), 15513–15520.
(102) Jung, G.-Y.; Li, Z.; Wu, W.; Chen, Y.; Olynick, D. L.; Wang, S.-Y.; Tong, W. M.; Williams, R. S. Vapor-Phase Self-Assembled Monolayer for Improved Mold Release in Nanoimprint Lithography. *Langmuir* **2005**, *21* (4), 1158–1161.
(103) Yadav, A. R.; Sriram, R.; Carter, J. A.; Miller, B. L. Comparative Study of Solution–Phase and Vapor–Phase Deposition of Aminosilanes on Silicon Dioxide Surfaces. *Materials Science and Engineering: C* **2014**, *35*, 283–290.
(104) Ashurst, W. R.; Carraro, C.; Maboudian, R.; Frey, W. Wafer Level Anti-Stiction Coatings for MEMS. *Sensors and Actuators A: Physical* **2003**, *104* (3), 213–221.
(105) Ashurst, W. R.; Carraro, C.; Maboudian, R. Vapor Phase Anti-Stiction Coatings for MEMS. *IEEE Transactions on Device and Materials Reliability* **2003**, *3* (4), 173–178.
(106) Slavov, S. V.; Sanger, A. R.; Chuang, K. T. Mechanism of Silation of Alumina with Hexamethyldisilazane. *J. Phys. Chem. B* **1998**, *102* (28), 5475–5482.
(107) Jönsson, U.; Olofsson, G.; Malmqvist, M.; Rönnberg, I. Chemical Vapour Deposition of Silanes. *Thin Solid Films* **1985**, *124* (2), 117–123.
(108) Qin, D.; Xia, Y.; Whitesides, G. M. Soft Lithography for Micro- and Nanoscale Patterning. *Nat. Protocols* **2010**, *5* (3), 491–502.
(109) Husseini, G. A.; Peacock, J.; Sathyapalan, A.; Zilch, L. W.; Asplund, M. C.; Sevy, E. T.; Linford, M. R. Alkyl Monolayers on Silica Surfaces Prepared Using Neat, Heated Dimethylmonochlorosilanes with Low Vapor Pressures. *Langmuir* **2003**, *19* (12), 5169–5171.
(110) Dong, H.; Li, C. M.; Zhou, Q.; Sun, J. B.; Miao, J. M. Sensitive Electrochemical Enzyme Immunoassay Microdevice Based on Architecture of Dual Ring Electrodes with a Sensing Cavity Chamber. *Biosensors and Bioelectronics* **2006**, *22* (5), 621–626.
(111) Vos, R.; Rolin, C.; Rip, J.; Conard, T.; Steylaerts, T.; Cabanilles, M. V.; Levrie, K.; Jans, K.; Stakenborg, T. Chemical Vapor Deposition of Azidoalkylsilane Monolayer Films. *Langmuir* **2017**.

(112) Zhong, J.; Chinn, J.; Roberts, C. B.; Ashurst, W. R. Vapor-Phase Deposited Chlorosilane-Based Self-Assembled Monolayers on Various Substrates for Thermal Stability Analysis. *Ind. Eng. Chem. Res.* **2017**, *56* (18), 5239–5252.
(113) Wu, K.; Bailey, T. C.; Willson, C. G.; Ekerdt, J. G. Surface Hydration and Its Effect on Fluorinated SAM Formation on SiO2 Surfaces. *Langmuir* **2005**, *21* (25), 11795–11801.
(114) Lowe, R. D.; Pellow, M. A.; Stack, T. D. P.; Chidsey, C. E. D. Deposition of Dense Siloxane Monolayers from Water and Trimethoxyorganosilane Vapor. *Langmuir* **2011**, *27* (16), 9928–9935.
(115) Kumar, A.; Abbott, N. L.; Biebuyck, H. A.; Kim, E.; Whitesides, G. M. Patterned Self-Assembled Monolayers and Meso-Scale Phenomena. *Acc. Chem. Res.* **1995**, *28* (5), 219–226.
(116) Mendes, P. M.; Yeung, C. L.; Preece, J. A. Bio-Nanopatterning of Surfaces. *Nanoscale Research Letters* **2007**, *2* (8), 373.
(117) Khan, S.; Newaz, G. A Comprehensive Review of Surface Modification for Neural Cell Adhesion and Patterning. *J. Biomed. Mater. Res.* **2010**, *93A* (3), 1209–1224.
(118) Bhure, R.; Mahapatro, A. Surface Patterning Using Self Assembled Monolayers (SAMs). In *Biomaterials*; ACS Symposium Series; American Chemical Society, 2010; Vol. 1054, pp 65–107.
(119) Krämer, S.; Fuierer, R. R.; Gorman, C. B. Scanning Probe Lithography Using Self-Assembled Monolayers. *Chem. Rev.* **2003**, *103* (11), 4367–4418.
(120) Dressick, W. J.; Calvert, J. M. Patterning of Self-Assembled Films Using Lithographic Exposure Tools. *Jpn. J. Appl. Phys.* **1993**, *32* (12S), 5829.
(121) Potochnik, S. J.; Pehrsson, P. E.; Hsu, D. S. Y.; Calvert, J. M. Selective Copper Chemical Vapor Deposition Using Pd-Activated Organosilane Films. *Langmuir* **1995**, *11* (6), 1841–1845.
(122) Dulcey, C. S.; Georger, J. H.; Krauthamer, V.; Stenger, D. A.; Fare, T. L.; Calvert, J. M. Deep UV Photochemistry of Chemisorbed Monolayers: Patterned Coplanar Molecular Assemblies. *Science* **1991**, *252* (5005), 551–554.
(123) Stenger, D. A.; Georger, J. H.; Dulcey, C. S.; Hickman, J. J.; Rudolph, A. S.; Nielsen, T. B.; McCort, S. M.; Calvert, J. M. Coplanar Molecular Assemblies of Amino- and Perfluorinated Alkylsilanes: Characterization and Geometric Definition of Mammalian Cell Adhesion and Growth. *J. Am. Chem. Soc.* **1992**, *114* (22), 8435–8442.
(124) Sugimura, H.; Hanji, T.; Takai, O.; Masuda, T.; Misawa, H. Photolithography Based on Organosilane Self-Assembled Monolayer Resist. *Electrochimica Acta* **2001**, *47* (1), 103–107.
(125) Saito, N.; Haneda, H.; Sekiguchi, T.; Ohashi, N.; Sakaguchi, I.; Koumoto, K. Low-Temperature Fabrication of Light-Emitting Zinc Oxide Micropatterns Using Self-Assembled Monolayers. *Adv. Mater.* **2002**, *14* (6), 418–421.
(126) Matsuzawa, M.; Tokumitsu, S.; Knoll, W.; Sasabe, H. Effects of Organosilane Monolayer Films on the Geometrical Guidance of CNS Neurons. *Langmuir* **1998**, *14* (18), 5133–5138.
(127) Yamaguchi, M.; Ikeda, K.; Suzuki, M.; Kiyohara, A.; Kudoh, S. N.; Shimizu, K.; Taira, T.; Ito, D.; Uchida, T.; Gohara, K. Cell Patterning Using a Template of Microstructured

Organosilane Layer Fabricated by Vacuum Ultraviolet Light Lithography. *Langmuir* **2011**, *27* (20), 12521–12532.
(128) Ni, L.; Dietlin, C.; Chemtob, A.; Croutxé-Barghorn, C.; Brendlé, J. Hydrophilic/Hydrophobic Film Patterning by Photodegradation of Self-Assembled Alkylsilane Multilayers and Its Applications. *Langmuir* **2014**, *30* (33), 10118–10126.
(129) Nakagawa, M.; Ichimura, K. Photopatterning of Self-Assembled Monolayers to Generate Aniline Moieties. *Colloids and Surfaces A: Physicochemical and Engineering Aspects* **2002**, *204* (1), 1–7.
(130) Jonas, U.; Campo, A. del; Krüger, C.; Glasser, G.; Boos, D. Colloidal Assemblies on Patterned Silane Layers. *PNAS* **2002**, *99* (8), 5034–5039.
(131) Pirrung, M. C. How to Make a DNA Chip. *Angew. Chem. Int. Ed.* **2002**, *41* (8), 1276–1289.
(132) McGall, G. H.; Barone, A. D.; Diggelmann, M.; Fodor, S. P. A.; Gentalen, E.; Ngo, N. The Efficiency of Light-Directed Synthesis of DNA Arrays on Glass Substrates. *J. Am. Chem. Soc.* **1997**, *119* (22), 5081–5090.
(133) Wilson, D. S.; Nock, S. Recent Developments in Protein Microarray Technology. *Angewandte Chemie International Edition* **2003**, *42* (5), 494–500.
(134) Fodor, S. P.; Read, J. L.; Pirrung, M. C.; Stryer, L.; Lu, A. T.; Solas, D. Light-Directed, Spatially Addressable Parallel Chemical Synthesis. *Science* **1991**, *251* (4995), 767–773.
(135) Cheung, V. G.; Morley, M.; Aguilar, F.; Massimi, A.; Kucherlapati, R.; Childs, G. Making and Reading Microarrays. *Nature Genetics* **1999**, *21* (1s), 15.
(136) McGall, G. H.; Fidanza, J. A. Photolithographic Synthesis of High-Density Oligonucleotide Arrays. In *DNA Arrays*; Methods in Molecular Biology™; Humana Press, 2001; pp 71–101.
(137) Kalorama Information. The World Market for Microarrays : Market Research Report https://www.kaloramainformation.com/Microarrays-9618385/ (accessed Jan 18, 2018).
(138) Lipshutz, R. J.; Fodor, S. P. A.; Gingeras, T. R.; Lockhart, D. J. High Density Synthetic Oligonucleotide Arrays. *Nature Genetics* **1999**, *21* (1s), 20.
(139) Brown, P. O.; Botstein, D. Exploring the New World of the Genome with DNA Microarrays. *Nat Genet* **1999**, *21*, 33–37.
(140) Felix, N.; Corliss, D.; Petrillo, K.; Saulnier, N.; Xu, Y.; Meli, L.; Tang, H.; Silva, A. D.; Hamieh, B.; Burkhardt, M.; et al. EUV Patterning Successes and Frontiers. In *Extreme Ultraviolet (EUV) Lithography VII*; International Society for Optics and Photonics, 2016; Vol. 9776, p 97761O.
(141) Seshadri, K.; Froyd, K.; Parikh, A. N.; Allara, D. L.; Lercel, M. J.; Craighead, H. G. Electron-Beam-Induced Damage in Self-Assembled Monolayers. *J. Phys. Chem.* **1996**, *100* (39), 15900–15909.
(142) Lercel, M. J.; Craighead, H. G.; Parikh, A. N.; Seshadri, K.; Allara, D. L. Sub-10 Nm Lithography with Self-assembled Monolayers. *Applied Physics Letters* **1996**, *68* (11), 1504–1506.
(143) Lercel, M.; Redinbo, G.; Pardo, F.; Rooks, M.; Tiberio, R.; Simpson, P.; Craighead, H.; Sheen, C.; Parikh, A.; Allara, D. Electron-Beam Lithography with Monolayers of Alkylthiols and Alkylsiloxanes. *J. Vac. Sci. Technol. B* **1994**, *12* (6), 3663–3667.

(144) Lercel, M. J.; Tiberio, R. C.; Chapman, P. F.; Craighead, H. G.; Sheen, C. W.; Parikh, A. N.; Allara, D. L. Self-assembled Monolayer Electron-beam Resists on GaAs and SiO2. *Journal of Vacuum Science & Technology B: Microelectronics and Nanometer Structures Processing, Measurement, and Phenomena* **1993**, *11* (6), 2823–2828.

(145) Lercel, M. J.; Rooks, M.; Tiberio, R. C.; Craighead, H. G.; Sheen, C. W.; Parikh, A. N.; Allara, D. L. Pattern Transfer of Electron Beam Modified Self-assembled Monolayers for High-resolution Lithography. *Journal of Vacuum Science & Technology B: Microelectronics and Nanometer Structures Processing, Measurement, and Phenomena* **1995**, *13* (3), 1139–1143.

(146) Grigorescu, A. E.; Hagen, C. W. Resists for Sub-20-Nm Electron Beam Lithography with a Focus on HSQ: State of the Art. *Nanotechnology* **2009**, *20* (29), 292001.

(147) Terris, B. D.; Mamin, H. J.; Best, M. E.; Logan, J. A.; Rugar, D.; Rishton, S. A. Nanoscale Replication for Scanning Probe Data Storage. *Appl. Phys. Lett.* **1996**, *69* (27), 4262–4264.

(148) Zhang, G.-J.; Tanii, T.; Zako, T.; Hosaka, T.; Miyake, T.; Kanari, Y.; Funatsu, T.; Ohdomari, I. Nanoscale Patterning of Protein Using Electron Beam Lithography of Organosilane Self-Assembled Monolayers. *Small* **2005**, *1* (8–9), 833–837.

(149) Krupke, R.; Malik, S.; Weber, H. B.; Hampe, O.; Kappes, M. M.; v. Löhneysen, H. Patterning and Visualizing Self-Assembled Monolayers with Low-Energy Electrons. *Nano Lett.* **2002**, *2* (10), 1161–1164.

(150) Harnett, C. K.; Satyalakshmi, K. M.; Craighead, H. G. Low-Energy Electron-Beam Patterning of Amine-Functionalized Self-Assembled Monolayers. *Applied Physics Letters* **2000**, *76* (17), 2466–2468.

(151) Sato, T.; Hasko, D. G.; Ahmed, H. Nanoscale Colloidal Particles: Monolayer Organization and Patterning. *Journal of Vacuum Science & Technology B: Microelectronics and Nanometer Structures Processing, Measurement, and Phenomena* **1997**, *15* (1), 45–48.

(152) Choi, K. H.; Bourgoin, J. P.; Auvray, S.; Esteve, D.; Duesberg, G. S.; Roth, S.; Burghard, M. Controlled Deposition of Carbon Nanotubes on a Patterned Substrate. *Surf. Sci.* **2000**, *462* (1–3), 195–202.

(153) Pallandre, A.; Glinel, K.; Jonas, A. M.; Nysten, B. Binary Nanopatterned Surfaces Prepared from Silane Monolayers. *Nano Lett.* **2004**, *4* (2), 365–371.

(154) Senaratne, W.; Sengupta, P.; Jakubek, V.; Holowka, D.; Ober, C. K.; Baird, B. Functionalized Surface Arrays for Spatial Targeting of Immune Cell Signaling. *J. Am. Chem. Soc.* **2006**, *128* (17), 5594–5595.

(155) Cai, H.; Wolfenson, H.; Depoil, D.; Dustin, M. L.; Sheetz, M. P.; Wind, S. J. Molecular Occupancy of Nanodot Arrays. *ACS Nano* **2016**.

(156) Pillers, M.; Goss, V.; Lieberman, M. Electron-Beam Lithography and Molecular Liftoff for Directed Attachment of DNA Nanostructures on Silicon: Top-down Meets Bottom-Up. *Acc. Chem. Res.* **2014**, *47* (6), 1759–1767.

(157) Cai, H.; Wind, S. J. Improved Glass Surface Passivation for Single-Molecule Nanoarrays. *Langmuir* **2016**, *32* (39), 10034–10041.

(158) Shah, F. A.; Nan Kim, K.; Lieberman, M.; Bernstein, G. H. Roughness Optimization of Electron-Beam Exposed Hydrogen Silsesquioxane for Immobilization of DNA Origami.

Journal of Vacuum Science & Technology B, Nanotechnology and Microelectronics: Materials, Processing, Measurement, and Phenomena **2012**, *30* (1), 011806.
(159) Fetterly, C. R.; Olsen, B. C.; Luber, E. J.; Buriak, J. M. Vapor-Phase Nanopatterning of Aminosilanes with Electron Beam Lithography: Understanding and Minimizing Background Functionalization. *Langmuir* **2018**.
(160) Wasserman, S. R.; Tao, Y. T.; Whitesides, G. M. Structure and Reactivity of Alkylsiloxane Monolayers Formed by Reaction of Alkyltrichlorosilanes on Silicon Substrates. *Langmuir* **1989**, *5* (4), 1074–1087.
(161) Pujari, S. P.; Scheres, L.; Marcelis, A. T. M.; Zuilhof, H. Covalent Surface Modification of Oxide Surfaces. *Angew. Chem. Int. Ed.* **2014**, n/a-n/a.
(162) Maoz, R.; Burshtain, D.; Cohen, H.; Nelson, P.; Berson, J.; Yoffe, A.; Sagiv, J. Site-Targeted Interfacial Solid-Phase Chemistry: Surface Functionalization of Organic Monolayers via Chemical Transformations Locally Induced at the Boundary between Two Solids. *Angew. Chem. Int. Ed.* **2016**, *55* (40), 12366–12371.
(163) Berson, J.; Burshtain, D.; Zeira, A.; Yoffe, A.; Maoz, R.; Sagiv, J. Single-Layer Ionic Conduction on Carboxyl-Terminated Silane Monolayers Patterned by Constructive Lithography. *Nature Materials* **2015**, *14* (6), 613.
(164) Markov, A.; Wolf, N.; Yuan, X.; Mayer, D.; Maybeck, V.; Offenhäusser, A.; Wördenweber, R. Controlled Engineering of Oxide Surfaces for Bioelectronics Applications Using Organic Mixed Monolayers. *ACS Appl. Mater. Interfaces* **2017**, *9* (34), 29265–29272.
(165) Tran, N. T.; Flanagan, D. P.; Orlicki, J. A.; Lenhart, J. L.; Proctor, K. L.; Knorr, D. B. Polydopamine and Polydopamine–Silane Hybrid Surface Treatments in Structural Adhesive Applications. *Langmuir* **2018**, *34* (4), 1274–1286.
(166) Dellacherie, M. O.; Li, A. W.; Lu, B. Y.; Mooney, D. J. Covalent Conjugation of Peptide Antigen to Mesoporous Silica Rods to Enhance Cellular Responses. *Bioconjugate Chem.* **2018**.
(167) Zhang, F.-T.; Xu, L.; Chen, J.-H.; Zhao, B.; Fu, X.-Z.; Sun, R.; Chen, Q.; Wong, C.-P. Electroless Deposition Metals on Poly(Dimethylsiloxane) with Strong Adhesion As Flexible and Stretchable Conductive Materials. *ACS Appl. Mater. Interfaces* **2018**, *10* (2), 2075–2082.
(168) Sukham, J.; Takayama, O.; Lavrinenko, A. V.; Malureanu, R. High-Quality Ultrathin Gold Layers with an APTMS Adhesion for Optimal Performance of Surface Plasmon Polariton-Based Devices. *ACS Appl. Mater. Interfaces* **2017**, *9* (29), 25049–25056.
(169) Fu, P.; Guo, X.; Wang, S.; Ye, Y.; Li, C. Aminosilane as a Molecular Linker between the Electron-Transport Layer and Active Layer for Efficient Inverted Polymer Solar Cells. *ACS Appl. Mater. Interfaces* **2017**, *9* (15), 13390–13395.
(170) Blitz, J. P.; Murthy, R. S. S.; Leyden, D. E. Ammonia-Catalyzed Silylation Reactions of Cab-O-Sil with Methoxymethylsilanes. *J. Am. Chem. Soc.* **1987**, *109* (23), 7141–7145.
(171) Fang, G.-Y.; Xu, L.-N.; Cao, Y.-Q.; Wang, L.-G.; Wu, D.; Li, A.-D. Self-Catalysis by Aminosilanes and Strong Surface Oxidation by O 2 Plasma in Plasma-Enhanced Atomic Layer Deposition of High-Quality SiO 2. *Chemical Communications* **2015**, *51* (7), 1341–1344.

(172) Ye, S.; Jiang, L.; Wu, J.; Su, C.; Huang, C.; Liu, X.; Shao, W. Flexible Amoxicillin-Grafted Bacterial Cellulose Sponges for Wound Dressing: In Vitro and in Vivo Evaluation. *ACS Appl. Mater. Interfaces* **2018**.

(173) Kao, T.; Kohle, F.; Ma, K.; Aubert, T.; Andrievsky, A.; Wiesner, U. Fluorescent Silica Nanoparticles with Well-Separated Intensity Distributions from Batch Reactions. *Nano Lett.* **2018**, *18* (2), 1305–1310.

(174) Karim, A. H.; Jalil, A. A.; Triwahyono, S.; Sidik, S. M.; Kamarudin, N. H. N.; Jusoh, R.; Jusoh, N. W. C.; Hameed, B. H. Amino Modified Mesostructured Silica Nanoparticles for Efficient Adsorption of Methylene Blue. *Journal of Colloid and Interface Science* **2012**, *386* (1), 307–314.

(175) Xu, J.; Yang, P.; Sun, M.; Bi, H.; Liu, B.; Yang, D.; Gai, S.; He, F.; Lin, J. Highly Emissive Dye-Sensitized Upconversion Nanostructure for Dual-Photosensitizer Photodynamic Therapy and Bioimaging. *ACS Nano* **2017**, *11* (4), 4133–4144.

(176) Wassel, E.; Es-Souni, M.; Berger, N.; Schopf, D.; Dietze, M.; Solterbeck, C.-H.; Es-Souni, M. Nanocomposite Films of Laponite/PEG-Grafted Polymers and Polymer Brushes with Nonfouling Properties. *Langmuir* **2017**, *33* (27), 6739–6750.

(177) Li, H.; Zhang, J.; Zhou, X.; Lu, G.; Yin, Z.; Li, G.; Wu, T.; Boey, F.; Venkatraman, S. S.; Zhang, H. Aminosilane Micropatterns on Hydroxyl-Terminated Substrates: Fabrication and Applications. *Langmuir* **2010**, *26* (8), 5603–5609.

(178) Sathish, S.; Ricoult, S. G.; Toda-Peters, K.; Shen, A. Q. Microcontact Printing with Aminosilanes: Creating Biomolecule Micro- and Nanoarrays for Multiplexed Microfluidic Bioassays. *Analyst* **2017**, *142* (10), 1772–1781.

(179) George, A.; Blank, D. H. A.; ten Elshof, J. E. Nanopatterning from the Gas Phase: High Resolution Soft Lithographic Patterning of Organosilane Thin Films. *Langmuir* **2009**, *25* (23), 13298–13301.

(180) George, A.; Knez, M.; Hlawacek, G.; Hagedoorn, D.; Verputten, H. H. J.; van Gastel, R.; ten Elshof, J. E. Nanoscale Patterning of Organosilane Molecular Thin Films from the Gas Phase and Its Applications: Fabrication of Multifunctional Surfaces and Large Area Molecular Templates for Site-Selective Material Deposition. *Langmuir* **2012**, *28* (5), 3045–3052.

(181) Li, J.-R.; Garno, J. C. Elucidating the Role of Surface Hydrolysis in Preparing Organosilane Nanostructures via Particle Lithography. *Nano Lett.* **2008**, *8* (7), 1916–1922.

(182) Li, J.-R.; Lusker, K. L.; Yu, J.-J.; Garno, J. C. Engineering the Spatial Selectivity of Surfaces at the Nanoscale Using Particle Lithography Combined with Vapor Deposition of Organosilanes. *ACS Nano* **2009**, *3* (7), 2023–2035.

(183) Brownfield, A. L.; Causey, C. P.; Mullen, T. J. Effects of Surface Water on Organosilane Nanostructure Fabrication Using Particle Lithography. *Thin Solid Films* **2015**, *594*, *Part A*, 184–191.

(184) Kulkarni, S. A.; Lyles, V. D.; Serem, W. K.; Lu, L.; Kumar, R.; Garno, J. C. Solvent-Responsive Properties of Octadecyltrichlorosiloxane Nanostructures Investigated Using Atomic Force Microscopy in Liquid. *Langmuir* **2014**, *30* (19), 5466–5473.

(185) Ishida, N.; Nishihara, R.; Imanaka, H.; Imamura, K. Nanostructures of 3-Aminopropyltriethoxysilane Created on Flat Substrate by Combining Colloid

Lithography and Vapor Deposition. *Colloids and Surfaces A: Physicochemical and Engineering Aspects* **2016**, *495* (Supplement C), 39–45.
(186) Li, J.-R.; Ross, S. S.; Liu, Y.; Liu, Y. X.; Wang, K.; Chen, H.-Y.; Liu, F.-T.; Laurence, T. A.; Liu, G. Engineered Nanostructures of Haptens Lead to Unexpected Formation of Membrane Nanotubes Connecting Rat Basophilic Leukemia Cells. *ACS Nano* **2015**, *9* (7), 6738–6746.
(187) Surwade, S. P.; Zhou, F.; Li, Z.; Powell, A.; O'Donnell, C.; Liu, H. Nanoscale Patterning of Self-Assembled Monolayers Using DNA Nanostructure Templates. *Chem. Commun.* **2016**, *52* (8), 1677–1680.
(188) El Zubir, O.; Xia, S.; Ducker, R. E.; Wang, L.; Mullin, N.; Cartron, M. L.; Cadby, A. J.; Hobbs, J. K.; Hunter, C. N.; Leggett, G. J. From Monochrome to Technicolor: Simple Generic Approaches to Multicomponent Protein Nanopatterning Using Siloxanes with Photoremovable Protein-Resistant Protecting Groups. *Langmuir* **2017**, *33* (35), 8829–8837.
(189) Xia, S.; Cartron, M.; Morby, J.; Bryant, D. A.; Hunter, C. N.; Leggett, G. J. Fabrication of Nanometer- and Micrometer-Scale Protein Structures by Site-Specific Immobilization of Histidine-Tagged Proteins to Aminosiloxane Films with Photoremovable Protein-Resistant Protecting Groups. *Langmuir* **2016**, *32* (7), 1818–1827.
(190) Lau, U. Y.; Saxer, S. S.; Lee, J.; Bat, E.; Maynard, H. D. Direct Write Protein Patterns for Multiplexed Cytokine Detection from Live Cells Using Electron Beam Lithography. *ACS Nano* **2016**, *10* (1), 723–729.
(191) Kolodziej, C. M.; Maynard, H. D. Electron-Beam Lithography for Patterning Biomolecules at the Micron and Nanometer Scale. *Chem. Mater.* **2012**, *24* (5), 774–780.
(192) Mancini, R. J.; Paluck, S. J.; Bat, E.; Maynard, H. D. Encapsulated Hydrogels by E-Beam Lithography and Their Use in Enzyme Cascade Reactions. *Langmuir* **2016**, *32* (16), 4043–4051.
(193) Horzum, U.; Ozdil, B.; Pesen-Okvur, D. Differentiation of Normal and Cancer Cell Adhesion on Custom Designed Protein Nanopatterns. *Nano Lett.* **2015**, *15* (8), 5393–5403.
(194) Kim, S.; Marelli, B.; Brenckle, M. A.; Mitropoulos, A. N.; Gil, E.-S.; Tsioris, K.; Tao, H.; Kaplan, D. L.; Omenetto, F. G. All-Water-Based Electron-Beam Lithography Using Silk as a Resist. *Nature Nanotechnology* **2014**, *9* (4), 306–310.
(195) Kumagai, S.; Yoshii, S.; Yamada, K.; Fujiwara, I.; Matsukawa, N.; Yamashita, I. Nanopatterning of Vapor-Deposited Aminosilane Film Using EB Lithography for Ferritin Protein Adsorption. *J. Photopol. Sci. Technol.* **2005**, *18* (4), 495–500.
(196) Zhang, F.; Sautter, K.; Larsen, A. M.; Findley, D. A.; Davis, R. C.; Samha, H.; Linford, M. R. Chemical Vapor Deposition of Three Aminosilanes on Silicon Dioxide: Surface Characterization, Stability, Effects of Silane Concentration, and Cyanine Dye Adsorption. *Langmuir* **2010**, *26* (18), 14648–14654.
(197) Rébiscoul, D.; Perrut, V.; Morel, T.; Jayet, C.; Cubitt, R.; Haumesser, P. H. Alkoxysilane Layers Compatible with Cu Deposition: Towards New Diffusion Barriers? *Microelectronic Engineering* **2012**, *92*, 45–48.

(198) Raiber, K.; Terfort, A.; Benndorf, C.; Krings, N.; Strehblow, H.-H. Removal of Self-Assembled Monolayers of Alkanethiolates on Gold by Plasma Cleaning. *Surface Science* **2005**, *595* (1), 56–63.

(199) Ma, L.-C.; Subramanian, R.; Huang, H.-W.; Ray, V.; Kim, C.-U.; Koh, S. J. Electrostatic Funneling for Precise Nanoparticle Placement: A Route to Wafer-Scale Integration. *Nano Lett.* **2007**, *7* (2), 439–445.

(200) Grabar, K. C.; Freeman, R. G.; Hommer, M. B.; Natan, M. J. Preparation and Characterization of Au Colloid Monolayers. *Anal. Chem.* **1995**, *67* (4), 735–743.

(201) Haddada, M. B.; Blanchard, J.; Casale, S.; Krafft, J.-M.; Vallée, A.; Méthivier, C.; Boujday, S. Optimizing the Immobilization of Gold Nanoparticles on Functionalized Silicon Surfaces: Amine- vs Thiol-Terminated Silane. *Gold Bull* **2013**, *46* (4), 335–341.

(202) Dalstein, L.; Ben Haddada, M.; Barbillon, G.; Humbert, C.; Tadjeddine, A.; Boujday, S.; Busson, B. Revealing the Interplay between Adsorbed Molecular Layers and Gold Nanoparticles by Linear and Nonlinear Optical Properties. *J. Phys. Chem. C* **2015**, *119* (30), 17146–17155.

(203) Liebig, F.; Sarhan, R. M.; Sander, M.; Koopman, W.; Schuetz, R.; Bargheer, M.; Koetz, J. Deposition of Gold Nanotriangles in Large Scale Close-Packed Monolayers for X-Ray-Based Temperature Calibration and SERS Monitoring of Plasmon-Driven Catalytic Reactions. *ACS Appl. Mater. Interfaces* **2017**, *9* (23), 20247–20253.

(204) Hughes, R. A.; Menumerov, E.; Neretina, S. When Lithography Meets Self-Assembly: A Review of Recent Advances in the Directed Assembly of Complex Metal Nanostructures on Planar and Textured Surfaces. *Nanotechnology* **2017**, *28* (28), 282002.

(205) Jiang, L.; Chen, X.; Lu, N.; Chi, L. Spatially Confined Assembly of Nanoparticles. *Acc. Chem. Res.* **2014**, *47* (10), 3009–3017.

(206) Flauraud, V.; Regmi, R.; Winkler, P. M.; Alexander, D. T. L.; Rigneault, H.; van Hulst, N. F.; García-Parajo, M. F.; Wenger, J.; Brugger, J. In-Plane Plasmonic Antenna Arrays with Surface Nanogaps for Giant Fluorescence Enhancement. *Nano Lett.* **2017**, *17* (3), 1703–1710.

(207) Yang, J.; Ichii, T.; Murase, K.; Sugimura, H. Site-Selective Assembly and Reorganization of Gold Nanoparticles along Aminosilane-Covered Nanolines Prepared on Indium–Tin Oxide. *Langmuir* **2012**, *28* (20), 7579–7584.

(208) Berens, A. R.; Hopfenberg, H. B. Diffusion of Organic Vapors at Low Concentrations in Glassy PVC, Polystyrene, and PMMA. *Journal of Membrane Science* **1982**, *10* (2), 283–303.

(209) Song, X.; Ma, Y.; Wang, C.; Dietrich, P. M.; Unger, W. E. S.; Luo, Y. Effects of Protonation, Hydrogen Bonding, and Photodamaging on X-Ray Spectroscopy of the Amine Terminal Group in Aminothiolate Monolayers. *J. Phys. Chem. C* **2012**, *116* (23), 12649–12654.

(210) Sakai, Y.; Sadaoka, Y.; Matsuguchi, M. Humidity Sensors Based on Polymer Thin Films. *Sensors and Actuators B: Chemical* **1996**, *35* (1), 85–90.

(211) Lee, W.-J.; Chang, J.-G.; Ju, S.-P. Hydrogen-Bond Structure at the Interfaces between Water/Poly(Methyl Methacrylate), Water/Poly(Methacrylic Acid), and Water/Poly(2-Aminoethylmethacrylamide). *Langmuir* **2010**, *26* (15), 12640–12647.

(212) Berger, C. M.; Henderson, C. L. The Effect of Humidity on Water Sorption in Photoresist Polymer Thin Films. *Polymer* **2003**, *44* (7), 2101–2108.
(213) Macintyre, D. S.; Ignatova, O.; Thoms, S.; Thayne, I. G. Resist Residues and Transistor Gate Fabrication. *Journal of Vacuum Science & Technology B: Microelectronics and Nanometer Structures Processing, Measurement, and Phenomena* **2009**, *27* (6), 2597–2601.
(214) Turner, D. T. Water Sorption of Poly(Methyl Methacrylate): 1. Effects of Molecular Weight. *Polymer* **1987**, *28* (2), 293–296.
(215) Shokouhi, B.; Zhang, J.; Cui, B. Very High Sensitivity ZEP Resist Using MEK:MIBK Developer. *IET Micro Nano Letters* **2011**, *6* (12), 992–994.
(216) Hang, Q.; Hill, D. A.; Bernstein, G. H. Efficient Removers for Poly(Methylmethacrylate). *Journal of Vacuum Science & Technology B* **2003**, *21* (1), 91–97.
(217) Huang, W.; Qian, W.; El-Sayed, M. A. Coherent Vibrational Oscillation in Gold Prismatic Monolayer Periodic Nanoparticle Arrays. *Nano Lett.* **2004**, *4* (9), 1741–1747.
(218) Gangnaik, A. S.; Georgiev, Y. M.; Holmes, J. D. New Generation Electron Beam Resists: A Review. *Chem. Mater.* **2017**, *29* (5), 1898–1917.
(219) Mohammad, M. A.; Koshelev, K.; Fito, T.; Zheng, D. A. Z.; Stepanova, M.; Dew, S. Study of Development Processes for ZEP-520 as a High-Resolution Positive and Negative Tone Electron Beam Lithography Resist. *Jpn. J. Appl. Phys.* **2012**, *51* (6S), 06FC05.
(220) Cheng, Z. A.; Zouani, O. F.; Glinel, K.; Jonas, A. M.; Durrieu, M.-C. Bioactive Chemical Nanopatterns Impact Human Mesenchymal Stem Cell Fate. *Nano Lett.* **2013**, *13* (8), 3923–3929.
(221) Schvartzman, M.; Wind, S. J. Robust Pattern Transfer of Nanoimprinted Features for Sub-5-Nm Fabrication. *Nano Lett.* **2009**, *9* (10), 3629–3634.
(222) Nishida, T.; Notomi, M.; Iga, R.; Tamamura, T. Quantum Wire Fabrication by E-Beam Elithography Using High-Resolution and High-Sensitivity E-Beam Resist ZEP-520. *Jpn. J. Appl. Phys.* **1992**, *31* (12S), 4508.
(223) Anderson, A. S.; Dattelbaum, A. M.; Montaño, G. A.; Price, D. N.; Schmidt, J. G.; Martinez, J. S.; Grace, W. K.; Grace, K. M.; Swanson, B. I. Functional PEG-Modified Thin Films for Biological Detection. *Langmuir* **2008**, *24* (5), 2240–2247.
(224) White, L. D.; Tripp, C. P. Reaction of (3-Aminopropyl)Dimethylethoxysilane with Amine Catalysts on Silica Surfaces. *Journal of Colloid and Interface Science* **2000**, *232* (2), 400–407.
(225) Murphy, M. A.; Nordgren, C. E.; Fischetti, R. F.; Blasie, J. K.; Peticolas, L. J.; Bean, J. C. Structural Study of the Annealing of Alkylsiloxane Self-Assembled Monolayers on Silicon by High-Resolution X-Ray Diffraction. *J. Phys. Chem.* **1995**, *99* (38), 14039–14051.
(226) Turkevich, J.; Stevenson, P. C.; Hillier, J. A Study of the Nucleation and Growth Processes in the Synthesis of Colloidal Gold. *Discuss. Faraday Soc.* **1951**, *11* (0), 55–75.
(227) Kimling, J.; Maier, M.; Okenve, B.; Kotaidis, V.; Ballot, H.; Plech, A. Turkevich Method for Gold Nanoparticle Synthesis Revisited. *J. Phys. Chem. B* **2006**, *110* (32), 15700–15707.

(228) Cao, B.; He, X.; Fetterly, C. R.; Olsen, B. C.; Luber, E. J.; Buriak, J. M. Role of Interfacial Layers in Organic Solar Cells: Energy Level Pinning versus Phase Segregation. *ACS Appl. Mater. Interfaces* **2016**, *8* (28), 18238–18248.
(229) Nečas, D.; Klapetek, P. Gwyddion: An Open-Source Software for SPM Data Analysis. *centr.eur.j.phys.* **2012**, *10* (1), 181–188.
(230) Schindelin, J.; Arganda-Carreras, I.; Frise, E.; Kaynig, V.; Longair, M.; Pietzsch, T.; Preibisch, S.; Rueden, C.; Saalfeld, S.; Schmid, B.; et al. Fiji: An Open-Source Platform for Biological-Image Analysis. *Nature Methods* **2012**, *9* (7), 676–682.
(231) Grella, L.; Lorusso, G.; Niemi, T.; Adler, D. L. Simulations of SEM Imaging and Charging. *Nuclear Instruments and Methods in Physics Research Section A: Accelerators, Spectrometers, Detectors and Associated Equipment* **2004**, *519* (1), 242–250.
(232) Wilson, N. R.; Macpherson, J. V. Carbon Nanotube Tips for Atomic Force Microscopy. *Nature Nanotechnology* **2009**, *4* (8), 483–491.
(233) Liu, Y.; Shen, L. From Langmuir Kinetics to First- and Second-Order Rate Equations for Adsorption. *Langmuir* **2008**, *24* (20), 11625–11630.
(234) Im, H.; Bantz, K. C.; Lindquist, N. C.; Haynes, C. L.; Oh, S.-H. Vertically Oriented Sub-10-Nm Plasmonic Nanogap Arrays. *Nano Lett.* **2010**, *10* (6), 2231–2236.
(235) Tanaka, T.; Morigami, M.; Atoda, N. Mechanism of Resist Pattern Collapse during Development Process. *Jpn. J. Appl. Phys.* **1993**, *32* (12S), 6059.
(236) Desai, V. U.; Hartley, J. G.; Cady, N. C. Electron Beam Lithography Patterned Hydrogen Silsesquioxane Resist as a Mandrel for Self-Aligned Double Patterning Application. *Journal of Vacuum Science & Technology B, Nanotechnology and Microelectronics: Materials, Processing, Measurement, and Phenomena* **2016**, *34* (6), 061601.
(237) Chen, H.-W.; Verhaverbeke, S.; Gouk, R.; Leschkies, K.; Sun, S.; Bekiaris, N.; Visser, R. J. (Invited) Supercritical Drying: A Sustainable Solution to Pattern Collapse of High-Aspect-Ratio and Low-Mechanical-Strength Device Structures. *Meet. Abstr.* **2015**, *MA2015-02* (27), 1023–1023.
(238) George, A.; Blank, D. H. A.; ten Elshof, J. E. Nanopatterning from the Gas Phase: High Resolution Soft Lithographic Patterning of Organosilane Thin Films. *Langmuir* **2009**, *25* (23), 13298–13301.
(239) George, A.; Knez, M.; Hlawacek, G.; Hagedoorn, D.; Verputten, H. H. J.; van Gastel, R.; ten Elshof, J. E. Nanoscale Patterning of Organosilane Molecular Thin Films from the Gas Phase and Its Applications: Fabrication of Multifunctional Surfaces and Large Area Molecular Templates for Site-Selective Material Deposition. *Langmuir* **2012**, *28* (5), 3045–3052.
(240) Pick, C.; Argento, C.; Drazer, G.; Frechette, J. Micropatterned Charge Heterogeneities via Vapor Deposition of Aminosilanes. *Langmuir* **2015**, *31* (39), 10725–10733.
(241) Li, S.; Wang, X.; Cao, B.; Ye, K.; Li, Z.; Ding, J. Effects of Nanoscale Spatial Arrangement of Arginine–Glycine–Aspartate Peptides on Dedifferentiation of Chondrocytes. *Nano Lett.* **2015**, *15* (11), 7755–7765.
(242) Frei, R.; Blitz, J. P.; Gun'ko, V. M.; Frost, B. E.; Sergeev, V. S. Kinetics and Computational Studies of an Aminosilane Reaction with a Silsesquioxane Silanol. *The Journal of Physical Chemistry A* **2009**, *113* (24), 6612–6619.

(243) Chen, Y.; Xu, X.; Chen, H.; Miao, L.; Blanco, P.; Cai, M.-P.; Ngai, C. S. Sub-20 Nm Trench Patterning with a Hybrid Chemical Shrink and SAFIER Process; International Society for Optics and Photonics, 2009; Vol. 7273, p 72733I.
(244) Hong, S.; Takano, Y.; Kanda, T.; Kudo, T.; Padmanaban, M.; Tanaka, H.; Lee, S.-H.; Lee, J.-H.; Woo, S.-G. Advanced RELACS (Resolution Enhancment of Lithography by Assist of Chemical Shrink) Material for 193-Nm Lithography; International Society for Optics and Photonics, 2003; Vol. 5039, pp 195–207.
(245) 2015 International Technology Roadmap for Semiconductors (ITRS) https://www.semiconductors.org/main/2015_international_technology_roadmap_for_semiconductors_itrs/ (accessed Mar 17, 2018).
(246) Bencher, C.; Dai, H.; Miao, L.; Chen, Y.; Xu, P.; Chen, Y.; Oemardani, S.; Sweis, J.; Wiaux, V.; Hermans, J.; et al. Mandrel-Based Patterning: Density Multiplication Techniques for 15nm Nodes; International Society for Optics and Photonics, 2011; Vol. 7973, p 79730K.
(247) Lin, B. J. Making Double Patterning Cost Single. *JM3, JMMMGF* **2009**, *8* (1), 010101.
(248) Zimmerman, P. Double patterning lithography: double the trouble or double the fun? | SPIE Homepage: SPIE http://www.spie.org/newsroom/1691-double-patterning-lithography-double-the-trouble-or-double-the-fun?SSO=1 (accessed Jan 2, 2018).
(249) Crouse, M. M.; Uchida, R.; Dommelen, Y. van; Ando, T.; Schmitt-Weaver, E. P.; Takeshita, M.; Wu, S.; Routh, R. M. Litho-Only Double Patterning Approaches: Positive–Negative versus Positive–Positive Tone. *JM3, JMMMGF* **2009**, *8* (1), 011006.
(250) Maenhoudt, M.; Gronheid, R.; Stepanenko, N.; Matsuda, T.; Vangoidsenhoven, D. Alternative Process Schemes for Double Patterning That Eliminate the Intermediate Etch Step; International Society for Optics and Photonics, 2008; Vol. 6924, p 69240P.
(251) Bencher, C.; Chen, Y.; Dai, H.; Montgomery, W.; Huli, L. 22nm Half-Pitch Patterning by CVD Spacer Self Alignment Double Patterning (SADP); International Society for Optics and Photonics, 2008; Vol. 6924, p 69244E.
(252) Belyansky, M. P.; Conti, R.; Khan, S.; Zhou, X.; Klymko, N. R.; Yao, Y.; Madan, A.; Tai, L.; Flaitz, P.; Ando, T. Atomic Layer Deposition of Sidewall Spacers: Process, Equipment and Integration Challenges in State-of-the-Art Logic Technologies. *ECS Trans.* **2014**, *61* (3), 39–45.
(253) Choi, Y.-K.; King, T.-J.; Hu, C. A Spacer Patterning Technology for Nanoscale CMOS. *IEEE Transactions on Electron Devices* **2002**, *49* (3), 436–441.
(254) Jeong, H.; Lee, J.; Bok, C.; Lee, S. H.; Yoo, S. Fabrication of Vertical Silicon Nanotube Array Using Spacer Patterning Technique and Metal-Assisted Chemical Etching. *IEEE Transactions on Nanotechnology* **2017**, *16* (1), 130–134.
(255) Han, T.; Gu, M.; Grunow, S.; Liu, H.; Sankaran, S.; Liu, J. Forming a More Robust Sidewall Spacer with Lower k (Dielectric Constant) Value. In *2017 China Semiconductor Technology International Conference (CSTIC)*; 2017; pp 1–3.
(256) Faraz, T.; van Drunen, M.; Knoops, H. C. M.; Mallikarjunan, A.; Buchanan, I.; Hausmann, D. M.; Henri, J.; Kessels, W. M. M. Atomic Layer Deposition of Wet-Etch Resistant Silicon Nitride Using Di(Sec-Butylamino)Silane and N2 Plasma on Planar and 3D Substrate Topographies. *ACS Appl. Mater. Interfaces* **2017**, *9* (2), 1858–1869.

(257) Hsu, D. S.-H.; Yaguchi, H.; Sakamoto, R.; Maruyama, D.; Sakaida, Y.; Wang, W.; Huang, C.-Y.; Wu, W.-B.; Ho, B.-C.; Shih, C.-L. Carbon-Rich Spin on Sidewall Material for Self-Aligned Double Patterning Technology. In *Advances in Resist Materials and Processing Technology Xxvii, Pts 1 and 2*; Allen, R. D., Somervell, M. H., Eds.; Spie-Int Soc Optical Engineering: Bellingham, 2010; Vol. 7639, p UNSP 763908.

(258) Kim, H.; Sun, M.-C.; Hwang, S.; Kim, H.-M.; Lee, J.-H.; Park, B.-G. Fabrication of Asymmetric Independent Dual-Gate FinFET Using Sidewall Spacer Patterning and CMP Processes. *Microelectronic Engineering* **2018**, *185–186*, 29–34.

(259) Hsieh, W.; Liang, M.; Shieh, J. Organosilicate Polymer Mandrel for Self-Aligned Double Patterning Process. 9123656, September 1, 2015.

(260) Hashim, U.; Salleh, S.; Rahman, S. F. A.; Abdullah, A. R. A. J. Design and Fabrication of Nanowire-Based Conductance Biosensor Using Spacer Patterning Technique. In *2008 International Conference on Electronic Design*; 2008; pp 1–5.

(261) Dhuey, S.; Peroz, C.; Olynick, D.; Calafiore, G.; Cabrini, S. Obtaining Nanoimprint Template Gratings with 10 Nm Half-Pitch by Atomic Layer Deposition Enabled Spacer Double Patterning. *Nanotechnology* **2013**, *24* (10), 105303.

(262) Bao, X. Y.; Yi, H.; Bencher, C.; Chang, L. W.; Dai, H.; Chen, Y.; Chen, P. T. J.; Wong, H. S. P. SRAM, NAND, DRAM Contact Hole Patterning Using Block Copolymer Directed Self-Assembly Guided by Small Topographical Templates. In *2011 International Electron Devices Meeting*; 2011; pp 7.7.1-7.7.4.

(263) Miao, X.; Huli, L.; Chen, H.; Xu, X.; Woo, H.; Bencher, C.; Shu, J.; Ngai, C.; Borst, C. Double Patterning Combined with Shrink Technique to Extend ArF Lithography for Contact Holes to 22nm Node and Beyond; International Society for Optics and Photonics, 2008; Vol. 6924, p 69240A.

(264) Petrillo, K.; Horak, D.; Fan, S.; McLellan, E.; Colburn, M.; Metz, A.; Dunn, S.; Hetzer, D.; Cantone, J.; Ueda, K.; et al. Utilization of Spin-on and Reactive Ion Etch Critical Dimension Shrink with Double Patterning for 32 Nm and beyond Contact Level Interconnects; International Society for Optics and Photonics, 2009; Vol. 7273, p 72731A.

(265) Kim, J.-S.; Choi, C.-I.; Kim, M.-S.; Bok, C.-K.; Kim, H.-S.; Baik, K.-H. Implementation of Sub-150 Nm Contact Hole Pattern by Resist Flow Process. *Jpn. J. Appl. Phys.* **1998**, *37* (12S), 6863.

(266) Lee, T.-Y.; Yu, C.-Y.; Hsui, M.-Y.; Hayashi, R.; Hirayama, T.; Iwai, T.; Komano, H.; Shih, J. C.; Owe-Yang, D. C.; Ho, B.-C. Thermal Flow Property for 193nm Photoresist with Low Dispersion Polymer. *J. Photopol. Sci. Technol.* **2004**, *17* (4), 541–544.

(267) Ishibashi, T.; Toyoshima, T.; Yasuda, N.; Kanda, T.; Tanaka, H.; Kinoshita, Y.; Watase, N.; Eakin, R. Advanced Micro-Lithography Process with Chemical Shrink Technology. *Jpn. J. Appl. Phys.* **2001**, *40* (1R), 419.

(268) Arnold, W. H. Guest Editorial: Double-Patterning Lithography. *JM3, JMMMGF* **2009**, *8* (1), 011001.

(269) Nagahara, T.; Sekito, T.; Matsuura, Y. Resist Roughness Improvement by a Chemical Shrink Process; International Society for Optics and Photonics, 2016; Vol. 9777, p 97771J.

(270) Irizarry, R. A.; Bolstad, B. M.; Collin, F.; Cope, L. M.; Hobbs, B.; Speed, T. P. Summaries of Affymetrix GeneChip Probe Level Data. *Nucleic Acids Res* **2003**, *31* (4), e15–e15.
(271) Quackenbush, J. Computational Genetics: Computational Analysis of Microarray Data. *Nature Reviews Genetics* **2001**, *2* (6), 418–427.
(272) Okamoto, T.; Suzuki, T.; Yamamoto, N. Microarray Fabrication with Covalent Attachment of DNA Using Bubble Jet Technology. *Nature Biotechnology* **2000**, *18* (4), 438.
(273) Schena, M.; Heller, R. A.; Theriault, T. P.; Konrad, K.; Lachenmeier, E.; Davis, R. W. Microarrays: Biotechnology's Discovery Platform for Functional Genomics. *Trends in Biotechnology* **1998**, *16* (7), 301–306.
(274) Fodor, S. P. A. DNA SEQUENCING: Massively Parallel Genomics. *Science* **1997**, *277* (5324), 393–395.
(275) Schena, M.; Shalon, D.; Davis, R. W.; Brown, P. O. Quantitative Monitoring of Gene Expression Patterns with a Complementary DNA Microarray. *Science; Washington* **1995**, *270* (5235), 467.
(276) Martin, B. D.; Gaber, B. P.; Patterson, C. H.; Turner, D. C. Direct Protein Microarray Fabrication Using a Hydrogel "Stamper." *Langmuir* **1998**, *14* (15), 3971–3975.
(277) Jonkheijm, P.; Weinrich, D.; Schröder, H.; Niemeyer, C. M.; Waldmann, H. Chemical Strategies for Generating Protein Biochips. *Angewandte Chemie International Edition* **2008**, *47* (50), 9618–9647.
(278) Willner, I.; Katz, E. Integration of Layered Redox Proteins and Conductive Supports for Bioelectronic Applications. *Angewandte Chemie International Edition* **2000**, *39* (7), 1180–1218.
(279) Salaita, K.; Wang, Y.; Mirkin, C. A. Applications of Dip-Pen Nanolithography. *Nature Nanotechnology* **2007**, *2* (3), 145.
(280) Drmanac, R.; Sparks, A. B.; Callow, M. J.; Halpern, A. L.; Burns, N. L.; Kermani, B. G.; Carnevali, P.; Nazarenko, I.; Nilsen, G. B.; Yeung, G.; et al. Human Genome Sequencing Using Unchained Base Reads on Self-Assembling DNA Nanoarrays. *Science* **2010**, *327* (5961), 78–81.
(281) Vieu, C.; Carcenac, F.; Pépin, A.; Chen, Y.; Mejias, M.; Lebib, A.; Manin-Ferlazzo, L.; Couraud, L.; Launois, H. Electron Beam Lithography: Resolution Limits and Applications. *Applied Surface Science* **2000**, *164* (1–4), 111–117.
(282) Kolodziej, C. M.; Kim, S. H.; Broyer, R. M.; Saxer, S. S.; Decker, C. G.; Maynard, H. D. Combination of Integrin-Binding Peptide and Growth Factor Promotes Cell Adhesion on Electron-Beam-Fabricated Patterns. *J. Am. Chem. Soc.* **2012**, *134* (1), 247–255.
(283) Lau, U. Y.; Saxer, S. S.; Lee, J.; Bat, E.; Maynard, H. D. Direct Write Protein Patterns for Multiplexed Cytokine Detection from Live Cells Using Electron Beam Lithography. *ACS Nano* **2015**.
(284) Downing, T. L.; Soto, J.; Morez, C.; Houssin, T.; Fritz, A.; Yuan, F.; Chu, J.; Patel, S.; Schaffer, D. V.; Li, S. Biophysical Regulation of Epigenetic State and Cell Reprogramming. *Nat Mater* **2013**, *12* (12), 1154–1162.
(285) Dalby, M. J.; Gadegaard, N.; Oreffo, R. O. C. Harnessing Nanotopography and Integrin-Matrix Interactions to Influence Stem Cell Fate. *Nat Mater* **2014**, *13* (6), 558–569.

(286) Murphy, W. L.; McDevitt, T. C.; Engler, A. J. Materials as Stem Cell Regulators. *Nat Mater* **2014**, *13* (6), 547–557.
(287) Ventre, M.; Netti, P. A. Engineering Cell Instructive Materials to Control Cell Fate and Functions Through Material Cues and Surface Patterning. *ACS Appl. Mater. Interfaces* **2015**.
(288) Satav, T.; Huskens, J.; Jonkheijm, P. Effects of Variations in Ligand Density on Cell Signaling. *Small* **2015**, *11* (39), 5184–5199.
(289) Amschler, K.; Erpenbeck, L.; Kruss, S.; Schön, M. P. Nanoscale Integrin Ligand Patterns Determine Melanoma Cell Behavior. *ACS Nano* **2014**.
(290) Schvartzman, M.; Palma, M.; Sable, J.; Abramson, J.; Hu, X.; Sheetz, M. P.; Wind, S. J. Nanolithographic Control of the Spatial Organization of Cellular Adhesion Receptors at the Single-Molecule Level. *Nano Lett.* **2011**, *11* (3), 1306–1312.
(291) Pi, F.; Dillard, P.; Alameddine, R.; Benard, E.; Wahl, A.; Ozerov, I.; Charrier, A.; Limozin, L.; Sengupta, K. Size-Tunable Organic Nanodot Arrays: A Versatile Platform for Manipulating and Imaging Cells. *Nano Lett.* **2015**.
(292) Cherniavskaya, O.; Chen, C. J.; Heller, E.; Sun, E.; Provezano, J.; Kam, L.; Hone, J.; Sheetz, M. P.; Wind, S. J. Fabrication and Surface Chemistry of Nanoscale Bioarrays Designed for the Study of Cytoskeletal Protein Binding Interactions and Their Effect on Cell Motility. *Journal of Vacuum Science & Technology B* **2005**, *23* (6), 2972–2978.
(293) Delcassian, D.; Depoil, D.; Rudnicka, D.; Liu, M.; Davis, D. M.; Dustin, M. L.; Dunlop, I. E. Nanoscale Ligand Spacing Influences Receptor Triggering in T Cells and NK Cells. *Nano Lett.* **2013**, *13* (11), 5608–5614.
(294) Hell, S. W. Microscopy and Its Focal Switch. *Nat Meth* **2009**, *6* (1), 24–32.
(295) Huang, B.; Bates, M.; Zhuang, X. Super Resolution Fluorescence Microscopy. *Annu Rev Biochem* **2009**, *78*, 993–1016.
(296) Betzig, E.; Hell, S. W.; Moerner, W. E. The Nobel Prize in Chemistry 2014 http://www.nobelprize.org/nobel_prizes/chemistry/laureates/2014/press.html.
(297) Single-Molecule Localization Microscopy in Eukaryotes - Chemical Reviews (ACS Publications) https://pubs-acs-org.login.ezproxy.library.ualberta.ca/doi/full/10.1021/acs.chemrev.6b00667 (accessed Mar 17, 2018).
(298) Hell, S. W.; Sahl, S. J.; Bates, M.; Zhuang, X.; Heintzmann, R.; Booth, M. J.; Joerg Bewersdorf; Shtengel, G.; Hess, H.; Tinnefeld, P.; et al. The 2015 Super-Resolution Microscopy Roadmap. *J. Phys. D: Appl. Phys.* **2015**, *48* (44), 443001.
(299) Tijore, A.; Hariharan, S.; Yu, H.; Lam, C. R. I.; Wen, F.; Tay, C. Y.; Ahmed, S.; Tan, L. P. Investigating the Spatial Distribution of Integrin Β1 in Patterned Human Mesenchymal Stem Cells Using Super-Resolution Imaging. *ACS Appl. Mater. Interfaces* **2014**, *6* (18), 15686–15696.
(300) Chien, F.-C.; Kuo, C. W.; Yang, Z.-H.; Chueh, D.-Y.; Chen, P. Exploring the Formation of Focal Adhesions on Patterned Surfaces Using Super-Resolution Imaging. *Small* **2011**, *7* (20), 2906–2913.
(301) XV.—The Relation of Aperture and Power in the Microscope (continued) - Abbe - 1883 - Journal of Microscopy - Wiley Online Library http://onlinelibrary.wiley.com.login.ezproxy.library.ualberta.ca/doi/10.1111/j.1365-2818.1883.tb05956.x/abstract (accessed Jan 7, 2018).

(302) Dai, M.; Jungmann, R.; Yin, P. Optical Imaging of Individual Biomolecules in Densely Packed Clusters. *Nature Nanotechnology* **2016**, *11* (9), 798.
(303) Rust, M. J.; Bates, M.; Zhuang, X. Sub-Diffraction-Limit Imaging by Stochastic Optical Reconstruction Microscopy (STORM). *Nat Meth* **2006**, *3* (10), 793–796.
(304) Betzig, E.; Patterson, G. H.; Sougrat, R.; Lindwasser, O. W.; Olenych, S.; Bonifacino, J. S.; Davidson, M. W.; Lippincott-Schwartz, J.; Hess, H. F. Imaging Intracellular Fluorescent Proteins at Nanometer Resolution. *Science* **2006**, *313* (5793), 1642–1645.
(305) van de Linde, S.; Löschberger, A.; Klein, T.; Heidbreder, M.; Wolter, S.; Heilemann, M.; Sauer, M. Direct Stochastic Optical Reconstruction Microscopy with Standard Fluorescent Probes. *Nat. Protocols* **2011**, *6* (7), 991–1009.
(306) Yang, X.; Zhanghao, K.; Wang, H.; Liu, Y.; Wang, F.; Zhang, X.; Shi, K.; Gao, J.; Jin, D.; Xi, P. Versatile Application of Fluorescent Quantum Dot Labels in Super-Resolution Fluorescence Microscopy. *ACS Photonics* **2016**, *3* (9), 1611–1618.
(307) Vogelsang, J.; Steinhauer, C.; Forthmann, C.; Stein, I. H.; Person-Skegro, B.; Cordes, T.; Tinnefeld, P. Make Them Blink: Probes for Super-Resolution Microscopy. *ChemPhysChem* **2010**, *11* (12), 2475–2490.
(308) Holden, S.; Sage, D. Imaging: Super-Resolution Fight Club. *Nat Photon* **2016**, *10* (3), 152–153.
(309) Single-Molecule Localization Microscopy • Software Benchmarking http://bigwww.epfl.ch/smlm/challenge2016/index.html (accessed Mar 17, 2018).
(310) Schmied, J. J.; Raab, M.; Forthmann, C.; Pibiri, E.; Wünsch, B.; Dammeyer, T.; Tinnefeld, P. DNA Origami–Based Standards for Quantitative Fluorescence Microscopy. *Nat. Protocols* **2014**, *9* (6), 1367–1391.
(311) Palma, M.; Abramson, J.; Gorodetsky, A.; Nuckolls, C.; Sheetz, M. P.; Wind, S. J.; Hone, J. Controlled Confinement of DNA at the Nanoscale: Nanofabrication and Surface Bio-Functionalization. *Methods Mol Biol* **2011**, *749*, 169–185.
(312) Gokan, H.; Esho, S.; Ohnishi, Y. Dry Etch Resistance of Organic Materials. *J. Electrochem. Soc.* **1983**, *130* (1), 143–146.
(313) Chang, T. H. P. Proximity Effect in Electron‐beam Lithography. *Journal of Vacuum Science and Technology* **1975**, *12* (6), 1271–1275.
(314) Mattheyses, A. L.; Simon, S. M.; Rappoport, J. Z. Imaging with Total Internal Reflection Fluorescence Microscopy for the Cell Biologist. *J Cell Sci* **2010**, *123* (21), 3621–3628.
(315) Huang, B.; Wang, W.; Bates, M.; Zhuang, X. Three-Dimensional Super-Resolution Imaging by Stochastic Optical Reconstruction Microscopy. *Science* **2008**, *319* (5864), 810–813.
(316) Dempsey, G. T.; Bates, M.; Kowtoniuk, W. E.; Liu, D. R.; Tsien, R. Y.; Zhuang, X. Photoswitching Mechanism of Cyanine Dyes. *J. Am. Chem. Soc.* **2009**, *131* (51), 18192–18193.
(317) Heilemann, M.; Margeat, E.; Kasper, R.; Sauer, M.; Tinnefeld, P. Carbocyanine Dyes as Efficient Reversible Single-Molecule Optical Switch. *J. Am. Chem. Soc.* **2005**, *127* (11), 3801–3806.
(318) Zanetti-Domingues, L. C.; Martin-Fernandez, M. L.; Needham, S. R.; Rolfe, D. J.; Clarke, D. T. A Systematic Investigation of Differential Effects of Cell Culture Substrates on the Extent of Artifacts in Single-Molecule Tracking. *PLoS One* **2012**, *7* (9).

(319) Groll, J.; Moeller, M. Chapter 1 - Star Polymer Surface Passivation for Single-Molecule Detection. In *Methods in Enzymology*; Walter, N. G., Ed.; Single Molecule Tools: Fluorescence Based Approaches, Part A; Academic Press, 2010; Vol. 472, pp 1–18.

(320) Hua, B.; Han, K. Y.; Zhou, R.; Kim, H.; Shi, X.; Abeysirigunawardena, S. C.; Jain, A.; Singh, D.; Aggarwal, V.; Woodson, S. A.; et al. An Improved Surface Passivation Method for Single-Molecule Studies. *Nat Meth* **2014**, *11* (12), 1233–1236.

(321) Tessler, L. A.; Donahoe, C. D.; Garcia, D. J.; Jun, Y.-S.; Elbert, D. L.; Mitra, R. D. Nanogel Surface Coatings for Improved Single-Molecule Imaging Substrates. *Journal of The Royal Society Interface* **2011**, *8* (63), 1400–1408.

(322) Chaumont, F. de; Dallongeville, S.; Chenouard, N.; Hervé, N.; Pop, S.; Provoost, T.; Meas-Yedid, V.; Pankajakshan, P.; Lecomte, T.; Montagner, Y. L.; et al. Icy: An Open Bioimage Informatics Platform for Extended Reproducible Research. *Nature Methods* **2012**, *9* (7), 690.

(323) Palma, M.; Abramson, J. J.; Gorodetsky, A. A.; Nuckolls, C.; Sheetz, M. P.; Wind, S. J.; Hone, J. Controlled Confinement of DNA at the Nanoscale: Nanofabrication and Surface Bio-Functionalization. In *DNA Nanotechnology*; Zuccheri, G., Samorì, B., Eds.; Methods in Molecular Biology; Humana Press, 2011; pp 169–185.

(324) Cox, S.; Rosten, E.; Monypenny, J.; Jovanovic-Talisman, T.; Burnette, D. T.; Lippincott-Schwartz, J.; Jones, G. E.; Heintzmann, R. Bayesian Localization Microscopy Reveals Nanoscale Podosome Dynamics. *Nat Meth* **2012**, *9* (2), 195–200.

(325) Hu, Y. S.; Nan, X.; Sengupta, P.; Lippincott-Schwartz, J.; Cang, H. Accelerating 3B Single-Molecule Super-Resolution Microscopy with Cloud Computing. *Nature Methods* **2013**, *10* (2), 96.

(326) Pan, H.; Xia, Y.; Qin, M.; Cao, Y.; Wang, W. A Simple Procedure to Improve the Surface Passivation for Single Molecule Fluorescence Studies. *Phys. Biol.* **2015**, *12* (4), 045006.

(327) Funatsu, T.; Harada, Y.; Tokunaga, M.; Saito, K.; Yanagida, T. Imaging of Single Fluorescent Molecules and Individual ATP Turnovers by Single Myosin Molecules in Aqueous Solution. *Nature* **1995**, *374* (6522), 555–559.

(328) Granéli, A.; Yeykal, C. C.; Prasad, T. K.; Greene, E. C. Organized Arrays of Individual DNA Molecules Tethered to Supported Lipid Bilayers. *Langmuir* **2006**, *22* (1), 292–299.

(329) Howorka, S.; Hesse, J. Microarrays and Single Molecules: An Exciting Combination. *Soft Matter* **2014**, *10* (7), 931.

(330) Jungmann, R.; Steinhauer, C.; Scheible, M.; Kuzyk, A.; Tinnefeld, P.; Simmel, F. C. Single-Molecule Kinetics and Super-Resolution Microscopy by Fluorescence Imaging of Transient Binding on DNA Origami. *Nano Letters* **2010**, *10* (11), 4756–4761.

(331) Super-Resolution Fingerprinting Detects Chemical Reactions and Idiosyncrasies of Single DNA Pegboards - Nano Letters (ACS Publications) https://pubs-acs-org.login.ezproxy.library.ualberta.ca/doi/full/10.1021/nl304415b (accessed Mar 17, 2018).

(332) Visnapuu, M.-L.; Duzdevich, D.; Greene, E. C. The Importance of Surfaces in Single-Molecule Bioscience. *Mol Biosyst* **2008**, *4* (5), 394–403.

(333) Dunne, J.; Drescher, B.; Riehle, H.; Hadwiger, P.; Young, B. D.; Krauter, J.; Heidenreich, O. The Apparent Uptake of Fluorescently Labeled SiRNAs by Electroporated Cells Depends on the Fluorochrome. *Oligonucleotides* **2003**, *13* (5), 375–380.

(334) Hughes, L. D.; Rawle, R. J.; Boxer, S. G. Choose Your Label Wisely: Water-Soluble Fluorophores Often Interact with Lipid Bilayers. *PLoS One* **2014**, *9* (2).
(335) Lu, T.; Lin, Z.; Ren, J.; Yao, P.; Wang, X.; Wang, Z.; Zhang, Q. The Non-Specific Binding of Fluorescent-Labeled MiRNAs on Cell Surface by Hydrophobic Interaction. *PLOS ONE* **2016**, *11* (3), e0149751.
(336) Zanetti-Domingues, L. C.; Tynan, C. J.; Rolfe, D. J.; Clarke, D. T.; Martin-Fernandez, M. Hydrophobic Fluorescent Probes Introduce Artifacts into Single Molecule Tracking Experiments Due to Non-Specific Binding. *PLoS One* **2013**, *8* (9).
(337) Daniels, C. R.; Reznik, C.; Landes, C. F. Dye Diffusion at Surfaces: Charge Matters. *Langmuir* **2010**, *26* (7), 4807–4812.
(338) Helenius, J.; Brouhard, G.; Kalaidzidis, Y.; Diez, S.; Howard, J. The Depolymerizing Kinesin MCAK Uses Lattice Diffusion to Rapidly Target Microtubule Ends. *Nature* **2006**, *441* (7089), 115–119.
(339) Rider, D. A.; Harris, K. D.; Wang, D.; Bruce, J.; Fleischauer, M. D.; Tucker, R. T.; Brett, M. J.; Buriak, J. M. Thienylsilane-Modified Indium Tin Oxide as an Anodic Interface in Polymer/Fullerene Solar Cells. *ACS Appl. Mater. Interfaces* **2009**, *1* (2), 279–288.
(340) Muhammad, M.; Buswell, S. C.; Dew, S. K.; Stepanova, M. Nanopatterning of PMMA on Insulating Surfaces with Various Anticharging Schemes Using 30 KeV Electron Beam Lithography. *Journal of Vacuum Science & Technology B* **2011**, *29* (6), 06F304.
(341) Dedecker, P.; Duwé, S.; Neely, R. K.; Zhang, J. Localizer: Fast, Accurate, Open-Source, and Modular Software Package for Superresolution Microscopy. *JBO, JBOPFO* **2012**, *17* (12), 126008.
(342) Mortensen, K. I.; Churchman, L. S.; Spudich, J. A.; Flyvbjerg, H. Optimized Localization Analysis for Single-Molecule Tracking and Super-Resolution Microscopy. *Nat Meth* **2010**, *7* (5), 377–381.
(343) Verwey, E. J. W.; Overbeek, J. T. G.; Nes, K. van. *Theory of the Stability of Lyophobic Colloids: The Interaction of Sol Particles Having an Electric Double Layer*; Elsevier Publishing Company, 1948.
(344) Van Oss, C. J. *Interfacial Forces in Aqueous Media*, 2nd ed.; Taylor & Francis,: Boca Raton, Fla. :, 2006.
(345) Derjaguin: Theory of stability of highly charged... - Google Scholar https://scholar.google.com/scholar_lookup?author=BV.%20Derjaguin&author=LD.%20Landau&journal=Zh.%20Eksp.%20Teor.%20Fiz&volume=15&pages=663&publication_year=1945 (accessed Mar 17, 2018).
(346) Suresh, L.; Walz, J. Y. Effect of Surface Roughness on the Interaction Energy between a Colloidal Sphere and a Flat Plate. *Journal of Colloid and Interface Science* **1996**, *183* (1), 199–213.
(347) Jain, I. P.; Lal, C.; Jain, A. Hydrogen Storage in Mg: A Most Promising Material. *International Journal of Hydrogen Energy* **2010**, *35* (10), 5133–5144.
(348) Haagsma, J. Sputtered Magnesium Aluminum and Magnesium Aluminum Titanium Alloys for Hydrogen Storage, University of Alberta: Edmonton, 2011.
(349) Liu, Y.; Park, J.; Chang, J. H. C.; Tai, Y. C. Thin-Film Magnesium as a Sacrificial and Biodegradable Material. In *2014 IEEE 27th International Conference on Micro Electro Mechanical Systems (MEMS)*; 2014; pp 656–659.

(350) Walker, P.; Tarn, W. H. *CRC Handbook of Metal Etchants*; CRC Press: Boca Raton, 1991.
(351) *Handbook of Chemistry and Physics : A Ready-Reference Book of Chemical and Physical Data.*; Chemical Rubber Co.,: Cleveland :, 2004.
(352) Currivan, J. A.; Siddiqui, S.; Ahn, S.; Tryputen, L.; Beach, G. S. D.; Baldo, M. A.; Ross, C. A. Polymethyl Methacrylate/Hydrogen Silsesquioxane Bilayer Resist Electron Beam Lithography Process for Etching 25 Nm Wide Magnetic Wires. *Journal of Vacuum Science & Technology B* **2014**, *32* (2), 021601.
(353) Rommel, M.; Weis, J. Hydrogen Silsesquioxane Bilayer Resists—Combining High Resolution Electron Beam Lithography and Gentle Resist Removal. *Journal of Vacuum Science & Technology B* **2013**, *31* (6), 06F102.
(354) Tsang, M.; Herrault, F.; Shafer, R. H.; Allen, M. G. Methods for the Microfabrication of Magnesium. In *2013 IEEE 26th International Conference on Micro Electro Mechanical Systems (MEMS)*; 2013; pp 347–350.
(355) Passi, V.; Lecestre, A.; Krzeminski, C.; Larrieu, G.; Dubois, E.; Raskin, J.-P. A Single Layer Hydrogen Silsesquioxane (HSQ) Based Lift-off Process for Germanium and Platinum. *Microelectronic Engineering* **2010**, *87* (10), 1872–1878.
(356) Elsner, H.; Meyer, H.-G.; Voigt, A.; Grützner, G. Evaluation of Ma-N 2400 Series DUV Photoresist for Electron Beam Exposure. *Microelectronic Engineering* **1999**, *46* (1), 389–392.
(357) Byun, I.; Coleman, A. W.; Kim, B. Transfer of Thin Au Films to Polydimethylsiloxane (PDMS) with Reliable Bonding Using (3-Mercaptopropyl)Trimethoxysilane (MPTMS) as a Molecular Adhesive. *J. Micromech. Microeng.* **2013**, *23* (8), 085016.
(358) Jiang, M.; Kurvits, J. A.; Lu, Y.; Nurmikko, A. V.; Zia, R. Reusable Inorganic Templates for Electrostatic Self-Assembly of Individual Quantum Dots, Nanodiamonds, and Lanthanide-Doped Nanoparticles. *Nano Lett.* **2015**, *15* (8), 5010–5016.
(359) Schmied, J. J.; Forthmann, C.; Pibiri, E.; Lalkens, B.; Nickels, P.; Liedl, T.; Tinnefeld, P. DNA Origami Nanopillars as Standards for Three-Dimensional Superresolution Microscopy. *Nano Lett.* **2013**, *13* (2), 781–785.
(360) Lyu, M.; Wang, W.; Wang, H.; Wang, H.; Li, G.; Chen, N.; Situ, G. Deep-Learning-Based Ghost Imaging. *Scientific Reports* **2017**, *7* (1), 17865.